RARE ISOTOPE PRODUCTION

By

Michal Mocko

A DISSERTATION

Submitted to
Michigan State University
in partial fulfillment of the requirements
for the degree of

DOCTOR OF PHILOSOPHY

Department of Physics and Astronomy

2006

ABSTRACT

RARE ISOTOPE PRODUCTION

By

Michal Mocko

Projectile fragmentation is one of the prominent methods of rare isotope beam production. A series of projectile fragmentation experiments have been performed using ^{40}Ca, ^{48}Ca, ^{58}Ni, and ^{64}Ni primary beams at 140 MeV/u and ^{86}Kr at 64 MeV/u. Two targets: ^{9}Be and ^{181}Ta were used in the present experiments in order to investigate the target and projectile dependence of the fragmentation production cross sections. The study resulted in 1740 measured cross sections created in reactions of 10 systems.

The fitted parameters of the momentum distributions are compared to the systematics and parameterizations derived from the high energy projectile or target fragmentation reactions. Extracted width parameter corresponding to the "pure" fragmentation component of the momentum distribution is in good agreement with the limiting fragmentation models, and consistent with the relativistic energy projectile fragmentation experiments. The fragmentation cross sections are reproduced well by the empirical parameterization EPAX, while discrepancies in tails of the isotopic distributions and for elements close to the neutron-rich projectiles were observed.

Fragmentation cross section target dependence is more complex than the trend suggested by the limiting fragmentation framework. Nevertheless the rather small enhancement of the fragmentation cross section when using ^{181}Ta target does not translate to the production yields because of relatively small atom density in tantalum versus beryllium material. The projectile dependence of the fragmentation cross section resembles isoscaling for light fragments but is more complicated for heavier fragments.

Calculations by three different theoretical models are presented. A macroscopic geometrical Abrasion-Ablation model results in excellent reproduction of the cross section distribution, with only two fitted parameters for each reaction system. A macroscopic-microscopic Heavy Ion Phase Space Exploration (HIPSE) model yields very good description of the fragment velocity distributions for all reaction systems involving ^{9}Be target, but fails in the case of ^{181}Ta target showing the limits of its applicability. A more sophisticated microscopic Antisymmetrized Molecular Dynamics (AMD) calculation can only be applied to reaction systems containing ^{9}Be target. The AMD does not reproduce the fragment velocity distributions. However, its description of the fragmentation cross sections is similar in quality as the HIPSE model comparison.

to my wife Veronika

ACKNOWLEDGMENTS

I would like to start by thanking my Ph.D. supervisor Professor M. Betty Tsang for providing the opportunity to do my dissertation research at the NSCL. I was fortunate enough to join a new project on projectile fragmentation that she had started only a short time before I came to MSU. I really appreciate her determination and persistence in whatever she does: starting with the experiments and ending with the data analysis. Her ability to get things "organized" and "done" is admirable. I have learned a lot about doing data analysis by working with her. I would like to thank her for the continuing support and guidance during my stay at MSU.

Being a part of the HiRA group headed by Professor W. G. Lynch really broadened my experience, by giving me the ability to help to work on development of a new detector system like the High Resolution Array. Even though I worked on a different project than the rest of the HiRA, they never let me feel isolated. It has been my privilege to work with a group of people like them. Over the years the group had its share of postdocs coming through, and all of them are people I enjoyed working and interacting with. Any question or problem related to my data analysis or issues with PAW were always answered by Giuseppe Verde. I enjoyed having Marc-Jan van Goethem as a friend and colleague, and being able to discuss anything from the most compelling physics questions to chatting over a cup of good coffee. Michael Famiano is the most hard working person I have met in my life. Despite his very busy schedule he got me started with object-oriented data analysis using the ROOT framework, and he always found time to address the endless problems I experienced in the beginning.

All of this probably would not be possible without my very good friend and "coffee buddy" Mark Wallace. He has been greatly helpful since my joining of the HiRA group. He always found time to help or explain things I could not grasp. I really enjoyed having him at RIKEN for one of our projectile fragmentation experiments.

Life would have been much tougher without our regular 10 o'clock coffee.

I am thankful to Ingo Wiedenhöver for allowing me to work with him and introducing me to the A1900 fragment separator during the busy commissioning period. I am grateful for the opportunity to work with Andreas Stolz. He helped me to understand the A1900 and has always been there when I needed help, whether it be the analysis and understanding the data acquisition or any kind of *physics* question. He even squeezed the proofreading of this manuscript to his already very busy schedule! I would also like to thank other members of the A1900 group at the NSCL: Thomas Baumann, Thomas Ginter, Mauricio Portillo and Mathias Steiner.

I am indebted to Prof. Hiroyoshi Sakurai and Nori Aoi for their invaluable help and providing very hospitable environment for me and my colleagues during our fragmentation experiment at RIPS fragment separator at RIKEN. I want to acknowledge all postdocs, graduate students and staff scientists working at Radioactive Isotope Physics Laboratory at RIKEN for their help and support during my stay in Wakoshi.

I am grateful to Mikhail and Lyudmila Andronenko and Hui Hua for their help during the data analysis. I really appreciate the help of Sergei Lukyanov, who carefully checked every single momentum distribution (out of 1740) presented in this dissertation. Oleg Tarasov's help was indispensable, especially during the first fragmentation experiments and I greatly acknowledge his help during my studies.

I would like to acknowledge also other members of the HiRA group like Andrew Rogers, Franck Delaunay, Jenny Lee, Wanapeng Tan for their support and help during my graduate studies. I acknowledge the help of fellow graduate students Jeremy Armstrong and Ivan Brida with reading the manuscript of this dissertation.

The dissertation would not be complete without the extensive calculations I have done in order to understand the experimental data. I enjoyed interacting and working with many theorists, and this experience definitely deepened and broadened my understanding of the physics of nuclear reactions. I hereby want to express my thanks

and gratitude to Akira Ono for his help with the AMD code, Denis Lacroix for introducing me to his HIPSE model, Bob Charity for many useful discusions and help using GEMINI, and Pawel Danielewicz for his support and fruitful discussions.

Last, but not least I want to thank my parents Miroslav and Anna Mocko for always being there for me and for their continuous support and help. I am grateful to my wife Veronika for her endless love, support and belief in me.

Contents

List of Figures

IMAGES IN THIS DISSERTATION ARE PRESENTED IN COLOR

List of Tables

Chapter 1

Introduction

The nucleus is the core of the atom. Containing more than 99.9% of the atom's mass, the nucleus defines its center and influences the chemical properties of the atom through its electrical charge. A nucleus is composed of Z protons and N neutrons which determine its mass number $A = N + Z$. Since the protons and neutrons have similar mass and behave similarly in the realm of the strong interaction they are called nucleons. They themselves have a sub-structure, quarks and gluons, with the gluons holding the quarks together in a tightly bound entity [1–3]. This results in the attractive force between nucleons as the residue of the quark and gluon interactions [4].

Nuclei come in a large variety of combinations of protons and neutrons. However, due to fundamental laws of nature, which are still being investigated, not all combinations are possible. Figure 1.1 illustrates the landscape of those nuclei that we presently think might exist in a map spanned by the number of protons on one axis and the number of neutrons on the other. This landscape shows several thousands of nuclei that are expected to be bound by the strong force. Of these, slightly fewer than 300 isotopes make up the assortment of the 82 stable elements (marked as black squares in Figure 1.1) that exist in nature. When displayed in the representation of a nuclear landscape, these stable isotopes lie along a slightly curved line, called the line of stability (or the valley of stability) [6]. There are thousands of unstable nuclides

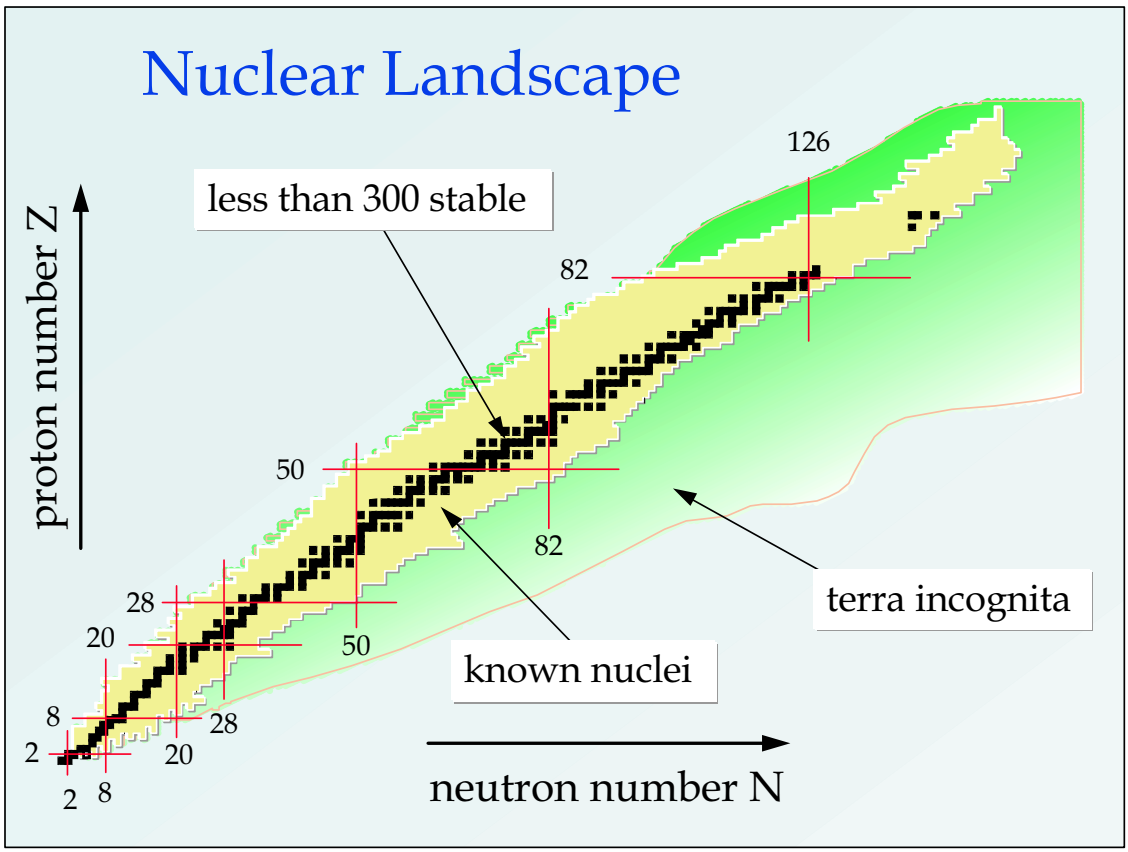

Figure 1.1: Nuclear landscape — nuclei shown in proton versus neutron number representation [5].

which are bound against the release of protons and neutrons, but they are subject to α [7] and/or β [8] decay. Some of the unstable nuclei have very long half lives and can be found on Earth. Others are man-made, while thousands more have not been discovered. The yellow region in Figure 1.1 indicates short lived nuclei that have been produced in laboratories. By adding either protons or neutrons one moves away from the valley of stability, finally reaching what is referred to as the drip lines [9] where the nuclear binding ends because the forces between the neutrons and protons are no longer strong enough to hold these particles together.

Many thousands of radioactive nuclei with very small or very large N/Z ratios are yet to be explored. In the nuclear landscape they form the *terra incognita* indicated in green [10]. The proton drip line has been reached experimentally for all odd Z nuclei up to $Z = 91$ [11], because the long range Coulomb repulsion among the protons

prohibits formation of extremely proton-rich nuclides. In contrast, the neutron drip line is considerably further away from the valley of stability [11], hence harder to approach. Except for the lightest nuclei where it has been reached experimentally, the neutron drip line is estimated on the basis of nuclear models, therefore it is very uncertain due to the extrapolations involved.

The red lines in Figure 1.1 show the "magic numbers" known around the valley of stability [12]. However, since the structure of nuclei is expected to change significantly as the drip lines are approached, we do not know how nuclear shell structure evolves at the extreme nuclear asymmetries.

For decades, nuclear physics experiments have been performed with reactions between beams and targets of stable nuclei found in nature. Basic properties of the atomic nuclei have been discovered and many fundamental models developed (e. g., Weizsäcker mass formula [13], shell model [6], etc.). In order to understand nuclear matter, we need to explore and study not only the properties of stable nuclei, but also those close to the limits of nuclear existence. These investigations of unstable nuclei pose a great experimental challenge. Such studies at the extremes will provide important insights into the structure of nuclei, the dynamics of nuclear reactions, the underlying symmetries of nature, and the nucleus as a fundamental many-body system governed by the strong interaction. With recent developments in heavy-ion accelerators and rare isotope beam production many new surprising phenomena have been observed in unstable nuclei (e. g., neutron halo [14], neutron and proton skins of nuclei far from stability [15, 16], large deformations of neutron rich isotopes [17], etc.).

Further study of the unexplored regions of the nuclear landscape will provide answers to many important questions outlined in the "Scientific opportunities with Fast Fragmentation Beams from RIA" [18]:

- What is the origin of the elements in the cosmos?

- Where are the limits of nuclear existence?
- What are the properties of nuclei with extreme N/Z ratios?
- What are the properties of bulk neutron-rich matter under extreme conditions of temperature and density?
- How must existing theoretical models be changed to describe the properties of rare isotopes?
- How are the properties of rare isotopes related to the basic nucleon-nucleon interaction?

Projectile fragmentation reactions serve as an important tool for producing the rare isotope beams used in a wide variety of experiments looking for answers to the above mentioned questions. The presented dissertation explores the fragmentation reaction mechanisms, to better understand and optimize the production of rare isotopes. It allows experimenters to better estimate and optimize the yields of the rare ion beams available for their studies.

Understanding fragmentation reactions is not only important for the fundamental science experiments investigating new phenomena with exotic isotope species, but is also needed in many applications. Three concrete applications of fragmentation reactions will be mentioned here briefly: space radiation, heavy-ion therapy and nuclear waste transmutation.

Space radiation consists of many components, from which the high energy and high-charge ions constitute about 1%. High energy highly charged ions possess significantly higher ionizing power this means they have a greater potential for radiation-induced damage. Since nuclear fragmentation is an important reaction mechanism for these relativistic heavy ions, better understanding and modeling of these processes is very important [19]. Realistic simulations of the radiation damage to equipment and humans are essential for the success of any space missions that last an extensive period

of time. Realizing that there is a lack of experimental data, NASA joined efforts with the Brookhaven National Laboratory in building the NASA Space Radiation Laboratory (NSRL) in Brookhaven, New York [20]. The new facility will study the reactions of heavy ions in various biological materials (tissues, cells or DNA in solution). It also evaluates industrial samples for their suitability in spacecraft shielding.

Heavy-ion therapy is a new emerging technique to treat tumors resistant to other conventional treatment methods. Close to the end of a heavy-ion track, there is a well localized energy deposition by the ion. This maximum in the stopping power is called the Bragg peak. When positioned properly, the peak concentrates the damage to the tumor tissue and minimizes the radiobiological effects to the surrounding tissue [21]. Fragmentation of the heavy-ion beams used to treat tumors may produce lighter isotopic species that may penetrate deeper into the healthy tissue. The energy deposited by the beam and the produced ions causes a severe damage to both helices of the DNA of a cell nucleus, also referred to as "double strand breaks" [22]. Therefore, energy and mass of the treatment means used are constrained by the number of the fragment species created in the treatment tissue. Better understanding of the fragmentation reaction mechanism improves calculations of the radiation damage inflicted by the fragments of the treatment heavy-ion beam. A pilot program of treatment using relativistic ions of ^{12}C was started in 1997 at GSI in Darmstadt, Germany [23]. Based on the results of this project, a new cancer therapy center [24] is under construction in Heidelberg, Germany.

Nuclear waste is predominantly comprised of used fuel discharged from operating reactors. Almost all issues related to risks arising from long-term disposal of spent nuclear fuel are attributable to about 1% of its content [25]. This small fraction consists of transuranic elements and long-lived isotopes of iodine and technetium. Transmutation [26] of these isotopes by a proton beam can decrease the toxic nature of the spent fuel below that of natural uranium ore, reducing the challenges associated with long-term storage. In order to optimize the nuclear waste transmutation

it is very important to study and understand the spallation (target fragmentation) reaction mechanism. Realizing the difficulties connected with long-term storage of the nuclear waste materials, large collaborations such as the Advanced Fuel Cycle Initiative at Los Alamos National Laboratory [27] have been formed to identify the relevant cross sections and thereby address the scientific questions concerning the nuclear waste transmutation as a solution of the nuclear waste problem.

These three examples of nuclear fragmentation applications are by no means exhaustive; they only illustrate the broad impact of the fragmentation reaction research in human society. This dissertation, however, focuses mainly on the study of cross sections and the reaction mechanism of projectile fragmentation reactions in basic science.

1.1 Rare isotope beam production

The two most prominent techniques to produce rare isotope beams are Isotope Separation On-Line (ISOL) and in-flight Projectile Fragmentation (PF) [28]. The underlying principle of the production of the exotic nuclei is to transform the stable nuclei into unstable species using nuclear reactions.

In an ISOL facility the radioactive nuclei are produced essentially at rest in a thick target by bombardment with particles from a driver accelerator. After ionization and mass separation, the nuclei of rare isotopes are accelerated in a post-accelerator (see the left panel of Figure 1.2). A wide range of primary beams including thermal neutrons [29], high energy protons [30], intermediate energy heavy ions [31] can be used as projectiles. For the thick target construction high Z materials are used such as tantalum or uranium. Similarly a range of different types of post-accelerators are being used including cyclotrons [32], linacs [33], and tandem accelerators [34].

Post-accelerators — optimized for high quality beams — provide easy energy variability, high energy precision and small emittances. These characteristics are re-

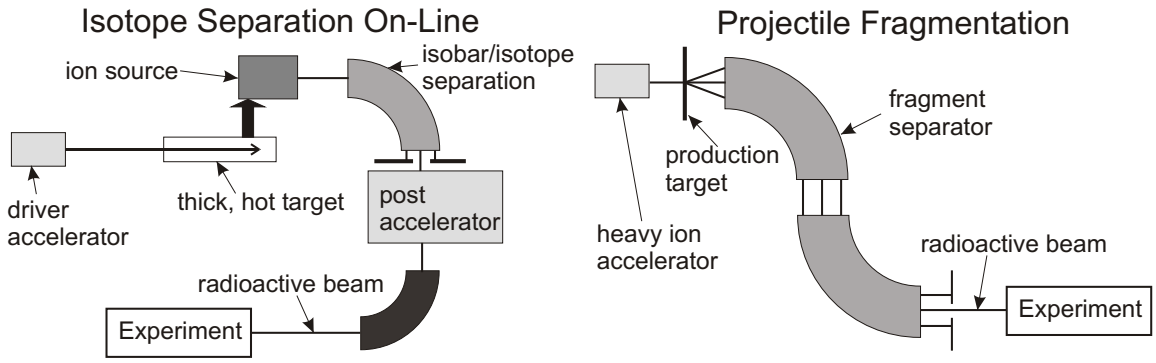

Figure 1.2: Schematic representation of an ISOL (left) and an in-flight Projectile Fragmentation (right) technique to produce rare isotope beams.

quired by many experiments in nuclear structure and nuclear astrophysics. Another advantage of ISOL facilities is the high luminosity that can be achieved through the combination of a thick production target and a very intense primary beam. The time delay resulting from the stopping, ionization and extraction of the radioactive fragments from the production target and forming a secondary ion beam limits the production of particularly short-lived rare isotope beams. The extraction of the rare isotope species from the target material is done using chemical methods which make the whole process charge, Z, dependent. Modern day facilities that use this production technique include: the REX-ISOLDE facility [33] at CERN in Geneva, Switzerland and the ISAC facility [30] at TRIUMF in Vancouver, Canada.

In an in-flight PF facility, as illustrated in the right panel of Figure 1.2, an energetic heavy-ion beam is fragmented when it interacts with a (production) target. The desired reaction products are subsequently transported to an experiment after mass, charge and momentum selection in a fragment separator. In-flight fission of very heavy beams, and also charge exchange and transfer reactions, have been used as an alternative to projectile fragmentation. The high energy that the fragments automatically carry from the primary beam in this production method, eliminates the need for post-acceleration. The in-flight production also means that the experiments with radioactive fragments as a secondary beam can be done promptly. Because they

are only delayed by the flight time through the separator and beam line system, typically < 1 μs, production of very short-lived exotic nuclides is possible. Contemporary facilities using the PF method of rare isotope beam production include: Riken Accelerator Research Facility (RARF) [35] at RIKEN in Wako-shi, Japan and the Coupled Cyclotron Facility (CCF) [36] at NSCL in East Lansing, MI.

These two techniques of rare isotope beam production are, in many respects, complementary. Different classes of experiments impose very different requirements on rare isotope beams in terms of velocity, momentum and angular spread and purity, allowing experimenters to choose the most suitable secondary beam production method possible.

1.2 Projectile fragmentation reactions

Nuclear reaction [37] is the single most important technique to probe the fundamental properties of nuclear matter. Nuclear collisions are usually classified according to the impact parameter and the incident energy of the projectile. We associate peripheral collisions with large impact parameters and central collisions with small impact parameters. In terms of the kinetic energy the collisions are usually categorized as low ($<$ 20 MeV/u), intermediate (20–200 MeV/u) and high energy ($>$200 MeV/u). Projectile fragmentation reactions are peripheral collisions of heavy ions at intermediate to high energies, when the projectile breaks up — fragments into one or more heavy ions — on impact with the target nucleus. More central collisions of heavy ions in intermediate to high energy regime, also referred to as multifragmentation reactions [38], occur when the interaction region of the reaction system shatters into many smaller pieces (i. e. clusters).

From the experimental viewpoint, two classes of fragmentation reactions are recognized: target fragmentation, more commonly referred to as spallation, and projectile fragmentation, as described above. These two reaction categories are identical in the

center of mass frame of reference, allowing one to use the same theoretical treatment and model description. However, the experimental techniques used in their study and the historical evolution were quite different.

Target fragmentation reactions have been investigated for more than four decades and large number of data sets are available. Many of the fragmentation models, parameterizations and systematics are based on the target spallation experimental data. Projectile fragmentation reactions were experimentally inaccessible until the 1970s when high-energy heavy-ion beams became available [39,40]. The first pioneering projectile fragmentation experiments at relativistic energies with ^{40}Ar and ^{48}Ca beams were carried out at Bevalac at Lawrence Berkeley Laboratory (LBL) [41, 42]. These experiments showed the potential of this method to produce rare isotope beams, and many fragment separators have been constructed (e. g., A1200 (Analysis 1200) at MSU [43], FRS (FRagment Separator) at GSI [44], RIPS (RIken Projectile fragment Separator) at RIKEN [35]) utilizing this technique.

The first attempts to describe the projectile fragmentation reactions were done at LBL. In 1973 Bowman, Swiatecki and Tsang introduced the Abrasion-Ablation (AA) reaction model [45]. Which forms the basis of our understanding of the fragmentation reactions. This simple model approximates the reaction in two stages; Figure 1.3 illustrates the two very distinct processes. The nuclei are treated as perfect spheres colliding on classical parallel trajectories separated by the impact parameter, b. Any alteration from the straight path is neglected in the model because it assumes that the projectile is moving with relativistic velocity. At the end of the abrasion stage the overlap (participant) region of two spherical nuclei is removed. In its simplest form, no treatment of the participant region is necessary to explain the data using the AA model. The abrasion stage ends with a deformed and highly excited prefragment which decays in the second ablation stage by evaporating light clusters, nucleons and gamma radiation. The second step of the AA model is much slower ($\approx 10^{-16}$–10^{-18} s, depending on the excitation energy) as compared to the abrasion step ($\approx 10^{-23}$ s).

Since its introduction in 1973, many different versions of the AA model have been developed. Many of these AA models differ in the second ablation stage. There is one common feature of all the AA models: the inability to predict the excitation energy of the prefragment. Most of the models rely on various parameterizations of the excitation energy and in many cases it is taken as a free parameter. The details of the AA model used in this dissertation are explained in Section 5.1.1.

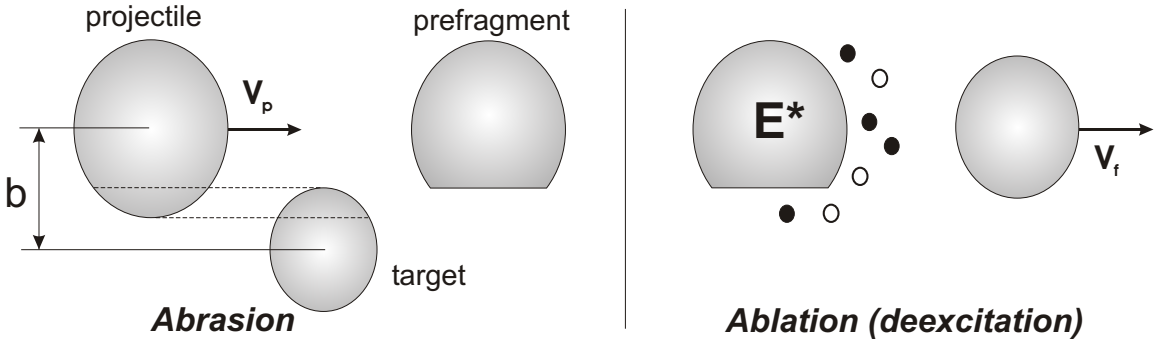

Figure 1.3: Projectile fragmentation reaction in a two step Abrasion-Ablation model.

While there are many puzzling aspects to the fragmentation phenomenon, it does display some simplifying characteristics at high incident energies. For example, many experimental observables in peripheral collisions at high incident energies (>200 MeV/u), such as charge or multiplicity distributions, vary little with incident energy and target mass. This "limiting fragmentation" behavior forms the basis for the EPAX parameterization used to calculate the secondary beam rates in many radioactive beam facilities and even the rates predicted for the next generation rare isotope facility [46]. This parameterization assumes that the isotopic distributions and their dependence on the isospin of the projectile and target are consistent with limiting fragmentation. However, EPAX derives its results from a careful empirical fit to a limited data set of production cross sections measured under a wide variety of experimental conditions. As the parameterization is not based upon a specific theory for projectile fragmentation, EPAX is better at interpolating between measured data points taken under similar conditions than at predicting the production of an isotope

further away from the valley of stability. The original EPAX parameterization [47] included only the target spallation data; it was revisited in 2000 [48] and improved by including, the contemporary projectile fragmentation data available.

The threshold energy for the limiting fragmentation is not uniquely defined and fragmentation data in the intermediate energy range are rather scarce. Very little data exist to examine the detailed dependence of isotopic distributions on target and beam in the intermediate energy regime. As Sümmerer *et al.* [48] pointed out: "It would be interesting, however, to compare EPAX also to cross sections obtained at lower incident energies once high-quality data become available.". The present study in this dissertation provides high-quality and comprehensive projectile fragmentation data at intermediate energy available from the Coupled Cyclotron Facility at the National Superconducting Cyclotron Laboratory at Michigan State University.

1.3 Organization of dissertation

The dissertation is organized in the following way. Chapter 2 introduces the experimental method used for the fragmentation measurements. The description of the fragment separators, the A1900 at the NSCL and RIPS at RIKEN, along with experimental details of the measurements are also included. Chapter 3 describes the principal steps taken in the analysis of the experimental data, emphasis is given to the discussion of the fragmentation production cross section extraction. In Chapter 4 the experimental data are presented, starting with the discussion of the momentum distributions and ending with the cross sections of fragments and nucleon pick-up reactions measured in our experiments. Three different theoretical models of fragmentation reactions are introduced in Chapter 5, along with the comparisons to the experimental data. Conclusions of the dissertation are summarized in Chapter 6. The measured experimental cross sections of fragments and nucleon pick-up products are listed in the Appendix.

Chapter 2

Experimental setup

The present experiments were carried out at two laboratories — NSCL and RIKEN. A series of four fragmentation experiments with ^{40,48}Ca and ^{58,64}Ni projectiles at 140 MeV/u using the A1900 fragment separator were carried out at the NSCL. The fragmentation experiment using the ^{86}Kr primary beam at 64 MeV/u was done at RIKEN using the RIPS fragment separator. In this chapter a description of the method of measurement is followed by introduction of the particle identification techniques common to all experiments. Since the details of the experimental setup differ, the fragment separators and the detector setups for the NSCL and RIKEN measurements are discussed separately.

2.1 Method of measurement

One of our goals is to perform comprehensive measurements of fragmentation production cross sections produced in the reactions of 5 different projectiles in intermediate energy regime. The emitted fragments were collected and identified with a fragment separator. In order to obtain the final production cross sections, one must understand how to correctly reconstruct the fragment distributions in angular and momentum coordinate spaces. The angular distributions are not directly measured in our exper-

iments and are taken as an efficiency correction from simulations and are referred to as the transmission correction in Chapter 3. The momentum distributions of fragments are measured in the magnetic field of the fragment separator. Because of the limited momentum acceptance of current fragment separators ($\approx \pm$(2–3)% around the central momentum) the momentum distributions must be measured by multiple magnetic settings of the fragment separator. In doing so, one can use two methods of obtaining the momentum distributions running the fragment separator with its full momentum acceptance or running with a narrow momentum acceptance.

The full momentum acceptance of the fragment separator is generally used in production mode to maximize the production yield of the rare isotope beams. We chose the narrow momentum acceptance mode for our experiments since the main objectives of our experiments were to measure comprehensive sets of fragmentation cross sections minimizing the associated uncertainties. The following issues have been considered in choosing the narrow momentum acceptance mode: primary beam charge states, transmission characteristics, particle identification, number of magnetic setting, optimum use of the beam intensity and the electronic dead time.

The energetic heavy ions can pick-up, exchange or loose electrons when they traverse a foil of a given material composition. These complex interactions depend on the heavy-ion energy and charge of both projectile and target. The heavy ions then emerge from the foil in different charge states — differing by number of electrons they possess. Fragment production rate is approximately 10^3–10^4 lower than the primary beam intensity or its charge states. If the full momentum acceptance of the fragment separator is used, regions of the magnetic rigidity that accepts the charge states must be blocked off. This large difference precludes the measurements of fragments and the primary beam (or its charge states) in one magnetic rigidity, $B\rho$, setting. If narrow momentum acceptance is used we can map the $B\rho$ space between the charge states of the primary beam resulting in a better optimization of the beam intensity and a reduction of the data acquisition dead time.

In order to measure the absolute fragmentation cross sections, we need to understand the transmission characteristics of the fragment separator. These characteristics express the efficiency of our measurement. With the full momentum acceptance we are also filling the spatial acceptance of the fragment separator. Optical abberations start to play more important role for particles traveling farther away from the optical axis of the separator. On the other hand if we restrict ourselves to a narrow momentum acceptance we are limited to particles traveling very close to the optical axis of the separator and therefore minimizing the effects of the optical abberations. The experimental measurement of the transmission is very difficult because it requires accurately knowing the cross sections. The transmission is determined by an ion-optical calculation. Transmission for particles within the narrow momentum acceptance of the fragment separator can be simulated more accurately. This consideration favors narrow momentum acceptance mode.

With wide momentum acceptance, particle identification requires a measurement of the magnetic rigidity at the dispersive image plane, to correct for the different particle trajectories. In narrow momentum acceptance mode no additional position sensitive detectors are required at the dispersive image plane, because the particles are bound to very similar trajectories and the momentum is determined by the magnetic rigidity setting of the fragment separator. This consideration again favors narrow momentum acceptance mode.

One disadvantage of narrow momentum acceptance is that it requires more magnetic settings of the fragment separator compared to the wide momentum acceptance to cover the same range in $B\rho$. But with narrow momentum acceptance we gain other advantages: measurement between the charge states of the primary beam, easier particle identification, and better utilization of the beam time (data acquisition dead time characteristics).

2.2 Particle identification

Particle identification was obtained by using the $B\rho$-ToF-ΔE-TKE method [44] on an event-by-event basis. The magnetic rigidity, $B\rho$, was given by the magnetic setting of the fragment separator. Fragment time of flight, ToF, energy loss , ΔE, and total kinetic energy, TKE, were measured by charged-particle detectors. The determination of these four quantities $B\rho$, ToF, ΔE, TKE defines unambiguously the momentum, p, mass and charge numbers A and Z along with the charge state, Q, for every ion.

The magnetic rigidity, $B\rho$, of a charged particle, can be expressed as a function of the A/Q ratio:

$$B\rho = \beta\gamma uc \times \frac{A}{Q}, \tag{2.1}$$

where c is the speed of light in vacuum, $\beta = v/c$ is the velocity of the charged particle, $\gamma = 1/\sqrt{1-\beta^2}$ is the relativistic factor and u is the atomic mass unit.

The time of flight, ToF, of a charged particle through a distance, L, is given by its velocity, β, as follows

$$ToF = \frac{L}{c\beta}. \tag{2.2}$$

The Bethe-Bloch formula [49] connects the differential energy losses, $-\mathrm{d}E/\mathrm{d}x$, of a charged particle, with nuclear charge, Z, and velocity, β, in a material with the mean ionization potential, I:

$$-\frac{\mathrm{d}E}{\mathrm{d}x} = \frac{4\pi e^4 n}{m_e c^2 \beta^2} \cdot Z^2 \cdot \left[\ln\left(\frac{2m_e c^2}{I} \cdot \frac{\beta^2}{1-\beta^2}\right) - \beta^2\right], \tag{2.3}$$

where e is elementary charge, and n is the electron density of the material. Hence, the energy loss of a charged particle in a thin detector can be expressed as:

$$\Delta E = K_1 Z^2 \times \left[1 - \frac{1}{\beta^2}\ln\left(\frac{K_2\beta^2}{1-\beta^2}\right)\right], \tag{2.4}$$

where K_1 and K_2 are parameters containing all medium specific and universal con-

stants.

The total kinetic energy, TKE, of a charged particle is given by its mass number, A, and the relativistic factor γ:

$$TKE = (\gamma - 1) \times Auc^2. \tag{2.5}$$

This gives one uniquely the mass, A, provided that one knows the velocity, β.

The A/Q ratio for a given charged particle with the magnetic rigidity, $B\rho$, is obtained by expressing the β from Equation (2.2) and inserting it into Equation (2.1). The energy loss, ΔE, in a thin layer of matter, is proportional to the square of nuclear charge (Equation (2.4)), providing the resolution of nuclear charge, Z. Finally, the relation between the total kinetic energy, TKE, and particle mass, A, (Equation (2.5)) is utilized to calculate the charge state, Q, using the A/Q ratio from Equation (2.1).

The general $B\rho$-ToF-ΔE-TKE identification technique can be reduced to the $B\rho$-ToF-ΔE method, when $Q = Z$ for all charged particles of interest (i. e. all ions of interest are fully stripped of electrons). In this special case the determination of the total kinetic energy, TKE, is not necessary, because the measurement of the magnetic rigidity, $B\rho$, yields the A/Z ratio (Equation (2.1)). The nuclear charge, Z, is calculated from Equation (2.4) based on the energy loss ΔE, while the particle velocity, β, is determined from the time of flight, ToF, in Equation (2.2).

2.3 Experimental setup for the NSCL experiments

In 1999–2001 the National Superconducting Cyclotron Laboratory(NSCL) underwent a major upgrade [36]. The two superconducting cyclotrons (K500 and K1200) had previously been used to accelerate heavy-ion beams individually. In the new Coupled Cyclotron Facility (CCF) [36, 51, 52], the two cyclotrons are coupled so the facility

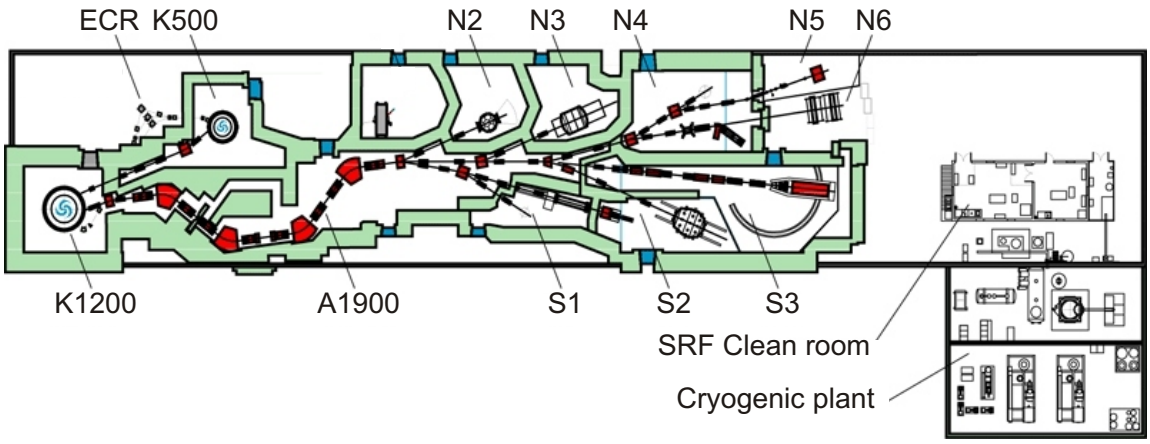

Figure 2.1: Layout of the experimental areas at the NSCL. The Coupled Cyclotron Facility consisting of the K500 and K1200 cyclotrons and the A1900 fragment separator is shown with respect to the experimental vaults N2–N6 and S1–S3.

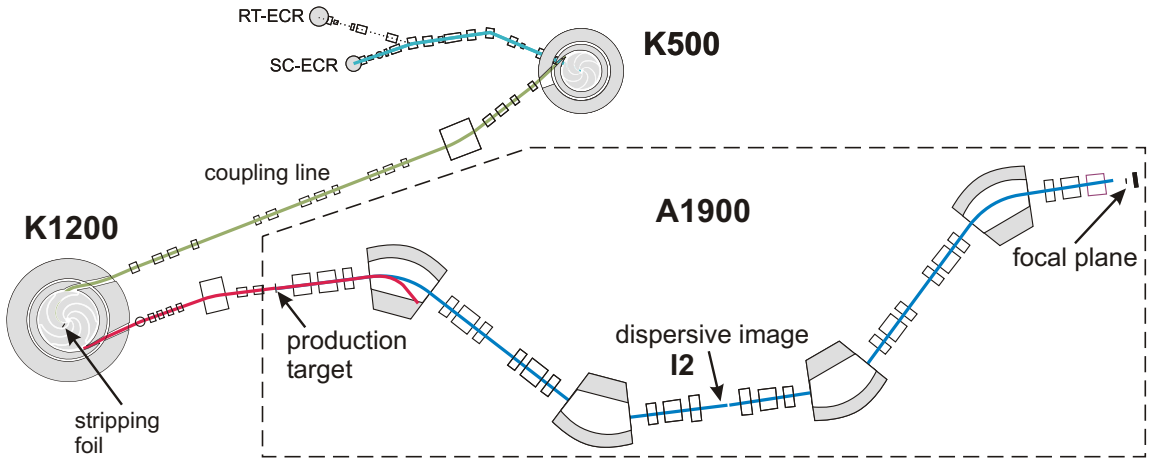

Figure 2.2: A schematic of the Coupled Cyclotron Facility at the NSCL [50]. RT-ECR and SC-ECR are Room Temperature and Superconducting ECR ion sources. The K500 and K1200 cyclotrons are connected by the coupling line. The A1900 fragment separator is enclosed in the dashed-line area.

is able to deliver higher beam intensities at higher energies. Figure 2.1 shows the layout of the experimental building at the NSCL housing the CCF. The CCF, as shown in more detailed view in Figure 2.2, consists of the K500 cyclotron, K1200 cyclotron and the A1900 fragment separator. The main function of the CCF is to produce and deliver rare-isotope beams (RIB) to any of the 8 experimental vaults (labeled S1–S3 and N2–N6 in Figure 2.1). The CCF is able to accelerate all stable ion

beams, from hydrogen to uranium, prepared by either the Room Temperature [53] or Superconducting [54] Electron Cyclotron Resonance ion sources, also referred to as RT-ECR and SC-ECR in Figure 2.2. To date, 20 primary beams from oxygen to bismuth have been developed.

The CCF uses the projectile fragmentation technique to produce secondary beams of exotic isotopes. Since 2001 more than 330 secondary beams have been delivered to various experiments. To produce a rare isotope beams, first a stable beam (such as ^{40}Ca, ^{48}Ca, etc.) is accelerated in the K500 cyclotron to energies of approximately 10–20 MeV/u ($\approx$ 0.2 c) (Figure 2.2). As the beam is injected into the K1200 cyclotron, it passes through a carbon stripper foil increasing its charge state substantially to maximize its energy in the final stage of acceleration. For ions with mass number $A \leq 136$ the maximum energy attained in the K1200 is approximately 120–140 MeV/u ($\approx$ 0.5 c). The accelerated heavy-ion (primary) beam strikes a production target,

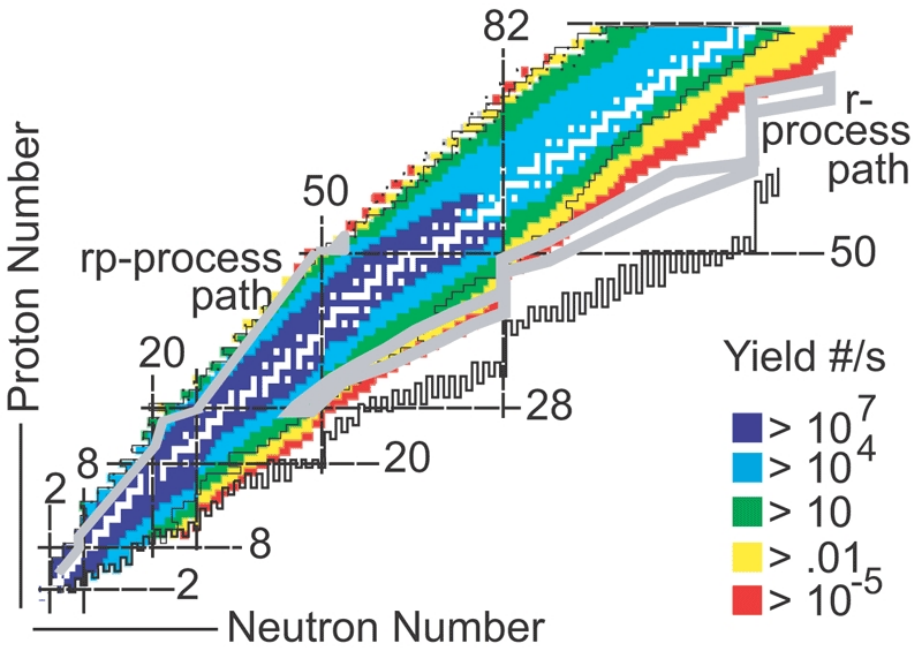

Figure 2.3: Calculated yields of different isotope species for the Coupled Cyclotron Facility at the NSCL-MSU [36]. Nuclides are plotted in proton versus neutron number representation. The colors represent the yield in number of particles per second in logarithmic scale.

creating various isotopic species lighter (fragmentation) or slightly heavier (nucleon pick-up) than the primary beam nucleus. The A1900 fragment separator works as an "isotopic filter" — separating and transporting specific rare isotope(s) to different beam lines for experiments [50]. Figure 2.3 displays calculated rates (by EPAX [48]) for different rare isotopes produced by the CCF [36] in the proton versus neutron number (nuclear chart) representation.

2.3.1 Primary beam and reaction targets

In the study carried out at the NSCL we used four primary beams: ^{40,48}Ca and ^{58,64}Ni. Basic characteristics of these beams, like charge state and energy, are listed in Table 2.1. The primary beam intensity was controlled by a series of meshes (attenuators), allowing experimenters to attenuate primary beam intensity from a factor of 1 to 10^6, with a step size of approximately a factor of 3. Beam spot in the target plane was approximately $2 \times 2\,\mathrm{mm}^2$ (determined using a CCD camera looking at a viewing plate covered with phosphorous material, scintillating upon interaction with charged particles).

Table 2.1: List of all primary beams used in our experiments. Nominal energies and charge states of the primary beams are given at the exit of ECR, K500 and K1200 respectively. Energy in the A1900 is determined by measuring the $B\rho$.

Ion ECR	Charge state K500	E (MeV/u) K500	Charge state K1200	E (MeV/u) Nominal	E (MeV/u) A1900
$^{40}Ca^{8+}$	8+	12.36	19+	140.00	140.81
$^{48}Ca^{8+}$	8+	12.23	19+	140.00	141.96
$^{58}Ni^{11+}$	11+	12.35	27+	140.00	140.96
$^{64}Ni^{11+}$	11+	12.35	27+	140.00	141.23

One of the goals of our experiments was to investigate the target dependence of the fragment yields. In our measurements we used two target materials — Be (beryllium) and Ta (tantalum). Due to its relatively large nuclear number density, beryllium is a commonly used material for production targets at fragmentation facilities. Beryllium

forms a mechanically stable solid material from which a sturdy self-supporting target can be easily manufactured, with relatively good heat transfer and radiation hardness. The tantalum target was chosen to investigate the dependence of the fragmentation cross section and the production yield dependence on the nuclear charge and neutron-proton asymmetry of the target material.

Table 2.2 lists all beam-target combinations used in our fragmentation experiments at the NSCL along with energy of the primary beam before, in the middle, and after the target material. All combinations of two targets, ^{9}Be, and ^{181}Ta and four primary beams, $^{40,\ 48}$Ca, and ^{58,64}Ni, were used in our fragmentation experiments carried out at the NSCL. The ^{9}Be target thickness was chosen as a reasonable compromise between maximizing the yield of the observed fragments and minimizing the effects of the energy loss, angular and energy straggling on the final fragment momentum distributions. In order to ensure these effects were comparable for both targets, the thickness of the ^{181}Ta target was chosen such that the energy losses of all primary beams were similar to the ^{9}Be target ($\approx$ 4–9 MeV/u). The data could then be taken with both targets using the same magnetic settings, thus, minimizing the number of settings required in the experiments.

2.3.2 A1900 Fragment separator

Since its commissioning in 2001 the A1900 fragment separator have been used routinely to separate and deliver rare isotope beams to experiments at the NSCL. In our experiments the A1900 was used to collect and identify the emitted fragments. Figure 2.2 depicts the A1900 fragment separator as part of the CCF at the NSCL. A more detailed view of the A1900 is shown in Figure 2.4. The A1900 consists of 4 superconducting dipoles D1–D4, with a radius of 3 m and a bending angle of 45°. The A1900 uses 24 quadrupoles grouped in 8 cryostats.

The A1900 fragment separator was constructed with a considerably larger (10×) angular acceptance than its predecessor the A1200 device [43]. Angular and mo-

Table 2.2: List of targets used in the series of experiments at the NSCL. Measured thickness is determined by measuring energy losses of the primary beam in the target material. Energy of the primary beam before, in the middle and after the target material are also given.

Beam	Target material	Measured thickness (mg/cm^2)	Energy before target (MeV/u)	Energy middle target (MeV/u)	Energy after target (MeV/u)
^{40}Ca	Be	103	140.81	138.41	135.98
	Ta	221		137.48	134.11
^{48}Ca	Be	105	141.96	139.93	137.89
	Ta	228		139.12	136.24
^{58}Ni	Be	104	140.96	137.68	134.35
	Ta	226		136.35	131.64
^{64}Ni	Be	105	141.23	138.24	135.20
	Ta	225		137.08	132.85

Table 2.3: Fundamental parameters of the A1900 fragment separator [55].

Parameter	A1900
Max. rigidity (Tm)	6
Solid angle (msr)	8
Momentum acceptance (%)	5
Dispersion (mm/%)	59.5
Resolving power	2915

mentum acceptances determine the overall efficiency for collecting the fragmentation products. While we used the narrow momentum acceptance mode in our measurements, the large momentum acceptance is usually utilized in the production mode, when one wants to transmit a large fraction of the desired fragment to an experiment. Fundamental parameters characterizing the A1900 fragment separator are listed in Table 2.3.

The principle of operation of the A1900 fragment separator in the production mode is illustrated below. The exotic fragments are produced by the fragmentation of the primary beam in a production target and have the initial beam velocity (left panel of Figure 2.5). The mixture of unreacted primary and secondary ions is bent by the D1

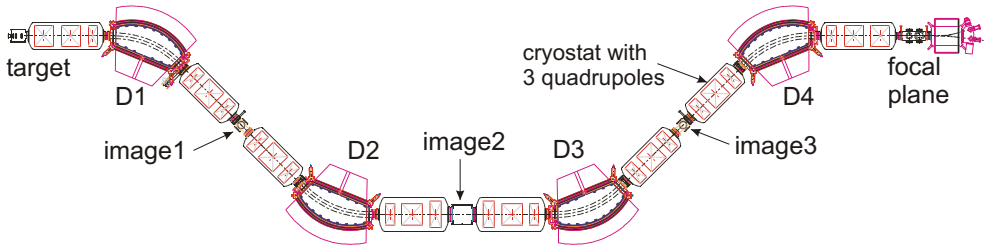

Figure 2.4: Detailed view of the A1900 fragment separator. Bending dipoles are labeled D1–D4. The five focal planes are labeled as target, image 1, image 2, image 3 and focal plane. Eight cryostats each housing 3 quadrupoles one is also indicated.

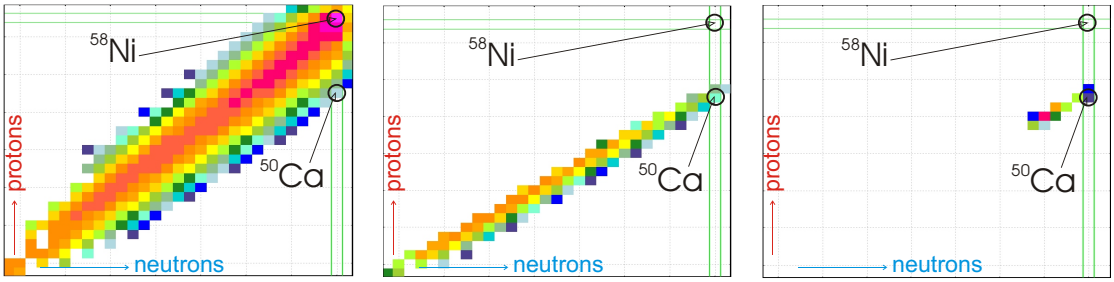

Figure 2.5: Distribution of fragments in the chart of nuclides (proton versus neutron number) at three positions along the axis of the A1900 fragment separator: target, dispersive image, focal plane, respectively from left to right. Simulation is provided for the production of ^{50}Ca in fragmentation of ^{58}Ni on a ^{9}Be target, with momentum acceptance, 1%, target thickness, 300 mg/cm^2, and degrader thickness, 200 mg/cm^2. Simulation was done using LISE++ [56].

and D2 dipoles to select a single magnetic rigidity, $B\rho$, using a momentum slit (middle panel of Figure 2.5). Isotopic selection is completed by passing the ions through an energy-degrading "wedge", placed after the momentum slit in the intermediate image plane (image 2 in Figure 2.4). Ions enter the degrader with a single $B\rho$ but may have different charges, Q, and atomic mass numbers, A, and exit with different momenta that depend on Q and A. A second dispersive beam line then provides, in most cases, isotopic separation (right panel of Figure 2.5). The nature and the thickness of the production target and the energy degrader, as well as the sizes of momentum apertures, are parameters that are adjusted to control the secondary beam intensity and purity [50].

We used the A1900 fragment separator in stand alone mode with narrow mo-

mentum acceptance (0.2% in dp/p). Particle identification was achieved using the detectors mounted in the focal plane detector box. We tried to minimize all factors that introduce uncertainties to our measurement. There was no degrader material used in the intermediate image plane in order to diminish the transmission uncertainties. (The wedge was used only during the measurement of ^{50}Ca produced in ^{58}Ni+^{9}Be reaction, as discussed in Section 4.3.2.)

2.3.3 Detectors at the A1900 fragment separator

Particle identification detectors

It is a good approximation to assume that all fragments produced in our experiments at 140 MeV/u are predominantly fully stripped of electrons ($Q = Z$). (From the charge state distribution measurement for the primary beams we expect less than 2% contribution from hydrogen-like charge states for all projectile-target combinations except nickel projectiles on a tantalum target where it is less than 5%.) This means we can use the simpler particle identification method, $B\rho$-ToF-ΔE, discussed in Section 2.2. In this case the measurement of three quantities, the magnetic rigidity, $B\rho$, time of flight, ToF, and energy loss, ΔE, suffice to identify the various species. Since we used the narrow momentum acceptance mode (0.2% in dp/p), the $B\rho$ values are given by the magnetic field settings of the fragment separator.

For the time of flight (ToF in Equation (2.2)) detector we used a plastic scintillator with thickness of 100 mm and an area, $150 \times 100\,\mathrm{mm}^2$, placed at the focal plane as the last detector. The radio frequency (RF) pulse of the cyclotron is used as a time reference. The plastic scintillator (SCIN) provided an event trigger and the ToF start signal. The time of flight was stopped by the RF pulse. The time structure of the primary beam produced by the CCF spans approximately 2–4 ns due to multi-turn extraction in the K1200 cyclotron. Nevertheless, we are able to resolve the mass for all fragments in our experiments. The length of the time of flight path (the distance

from target to the focal plane position along the fragment separator axis) was taken 35.48 m.

Table 2.4: The magnetic rigidity, $B\rho$, values of $N = Z$ settings, used for particle ID calibration for every primary beam discussed in the text.

Primary beam	$B\rho$(Tm)
^{40}Ca	3.12
^{48}Ca	3.20
^{58}Ni	3.60
^{64}Ni	3.30

For energy loss measurement (ΔE in Equation (2.4)) we used a 500 μm thick silicon PIN (Positive Intrinsic Negative) detector. The active area of the PIN detector is $50 \times 50\,\mathrm{mm}^2$.

A PID spectrum is obtained by plotting the energy loss, ΔE, versus the time of flight, ToF. Figure 2.6 displays a simulated PID spectrum for the ^{58}Ni+^{9}Be reaction using LISE++ [56]. The individual fragments are displayed as well separated groups of events forming characteristic bands in horizontal and vertical directions. All nuclides with a constant neutron excess, $N - Z$, form vertical bands in Figure 2.6. The slightly tilted horizontal bands correspond to isotopes of individual elements. The leftmost vertical band corresponds to fragments with $N = Z$, the neighboring band corresponding to $N - Z = 1$, etc. (The time of flight was simulated such that the more neutron-rich fragments are located to the right of the $N - Z = 0$ band.) By recognizing these characteristic features of the PID spectrum we can easily identify nuclides with different $N - Z$. Identification of the element bands is done by locating "the hole", which corresponds to particle unbound ^{8}Be nucleus, as shown in the magnified region of the PID spectrum in Figure 2.6 allows one to identify all fragments. For reference, the isotope of ^{30}P and the band corresponding to isotopes of calcium ($Z = 20$) are labeled in Figure 2.6. The magnetic rigidity setting for a given reaction allowing the observation of the $N - Z = 0$ band is also referred to as the "$N = Z$ setting". The $N = Z$ magnetic rigidity settings of the A1900 fragment separator used

in the PID calibrations for all primary beams are listed in Table 2.4.

The ΔE and ToF detectors are calibrated using the fragments from the $N = Z$ setting, to the calculated values of ToF and ΔE using the LISE++ code [56]. First the ΔE and ToF values are calculated using LISE++ for the fragments identified in the $N = Z$ setting. Then the channel values of ΔE and ToF are extracted from the experimental spectrum and the coefficients of a linear calibration from channels to MeV and ns are obtained for ΔE and ToF, respectively. Next, the coefficients, K_1 and K_2, of Equation (2.4) are fitted to reproduce the nuclear charge numbers of all identified fragments in the $N = Z$ setting. After this calibration the Equation (2.1), (2.2) and (2.4) are used to calculate the momentum, nuclear charge and mass numbers for all fragments in our analysis. The PID calibration was done for each projectile separately.

Position sensitive detectors

The detection of the position of particles traveling through the fragment separator is important for diagnostic purposes (measurement of the positions and angles ensures that the magnetic rigidity tune corresponds to the ion optical calculation). In the case of wide/full momentum acceptance, position measurement gives the momentum of fragments. A total of four position sensitive Parallel Plate Avalanche Counters (PPAC) detectors is installed in the intermediate image (2) and the focal plane (2) along the fragment separator axis.

The principle of the PPAC detectors is described here. A charged particle ionizes the gas in the active volume of the detector. The electrons freed in the ionization process are multiplied in a cascade (avalanche), by ionizing surrounding gas molecules, in high electric field in the active volume as shown in Figure 2.7.

PPACs used in the A1900 fragment separator have segmented cathodes, providing the position sensitivity. Figure 2.8 shows two different (front and side) views of a PPAC detector. Each detector consists of two separate chambers sharing one anode

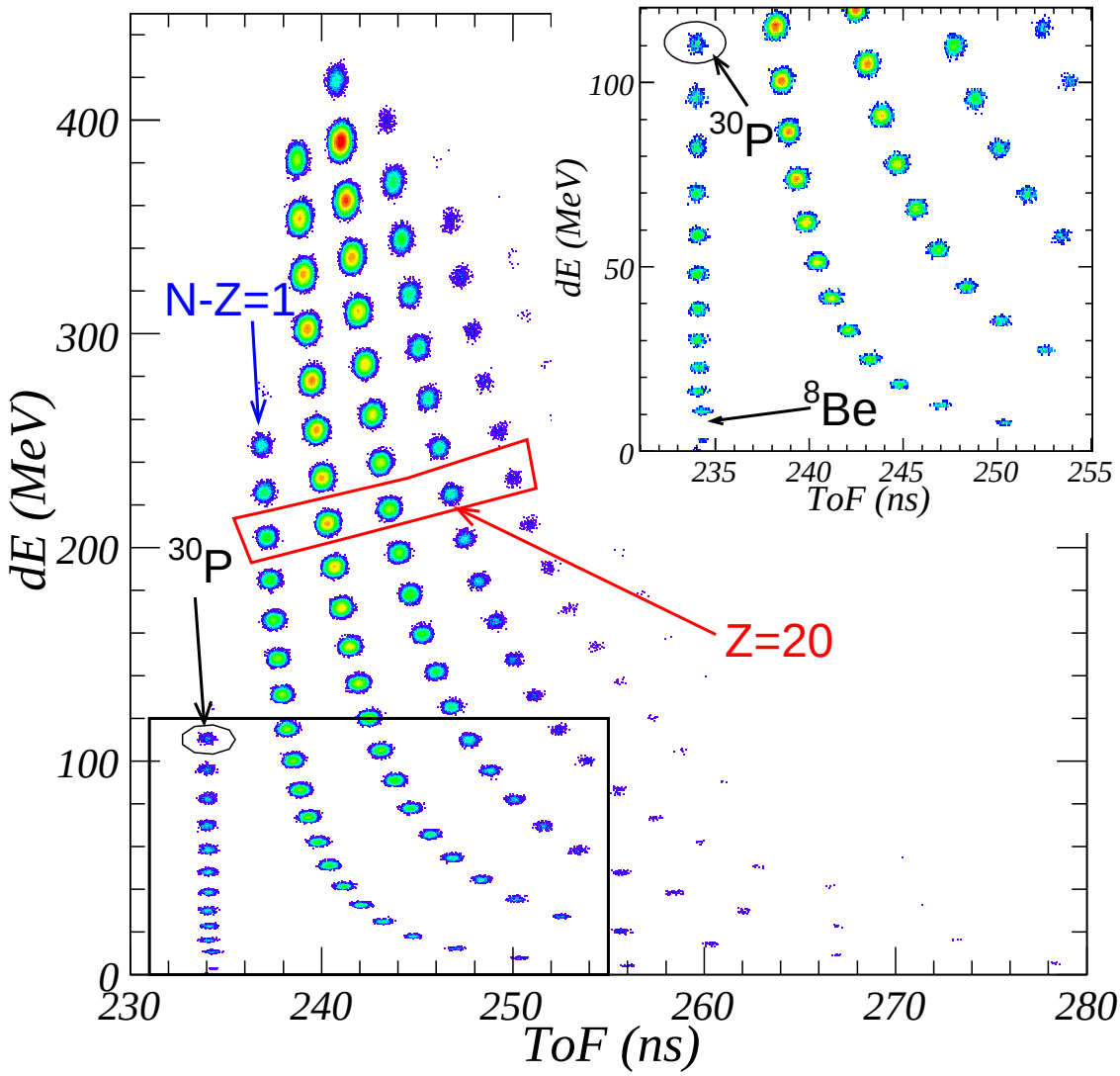

Figure 2.6: The PID spectrum of a simulated of $N = Z$ setting for ^{58}Ni+^{9}Be reaction at 140 MeV/u using LISE++ [56] for the A1900 fragment separator. Parameters of the simulation: $B\rho$=3.6 Tm, 0.2% momentum acceptance.

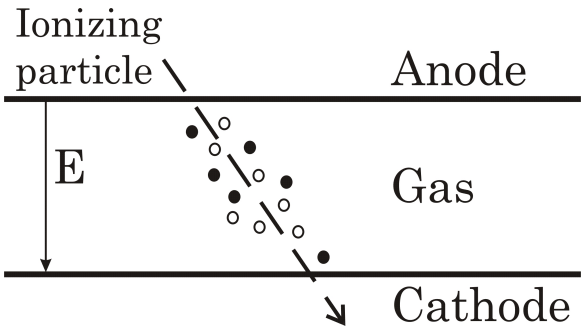

Figure 2.7: Principle of operation of an avalanche counter. The charged particle ionizes the gas in sensitive volume of the detector between the anode and cathode. The electrons freed in this process are multiplied in an avalanche, creating an electric signal in the cathode.

foil. Segmented cathodes have evaporated strips connected to the readout electronics. Two different designs of PPAC detectors are used in the A1900, referred to as I2 PPACs and FP PPACs.

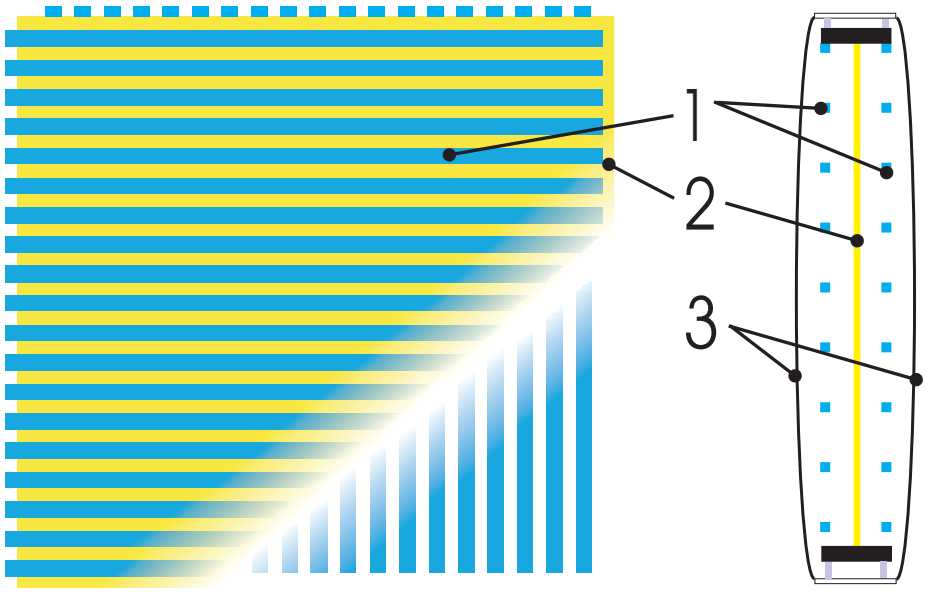

Figure 2.8: The front (left panel) and side (right panel) view of a Parallel Plate Avalanche Counter (PPAC). 1 — cathode plane with horizontal strips, 2 — common anode plane, 3 — cathode plane with vertical strips

A pair of I2 PPAC detectors is installed at the dispersive image of the A1900 on a retractable platform. Each detector has an active area of $400 \times 100\,\mathrm{mm}^2$ corresponding to 160×32 strips. Every strip is individually read out using the Front End

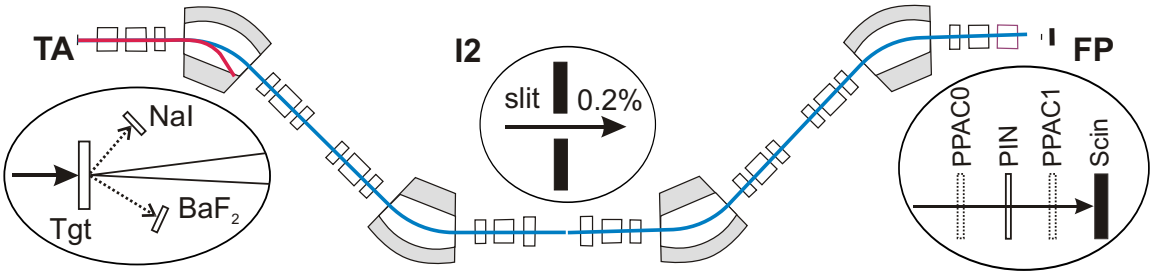

Figure 2.9: Detector setups in the A1900 used for our fragmentation experiments. Beam intensity monitors (NaI(Tl) and BaF_2) shown in the target area (TA), momentum slit at intermediate image (I2) and the particle identification setup (PIN and Scin) at the focal plane (FP). The position sensitive PPAC0 and PPAC1 were used to track the fragment trajectories.

Electronics (FEE) boards. This arrangement of the read out allows experimenters to use the detectors up to the particle rates of 1 MHz.

The ion optics of the A1900 fragment separator is set up such that the particles with different momentum have different spatial positions in the horizontal plane. Hence, the measurement of position at the intermediate image is equivalent to the measurement of momentum. In our experiments the I2 PPACs were used only for the measurements of momentum of the primary beam and its charge states (see analysis of the charge state distributions in Section 3.1). These detectors were removed from the beam during our fragment cross section measurements, because they were not needed in narrow momentum acceptance mode.

Each of the two focal plane PPAC (FP-PPAC) detectors have an active area of $100 \times 100\,\mathrm{mm}^2$ with resistive read-outs. The strips are interconnected by a resistor chain and read out by two channels on both ends. Hence one PPAC detector provides signals in 5 channels: left, right, up, down and anode. These detectors were used for the tracking all fragments during our fragmentation experiments (Figure 2.9). Tracking of the fragments at two different positions along the fragment separator axis at the FP (before and after the PIN detector) allowed us to interpolate the paths to ensure that all fragments were hitting the active area of the PIN detector (Figure 2.9).

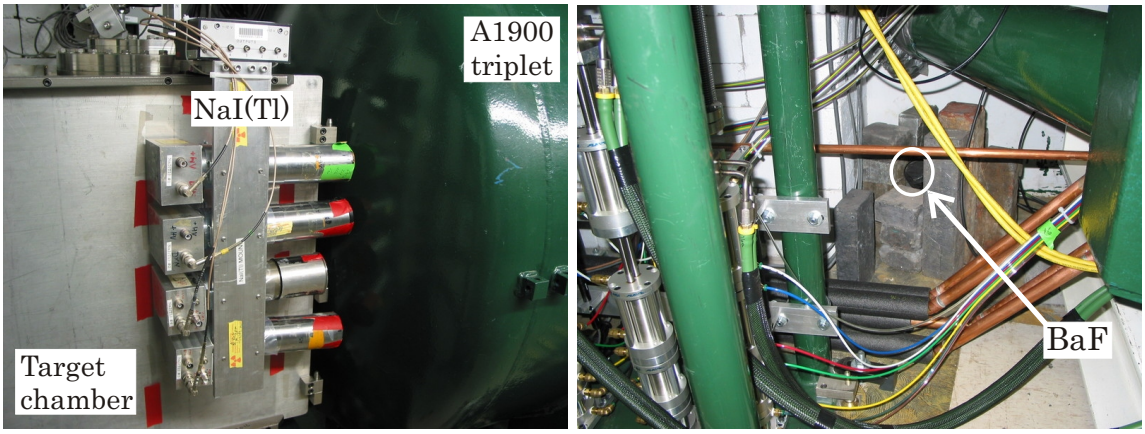

Figure 2.10: Photographs of the two beam intensity monitoring devices. Left panel: four NaI(Tl) detectors attached to a ladder; Right panel: BaF_2 detector in a lead fortress (used to shield the detector from the background gamma radiation).

Primary beam intensity monitors

For overall normalization of fragment yields, precise continuous measurement of primary beam intensity is required. In order to calculate absolute fragmentation cross sections we needed to know the absolute primary beam intensity. Intensities of the primary beam ranged from 10^6 to 10^{10} particles per second (pps) during our production runs. The absolute beam intensity is measured by a Faraday Cup (FC) which stops the primary beam, at the CCF. As the direct measurement by a charged-particle detector is not possible, because of the high rates of the primary beam used in our experiments ($> 10^6$ pps), we used an indirect method to determine the beam intensity by monitoring the radiation created by beam-target interactions.

The flux of light particles and gamma radiation emitted in the interactions of the primary beam with the production target is proportional to the beam intensity. This feature provides means to monitor the primary beam intensity continuously. Two detector systems of light particles and gamma radiation were used in order to cover the primary beam intensity range used in our experiments (approximately 4 orders of magnitude). The first detector configuration was an array of four NaI(Tl) crystals; the second one was a single BaF_2 crystal coupled to a photomultiplier tube (Figure 2.9).

The NaI(Tl) array consists of 4 crystals mounted on a ladder which is attached to the outside of the target vacuum chamber (left panel of Figure 2.10) approximately 30 cm from the target at an angle of approximately 45°. The bias voltages and discriminator levels were set up to detect the high energy charged particles emitted in the reaction of the primary beam and target.

The BaF_2 detector was shielded from the surrounding gamma radiation in the target area by a lead fortress. It was placed on the floor behind the target chamber (right panel of Figure 2.10) approximately 130 cm from the target at an angle of approximately 72°. The bias voltage and the discriminator level were set up to detect the gamma radiation created in the beam-target interactions.

Calibration of the absolute beam intensity monitor was performed using a Faraday Cup. The FC was placed in the extraction channel of the K1200 cyclotron (Z001) in the case of ^{58}Ni fragmentation, and the FC was placed in the target box of the A1900 fragment separator for ^{40,48}Ca and ^{64}Ni primary beams. For the NaI(Tl) array the background count due to radiation produced by activated target area has been subtracted. This rate was determined by simply measuring the ambient radiation in the target area with no beam on target. Since the beam intensity monitoring technique relies on nuclear reactions of the projectile and target nuclei, it is necessary to perform the beam intensity monitor calibration for each beam-target combination. For every beam-target combination we performed 3 beam monitor calibrations (at the beginning, middle and end of an experiment). With the three calibration measurements we confirmed that changes (e.g., due to activation of the target area, beam spot position) during our experiment were negligible.

2.3.4 Magnetic rigidity settings

Measurement of the momentum distributions for a wide range of fragments was carried out by systematically scanning across the magnetic rigidity settings of the A1900 fragment separator. Figure 2.11 and 2.12 show magnetic rigidity, $B\rho$, settings used

for all the primary beams with the ^{9}Be and ^{181}Ta targets. The individual points in Figure 2.11 and 2.12 represent the magnetic rigidity settings of the A1900 fragment separator. The horizontal bars display the momentum acceptance for individual $B\rho$ settings. For ^{40}Ca we took measurements between 3.2–4.2 Tm in 33 steps and for ^{48}Ca we scanned region between 3.2–5.1 Tm in 50 settings. For ^{58}Ni and ^{64}Ni beams we took data between 3.25–4.3 Tm in 26 steps and 3.3–4.5 Tm in 34 settings, respectively.

The gaps in the $B\rho$ coverage correspond to the primary beam and its charge states rigidity (Figure 2.11 and 2.12). The primary beam intensity was optimized at each magnetic rigidity such that the counting rate of the PIN detector was approximately 700–900 counts per second. The detection efficiency of the PIN detector is close to 100% when the counting rates are below 1 kHZ.

2.3.5 Data acquisition system

Figure 2.13 shows a schematic diagram of the electronic circuit used in the A1900 fragmentation experiments. The trigger was produced by the focal plane scintillator

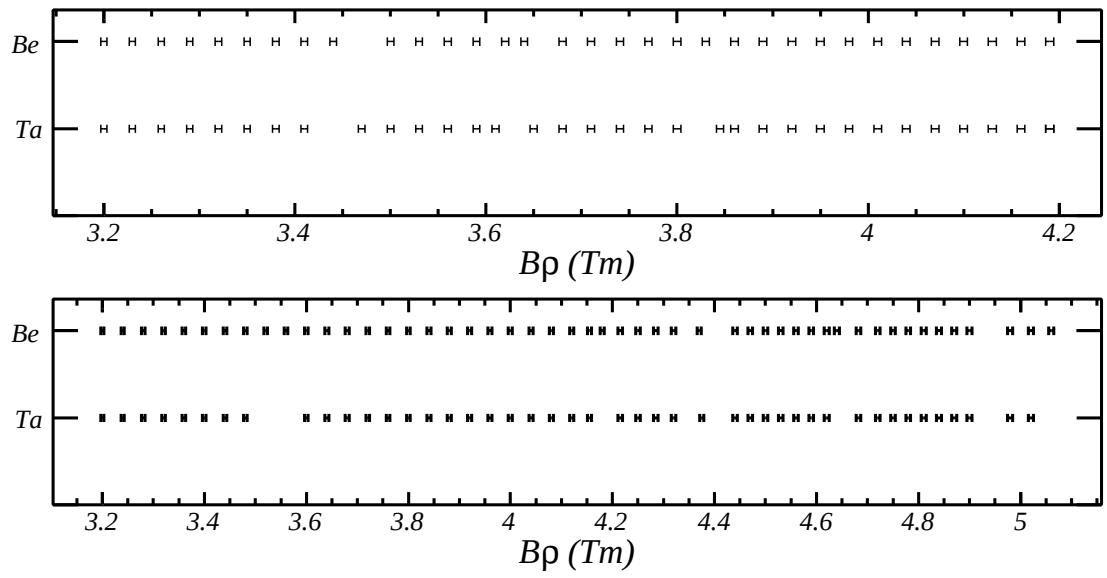

Figure 2.11: Magnetic rigidity settings for Ca primary beams. Top panel for ^{40}Ca and bottom panel for ^{48}Ca. The error bars in horizontal direction indicate the 0.2% in dp/p momentum acceptance in the $B\rho$ space.

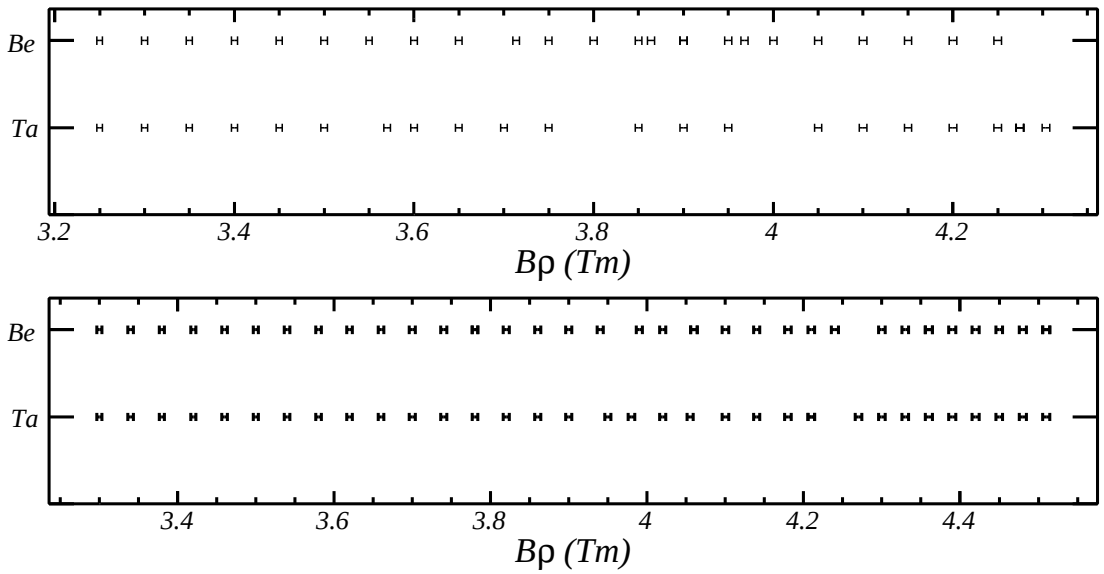

Figure 2.12: Magnetic rigidity settings for Ni primary beams. Top panel for ^{58}Ni and bottom panel for ^{64}Ni. The error bars in horizontal direction indicate the 0.2% in dp/p momentum acceptance in the $B\rho$ space.

signals (labeled as FP SCI N&S in Figure 2.13). The time of flight was measured by the FP SCI with respect to the Cyclotron Radio Frequency (RF).

The focal plane PPAC (Parallel Plate Avalanche Counter) detectors with standard readout provide signals in 5 channels (up, down, left, right and anode signals). All channels from the two PPAC detectors are denoted by using thick line in Figure 2.13.

Timing and analog signals were digitized using standard CAMAC (Computer Automated Measurement And Control) Analog to Digital Converters (ADC), Charge to Digital Converters (QDC), and Time to Digital Converters (TDC). The CAMAC bus was interfaced through the Versa Module Eurocard (VME) to CAMAC Branch Driver (CES CBD8210) and controlled by a personal computer (PC) running the standard NSCL data acquisition system NSCLDAQ [57] in the Linux operating system. The data were collected and distributed by the SpectroDaq server [57]. The NSCLDAQ allows users to run multiple simultaneous online analyses using the NSCL SpecTcl [58], plus archive the data on the network filesystem. The final back-up of the experimental data was stored in a 100 GB Digital Linear Tape (DLT).

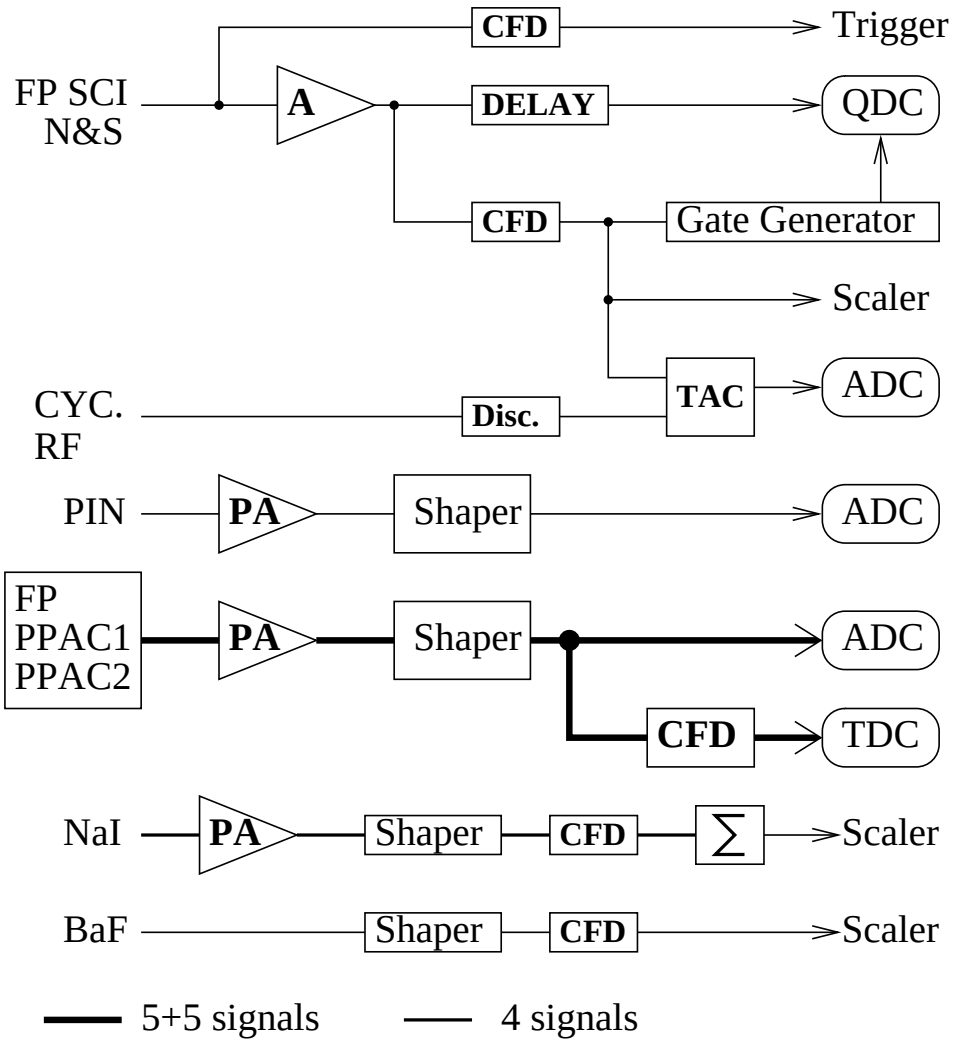

Figure 2.13: Schematic diagram of the electronic diagram used for the A1900 fragmentation experiments.

2.4 Experimental setup for RIKEN experiment

Projectile fragmentation experiment using ^{86}Kr beam was performed at RIKEN (The Institute of Physical & Chemical Research) Accelerator Research Facility (RARF) in Wako-shi, Japan. The layout of the RARF facility at RIKEN is shown in Figure 2.14. The beam of ^{86}Kr was accelerated in the Ring Cyclotron (K540 in Figure 2.14) and delivered to experimental area D (Figure 2.14). The fragments were analyzed and identified using the RIKEN Projectile-fragment Separator (RIPS).

Figure 2.14 shows the RIPS fragment separator located across two adjacent rooms D and E6. More detailed view of the RIPS is shown in Figure 2.15. Primary production targets were located in the target position of RIPS (Figure 2.15). Projectile-like fragments produced in interactions of the primary beam with the target nuclei were collected in the RIPS fragment separator and transported to doubly achromatic focal plane F2 (Figure 2.15). Detector setups at focal planes F2 and F3 allow us to identify all fragments reaching F2. In order to cover the full momentum space we changed the magnetic settings of the two dipole magnets D1 and D2.

2.4.1 Primary beam and reaction targets

Ions of $^{86}Kr^{30+}$ were accelerated in the K540 ring cyclotron at RIKEN. The primary beam energy, determined to be 63.77 MeV/u, was measured by a direct measurement of the magnetic rigidity using the RIPS. The beam intensity, which was adjusted by a beam attenuator at the exit of the Electron Cyclotron Resonance (ECR) ion source varied from 10^6 to 10^{11} particles per second (pps), during our experiment. Beam spot size on the target was approximately 1 mm in diameter.

For the fragmentation experiments with the ^{86}Kr primary beam, two target materials ^{9}Be and ^{181}Ta were used. Energy of the primary beam before, in the middle, and after the target is listed in Table 2.5, along with the measured thickness of the target materials from energy loss consideration. The target thickness was chosen as a reason-

able compromise between minimizing the distortion of the momentum distributions and maximizing the yields of reaction products.

Table 2.5: Primary beam energy measured and target thickness measurement in the ^{86}Kr experiment. Energy before, in the middle and after the target is also listed.

Target	Thickness measured (mg/cm^2)	Energy before (MeV/u)	middle (MeV/u)	after (MeV/u)
^{9}Be	96	63.77	57.90	51.60
^{181}Ta	153	63.77	58.02	51.89

2.4.2 RIPS fragment separator

The fundamental parameters characterizing the RIPS fragment separator are listed in Table 2.6. Since its commission in the beginning of the 1990s, it has been routinely

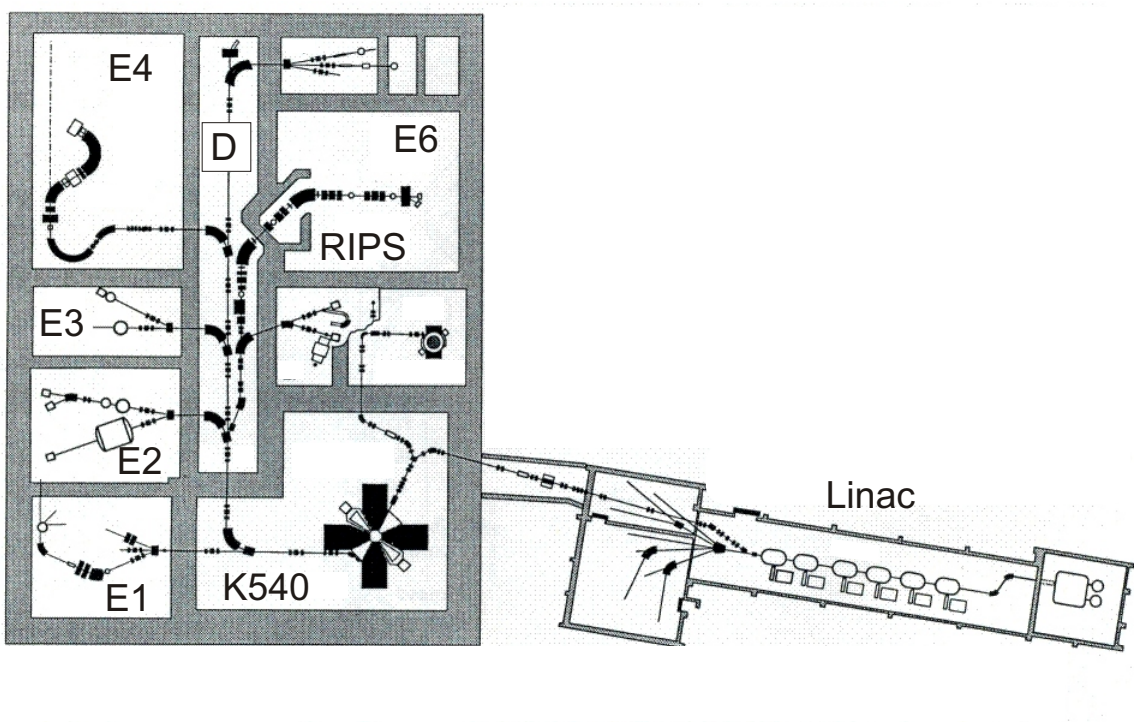

Figure 2.14: Layout of RIKEN Accelerator Research Facility (RARF) [35]. The K540 cyclotron is shown with respect to the experimental areas labeled as E1–E6. The RIPS fragment separator is located across the two adjacent rooms D and E6.

used to deliver a variety of radioactive beams for experiments. Configuration of the RIPS fragment separator in the RARF facility is shown in Figure 2.14. It consists of two 45° dipole magnets, twelve quadrupoles (Q1–Q12), and four sextupoles (SX1–SX4). The first section with a configuration of Q-Q-Q-SX-D-SX-Q gives a dispersive focus at F1 allowing measurement of the magnetic rigidity of the particles. The second section with a configuration of Q-Q-SX-D-SX-Q-Q-Q compensates the dispersion of the first section and gives a doubly achromatic focus at F2. Quadrupole triplet of the last section gives the third focus at F3, where special experimental setups can be installed [35].

For our fragmentation experiment the main particle identification detection setup was placed in F3 focal plane (Figure 2.15).

Table 2.6: Fundamental parameters of the RIPS fragment separator [35].

Parameter	RIPS
Max. rigidity (Tm)	5.76
Solid angle (msr)	5
Momentum acceptance (%)	6
Dispersion (mm/%)	24
Resolving power	1600

2.4.3 Detectors at the RIPS fragment separator

Charged-particle detectors installed at the RIPS fragment separator were used for particle identification and primary beam intensity monitoring. Figure 2.15 shows the RIPS fragment separator with all the detector setups used in the ^{86}Kr fragmentation experiment in ovals next to focal planes F0, F2 and F3.

Particle identification detectors

In section 2.2, we introduced the particle identification method used. The charge state distributions of ^{86}Kr primary beam at 64 MeV/u are much broader as compared to

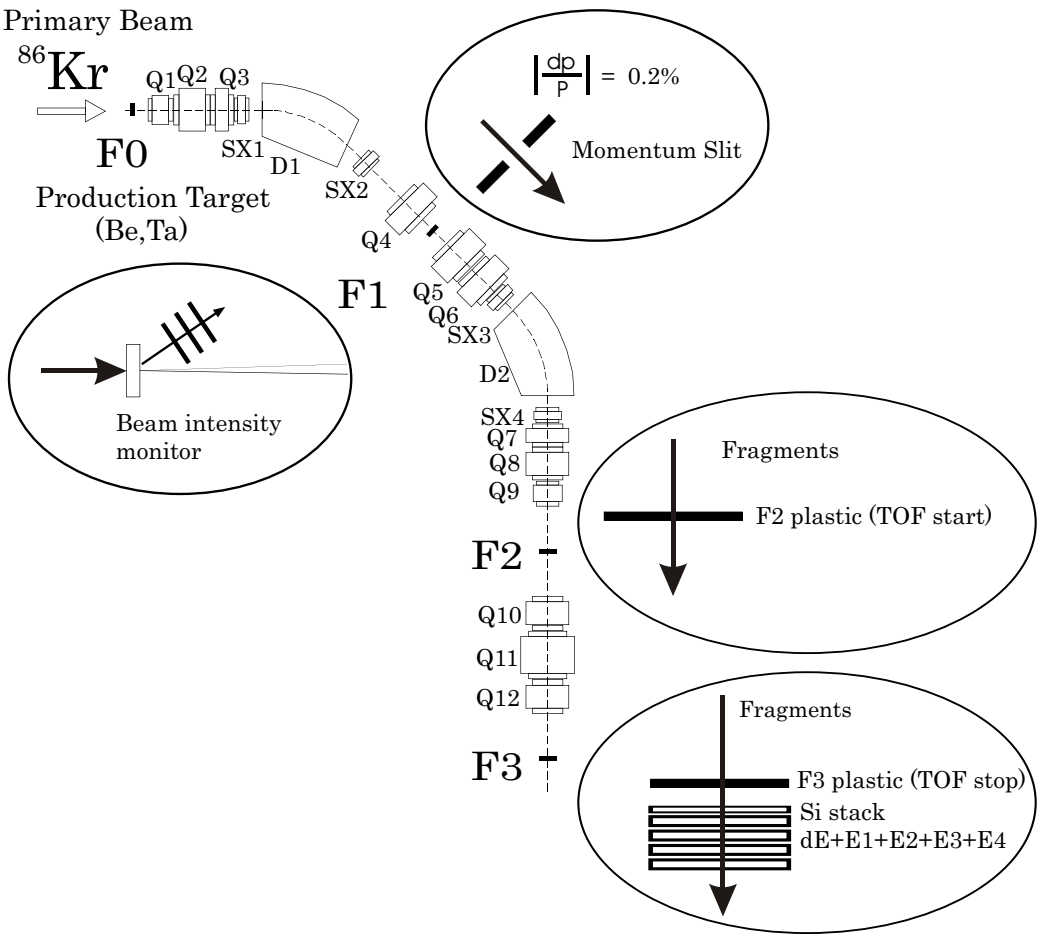

Figure 2.15: RIPS setup used for the fragmentation experiment [59]. Beam intensity monitor MOMOTA was placed at F0, particle identification setup was placed at F2 and F3 focal planes. Momentum slit at F1 defined the momentum acceptance.

primary beams measured at the NSCL. Hence, a significant contamination also from the charge states of individual fragments is expected (more than 10% in hydrogen-like charge state for the primary beam after passing through the ^{9}Be target). To identify the momentum, mass and nuclear charge numbers along with the charge state of each fragment, the full $B\rho$-ToF-ΔE-TKE particle identification technique must be used (as explained in Section 2.2).

The magnetic rigidity, $B\rho$ is given by selecting different magnetic settings of the

fragment separator. The time of flight, ToF, is measured between two 500 μm-thick plastic scintillators on the flight path of 6 m mounted at the F2 and F3 planes, respectively. This is displayed in the ovals next to F2 and F3 focal planes in Figure 2.15. A stack of five silicon detectors was used to measure energy loss, ΔE, and total kinetic energy, TKE. The silicon stack is comprised of one 300 μm-thick detector and four 500 μm-thick detectors. The stack was installed at the very end of the RIPS beamline, as shown in the oval next to F3 in Figure 2.15. Energy loss simulations showed that all particles heavier than argon will be stopped in this arrangement of silicon detectors.

Primary beam intensity monitoring

The primary beam intensity is an essential quantity to calculate the absolute fragmentation cross sections. We monitored the primary beam intensity using a telescope called MOMOTA. It consists of three plastic scintillators and detects the light particles produced in nuclear reactions in the production target. We required triple coincidence rates to reduce the detector background. Figure 2.16 shows a schematic drawing of the beam monitor telescope at the target position.

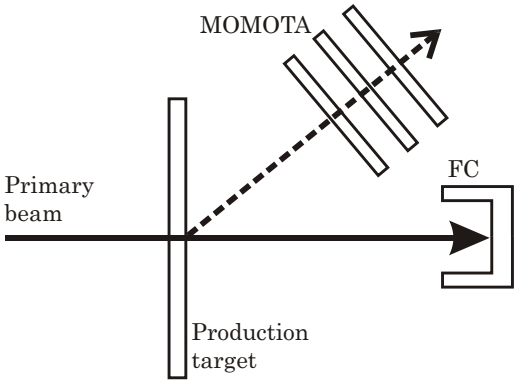

Figure 2.16: A schematic view of the MOMOTA beam intensity monitor with respect to the target and the downstream Faraday Cup (FC).

As MOMOTA beam monitor was located further downstream from the target position as the scattered particles off the FC influenced the MOMOTA reading during the beam intensity calibration. Unlike the NSCL experiments, we could not use the

Faraday Cup (FC) to calibrate the MOMOTA beam monitor. Instead, the absolute calibration of the MOMOTA telescope was provided by the direct rate measurement of primary beam charge state $^{86}Kr^{33+}$ and $^{86}Kr^{31+}$ for ^{9}Be and ^{181}Ta targets, respectively, at the F2 focal plane by the plastic scintillator (detailed discussion in Section 3.2.2).

2.4.4 Magnetic rigidity settings

Measurement of the momentum distributions for a wide range of fragments was carried out by changing the magnetic rigidity settings of the RIPS fragment separator. Figure 2.17 shows the magnetic rigidity settings used for ^{9}Be and ^{181}Ta targets. Settings for the ^{9}Be target covered the range in $B\rho$ from 1.79 to 2.93 Tm in 45 steps. Settings for the ^{181}Ta target covered much smaller range in $B\rho$ from 1.79 to 2.35 Tm in 29 steps, because the charge state distribution of ^{86}Kr at 64 MeV/u is much broader than in the case of the ^{9}Be target, resulting in significant contamination of the PID spectrum.

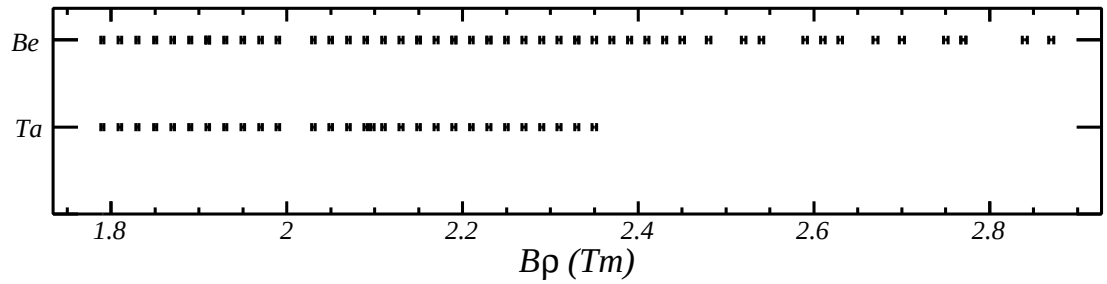

Figure 2.17: Magnetic rigidity coverage for the ^{86}Kr runs. The error bars in horizontal direction indicate the 0.2% in dp/p momentum acceptance in the $B\rho$ space.

The step size we used for the overall scanning was 0.03 Tm. To avoid the charge states of the primary beam from coming to the focal plane detectors (at F2 and F3) the corresponding $B\rho$ settings were not taken, forming the gaps in the magnetic rigidity, $B\rho$ coverage in Figure 2.17. At each magnetic rigidity setting we optimized the beam intensity such that the counting rate of the silicon stack detector was $\lesssim 1,000$ counts per second.

2.4.5 Data acquisition system

Figure 2.18 shows a schematic diagram of the electronic circuit of ^{86}Kr fragmentation experiment. The event trigger was generated by the F2 plastic scintillator. The timing and analog signals were digitized by standard CAMAC (Computer Automated Measurement and Control) Analog to Digital Converters (ADC), Charge to Digital Converters (QDC), and Time to Digital Converters (TDC).

The data were collected using the standard data acquisition software at RIKEN [60]. The online data analysis has been done using the ANAPAW [61], a tailored version of the Physics Analysis Workstation (PAW) [62] for the online analysis. All the data were archived to 120m Digital Audio Tapes (DAT).

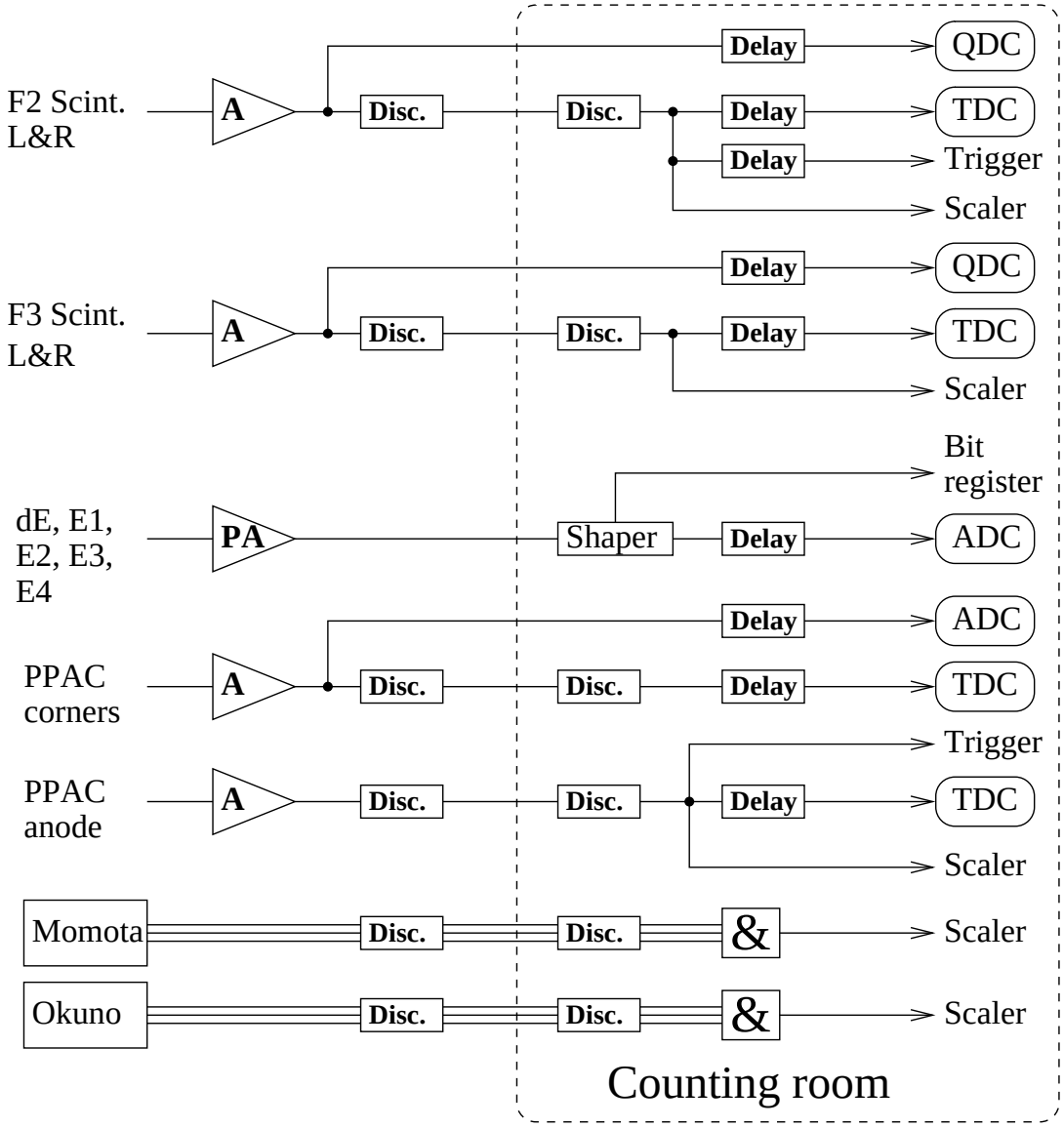

Figure 2.18: Block schematic of the electronic circuit used for the ^{86}Kr fragmentation experiment at RIKEN.

Chapter 3

Data analysis

The primary beam charge state measurements are presented in the beginning of the chapter. It is followed by description of the analysis procedures for the beam intensity calibration, particle identification, differential cross section evaluation, angular transmission correction and momentum distribution. The method of fragmentation production cross section calculation and the uncertainty evaluation are discussed at the end of the chapter.

3.1 Primary beam charge state distributions

In our experiment, we want to avoid detecting charge states of the primary beam — as discussed in Section 2.1. Therefore, it is important to know the positions and widths of these distributions in the magnetic rigidity space. Different charge states, Q, of one ion with mass number, A, traveling at velocity, β, are spatially separated in a magnetic field according to Equation (2.1). In our case the two neighboring charge states were spatially separated in the dispersive plane of the fragment separator due to different bending radii in the magnetic field.

The charge states of the primary beam were measured by tuning the fragment separator to a $B\rho$ between the magnetic rigidities of two neighboring charge states,

allowing us to observe their relative $B\rho$ distributions. For each measured beam-target combination the results were normalized with respect to each other and the probabilities for different charge states were calculated. A series of the primary beam charge state distribution measurements have been done for ^{58,64}Ni and ^{86}Kr, for which two neighboring charge state distributions fit within the acceptance of the fragment separator.

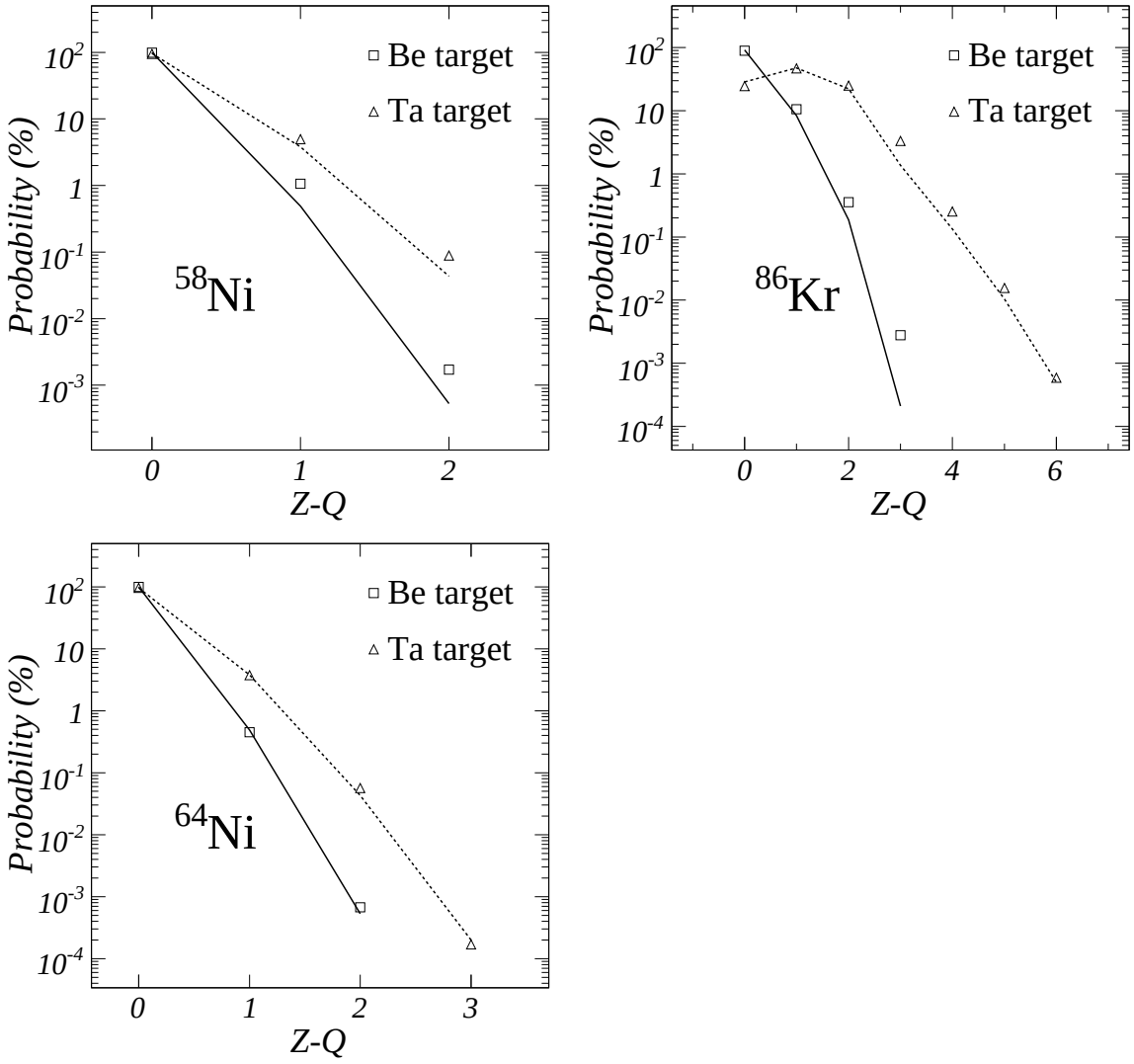

Figure 3.1: Primary beam charge state probability distributions for ^{58,64}Ni and ^{86}Kr primary beams plus ^{9}Be (open squares) and ^{181}Ta (open triangles) targets plotted as a function of number of electrons $Z - Q$. Solid and dashed lines show calculation by GLOBAL parameterization [63] as implemented in LISE++ [56] for ^{9}Be and ^{181}Ta target, respectively.

The separation of two neighboring charge states in $B\rho$ for ions of Ca is larger (≥ 5 % in dp/p) than the momentum acceptance of the A1900 fragment separator (≈ 5 % in dp/p) so the charge state distributions were not measured for ^{40,48}Ca beams.

The charge state distributions measured for ^{58,64}Ni and ^{86}Kr beams at 140 MeV/u and 64 MeV/u, respectively, are presented in Figure 3.1 in terms of probability as a function of number of electrons, $Z - Q$. The distributions obtained on ^{9}Be and ^{181}Ta target are presented as open squares and triangles, respectively. The experimental data are compared to a leading parameterization of the charge state distribution — GLOBAL [63], shown as solid (^{9}Be) and dashed (^{181}Ta) lines. The target thicknesses used in the experiments were much larger than the equilibration thickness so all the GLOBAL calculations were done for the equilibration thickness of the target material. The charge state probability distributions are wider for ^{181}Ta for all projectiles shown in Figure 3.1. All probability distributions are reproduced rather well in spite of the fact the parameterization GLOBAL, was derived for $Z > 28$ ions. Some discrepancies are observed in the case of ^{58}Ni and ^{86}Kr projectiles. The GLOBAL code has no isotope dependences; the calculated distributions for ^{58}Ni and ^{64}Ni are identical. However, the experimental data show broader probability distributions in the case of the ^{58}Ni projectile (especially for ^{9}Be). The experimental data and GLOBAL predictions for ^{86}Kr^{33+} differ by a factor of 10, while the experimental data for ^{181}Ta target are reproduced well up to $Z - Q = 6$.

3.2 Calibration of beam intensity monitors

3.2.1 NSCL experiments

Precise knowledge of the primary beam intensity is essential in determination of the absolute fragmentation production cross sections. In the fragmentation experiments carried out at the NSCL we used two primary beam intensity monitors referred to as NaI(Tl) and BaF_2 (Section 2.3.3). Since the experiments were carried out at different

times over the course of almost two and half years there are small differences in the experimental configuration and analysis procedures including the primary beam intensity monitoring.

The primary beam intensity monitors were calibrated with respect to the Faraday Cup (FC) beam current measurement. For the ^{58}Ni fragmentation experiment only one FC was available (Z001); for the other systems (^{40,48}Ca and ^{64}Ni), another FC was located in the target box (Z014). Figure 3.2 shows the Z001 FC (left) in the extraction channel and Z014 FC (right) in the target box, in front of the A1900 fragment separator (right). Since both FC's are installed upstream from the target position (which is Z015) it is not possible to measure the beam current and monitor the counts of the secondary particles from the target simultaneously. We assume the beam intensity variations over a short period of time (2–3 minutes) are negligible. The beam current is taken as an average from multiple instantaneous measurements 5 seconds apart in duration of up to approximately 1 minute. Immediately after the

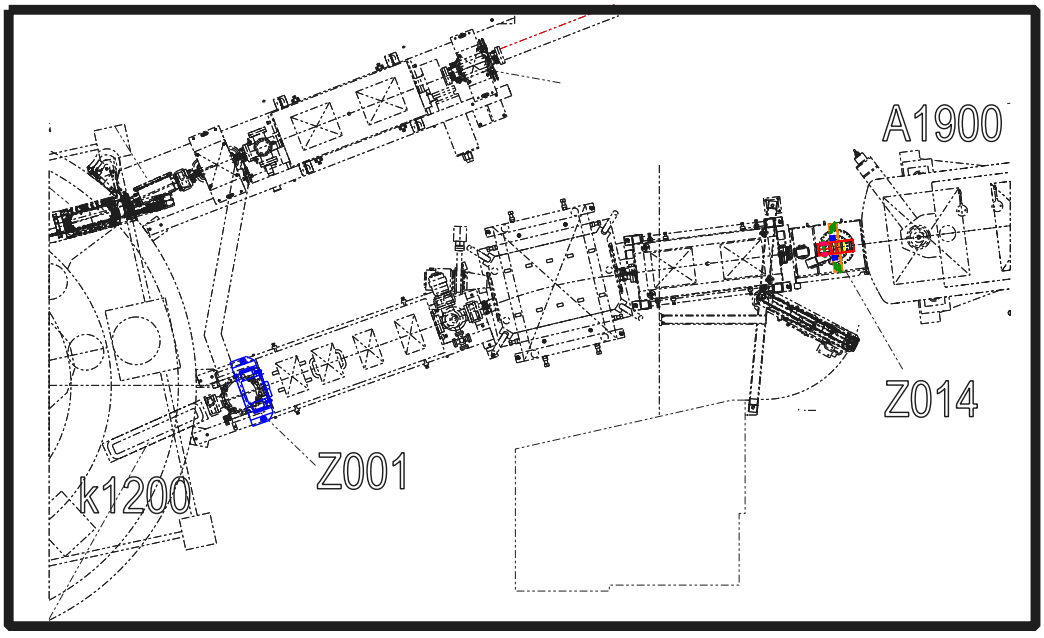

Figure 3.2: Faraday cups Z001 and Z014 in the extraction beam line and the target box, shown relative to the K1200 cyclotron and the A1900 fragment separator. The Z001 and Z014 Faraday Cups are magnified by a factor of 4 in the presented drawing.

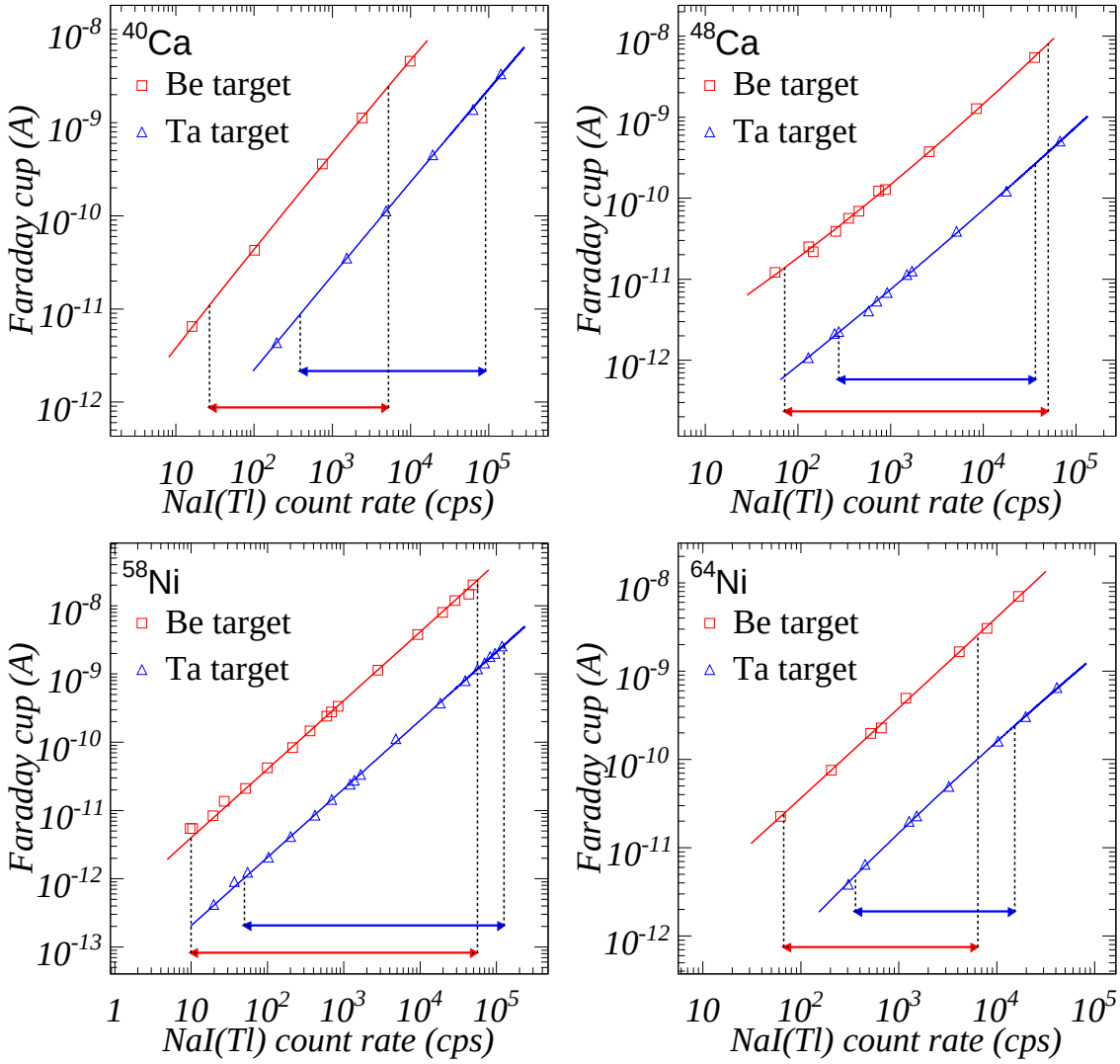

Figure 3.3: NaI(Tl) beam monitor calibration for all primary beams. Beam current measured by the Faraday Cup is plotted as a function of the NaI(Tl) background subtracted counting rate. Calibration data for ^{9}Be target are shown as red open squares and ^{181}Ta target as blue open triangles. ^{181}Ta target FC reading is offset by a factor of 0.1 in FC current reading for clarity. Solid lines through the calibration data show the fit by a second order polynomial in logarithmic representation. Horizontal arrows indicate the range of the NaI(Tl) counting rate used in our fragmentation experiments for both ^{9}Be and ^{181}Ta targets.

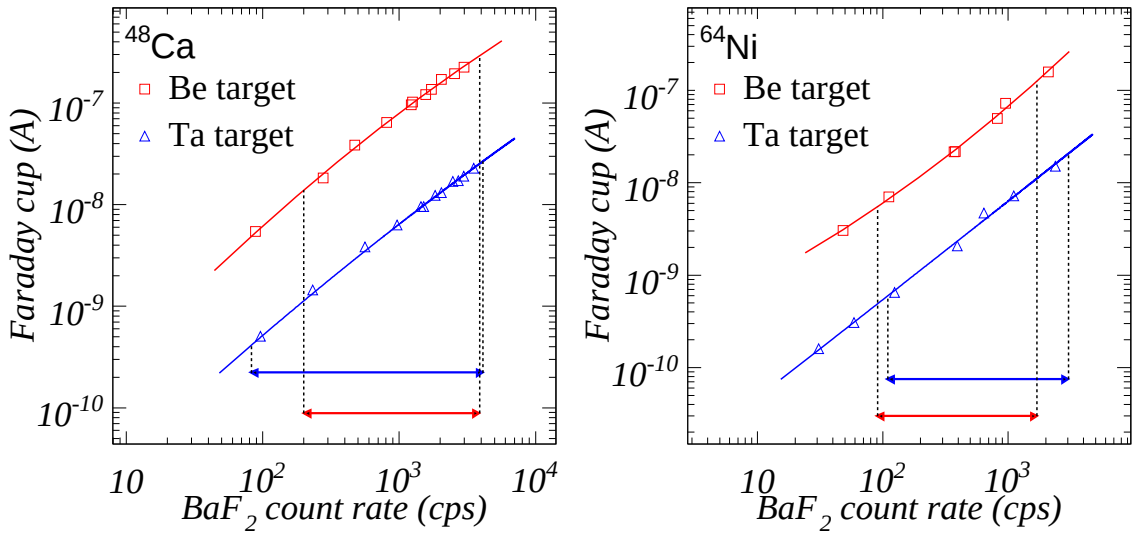

Figure 3.4: BaF_2 beam monitor calibration for primary beams mentioned in the text. Beam current measured by the Faraday Cup is plotted as a function of the BaF_2 background subtracted counting rate. Calibration data for ^{9}Be target are shown as red open squares and ^{181}Ta target as blue open triangles. ^{181}Ta target FC reading is offset by a factor of 0.1 in FC current reading for clarity. Solid lines through the calibration data show the fit by a second order polynomial in logarithmic representation. Horizontal arrows indicate the range of the BaF_2 counting rate used in our fragmentation experiments for both ^{9}Be and ^{181}Ta targets.

beam current measurement is taken the FC is retracted from the primary beam and the counts of the beam intensity monitors are recorded in scalers for 1–2 minutes. By repeating this procedure and varying the beam intensity by a series of meshes (attenuators), we obtained a dependence of the primary beam current and the beam monitor count rate. Since the beam monitors used are sensitive to the reactions of beam with target the calibration depends on the target material. The beam monitor calibrations were measured three times during each of the 4 fragmentation experiments (the beginning, middle and end). No time dependence of the calibration was observed during our experiments. For each set of beam intensity calibration a measurement of the background radiation was performed by stopping the primary beam at the exit of the ECR ion source.

Figure 3.3 shows all the NaI(Tl) monitor calibrations for ^{40,48}Ca and ^{58,64}Ni beams, in terms of correlation of the FC current reading with the background subtracted

count rate of the NaI(Tl) monitor. The calibrations with ^{9}Be target are shown as red squares and with ^{181}Ta as blue triangles. The fit by a second order polynomial in logarithmic representation is displayed as red (^{9}Be) and blue (^{181}Ta) solid line. The horizontal arrows indicate the range of applicability of our primary beam intensity calibration with the NaI(Tl) monitor. The calibration data are described by our fit function within 7–10% over the range of beam intensity we measured. In the case of the more neutron-rich projectiles ^{48}Ca and ^{64}Ni, when the beam current exceeded beyond 10^{-7} A, we used the BaF_2 monitor. The lower part was calibrated using the NaI(Tl) monitor and the upper part using the BaF_2 monitor. Figure 3.4 displays the calibration curves of the BaF_2 beam intensity monitor.

The calibration curves shown in Figure 3.3 and 3.4 are used in the analysis to determine the total number of beam particles traversing the target in each run.

3.2.2 RIKEN experiment

Primary beam intensity monitoring for ^{86}Kr fragmentation experiment was provided by the MOMOTA telescope placed at forward angle outside the target chamber as described in Section 2.4.3.

The FC was located after the target. This arrangement, in principle, allowed us to simultaneously measure the beam current (FC) and the secondary particle count rate (MOMOTA). Unfortunately, the primary beam reacts with the FC material and the back-scattered radiation affects the count rate of the MOMOTA monitor. This introduced an uncertainty upward of 15–20%. Thus we had to use a different method of beam intensity monitor calibration.

For the ^{86}Kr+^{9}Be system we measured the absolute beam intensity by counting $^{86}Kr^{33+}$ ions directly using the F2 plastic scintillator. From the measured charge state distribution as shown in Figure 3.1, the $^{86}Kr^{33+}$ charge state is 0.028% of the ^{86}Kr primary beam. During a 16 minute interval we recorded 1,054,792 events of $^{86}Kr^{33+}$ in the F2 scintillator, 10,607 counts were recorded in the MOMOTA telescope at the

same time. Background measurement yielded a background count rate of 0.008 cps in the F2 scintillator and 0 cps in the MOMOTA telescope. The background subtracted count rate of the MOMOTA telescope is directly proportional to the primary beam intensity.

In the case of ^{181}Ta we measured the absolute beam intensity by counting $^{86}Kr^{31+}$ ions directly in the F2 plastic scintillator. The $^{86}Kr^{31+}$ charge state probability is 0.016% of the primary beam ^{86}Kr. During a 4 minute measurement we recorded 214,525 events of $^{86}Kr^{31+}$ in the F2 scintillator and 479 counts were recorded in the MOMOTA beam intensity monitor.

3.3 Particle identification

The general particle identification method utilized in our fragmentation experiments is described in detail in Section 2.2. Since there are underlying differences in detector setups and details in the method of measurement of particle identification observables, we describe the particle identification analysis of the NSCL and RIKEN experiments separately.

3.3.1 NSCL experiments

The particle identification detector setup was located in the focal plane box of the A1900 fragment separator as shown in Figure 2.9. As discussed in Section 2.3.3 we used the $B\rho$-ToF-ΔE particle identification technique for all beam-target combinations measured at the NSCL, because we have $Q = Z$ for all fragments of interest. This simplifies the whole particle identification analysis because now by plotting the energy loss, ΔE, in the PIN detector versus the time of flight, ToF, for a fixed $B\rho$, we can separate all fragments traveling through the fragment separator. A typical raw experimental particle identification pattern is shown in the left panel of Figure 3.5. The example provided is for the ^{48}Ca+^{9}Be reaction at Bρ = 3.2 Tm. We can

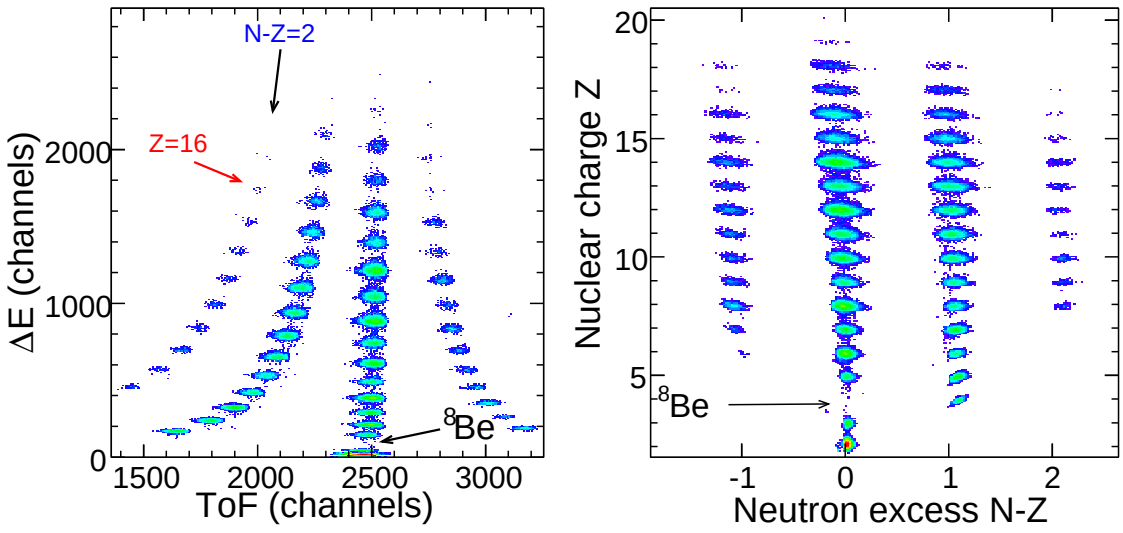

Figure 3.5: Uncalibrated (left panel) and calibrated (right panel) experimental particle identification (PID) spectra. The PID plots are shown for the ^{48}Ca+^{9}Be reaction at $B\rho = 3.2$ Tm.

see a clear separation of individual groups of events corresponding to different fragments. By recognizing the typical features of the PID spectrum and locating the hole corresponding to particle unbound ^{8}Be nucleus, as described in Section 2.3.3, we can identify all nuclides in the uncalibrated PID spectrum shown in the left panel of Figure 3.5. (The time of flight measurement was set up such that the more neutron-rich fragments are located to the left of the $N - Z = 0$ band.)

The values of ΔE and ToF in channels, were calibrated (Section 2.3.3) to the calculated energy loss and time of flight using the LISE++ code [56]. Then, parameters K_1 and K_2 in Equation (2.4) were fitted to the calculated values of energy loss and time of flight to reproduce observed nuclear charges, Z. Mass numbers were calculated using Equation (2.1). By performing the calibration for one $B\rho$ setting for each primary beam we can extract a set of calibration coefficients which allowed us to present all particle identification spectra in nuclear charge versus neutron excess $(N - Z)$ as shown in the right panel of Figure 3.5.

Fragment yields were extracted from calibrated particle identification spectra (example shown in the right panel of Figure 3.5) by counting events corresponding to

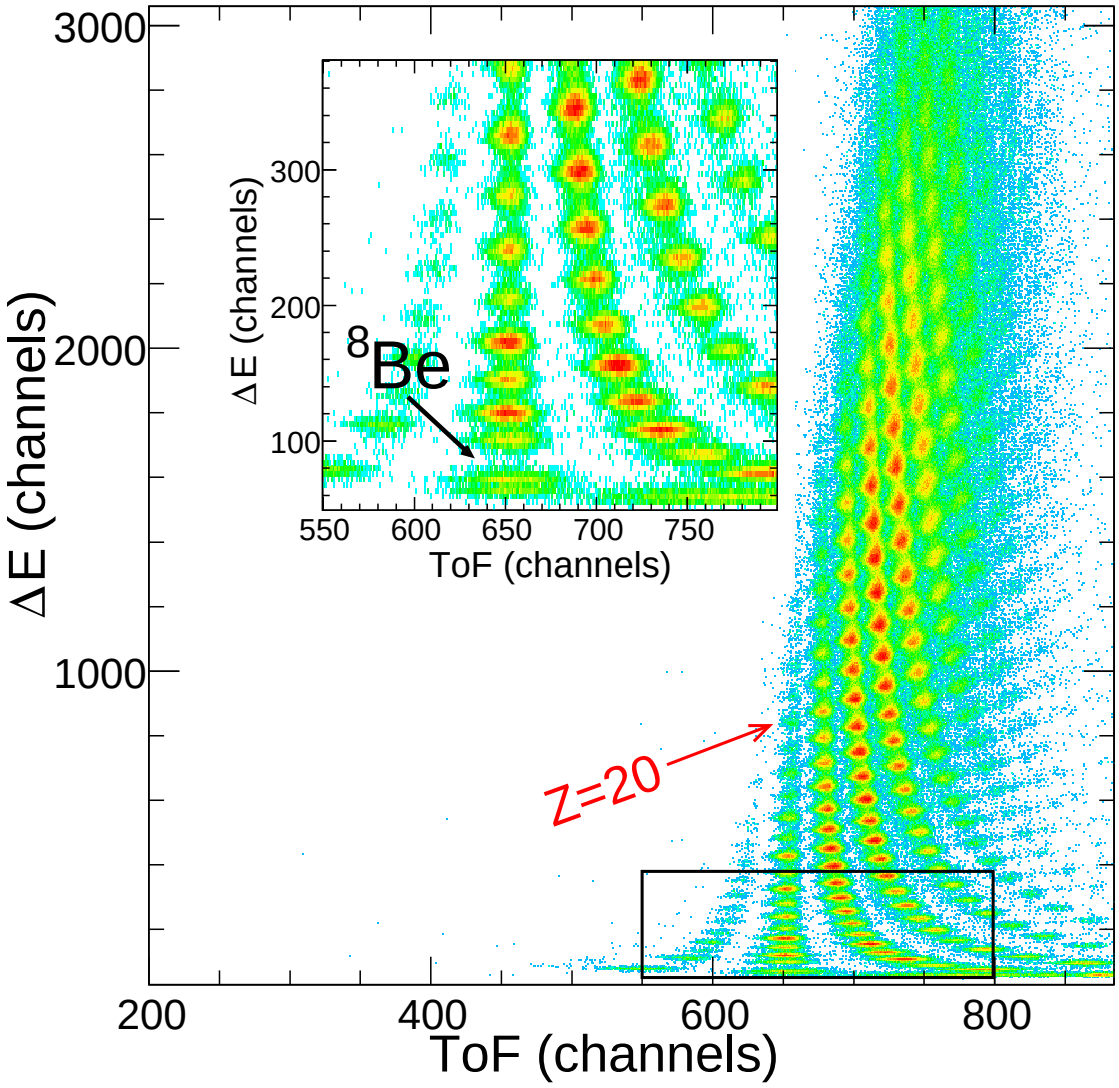

Figure 3.6: Uncalibrated particle identification spectrum of fragments created in reaction ^{86}Kr+^{181}Ta at $B\rho$=2.07 Tm. The inset shows zoomed area around the missing ^{8}Be.

individual isotopes. This procedure was applied to all magnetic rigidity settings and all beam-target combinations.

3.3.2 RIKEN experiment

At 64 MeV/u significant fractions of ^{86}Kr are not fully stripped of electrons after traversing the target. The charge state distribution of ^{86}Kr showed that approxi-

mately 10% of the primary beam intensity of ^{86}Kr is in ^{86}Kr^{35+} charge state after passing through the ^{9}Be target. The fraction is even larger in the case of ^{181}Ta target because the charge state distribution for ^{86}Kr primary beam is broader as discussed in Section 3.1. In this case we had to use the general $B\rho$-ToF-ΔE-TKE particle identification method. This technique allowed us to identify the momentum, p, mass number, A, nuclear charge, Z, and charge state, Q, for every fragment of interest by measuring four quantities the magnetic rigidity, $B\rho$, time of flight, ToF, energy loss, ΔE, and total kinetic energy, TKE.

Basic particle identification plot and calibration procedure is the same as in the case of the NSCL experiments. Figure 3.6 shows an uncalibrated particle identification plot, ΔE versus ToF, for a 2.07 Tm magnetic rigidity setting using ^{86}Kr+^{181}Ta reaction. The inset shows the zoomed area around the ^{8}Be hole. (The time of flight measurement was set up such that the more neutron-rich fragments are located to the right of the $N - Z = 0$ band.) From that reference point we can identify all isotopes in the PID spectrum. The ToF and ΔE detector calibrations were done following the same procedure used for the NSCL reaction systems. In the case of ^{86}Kr beam isotopes of all elements in the analysis ($Z \geq 25$) come in multiple charge states. The measurement of the total kinetic energy, TKE, must be used to provide clean separation.

The analysis procedure is demonstrated in Figure 3.7 for the ^{86}Kr+^{9}Be reaction run with 2.07 Tm magnetic rigidity setting. The left panel of the Figure 3.7 shows the energy loss, ΔE, versus time of flight, ToF, PID spectrum with gates around elements with $Z = 28$, 31 and 34. The right panel of Figure 3.7 plots the charge state, Q versus A/Q ratio plane for fragments with $Z = 28$, 31, and 34 gates from bottom to top, respectively. We see isotope charge states clearly separated for all elements showed. The counts of individual isotopes in different charge states for the differential cross section calculation were extracted from the charge state, Q, versus A/Q ratio plots.

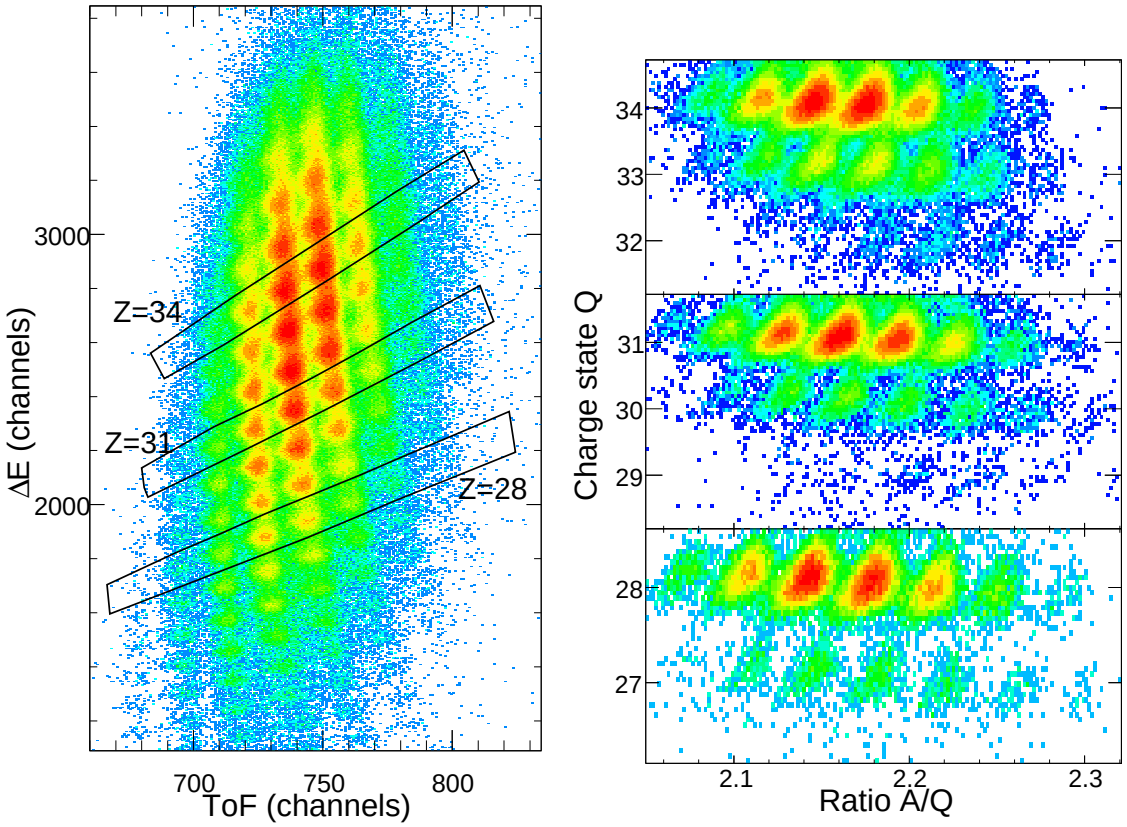

Figure 3.7: Particle identification spectrum for a 2.07 Tm magnetic rigidity setting for the ^{86}Kr+^{9}Be reaction. Left panel shows the PID with three gates around elements with $Z = 28$, 31 and 34. Right panel shows projections to charge state, Q, versus A/Q ratio plane of events within the corresponding nuclear charge gates $Z = 28$, 31, 34 from bottom to top, respectively.

3.4 Cross section analysis

3.4.1 Differential cross sections

Yield for a given fragment and the momentum acceptance of a magnetic rigidity setting are combined together with primary beam intensity determined by the calibration described in Section 3.2 to obtain the differential cross section, $\mathrm{d}\sigma/\mathrm{d}p$, using the following formula:

$$\frac{\mathrm{d}\sigma}{\mathrm{d}p}(A,Z) = \frac{N(A,Z)\cdot M_t}{I\cdot t\cdot N_A\cdot d_t\cdot \Delta p\cdot \tau_{LIVE}}, \tag{3.1}$$

where

$N(A,Z)$	Number of events for a fragment (A,Z),
I	Primary beam intensity during the run (s^{-1}),
t	Time duration of the run (s),
N_A	Avogadro's number (mol^{-1}),
M_t	Atomic number of target material ($gmol^{-1}$),
d_t	Target thickness (gcm^{-2}),
Δp	Momentum acceptance (0.2% in dp/p),
τ_{LIVE}	Live time correction.

By plotting the differential cross section, $d\sigma/dp$, as a function of momentum, p, for a given fragment a momentum distribution is obtained. The area of the momentum distribution, in this representation, is the fragment production cross section. The momentum distributions are discussed in more details in the following chapter. Here we focus our attention to the transmission correction factor evaluation and the momentum distribution fitting procedure.

3.4.2 Momentum distribution fitting procedure

Momentum distributions of fragmentation products provide insight into the fragmentation reaction mechanism. Momentum distributions of fragments created in relativistic heavy-ion fragmentation are well described by a Gaussian function [64]. It has been shown that the momentum distributions created in the intermediate energy (20–200 MeV/u) fragmentation are asymmetric [65]. We can separate the momentum distribution into two half Gaussians joined at maximum, p_0, the high momentum side created by a "pure" fragmentation mechanism characterized by σ_R and the low momentum side created by a "mixed" reaction mechanism described by σ_L [59]:

$$\frac{d\sigma}{dp} = \begin{cases} S \cdot \exp\left(-(p-p_0)^2/(2\sigma_L^2)\right) & \text{for } p \leq p_0, \\ S \cdot \exp\left(-(p-p_0)^2/(2\sigma_R^2)\right) & \text{for } p > p_0, \end{cases} \tag{3.2}$$

where S is the normalization parameter.

The experimental width parameters σ_L and σ_R, were extracted from the asymmetric experimental momentum distributions using fits with a modified Gaussian function of Equation (3.2). Such procedure, however, results in correlations among the three parameters p_0, σ_L, and σ_R characterizing the shape of the fragment momentum distributions. A minute change in the centroid, p_0, will result in different division of the total width of the momentum distribution between the σ_L and σ_R. These complications, however, do not affect the determination of the fragmentation production cross sections.

3.4.3 Evaluation of fragmentation production cross section

The fragmentation production cross section is obtained by integrating the area of the momentum distribution and divided by the transmission coefficient, ε. This transmission correction factor, ε, expresses the efficiency correction of our measurement is addressed in more details in the following section. The momentum distributions for fragments in our analysis were obtained by a systematic scan of the magnetic rigidity space as described in Sections 2.3.4 and 2.4.4 for the A1900 and RIPS fragment separator experiments. Most of the experimental momentum differential cross sections extend over 1–4 orders of magnitude (typical examples shown in Figure 4.1). Since the range in the $B\rho$ space covered in our experiments is limited, there are fragments in our data with parts of the momentum distribution (either low or high momentum side) not measured. Figure 3.8 shows examples of complete and incomplete momentum distributions of ^{50}V and ^{50}Mn fragments, respectively, produced in ^{64}Ni+^{9}Be fragmentation reactions.

The complete momentum distributions were fitted by a modified Gaussian function of Equation (3.2) by minimization of χ^2 method. Most of the experimental momentum distributions were described extremely well over almost three orders of magnitude (e. g., see ^{50}V in Figure 3.8). Overall approximately 60–80% (depending on

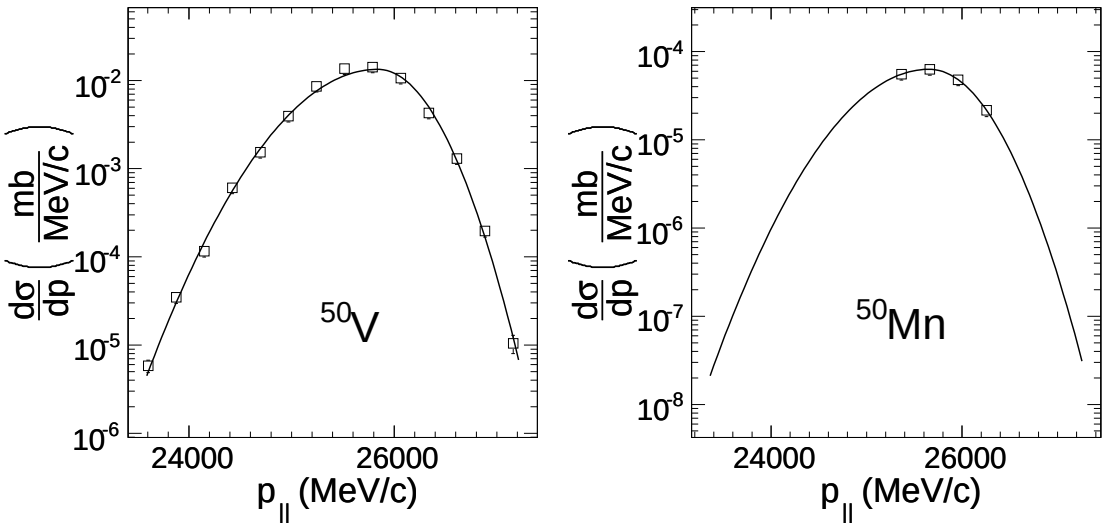

Figure 3.8: Momentum distributions of ^{50}V and ^{50}Mn created in fragmentation of ^{64}Ni on ^{9}Be target. Shown fragments demonstrate a typical complete (^{50}V) and incomplete (^{50}Mn) momentum distributions. Experimental data are depicted by open squares and the fit by modified Gaussian function of Equation (3.2) is shown as a solid line.

the reaction system) of the fragments have complete momentum distributions.

The above described fitting procedure was not suitable for the distributions with very few experimental points (< 5), or for distributions with missing left or right sides. In order to extract fragmentation production cross sections for these fragments and to minimize the uncertainties we took advantage of the larger set of completely measured momentum distributions. This set of data provided a data base for empirical systematics of the three parameters of the modified Gaussian function (Equation (3.2)): the matching point p_0, the variances of the left, σ_L, and the right, σ_R, sides. The analysis procedure for extraction of the production fragmentation cross sections for the fragments with incompletely measured momentum distributions is demonstrated in the case of fragmentation of ^{64}Ni on a ^{9}Be target.

In the top left panel of Figure 3.9, the fitting parameter p_0 is plotted as a function of fragment mass number. All p_0 determined by fitting of the experimental data with the modified Gaussian function were within 1% of the polynomial systematics shown as a solid line. This parameterization assumes that p_0 for a given mass number are identical, but the experimental data show deviations. In order to get an even

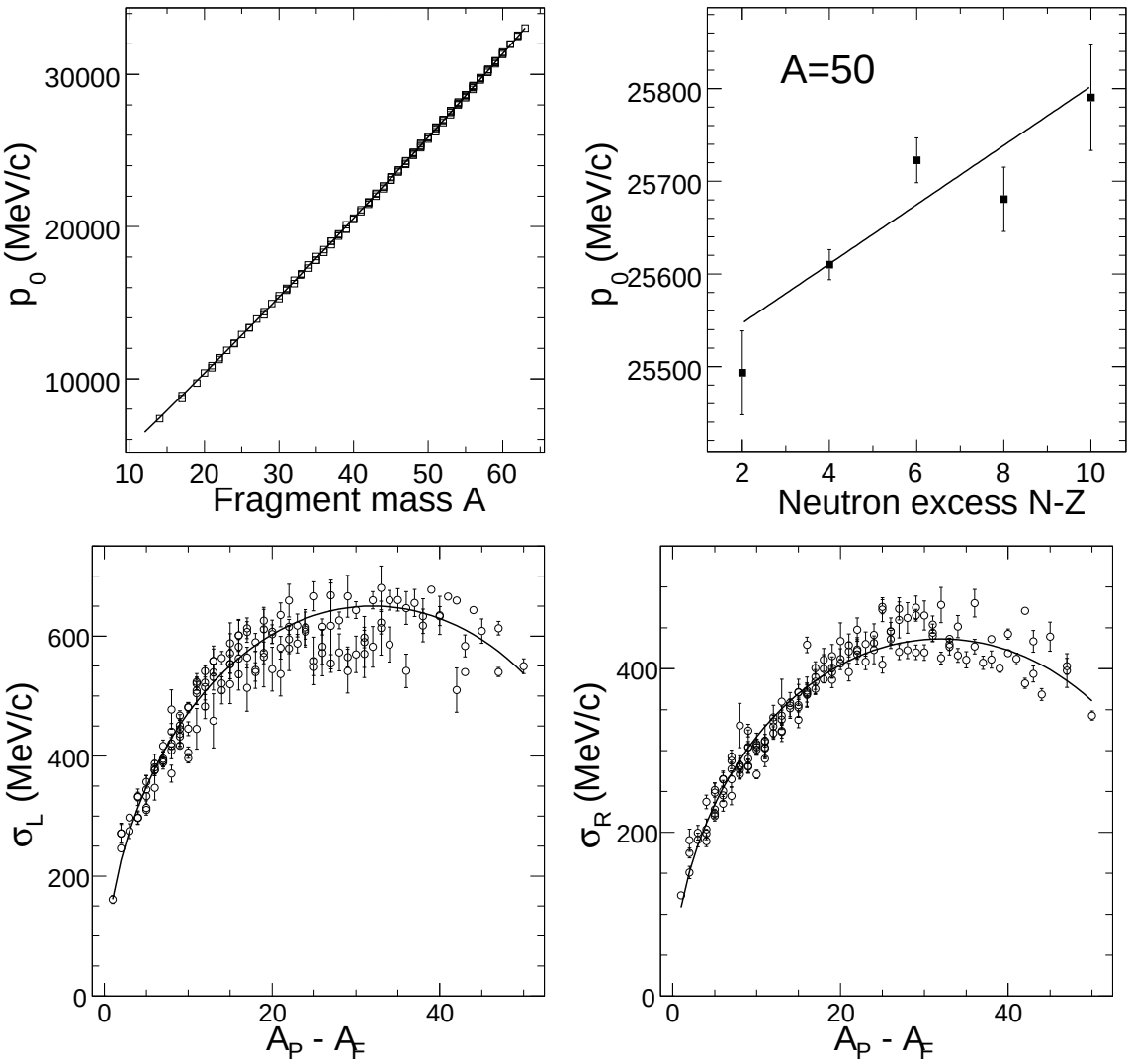

Figure 3.9: Systematics of the centroids and variances of the momentum distributions for the reaction ^{64}Ni+^{9}Be. Upper row shows the centroids, p_0; the variances, σ_L and σ_R, are shown in the bottom row.

more precise prescription for the centroids we fitted individual isobar chains as a function of neutron excess to get a "local" parameterization. The top right panel of Figure 3.9 shows a linear fit for the centroids of isobars $A = 50$. In this local systematics for the centroids it was shown that the experimental data were within 0.5% of the parameterization line. The variances σ_L and σ_R are modeled by the Goldhaber model [64]

$$\begin{aligned} \sigma_L &= \sigma_0^L \cdot \sqrt{\tfrac{A(A_P-A)}{A_P-1}}, \\ \sigma_R &= \sigma_0^R \cdot \sqrt{\tfrac{A(A_P-A)}{A_P-1}}, \end{aligned} \tag{3.3}$$

where A_P and A are atomic mass of the projectile and fragment respectively and σ_0^L, σ_0^R are used as fitting parameters. Best fits to the experimentally determined σ_L and σ_R are shown in bottom panels of Figure 3.9. To describe the experimental data $\sigma_0^L = 140$ and $\sigma_0^R = 94$ MeV/c were used. The incomplete momentum distributions were fitted with Equation (3.2) by having the centroid p_0 and variances σ_L and σ_R to range over values centered at values determined by the parameterization. The size of the interval over which the parameters were allowed to vary was $\pm 1\%$ for the centroid p_0 and $\pm 13\%$ for the variances σ_L and σ_R.

Figure 3.8 shows examples of complete and incomplete momentum distributions (open squares) along with the fitted modified Gaussian function of Equation (3.2) (solid line) for fragments ^{50}V and ^{50}Mn respectively.

All fragmentation cross sections σ_{frag} were calculated using

$$\sigma_{frag} = S \cdot \sqrt{\frac{\pi}{2}} \cdot (\sigma_L + \sigma_R), \tag{3.4}$$

where S, σ_L and σ_R are parameters of the modified Gaussian function (3.2). The calculation of fragmentation production cross section, σ_{frag}, in Equation (3.4) is equivalent to integrating Equation (3.2) over all momenta, p.

In the case of ^{86}Kr primary beam the total fragment yield is distributed over different charge states. For ^{86}Kr+^{9}Be reaction system we analyzed fragments with

$Z - Q = 0$ charge states. Since the measured charge state distribution for the primary beam is reproduced well for the ^{86}Kr+^{9}Be reaction, we use the GLOBAL code to correct the final cross sections for all fragments in the analysis. The calculated corrections vary between 1–9% for isotopes of $25 \leq Z \leq 36$ elements.

For the ^{86}Kr+^{181}Ta reaction we analyzed the three most abundant charge states ($Z - Q = 0$, 1, 2) in order to harvest most of the total cross section. The sum of these three charge states for the ^{86}Kr beam on ^{181}Ta target is reproduced very well by the GLOBAL calculation. The corrections for fragment cross sections in the ^{86}Kr+^{181}Ta analysis, calculated by GLOBAL, vary between 0.1–3% for isotopes of $25 \leq Z \leq 36$ elements.

3.4.4 Transmission correction evaluation

The transmission correction, ε, is essentially a correction factor for the experimental acceptance. It accounts for finite spatial and angular acceptance and transport efficiency of the fragment separator used in the experimental measurement. The difficulties in the evaluation of this correction arise from our inability to measure the essential ingredients. The transmission correction can be factored into momentum (longitudinal direction) and angular (transverse direction) transmission. The coordinate system used in our calculations and in further discussion is shown in Figure 3.10, where 'z' is in beam direction and 'x', 'y' are in plane perpendicular to the beam direction.

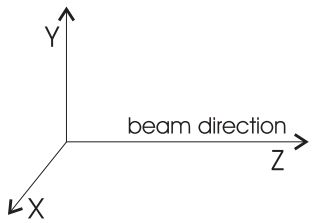

Figure 3.10: Coordinate system used in ion optical calculations of transmission correction. Where 'Z' is in the primary beam direction and 'X' and 'Y' are in the perpendicular plane.

In Section 2.1 we discussed that the narrow momentum acceptance implies simpler evaluation of the transmission. To evaluate the momentum acceptance (0.2% in dp/p) effect we used a universal Monte Carlo code for the transport of heavy ions through matter within ion-optical systems MOCADI [66]. All MOCADI simulations were carried out in the first order. The momentum acceptance was defined as a ratio of the number of particles transported to the focal plane of the fragment separator and the number of particles within ±0.1% of the central momentum in the target plane. This ratio is calculated only for particle transmitted in angular space with 100% probability, in order to ensure the separation of the angular and momentum transmission corrections. The momentum acceptance in our definition is independent of the magnetic rigidity setting and the fragment mass and charge. The momentum transmission in our case expresses the "effectiveness" of the momentum cut made by the slit system at the intermediate image of the fragment separator. The calculated momentum transmission is 96±2% and 98±2% for the A1900 and RIPS fragment separators, respectively. The uncertainties in the momentum slit opening and angular cut contribute to the final error of the momentum transmission. Calculated angular acceptance areas, used in the evaluation of the momentum transmission, of the two fragment separators are presented in Figure 3.11. Calculations were carried out using the primary beam (^{58}Ni and ^{86}Kr for the A1900 and RIPS respectively) with unrealistically large uniform angular distribution (±80 mrad) in both the θ ('x' direction) and ϕ ('y' direction) angles. Simulated plots in Figure 3.11 show the projection of particles transported to the focal plane of the fragment separator to the ϕ versus θ plane at the target position, thus defining the angular acceptance of the A1900 (left panel of Figure 3.11) and RIPS (right panel of Figure 3.11) fragment separators in our MOCADI simulations.

For evaluation of the angular transmission we used LISE++ [56]. This code uses analytical methods to calculate the transport of particles through the fragment separator, which enable it to execute the calculations much faster than Monte Carlo based

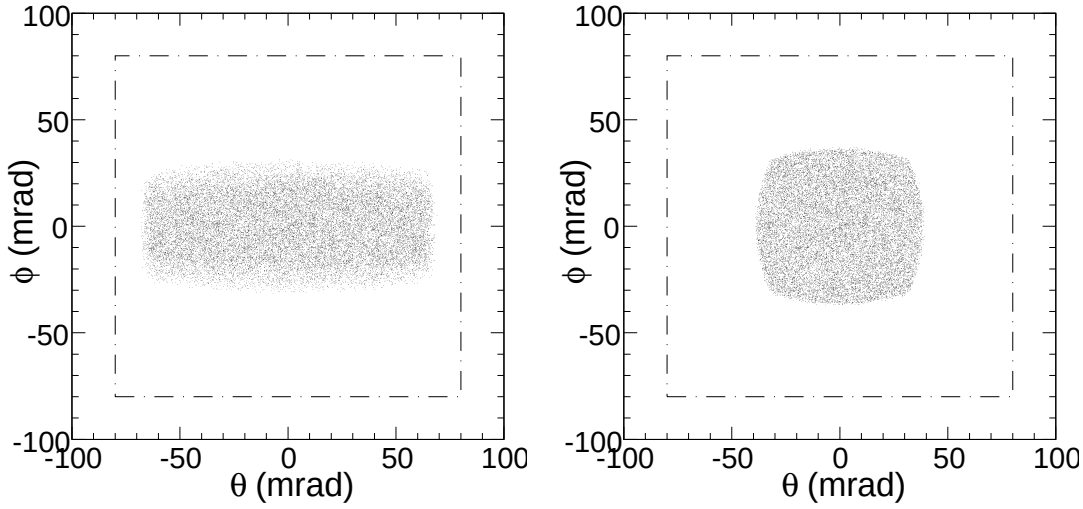

Figure 3.11: Angular acceptance of the A1900 (left panel) and RIPS (right panel) fragment separators as calculated by MOCADI in ϕ versus θ plane. Dashed-dotted line denotes the input angular distribution ($\pm$80 mrad) for the MOCADI calculation.

MOCADI. A benchmark calculation was performed for the ^{58}Ni+^{9}Be system using identical parameterization for the angular distributions of fragments and the primary beam emittance. In Figure 3.12 we show the calculated angular transmission curves using LISE++ and MOCADI codes. Since the overall agreement is better than 4%, we use LISE++ for all angular transmission calculations.

The angular transmission was defined as a portion of the angular distribution, for a given fragment, transported to the focal plane of the fragment separator. Results of the angular transmission calculations depend on the primary beam emittance and the fragment angular distribution assumptions. Since the experimental data for these two components are scarce, we had to rely on parameterizations and estimates.

The emittance of the primary beam is given by its spatial and angular distributions. The primary beam spot size in the target plane is approximately $2 \times 2\,\mathrm{mm}^2$, which gives us an estimate of the spatial component. The direct measurement of the angular distribution of the primary beam in the target plane is not available. We did get an estimate of the primary beam angular distribution for the ^{58}Ni primary beam by measuring the position and angular distributions at the intermediate image

(I2) of the A1900 fragment separator. In order to reproduce the measured distributions using MOCADI Gaussian profiles of the primary beam with variances in spatial $\sigma_{\mathrm{x}} = \sigma_{\mathrm{y}} = 1\,\mathrm{mm}$ and angular $\sigma_\theta = \sigma_\phi = 7\,\mathrm{mrad}$ coordinates were used.

Another estimate of the primary beam emittance can be inferred from the calculations for all beams delivered by the K1200 cyclotron in stand alone mode during the 1990s as shown in Figure 3.13. Most of the beam emittances fall within approximately $14\,\pi \cdot \mathrm{mm} \cdot \mathrm{mrad}$ in both 'x' and 'y' directions. If we assume the normalized emittance of the K1200 and the CCF is the same we can take the K1200 stand alone mode emittance as an upper limit of the CCF primary beam emittance. This result is consistent with the above mentioned conclusions of MOCADI calculation.

In the case of the RIKEN fragmentation experiment we had to rely solely on ion optical calculations [68]. The primary beam spot size in the target plane for the RIKEN experiment was approximately $1 \times 1\,\mathrm{mm}^2$. The ion optics calculations suggest that the emittance of the primary beam is roughly half of that at the CCF, resulting in $\sigma_\theta = \sigma_\phi = 3\,\mathrm{mrad}$ [68].

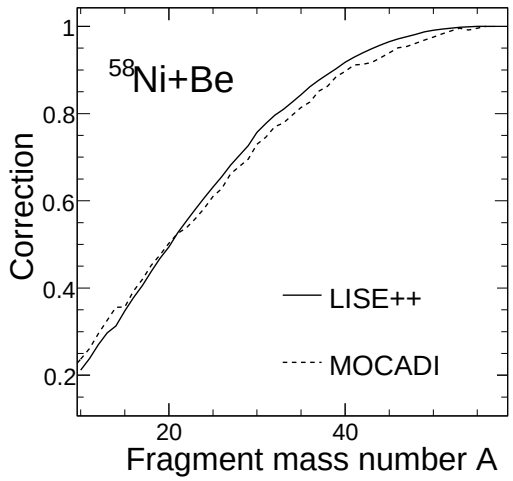

Figure 3.12: Comparison of angular transmission calculated using the LISE++ and MOCADI codes. Parameterization of Equation (3.5) for the variance of the transverse momentum distribution is used in both cases with $\sigma_0 = 100$ MeV/c and $\sigma_D = 200$ MeV/c. Primary beam emittance parameters: $\sigma_x = \sigma_y = 1$ mm and $\sigma_\theta = \sigma_\phi = 7$ mrad.

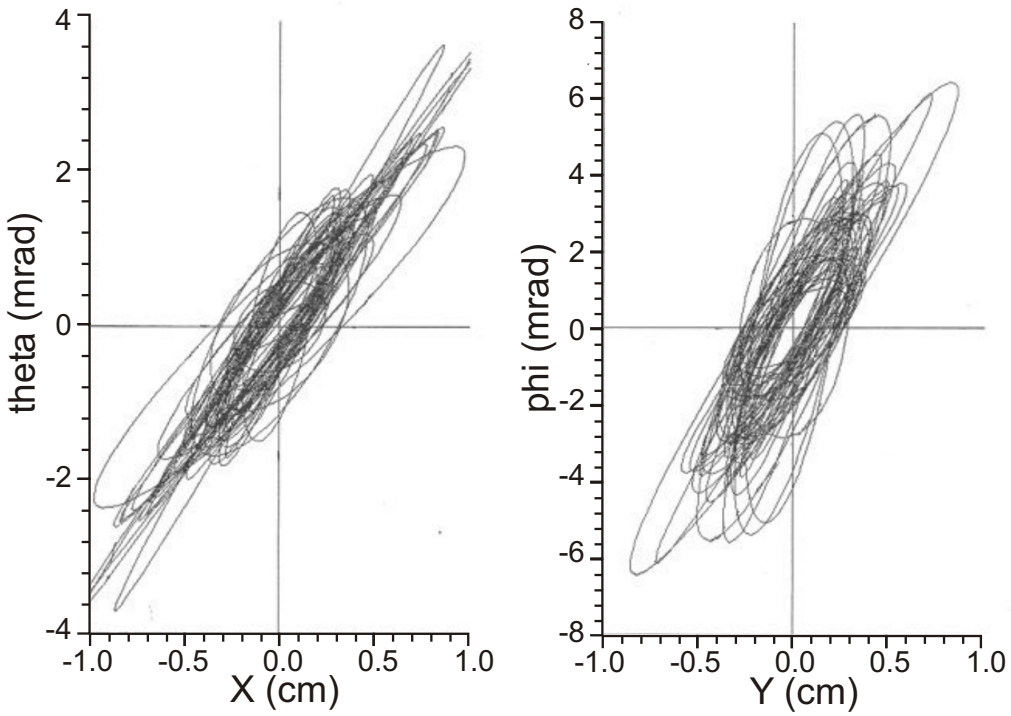

Figure 3.13: Calculations of the primary beam emittance ellipses in θ versus x phase space (left panel) and ϕ versus y phase space (right panel) for all primary beams delivered by the K1200 cyclotron in stand alone mode during the 1990s [67].

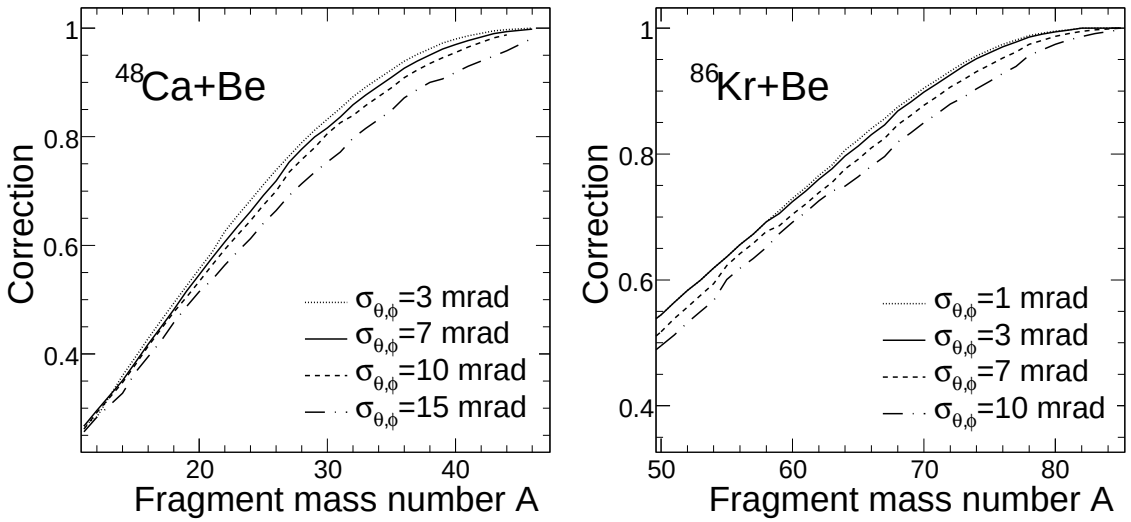

Figure 3.14: Angular transmission correction as a function of fragment mass number for the A1900 (^{48}Ca+^{9}Be) and RIPS (^{86}Kr+^{9}Be) fragment separators. The calculations were done for different values of variances of the Gaussian profile of the primary beam angular distributions, $\sigma_{\theta,\phi}$. All calculations used Equation (3.5) to evaluate the variance of the transverse momentum distribution $\sigma_{\perp}$ with $\sigma_0 = 100$ MeV/c, $\sigma_D = 200$ MeV/c.

Due to uncertainties associated with the determination of the primary beam angular distributions we carried out a series of angular correction calculations using the LISE++ code. The primary beam angular distributions were simulated with Gaussian profiles, in all cases, varying the variances, $\sigma_{\theta,\phi}$, in 'x' and 'y' directions respectively. The LISE++ calculations in Figure 3.14 for the A1900 fragment separator were done using the ^{48}Ca+^{9}Be reaction with $\sigma_{\theta,\phi}$ = 3, 7, 10 and 15 mrad, and for the RIPS fragment separator using the ^{86}Kr+^{9}Be reaction with $\sigma_{\theta,\phi}$ = 1, 3, 7 and 10 mrad. We see that the uncertainty of the $\sigma_{\theta,\phi}$ is within ±3 mrad of the above estimated values of 7 and 3 mrad for the A1900 and RIPS, respectively, resulting in the angular transmission correction uncertainty at the level of approximately 3–4%. For all angular transmission calculations we used $\sigma_\theta = \sigma_\phi = 7$ mrad, $\sigma_{\rm x} = \sigma_{\rm y} = 1$ mm for the NSCL primary beams and $\sigma_\theta = \sigma_\phi = 3$ mrad, $\sigma_{\rm x} = \sigma_{\rm y} = 0.75$ mm for the RIKEN primary beam as explained above.

Experimentally the longitudinal and the transverse components of momentum

distributions after fragmentation are equal (within 10%) in relativistic energy regime [69]. However, this is not the case at intermediate energies [70, 71]. Since there are no published experimental data available for the angular distributions of the fragments measured in our fragmentation experiments, we relied on the parameterization [70] of the variance of the transverse momentum distributions, $\sigma_\perp$:

$$\sigma_\perp^2 = \sigma_0^2 \frac{A(A_P - A)}{A_P - 1} + \sigma_D^2 \frac{A(A-1)}{A_P(A_P - 1)} \tag{3.5}$$

where A_P and A are mass numbers of the projectile and fragment, respectively. The first term in Equation (3.5) comes from the Goldhaber model for the width of a longitudinal momentum distribution and the second term results from the deflection of the projectile by the target nucleus [71]. σ_0 can be determined by our measurement of the longitudinal momentum distributions and σ_D, the orbital dispersion, is taken from Ref. [70], where it is shown to describe the fragmentation data of ^{16}O at 92.5 and 117.5 MeV/u. From the published data [70] we estimated the orbital dispersion parameter σ_D to be 185 ± 15 MeV/c for the NSCL experiments and 225 ± 25 MeV/c for the RIKEN experiment.

We were able to confirm the parameterization of Equation (3.5) with the fragment angular distributions measured in a separate experiment at the NSCL using the S800 spectrograph [73]. Figure 3.15 shows the angular distributions for ^{44}Ca and ^{59}Co fragments produced in the ^{64}Ni+^{9}Be reaction at 95 MeV/u. The angular distributions were reconstructed with the inverse mapping technique using the S800 spectrograph for the reaction ^{64}Ni+^{9}Be [72]. Based on the measured angular distributions in the 'x' direction, we calculated the variance of the transverse angular distribution $\sigma_\perp(\theta) = 33 \pm 2$ and 16 ± 1 mrad for ^{44}Ca and ^{59}Co fragments, respectively. These transverse angular distributions translate to transverse momentum widths $\sigma_\perp = 482 \pm 29$ and 319 ± 20 MeV/c for ^{44}Ca and ^{59}Co, while the parameterization (Equation (3.5)) predicts $\sigma_\perp = 446 \pm 12$ and 301 ± 12 MeV/c. There is a good agreement between the

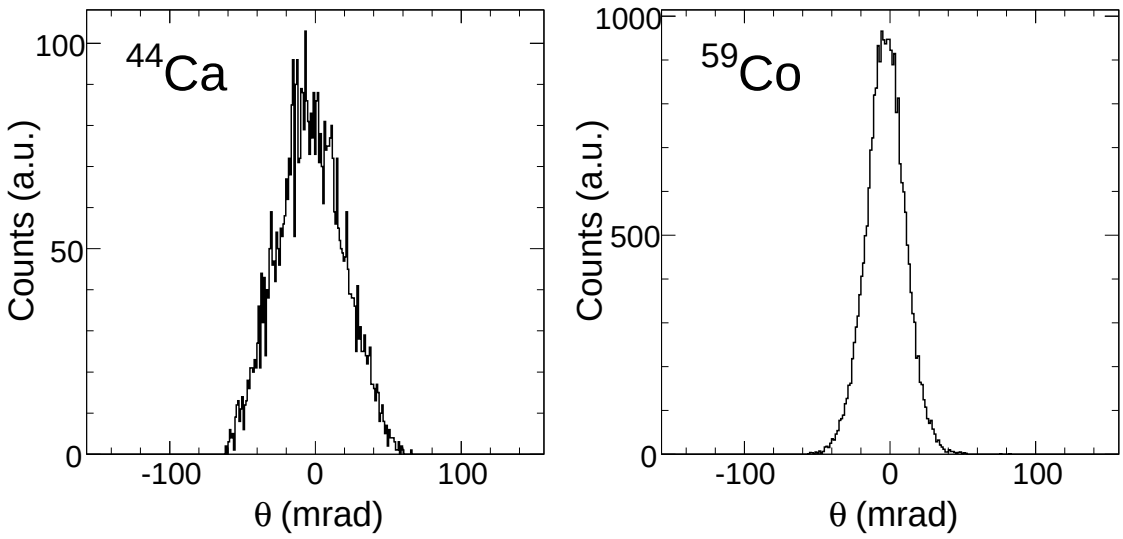

Figure 3.15: Angular distributions in the target plane for ^{44}Ca and ^{59}Co fragments from the ^{64}Ni+^{9}Be reaction, measured at the NSCL using the S800 spectrograph from Ref. [72]. See text for details.

measured width and predictions from Equation (3.5).

As was discussed in the previous sections, the experimental momentum distribution for our fragmentation data are described by a modified Gaussian function of Equation (3.2) characterized by two width parameters σ_L and σ_R. For the purposes of the angular transmission calculations we approximated the momentum distributions with equivalent Gaussian shape. The actual σ_0 parameter was determined by fitting $(\sigma_L + \sigma_R)/2$ from the experimental data. Values of σ_0 and σ_D parameters used in our transmission correction calculations are listed in Table 3.1.

Final transmission corrections were obtained as a product of the momentum and the angular transmission corrections. The calculated transmission correction, ε, is plotted as a function of fragment mass number in Figures 3.16 and 3.17 for all reaction systems. Figure 3.16 displays the mass dependence of the transmission correction for the ^{40}Ca (top panels), ^{48}Ca (bottom panels) beams with ^{9}Be (left panels), ^{181}Ta (right panels) targets. The transmission correction for the ^{58}Ni (top panels), ^{64}Ni (middle panels), and ^{86}Kr (bottom panels) beams with ^{9}Be (left panels), ^{181}Ta (right panels) targets are showed in Figure 3.17. The shaded region denotes the estimated

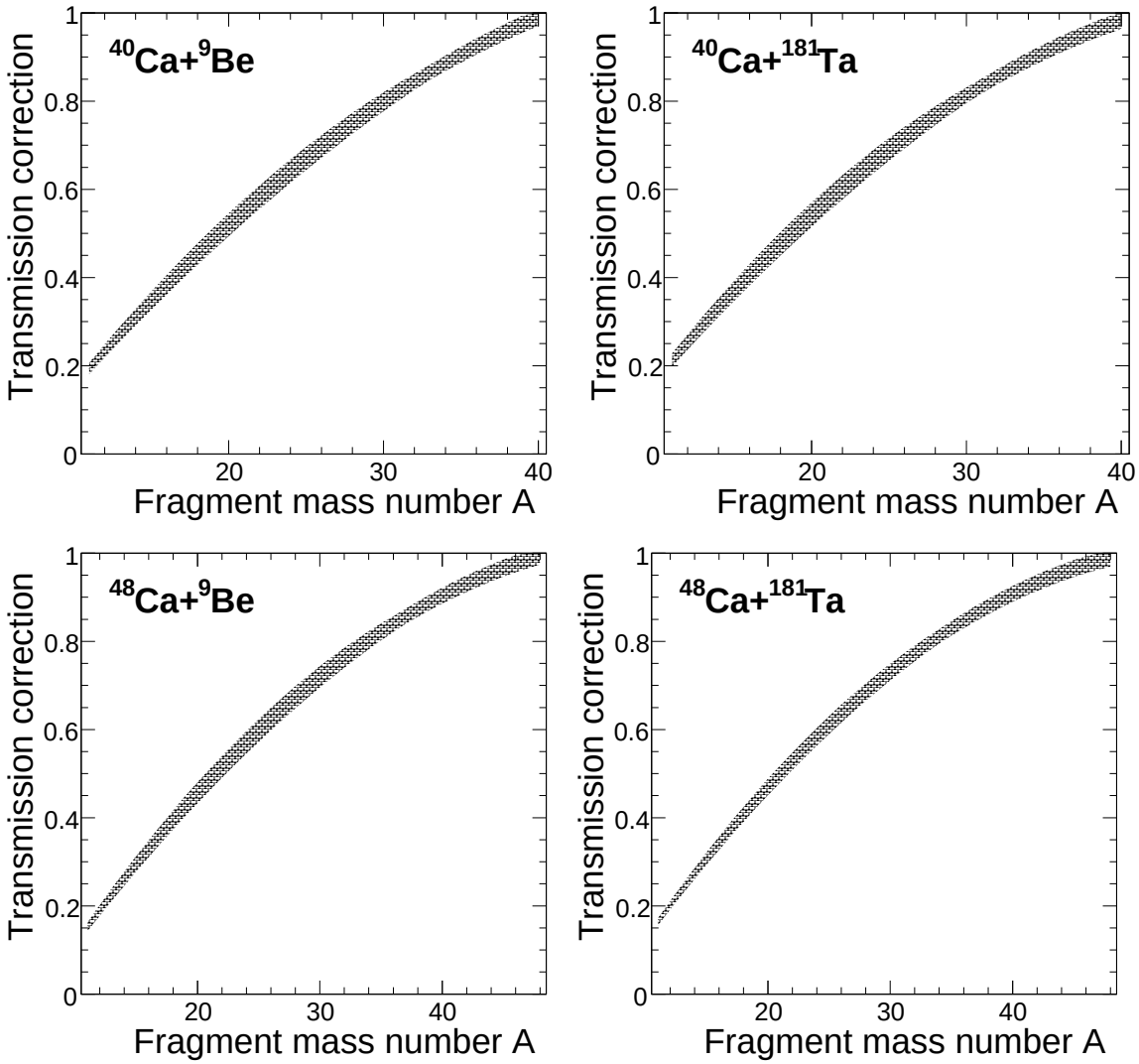

Figure 3.16: Final transmission correction, ε, as a function of fragment mass number for ^{40,48}Ca primary beams with ^{9}Be and ^{181}Ta obtained for 0.2% momentum acceptance.

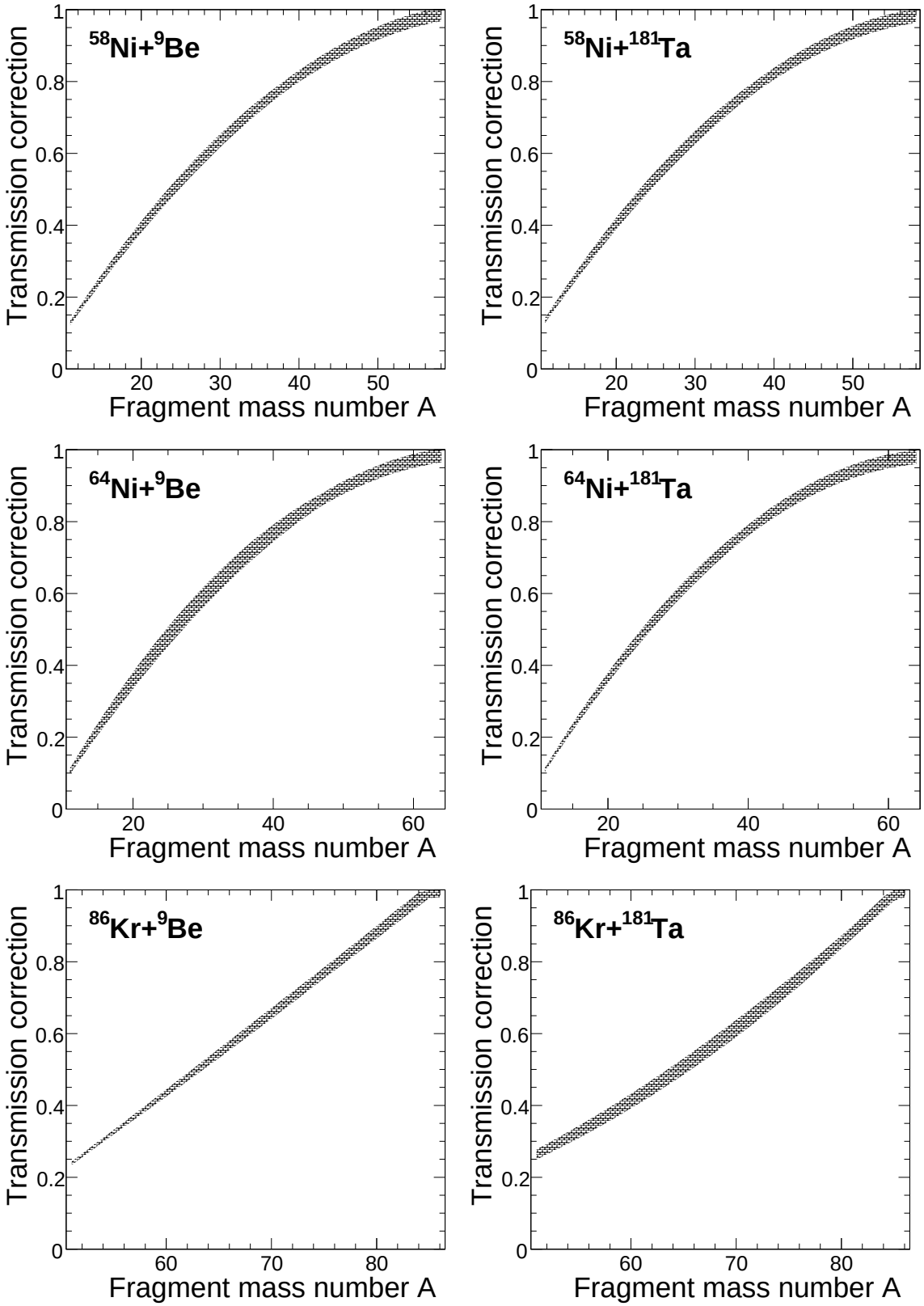

Figure 3.17: Final transmission correction, ε, as a function of fragment mass number for ^{58,64}Ni and ^{86}Kr primary beams with ^{9}Be and ^{181}Ta targets obtained for 0.2% momentum acceptance.

Table 3.1: Values of σ_0 and σ_D parameters in Equation (3.5) used in the angular transmission correction calculations for different primary beam target combinations.

Beam	Target	σ_0 (MeV/c)	σ_D (MeV/c)
^{40}Ca	^{9}Be	106 ± 4	185 ± 15
	^{181}Ta	101 ± 5	185 ± 15
^{48}Ca	^{9}Be	109 ± 5	185 ± 15
	^{181}Ta	106 ± 4	185 ± 15
^{58}Ni	^{9}Be	113 ± 3	185 ± 15
	^{181}Ta	110 ± 3	185 ± 15
^{64}Ni	^{9}Be	117 ± 5	185 ± 15
	^{181}Ta	114 ± 3	185 ± 15
^{86}Kr	^{9}Be	147 ± 5	225 ± 25
	^{181}Ta	153 ± 5	225 ± 25

uncertainty in the transmission correction factors which are dominated by the uncertainty of the σ_0 parameter for light fragments and the uncertainty of momentum transmission for heavy fragments.

3.5 Error analysis

The uncertainties in the final fragmentation cross section are calculated based on the statistical uncertainty, the beam intensity calibration (7–10%), the error calculated by the fitting procedure and the transmission uncertainty (2–8%). Uncertainty of the target thickness determination and momentum slit opening were estimated to be smaller than 2% and hence they are neglected in our error analysis. Other uncertainties like reaction losses in detectors and secondary reactions in the target material are smaller than 1% so their contributions are also neglected. For the fragments measured with incomplete momentum distributions, a systematic error stemming from the extrapolation of the parameterization of p_0, σ_L and σ_R were included in addition to the above mentioned errors.

Chapter 4

Experimental results

This chapter presents the experimental data extracted from the four projectile fragmentation experiments carried out at the NSCL and one at RIKEN. The fundamental parameters, such as the shape, maximum, and width of the momentum distributions of fragments are presented. The production fragmentation cross sections are compared to the empirical parameterization of the fragmentation cross sections and to published experimental data measured at higher incident energies. The target and projectile dependence of the measured fragmentation cross sections is discussed at the end of the chapter.

4.1 Momentum distributions

More quantitative discussion of the properties of the fragment momentum distributions is provided in this section. The obtained fragment momentum distributions are compared to high energy systematics.

The basic properties of the momentum distributions of the target or projectile fragmentation products were the subject of many studies [65, 74–76]. In general, the momentum distributions created in the fragmentation of relativistic projectiles are very well represented by Gaussian functions centered at velocities near that of the

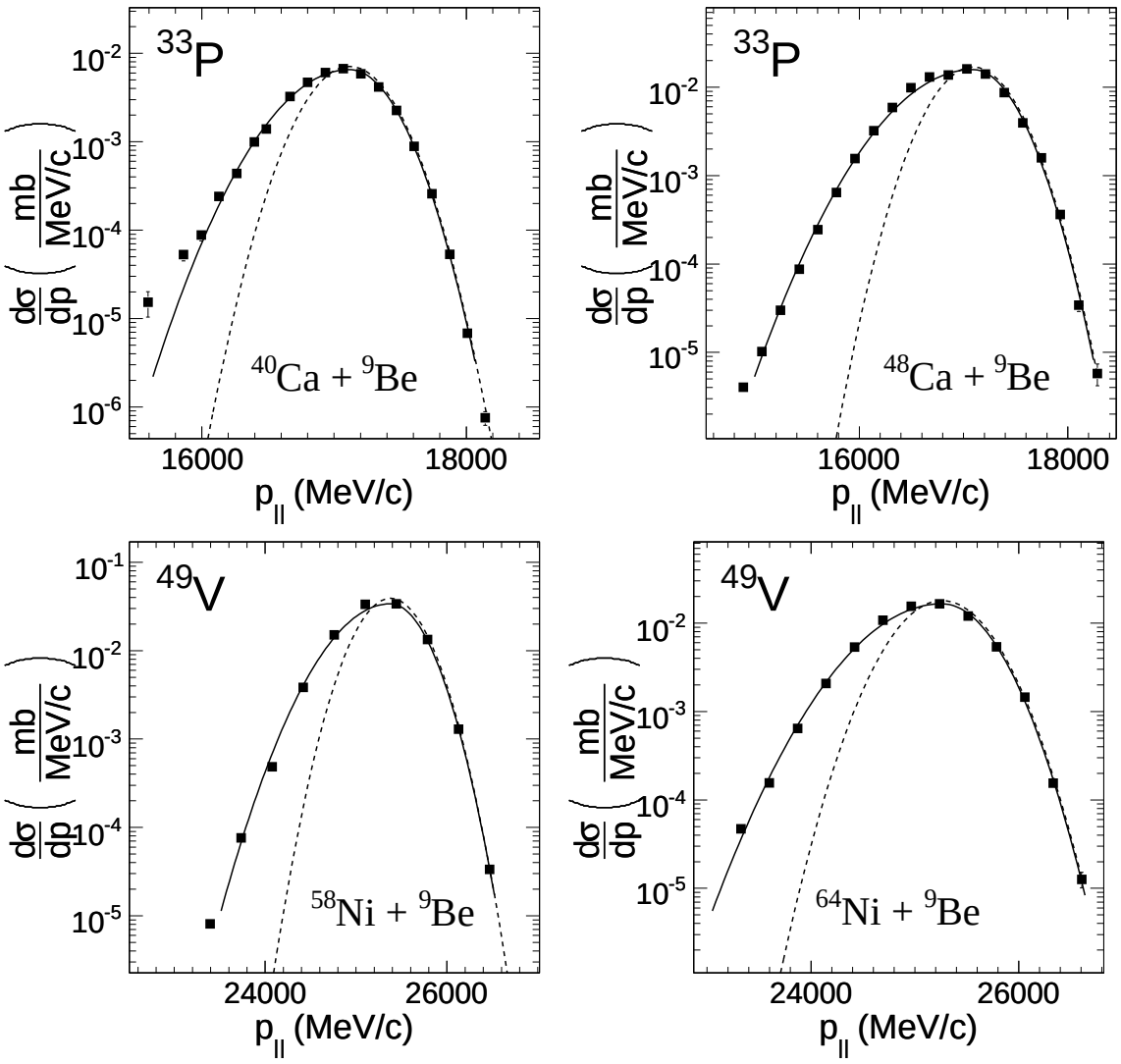

Figure 4.1: Examples of the momentum distributions. Distributions of ^{33}P are shown for the ^{40,48}Ca+^{9}Be and ^{49}V for the ^{58,64}Ni+^{9}Be systems. The solid line shows the modified Gaussian fit of Equation (4.1), and the dashed line shows the Gaussian fit to the high momentum side of the distribution.

projectile [75]. Many models and parameterizations have been developed to describe the variance (width) and the maximum of the Gaussian-shaped momentum distributions [64, 77].

On the other hand, the fragment momentum distributions at intermediate energies are asymmetric [65]; they can no longer be approximated with a Gaussian function. Different functions have been used to reproduce the asymmetric momentum distributions: Gaussian functions with a different cutoff [76], polynomial exponential

functions [65], or Gaussian functions with exponential tails [74]. Our experimental data are very well described by a modified Gaussian functions of Equation (4.1). To demonstrate the asymmetry of the measured momentum distributions, we show the momentum distributions of ^{33}P from the fragmentation of ^{40,48}Ca on a ^{9}Be target and ^{49}V from the ^{58,64}Ni+^{9}Be reaction in Figure 4.1. The solid lines in Figure 4.1 show the fits using the following modified Gaussian function:

$$\frac{d\sigma}{dp} = \begin{cases} S \cdot \exp\left(-(p-p_0)^2/(2\sigma_L^2)\right) & \text{for } p \leq p_0, \\ S \cdot \exp\left(-(p-p_0)^2/(2\sigma_R^2)\right) & \text{for } p > p_0, \end{cases} \tag{4.1}$$

where S is the normalization factor, p_0 is the centroid, σ_L and σ_R are width parameters of the "left" and "right" halves of the momentum distribution. The modified Gaussian function describes the experimental data over 3–4 orders of magnitude extremely well. On the contrary, the fit to the high momentum side of the momentum distribution by a symmetric Gaussian function (dashed curve) shows a large deficit in the low momentum part of the distribution.

4.1.1 Widths of the momentum distributions

At high bombarding energy ($>$ 200 MeV/u), the momentum distributions were found to be independent of the bombarding energy and the target. The observed widths of the experimental momentum distributions showed a parabolic dependence on fragment mass number. The Goldhaber model [64] developed in 1974 considers the projectile nucleus, as being composed of independent nucleons moving freely in a spherical potential well. The only correlations assumed in the model are those arising from momentum conservation. The momentum distribution of the nucleons results in total momentum zero at any time in the rest frame of the projectile nucleus. When a certain number of nucleons are removed suddenly from the projectile, the remaining residual fragment recoils in the opposite direction with the same momentum magni-

tude. Furthermore, assuming the isotropy of the internal momenta of the nucleons in the projectile, the recoil momentum distribution of the fragment, projected on a given axis, has a Gaussian shape. Goldhaber showed that the width σ of this distribution is related to the the masses of fragment, A, and projectile, A_P [64]:

$$\sigma = \sigma_0 \sqrt{\frac{A(A_P - A)}{A_P - 1}}, \tag{4.2}$$

where the σ_0 parameter, also called reduced width, is the root-mean-squared momentum of the individual nucleons, $< p_i^2 >$:

$$\sigma_0^2 = \frac{< p_i^2 >}{3}. \tag{4.3}$$

Assuming the nucleons are distributed in the projectile according to the Fermi gas model we have:

$$< p_i^2 >= \frac{3}{5} p_{Fermi}^2, \tag{4.4}$$

where p_{Fermi} is the Fermi momentum. By inserting this equality into Equation (4.3), we get:

$$\sigma_0^2 = \frac{p_{Fermi}^2}{5}. \tag{4.5}$$

Hence, the Goldhaber model relates the Fermi motion of the nucleons to the reduced widths of the fragment momentum distributions in the projectile fragmentation reactions.

The Fermi momentum, p_{Fermi}, can be experimentally obtained from quasielastic electron scattering. Moniz *et al.* [78] measured values of the Fermi momentum for target materials varying from ^{11}Li to ^{208}Pb. By interpolating their results, we estimated the p_{Fermi} to be approximately 250 MeV/c for ^{40,48}Ca and 260 MeV/c for ^{58,64}Ni and ^{86}Kr nuclei. Calculated reduced width, σ_0, parameters are listed in Table 4.1 along with the values determined from our experimental data.

In 1989 Morrissey [77], assuming that the momentum distribution is a convolution

Table 4.1: Goldhaber reduced width parameter, σ_0^R, for the right side and σ_0^L, for the left side of the experimental momentum distributions values listed for all investigated reaction systems. Last column shows the reduced width parameter of the Goldhaber model calculated based on the Fermi momentum from Ref. [78].

Beam material	Target material	σ_0^L (MeV/c)	σ_0^R (MeV/c)	Fermi mom. (MeV/c)
^{40}Ca	^{9}Be	125±10	85±8	112
	^{181}Ta	117±9	84±7	112
^{48}Ca	^{9}Be	134±9	89±6	112
	^{181}Ta	129±9	88±7	112
^{58}Ni	^{9}Be	133±10	97±5	116
	^{181}Ta	129±10	95±6	116
^{64}Ni	^{9}Be	140±7	94±5	116
	^{181}Ta	136±7	93±4	116
^{86}Kr	^{9}Be	175±11	121±8	116
	^{181}Ta	181±9	119±10	116

of the primary (fast) process and the subsequent sequential decay, and introduced a modified systematics for widths of the momentum distribution based on compilation of high energy fragmentation data (projectile and target). The momentum width in his systematics is given by:

$$\sigma = const \cdot \sqrt{A_P - A}, \tag{4.6}$$

where the constant is a parameter of the systematics, usually taken as 85–100 MeV/c. In the case of projectile fragmentation, it describes only the projectile-like fragments, while light fragment widths are generally overestimated, which can be already seen in the original paper.

Asymmetric momentum distributions in the intermediate energy regime are explained by existence of different, competing reaction mechanisms. Apart from the "pure" fragmentation component, which completely dominates at relativistic energies, both the low momentum tail typical for more dissipative processes [79] and the broadening associated with nucleon pick-up reactions in the prefragment formation

phase [80] will influence the shape of the final momentum distribution. There are two width parameters σ_R and σ_L in the description of our experimental momentum distributions for the left and right halves of the momentum distribution. Guided by the previous works [59,80,81] we assume the right side of the momentum distribution, σ_R, is completely dominated by the "pure" fragmentation reaction mechanism and the left side, σ_L, has more significant contributions from different reaction processes so it is not expected to behave according to the fragmentation parameterizations.

The extracted width parameters of the right side of the momentum distribution, σ_R, are shown as a function of fragment mass loss with respect to that of the projectile, $A_P - A$, in Figure 4.2 for ^{40,48}Ca, ^{58,64}Ni projectiles and in the top panels of Figure 4.4 for the ^{86}Kr beam. The experimental data do not follow monotonically-increasing trend with the number of removed nucleons from the projectile as suggested by the Morrissey systematics plotted as dashed curves in Figure 4.2, with $const = 85$ MeV/c. The disagreement with the experimental data is not surprising as this systematics based mainly on target residues from light-ion induced reactions was not meant for extrapolation towards large mass differences between the projectile and reaction products ($A_P - A > A_P/2$). The solid line shows the fit by Goldhaber formula (Equation (4.2)), where the reduced width, σ_0, is taken as a fitting parameter. The values of the Goldhaber reduced width parameter, σ_0^R, for the right side of the experimental momentum distributions, are listed in Table 4.1. For a given projectile the σ_0^R does not depend on the target material, but increases slightly with the mass of the projectile. The values of the σ_0^R extracted in our fragmentation experiment should be compared to the values calculated from the Fermi momenta measured with quasielastic electron scattering, listed also in Table 4.1. We see that the experimental values from this study are lower than the Fermi momentum values for all investigated beam-target combinations. This is in line with other intermediate and relativistic energy fragmentation experiments when similar discrepancies have been reported [75]. To explain the difference, Bertsch [82] in his model used Pauli correlations. Weber *et*

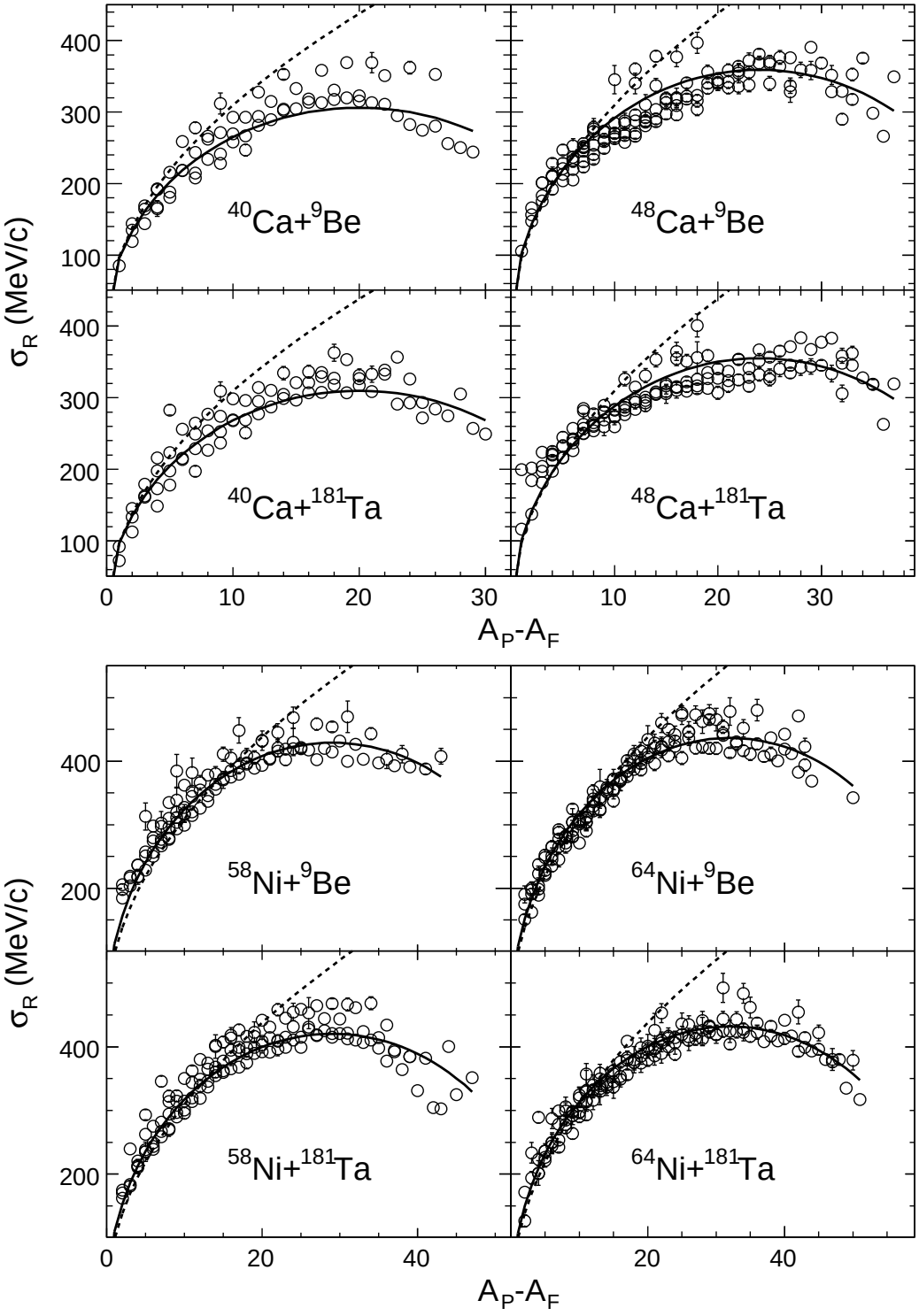

Figure 4.2: Width of the right side of the momentum distribution σ_R for the ^{40,48}Ca and ^{58,64}Ni primary beams on ^{9}Be and ^{181}Ta targets, plotted as a function of number of removed nucleons, $A_P - A$. The solid line shows the fit by Goldhaber formula with reduced width, σ_0^R, listed in Table 4.1 and the dashed line depicts the Morrissey systematics with *const*=85 MeV/c.

al. [75], alternatively, attributed the discrepancy to the mass loss in the evaporation stage which is not included in the Goldhaber model.

The values of the σ_0^R parameters for fragments created in fragmentation of ^{86}Kr at 64 MeV/u are larger ($\approx$ 120 MeV/c) than the ones obtained for the NSCL reaction systems ($\approx$ 90 MeV/c). However, no correlation with target material used in the projectile fragmentation reactions at different beam energies (64 and 140 MeV/u) has been observed, which is consistent with the conclusions of other similar investigations [59].

The width parameters of the left side of the momentum distribution, σ_L, are shown as a function of the mass loss of the fragment with respect to that of the projectile, $A_P - A$, in Figure 4.3 for the ^{40,48}Ca, ^{58,64}Ni projectiles and in the bottom panels of Figure 4.4 for the ^{86}Kr beam. The solid line through the data points represents a fit by the Goldhaber formula (Equation (4.2)), however this fit is just formal, because we do not expect any fragmentation formula to apply for the left side of the momentum distribution, σ_L (as discussed above). Nevertheless, it is clear that the experimental widths, σ_L, can be roughly described by the Goldhaber model using larger values for the reduced width parameter σ_0^L, as listed in Table 4.1.

4.1.2 Centroids of the momentum distributions

Fragment velocity after the reaction is a rather important experimental observable bearing information about the first stage of the reaction — abrasion. The observed momentum distributions peak near the beam velocity. Small deviations in fragment mean velocities, v_F, from the projectile velocity, v_P, can be seen in a simple picture as the friction phenomenon during nuclear reaction. Nuclear bonds are broken during the nucleon removal process, causing the projectile to slow down. In a model introduced

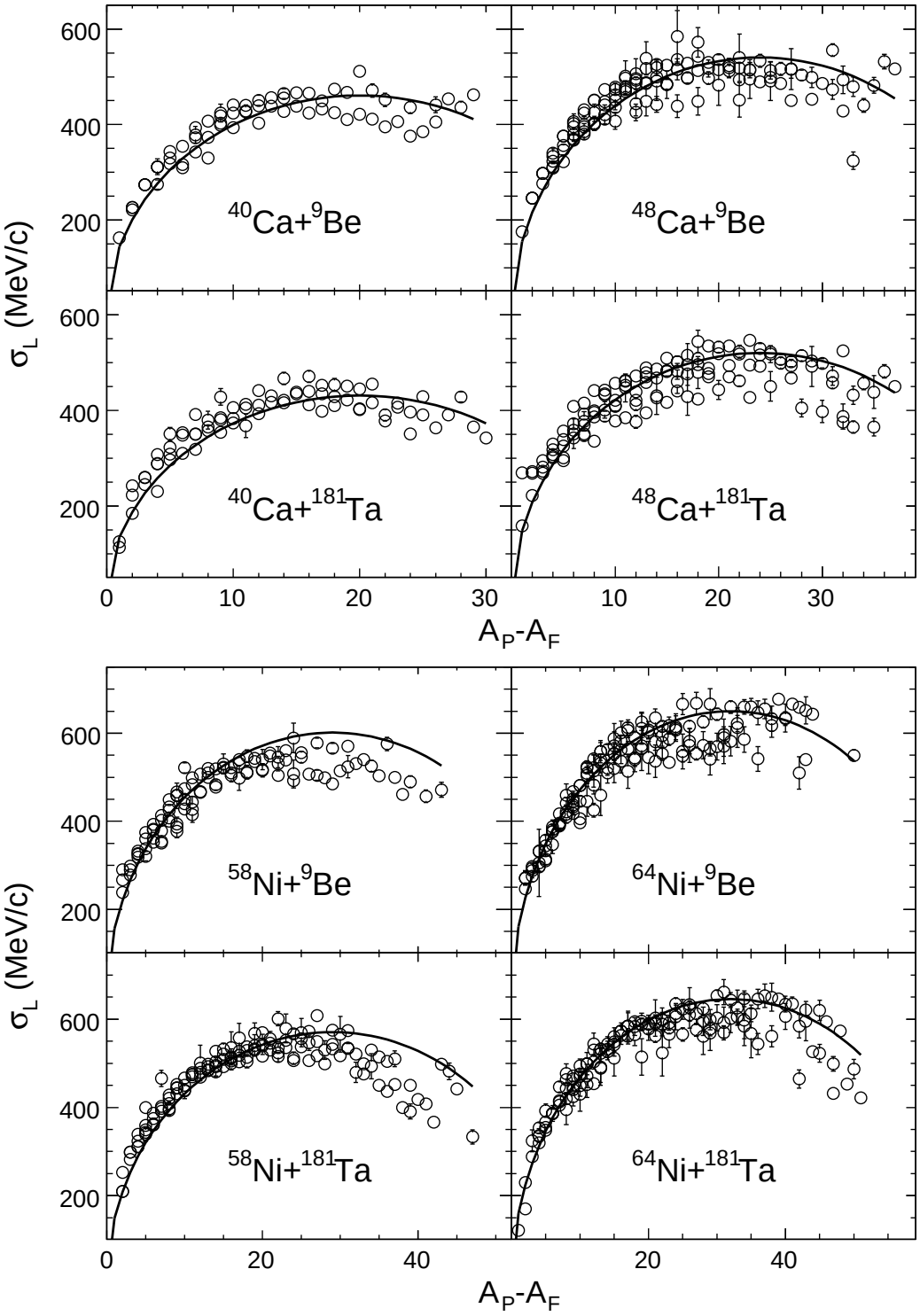

Figure 4.3: Width of the left side of the momentum distribution σ_L for the ^{40,48}Ca and ^{58,64}Ni primary beams on ^{9}Be and ^{181}Ta targets. The solid line shows the fit by Goldhaber formula with reduced width, σ_0^L, listed in Table 4.1.

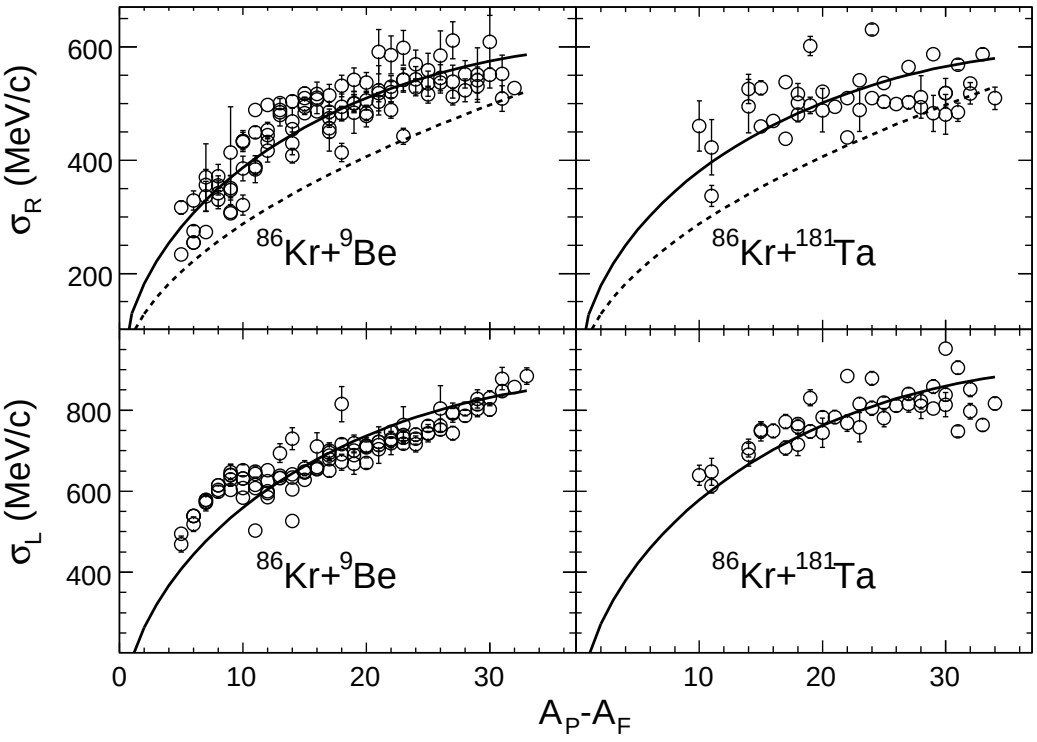

Figure 4.4: Width of the left σ_L and right σ_R sides of the momentum distribution for the ^{86}Kr primary beam on ^{9}Be and ^{181}Ta reaction targets. The solid line shows the fit by the Goldhaber formula with the reduced width listed in Table 4.1 and the dashed line depicts the Morrissey systematics with *const*=85 MeV/c.

by Borrel *et al.* [83] the fragment velocity deviation, v_F/v_P, is expressed as:

$$\frac{v_F}{v_P} = \sqrt{1 - \frac{8 \cdot (A_P - A)}{A \cdot E_P}}. \tag{4.7}$$

It depends on the mass of the projectile A_P and fragment A plus the energy of the beam E_P in units of MeV/u. The underlying idea is that the energy cost is 8 MeV per removed nucleon.

Other models describe the change of velocity in terms of the momentum transfer. A number of models have been proposed to treat the small momentum transfer from the bombarding particle. They all assume a two-step mechanism and treat the result as a quasi two-body system. Although differing in details of the initial interaction, Cumming *et al.* [84] realized they all predict the same functional form for the momentum transfer in the projectile reference frame $p_\parallel$ as

$$p_\parallel = \frac{\Delta E_T}{\beta} \cdot \left(1 + k(1 - \beta^2)^{1/2}\right) \tag{4.8}$$

where β is the projectile's velocity, ΔE_T is the energy transferred to the prefragment, and the parameter k sets the rate at which $p_\parallel$ decreases as β increases. Different authors arrived at different values of the ΔE_T and k parameters studying various systems. Kaufman [85] compiled high energy fragmentation data (0.4–2.1 GeV/u) and described the data with parameters $k = 0$ and $\Delta E_T = 13$ MeV/ΔA. On the other hand, Morrissey analyzed heavy residues from target spallation reactions [77] and obtained $k = 1$ and $\Delta E_T = 8$ MeV/ΔA.

Experimental fragment velocities, v_F, are calculated by translating the p_0 parameter of the modified Gaussian fitting function (Equation (4.1)) for every fragment in our analysis into the velocity space. In order to make the cross system comparisons clear, we plot them as relative deviations from the projectile velocity ($v_F/v_P - 1$) in %, in Figure 4.5, 4.6 and 4.7 for the ^{40,48}Ca, ^{58,64}Ni and ^{86}Kr beams, respectively.

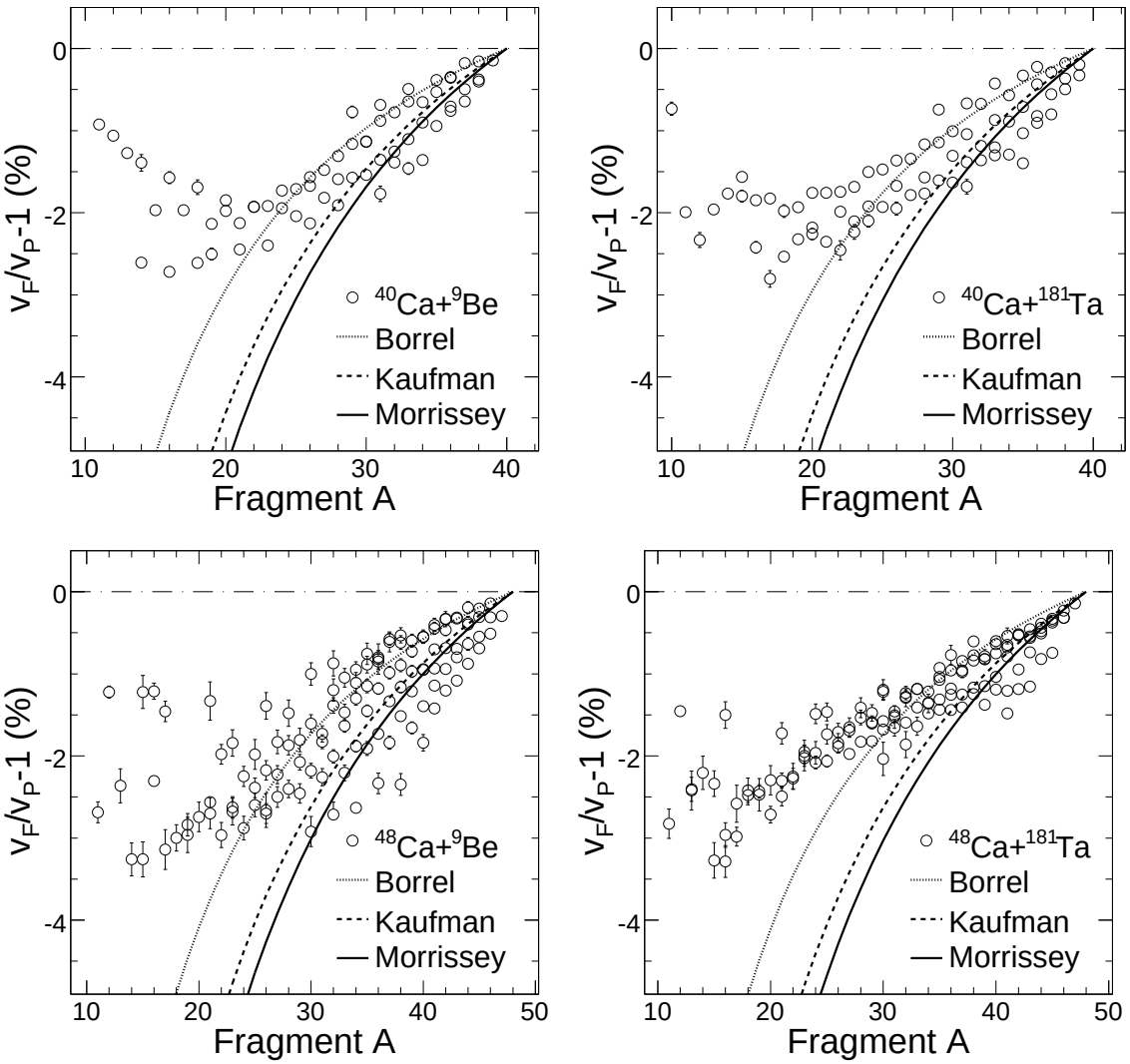

Figure 4.5: Relative deviations from the projectile velocity ($v_F/v_P - 1$) for all fragments with complete momentum distributions identified in the fragmentation of ^{40,48}Ca isotopes on ^{9}Be and ^{181}Ta targets plotted as a function of fragment mass number, A. Parameterizations of Borrel, Kaufman and Morrissey are shown as dotted, dashed and solid lines respectively.

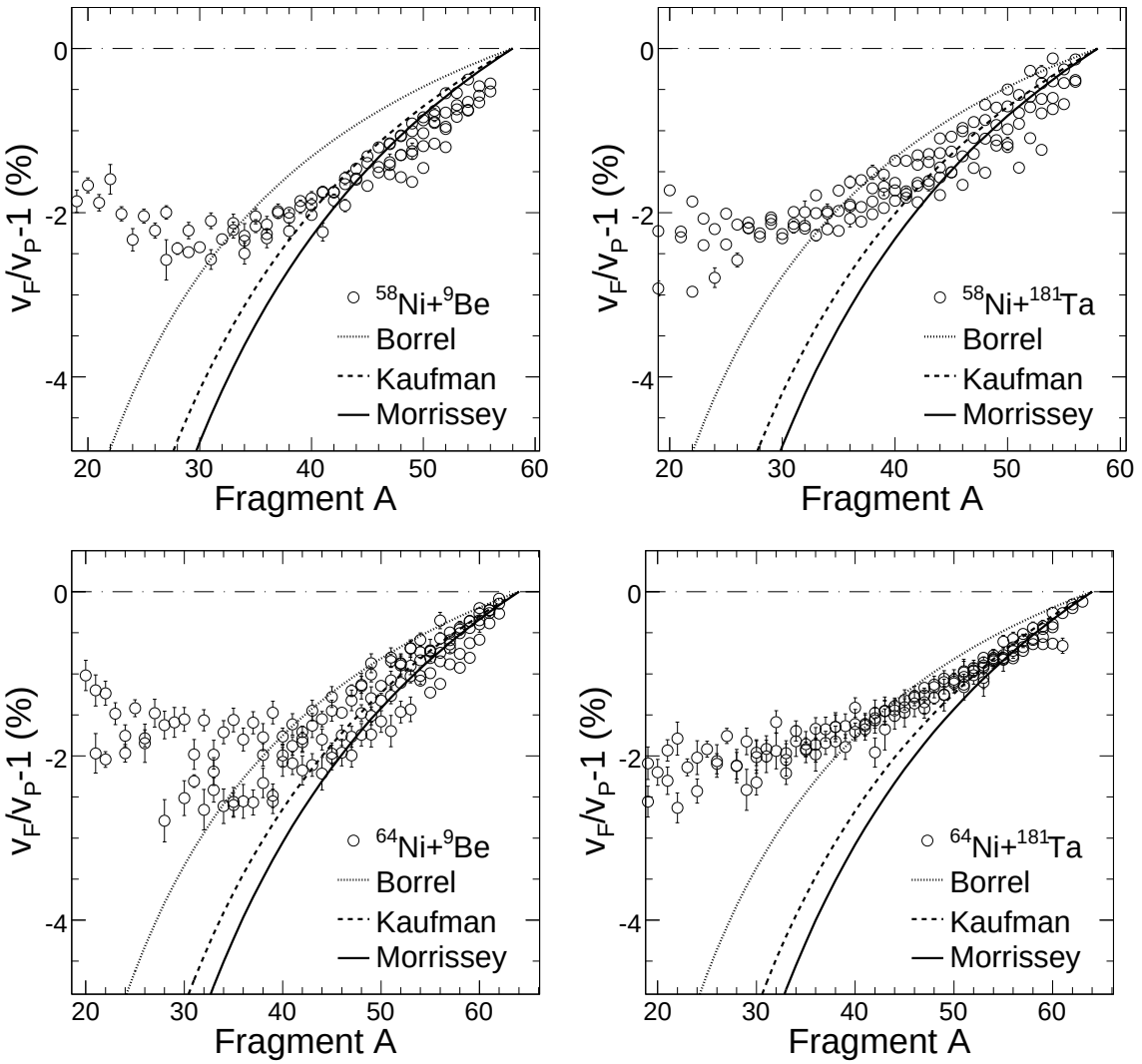

Figure 4.6: Relative deviations from the projectile velocity ($v_F/v_P - 1$) for all fragments with complete momentum distributions identified in the fragmentation of ^{58,64}Ni isotopes on ^{9}Be and ^{181}Ta targets plotted as a function of fragment mass number, A. Parameterizations of Borrel, Kaufman and Morrissey are shown as dotted, dashed and solid lines respectively.

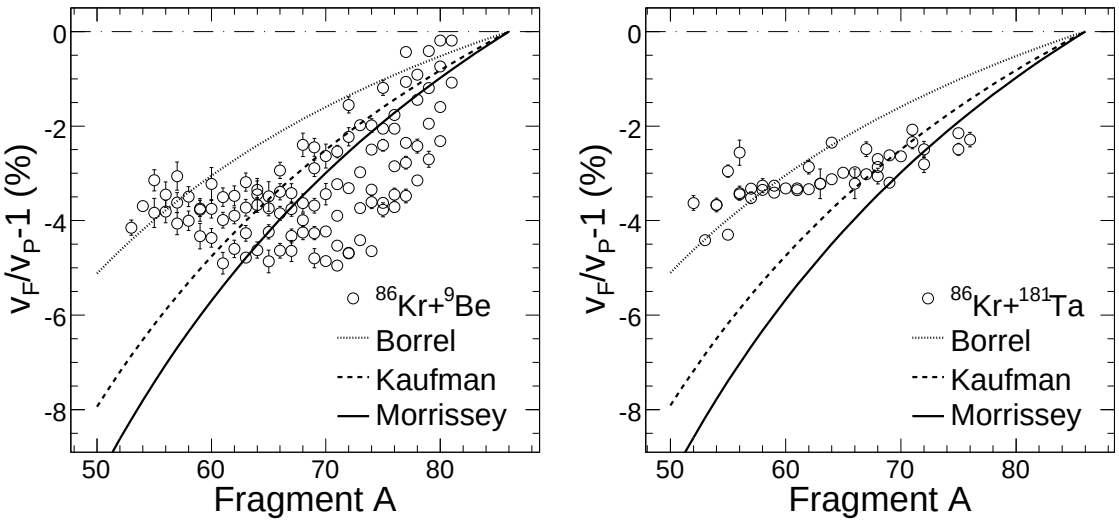

Figure 4.7: Relative deviations from the projectile velocity ($v_F/v_P - 1$) for all fragments with complete momentum distributions identified in the fragmentation of ^{86}Kr primary beam on ^{9}Be and ^{181}Ta targets plotted as a function of fragment mass number, A. Parameterizations of Borrel, Kaufman and Morrissey are shown as dotted, dashed and solid lines respectively.

The experimental data are shown as open circles and three calculations by models of Borrel, Kaufman and Morrissey are shown as dotted, dashed, and solid lines, respectively. The experimental fragment velocity deviations exhibit a considerable scatter making the comparisons with the above discussed parameterizations difficult. The studied projectile fragmentation data show no dependence of the fragment velocities on the projectile or the target material (within the scatter of the experimental data). The overall profile of the relative experimental velocity is similar for all the NSCL reaction systems (Figure 4.5 and 4.6) in that the velocities gradually decrease with the fragment mass number and saturate around -2%. All presented models predict a further decrease of the velocity with the mass number which is not experimentally observed. A clear deviation from the experimental data starts around 10 removed nucleons for the ^{40,48}Ca beams and around 15 removed nucleons for the ^{58,64}Ni beams. The Borrel parameterization predicts overall larger fragment velocities as compared to the systematics of Kaufman and Morrissey (see Figure 4.5 and 4.6). The Kaufman and Morrissey systematics, on the other hand, produce similar predictions for

velocities of projectile-like fragments. However, it must be noted that all presented parameterizations fail to reproduce the overall shape of the data.

For the ^{86}Kr reaction systems, only the fragments with $A > 50$ have been analyzed, so we only see an overall trend of the fragment velocities as a function of the fragment mass number, A in the vicinity of the projectile (Figure 4.7). In the case of ^{86}Kr+^{9}Be reaction the experimental data are scattered much more than the data of the NSCL reaction systems. This effect is most probably caused by a combination of much lower beam energy (64 MeV/u) and rather thick target ($\approx$ 100 mg/cm^2). The Borrel systematics predicts larger fragment velocities than the data for most of the fragments (left panel of Figure 4.7). The Kaufman and Morrissey calculations intersect the experimental data points close to the projectile, but deviate significantly for fragments with mass numbers 55–60. In the case of the ^{86}Kr+^{181}Ta reaction (right panel of Figure 4.7) the number of complete momentum distributions extracted is much lower than for the ^{86}Kr+^{9}Be system, making the conclusions more difficult. Due to broader charge state distributions of the ^{86}Kr beam on ^{181}Ta target a smaller range in the magnetic rigidity was covered for the ^{86}Kr+^{181}Ta reaction. The momentum distributions of fragments in the vicinity of the projectile were not measured (or measured completely). This limitation does not allow us to compare the experimental fragment velocities in the vicinity of the projectile to the parameterizations. The experimental velocities for lighter fragments $A \approx$ 52–65 are, again, larger than predicted by Kuafman and Morrissey parameterizations.

4.2 Fragmentation production cross sections

Fragmentation production cross sections were extracted according to the analysis procedure described in detail in Section 3.4.2. This section summarizes the results of the reaction cross section analysis for all studied systems. The vast majority of measured nuclides are classified as fragmentation reaction products. However, nucleon

exchange and pick-up isotopes have been also identified in our study. Table 4.2 lists the

Table 4.2: Number of fragments and pick-up (including exchange) cross sections measured for all reaction systems.

Beam	Target	Number of	
		fragments	pick-up
^{40}Ca	^{9}Be	100	11
	^{181}Ta	101	15
^{48}Ca	^{9}Be	176	26
	^{181}Ta	167	32
^{58}Ni	^{9}Be	184	12
	^{181}Ta	179	10
^{64}Ni	^{9}Be	240	3
	^{181}Ta	232	2
^{86}Kr	^{9}Be	180	0
	^{181}Ta	70	0
Total:		1629	111

number of measured fragmentation products and pick-up products (including nucleon exchange). The presented table should be understood as a summary of the nuclides identified in our study. It is by no means an exact summary of reaction mechanism for the various isotopes measured in our data. Because the experimental data were taken in separate experiments, scanning different parts of the magnetic rigidity spectrum, Table 4.2 only lists the number of cross sections we extracted.

Figure 4.8–4.12 present an overall view of the fragment cross sections in the style of the nuclear chart for all investigated reaction systems. The range of the measured cross sections spans over 8 orders of magnitude, from nb to hundreds of mb. Figure 4.8 and 4.9 present the isotope cross sections measured in the fragmentation of ^{40}Ca and ^{48}Ca, Figure 4.10 and 4.11 display the fragment cross sections of ^{58}Ni and ^{64}Ni and Figure 4.12 shows the ^{86}Kr beam fragmentation product cross sections. For reference, the projectile is represented by the symbol of box with a cross inside and the stable isotopes are highlighted with the black framed boxes. The number of nuclides and their position in the chart of nuclides (Figure 4.8–4.12) using ^{9}Be and ^{181}Ta target is very similar for all investigated systems except for the ^{86}Kr projectile where measurements

of fragments with ^{181}Ta target were incomplete.

Even though more neutron-rich fragments are expected to be produced by the neutron-rich projectile ^{48}Ca, the number of measured isotopes in ^{48}Ca (202) fragmentation is almost twice that of ^{40}Ca (111). On the other hand, for the ^{58}Ni and ^{64}Ni projectiles the cross section of 196 and 243 isotopes were measured, respectively. For the reactions of the ^{86}Kr beam, we did not have nucleon pick-up isotopes with full momentum distributions identified because of the rather limited range in magnetic rigidity covered.

4.3 Cross section comparisons

Before a more quantitative presentation of the measured fragmentation cross sections, we introduce the empirical parameterization of fragmentation cross sections (EPAX). Then the measured cross sections are compared to EPAX and previously published experimental data (where available).

4.3.1 EPAX parameterization

A large amounts of early spallation and subsequent projectile fragmentation data have stimulated an interest to understand the underlying dependences and correlations and to systematize them. By studying the numerous cross sections measured in different experiments in the relativistic energy regime, two very important facts have been learned [47]:

1. Fragment isotopic distributions become approximately energy independent above beam energy $\approx$ 200 MeV/u;

2. Target spallation cross sections for fragments close to the target nucleus produced by proton or heavy ion beams differ only by a constant factor close to the ratio of the total reaction cross section.

The terms "limiting fragmentation" and "factorization" [86] have been introduced to refer to the latter two observations. They formed the basis of many empirical parameterizations valid for specific projectile and target combinations [87]. In 1990 Sümmerer *et. al* [47] combined the efforts of many different groups developing empirical parameterizations into a universal empirical parameterization of cross sections (EPAX) version 1. This version has been refined and improved with inclusion of relativistic projectile fragmentation data available in 2000 resulting in EPAX version 2 [48].

In the EPAX2 parameterization [48] the fragmentation cross section of a fragment with mass, A, and nuclear charge, Z, created from projectile (A_p, Z_p) colliding with a target (A_t, Z_t) is given by

$$\sigma(A,Z) = Y_A n \exp\left(-R|Z_{prob} - Z|^{U_{\mathrm{n(p)}}}\right). \tag{4.9}$$

The first term Y_A describes the sum of the isobaric cross sections with mass number, A, and the second term $\exp\left(-R|Z_{prob} - Z|^{U_{\mathrm{n(p)}}}\right)$ is the so called charge dispersion, i. e. the distribution of the elemental cross sections around maximum value, Z_{prob}, for a given mass. The shape of the charge distribution is controlled by the width parameter, R, and the exponents, U_{n} and U_{p}, describing, the neutron-rich (n) and proton-rich (p) side, respectively. Where the neutron-rich fragments are defined with $Z_{prob} - Z > 0$ all others are considered proton-rich. The factor $n = \sqrt{R/\pi}$ normalizes the integral of the charge dispersion to unity.

The mass yield, Y_A, is parameterized as an exponential function of the number of removed nucleons, $A_p - A$,

$$Y_A = SP \exp\left[-P(A_p - A)\right]. \tag{4.10}$$

S is the overall scaling factor which accounts for the peripheral nature of the fragmentation reaction and proportional to the sum of the projectile and the target radii:

$$S = S_2(A_p^{1/3} + A_t^{1/3} + S_1). \tag{4.11}$$

With $S_1 = -2.38$ and $S_2 = 0.270$ being EPAX2 parameters. The slope of the exponential function in Equation (4.10), P, is taken as a function of the projectile mass, A_p, with $P_1 = -2.584$ and $P_2 = -7.57 \times 10^{-3}$ as EPAX parameters:

$$P = \exp\left(P_2 A_p + P_1\right). \tag{4.12}$$

The charge dispersion in Equation (4.9) is described by three parameters R, Z_{prob}, and $U_{n(p)}$. These parameters are strongly correlated [48] and are very difficult to obtain by a fitting technique. To account for the asymmetric nature of the shape of isobaric distributions, the exponents, U_{n} and U_{p}, for the neutron-rich and proton-rich sides are different. The maximum of the isobar distribution, Z_{prob}, lies in the valley of stability and it is parameterized as:

$$Z_{prob}(A) = Z_\beta(A) + \Delta, \tag{4.13}$$

where $Z_\beta(A)$ is approximated by a smooth function of the mass number, A:

$$Z_\beta(A) = \frac{A}{1.98 + 0.0155A^{2/3}}, \tag{4.14}$$

and the Δ parameter is found to be a linear function of the fragment mass, A, for heavy fragments and a quadratic function of A for lower masses:

$$\Delta = \begin{cases} \Delta_3 A^2 & \text{if } A < \Delta_4, \\ \Delta_2 A + \Delta_1 & \text{if } A \geq \Delta_4. \end{cases} \tag{4.15}$$

Where $\Delta_1 = -1.09$, $\Delta_2 = 3.05 \times 10^{-2}$, $\Delta_3 = 2.14 \times 10^{-4}$, and $\Delta_4 = 71.35$ are EPAX2 parameters. Similarly, the width parameter, R, of the charge distribution is parameterized as a function of the fragment mass, A, with $R_1 = 0.885$ and $R_2 = -9.82 \times 10^{-3}$ EPAX2 parameters:

$$R = \exp\left(R_2 A + R_1\right). \tag{4.16}$$

This description is sufficient to predict the cross sections of fragments located close to the line of stability and far from the projectile nucleus, also referred to as the "residue corridor". For fragments with masses close to the projectile, corrections to the parameters Δ, R, and Y_A are introduced, according to the following equations:

$$\Delta = \Delta\left[1 + d_1(A/A_p - d_2)^2\right], \tag{4.17}$$

$$R = R\left[1 + r_1(A/A_p - r_2)^2\right], \tag{4.18}$$

$$Y_A = Y_A\left[1 + y_1(A/A_p - y_2)^2\right]. \tag{4.19}$$

The corrections to Δ, R, and Y_A parameters are applied only for fragments with mass number, A, fulfilling $(A/A_p - d_2) > 0$, $(A/A_p - r_2) > 0$, and $(A/A_p - y_2) > 0$, respectively. With EPAX2 parameters $d_1 = -25.0$, $d_2 = 0.80$, $r_1 = 20.0$, $r_2 = 0.82$, and $y_1 = 200.0$, $y_2 = 0.90$, characterizing the corrections to the Δ, R, and Y_A parameters. A final correction is applied in the case of projectile nuclei far from the line of β-stability, $Z_\beta(A_p)$. In this case it has been shown that the fragment distributions keep some memory of the A/Z ratio of the projectile nucleus resulting in a correction to the maximum, Z_{prob}, of the charge distribution:

$$Z_{prob}(A) = Z_\beta(A) + \Delta + \Delta_m, \tag{4.20}$$

where Δ_m is expressed separately for neutron-rich ($(Z_p - Z_\beta(A_p)) < 0$) and proton-rich ($(Z_p - Z_\beta(A_p)) > 0$) projectiles:

$$\Delta_m = \begin{cases} (Z_p - Z_\beta(A_p))\,[n_1(A/A_p)^2 + n_2(A/A_p)^4] & \text{for neutron rich,} \\ (Z_p - Z_\beta(A_p))\exp\,[p_1 + p_2(A/A_p)] & \text{for proton rich,} \end{cases} \tag{4.21}$$

where $n_1 = 0.40$, $n_2 = 0.60$ and $p_1 = -10.25$, $p_2 = 10.10$ are parameters of EPAX2.

The EPAX2 parameterization altogether contains 24 parameters (S_1, S_2, P_1, P_2, R_1, R_2, Δ_1, Δ_2, Δ_3, Δ_4, U_n, U_1, U_2, U_3, n_1, n_2, p_1, p_2, d_1, d_2, r_1, r_2, y_1, and y_2), many of which are strongly inter-correlated. These parameters have been determined by a fit of the fragmentation data of ^{40}Ar [88], ^{48}Ca [42], ^{58}Ni [89], ^{86}Kr [75], ^{129}Xe [90], and ^{208}Pb [91] projectiles measured at 600, 212, 650, 500, 790, and 1000 MeV/u, respectively.

The main goal of the EPAX2 parameterization is to obtain a smooth analytic description of the fragmentation data within a factor of two [48]. The empirical parameterization assumes the limiting fragmentation regime when the fragmentation cross sections are no longer beam energy and target dependent. Since it is based on analytic formula, the cross section calculations are fast. Because of its simplicity, the EPAX2 parameterization has been implemented in many codes (MOCADI [66], LISE++ [56]). It is not only used to calculate the yields of rare isotopes for the existing (CCF-NSCL [52], GSI [44], RIKEN [35]), but also fragment yields for the next-generation radioactive beam facilities (RIA [92], FAIR [93], RI beam factory at RIKEN [94]). The EPAX2 is also available at `http://www-aix.gsi.de/~sue/epax/epax_v2.html`.

Since the EPAX2 parameterization is reproducing an "average" behavior of the fragmentation cross sections for a variety of beam-target combinations, it produces reliable results while interpolating between experimentally measured data points. The extrapolation to very exotic (neutron-rich or proton-rich) fragments may be unreliable, because the slopes of the isotopic distributions are only measured in the vicinity of their maxima. A minute change of the slope parameter may cause differences in

orders of magnitude in the extreme tails of the fragment isotopic distributions. Hence, the EPAX2 should be used with extreme caution when calculating yields for fragments very far from the experimentally measured regions.

4.3.2 Comparison to EPAX

The experimentally determined fragmentation production cross sections for the 10 reaction systems are plotted in Figure 4.13 (^{40}Ca+^{9}Be), Figure 4.14 (^{40}Ca+^{181}Ta), Figure 4.15 (^{48}Ca+^{9}Be), Figure 4.16 (^{48}Ca+^{181}Ta), Figure 4.17 (^{58}Ni+^{9}Be), Figure 4.18 (^{58}Ni+^{181}Ta), Figure 4.19 (^{64}Ni+^{9}Be), Figure 4.20 (^{64}Ni+^{181}Ta), Figure 4.21 (^{86}Kr+^{9}Be) and Figure 4.22 (^{86}Kr+^{181}Ta). Each panel represents isotope cross section data (filled squares) for one element, plotted as a function of neutron excess, $N-Z$, of each isotope. The nucleon pick-up and exchange cross sections are shown as filled triangles. All comparisons shown in Figure 4.13–4.22 were calculated using EPAX2 [48]. EPAX does not predict pick-up cross sections and the description of the light fragments ($A < A_P/2$) is generally not as good as the predictions for fragments closer to the projectile, because light fragments may be produced in more central collisions in other reaction mechanism such as multifragmentation. The maxima of very light elements with $Z < 9$ (for the NSCL reaction systems), which may be produced in more central reactions, do not agree with EPAX calculation. In general, isotope distributions from EPAX are wider than the measured ones, resulting in over-predictions for the very neutron-rich and proton-rich fragments for all investigated reaction systems measured at 140 and 64 MeV/u. This behavior is especially pronounced in the case of ^{40}Ca projectile.

For all investigated systems, we also observed differences between the EPAX calculated maximum of the isotopic distribution and the experimental data for elements close to the projectile. The differences between the EPAX maximum and the experimental data are noticeable for almost all projectiles measured at 140 MeV/u but are really pronounced for fragments of ^{86}Kr (E_{beam} = 64 MeV/u), which suggests

stronger sensitivity to the incident energy. This systematic discrepancy between the intermediate energy fragmentation data and EPAX parameterization has been reported by Sümmerer [97]. The Fermi spheres of the target and projectile nuclei have larger overlap at intermediate energies than at relativistic energies. There may be increasing contributions to the prefragments with charge numbers greater than that of the projectile from the transfer-type reactions. Subsequent decay of these primary fragments feeds the neutron-deficient isotopes close to the projectile.

The production of ^{50}Ca in the reaction of ^{58}Ni+^{9}Be represents the lowest cross section measured from among the NSCL reaction systems. To achieve the measurement of such low cross section (0.41 ± 0.16 nb), we used a thick ^{9}Be target (578 mg/cm^2). In addition, an Al degrader (240 mg/cm^2) was placed at the dispersive image (image 2 in Figure 2.4) position to further separate the fragments with the same A/Q ratios. The wedge is especially effective in deflecting the light fragments from reaching the focal plane detector setup, thus reducing the counting rate of the PIN detector, allowing us to use the maximum beam intensity. All other cross sections (including those in RIKEN) were measured without the use of the degrader. The lowest cross section (15 ± 7 pb) of the study was measured for a fragment ^{79}Cu produced in ^{86}Kr+^{9}Be reactions at 64 MeV/u.

4.3.3 Comparison to other data

In addition to our ^{40}Ca+^{9}Be data, Figure 4.13 also shows the fragmentation data of ^{40}Ca on a hydrogen target at 356 MeV/u [95]. The latter data are shown as open squares. Compared to our data, the isotope distributions obtained from the hydrogen target tend to be narrower than our data and the cross-sections are smaller. The narrower isotopic distributions generally indicate lower excitation energy reflecting lower center of mass energy for the system with hydrogen target.

Our fragmentation data of ^{48}Ca on ^{9}Be target are compared to the data measured at 212 MeV/u at Berkeley [42] shown as open squares in Figure 4.15. There are

differences between the two experimental data sets. Even though the fragmentation data of Ref. [42] were included in extracting the EPAX parameters, the deviation of this data set from the overall EPAX fit (by a factor of 3) was noted in the original paper [48]. On the other hand, our fragmentation data seem to agree pretty well with EPAX predictions except for a small shift of the maximum for elements (S–Ca) close to the projectile (discussed at the end of the previous section).

More recently, cross sections of ^{46,47}Ca, ^{44,45,46,47}K, ^{41,42,44,45}Ar and ^{39,40,41,42}Cl isotopes have been measured in the projectile fragmentation of ^{48}Ca on a deuterium target at 104 MeV/u [96]. These data are shown in Figure 4.15 as open triangles. As mentioned in Ref. [96], the cross sections for fragments with few nucleons removed obtained with the ^{2}H target are higher than our data with the ^{9}Be target as expected from EPAX. In the case of Ca and K isotopes, they are even higher.

The experimental cross sections for the reaction of ^{58}Ni+^{9}Be are plotted along with the relativistic energy fragmentation of ^{58}Ni on a ^{9}Be target at 650 MeV/u by Blank *et al.* [89] measured at GSI shown as open squares in Figure 4.17. The experiment of Blank *et al.* focused on the proton-rich side of the fragment spectrum for fragments of elements $21 \leq Z \leq 28$. Where there are overlapping data points, an interesting trend is observed. Where there are overlapping data points, an interesting trend is observed. The fragment cross-sections from the GSI experiment are consistently higher by 70% than our data for the proton-rich ($Z > N$) isotopes. In the slightly neutron-rich the GSI data are slightly lower by 30%. Unfortunately there are not enough overlaps between the two sets of data to determine if the widths of the distributions are wider or narrower.

In Figure 4.21 our cross section data are compared to an early experiment with ^{86}Kr projectile and ^{9}Be target at 650 MeV/u by Weber *et al.* [75], which were used to fit the EPAX parameterization [48]. For light fragmets the latter data show wider isotope distributions as compared to our fragmentation data analysis. The cross sections on top of the isotopic distributions for Co–Zn elements agree rather well with

the measurements done at very different energies. The isotopic distributions measured at 650 MeV/u generally appear wider than our measurement at 64 MeV/u. It must be noted that there is considerable scatter (Figure 4.21) in Weber *et al.* data, making detailed comparison of the distributions width very difficult.

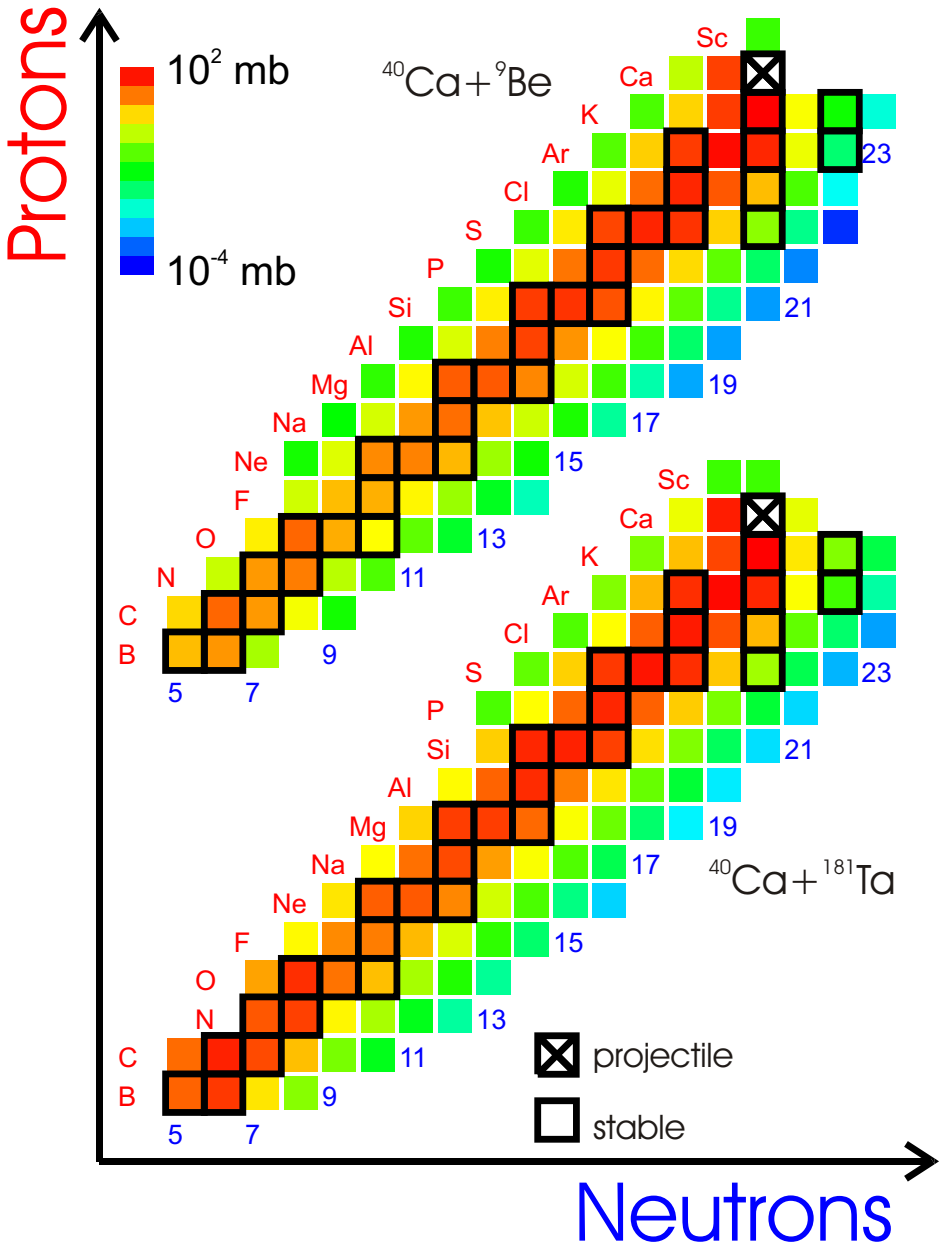

Figure 4.8: Nuclides identified in the fragmentation of ^{40}Ca projectile on two targets. There are 111 and 116 isotopes shown for ^{9}Be and ^{181}Ta targets respectively.

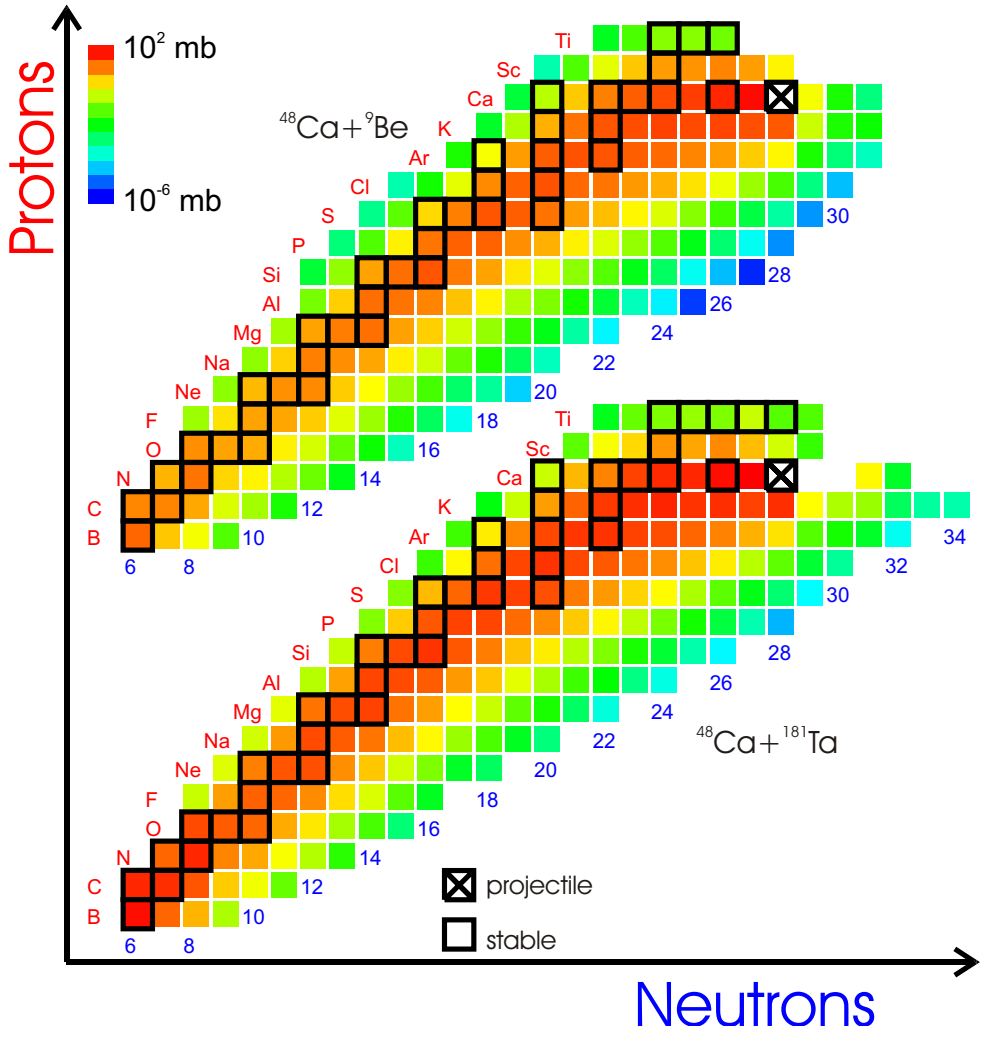

Figure 4.9: Nuclides identified in the fragmentation of ^{48}Ca projectile on two targets. There are 202 and 200 isotopes shown for ^{9}Be and ^{181}Ta targets respectively.

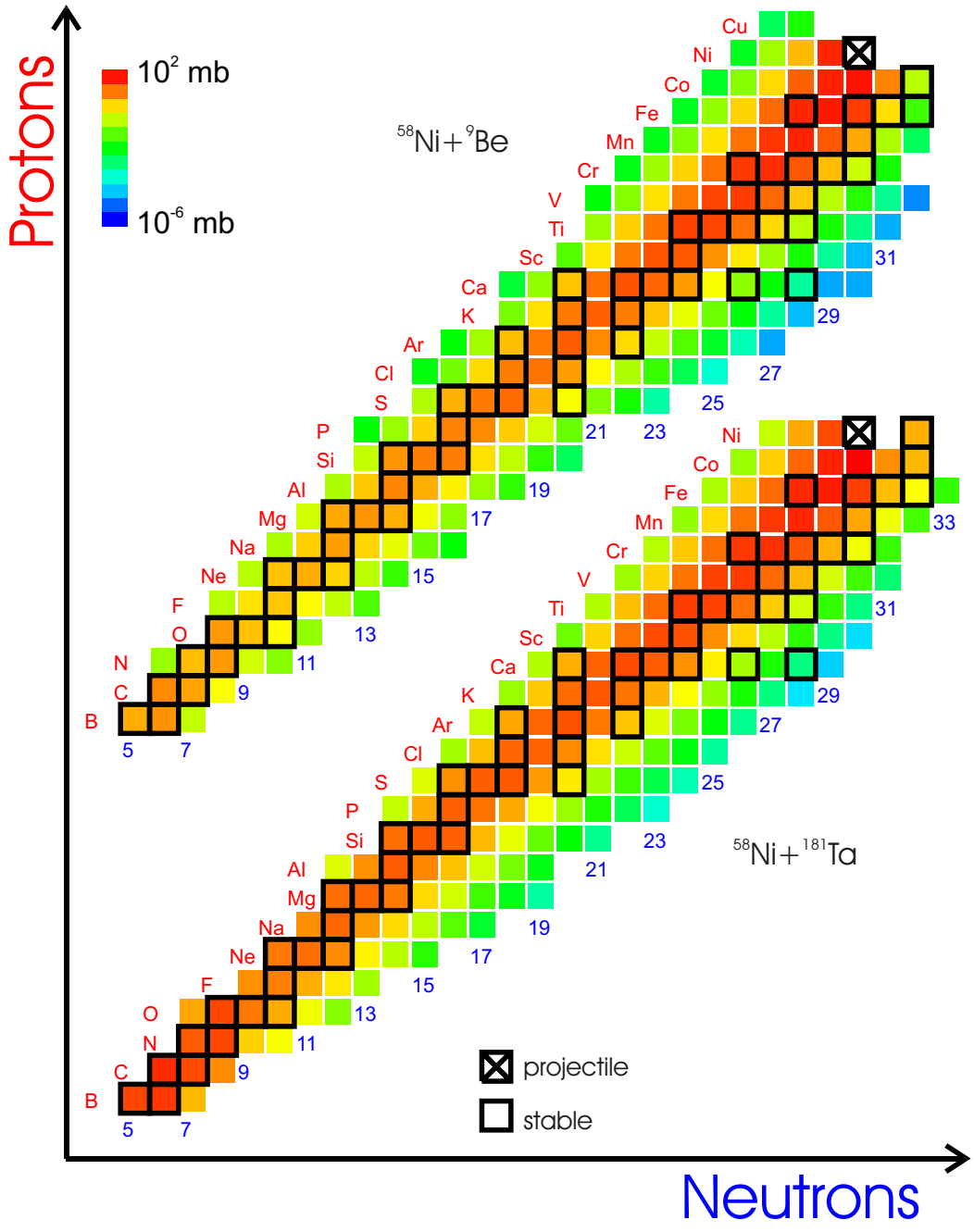

Figure 4.10: Nuclides identified in the fragmentation of ^{58}Ni projectile on two targets. There are 197 and 189 isotopes shown for ^{9}Be and ^{181}Ta targets respectively.

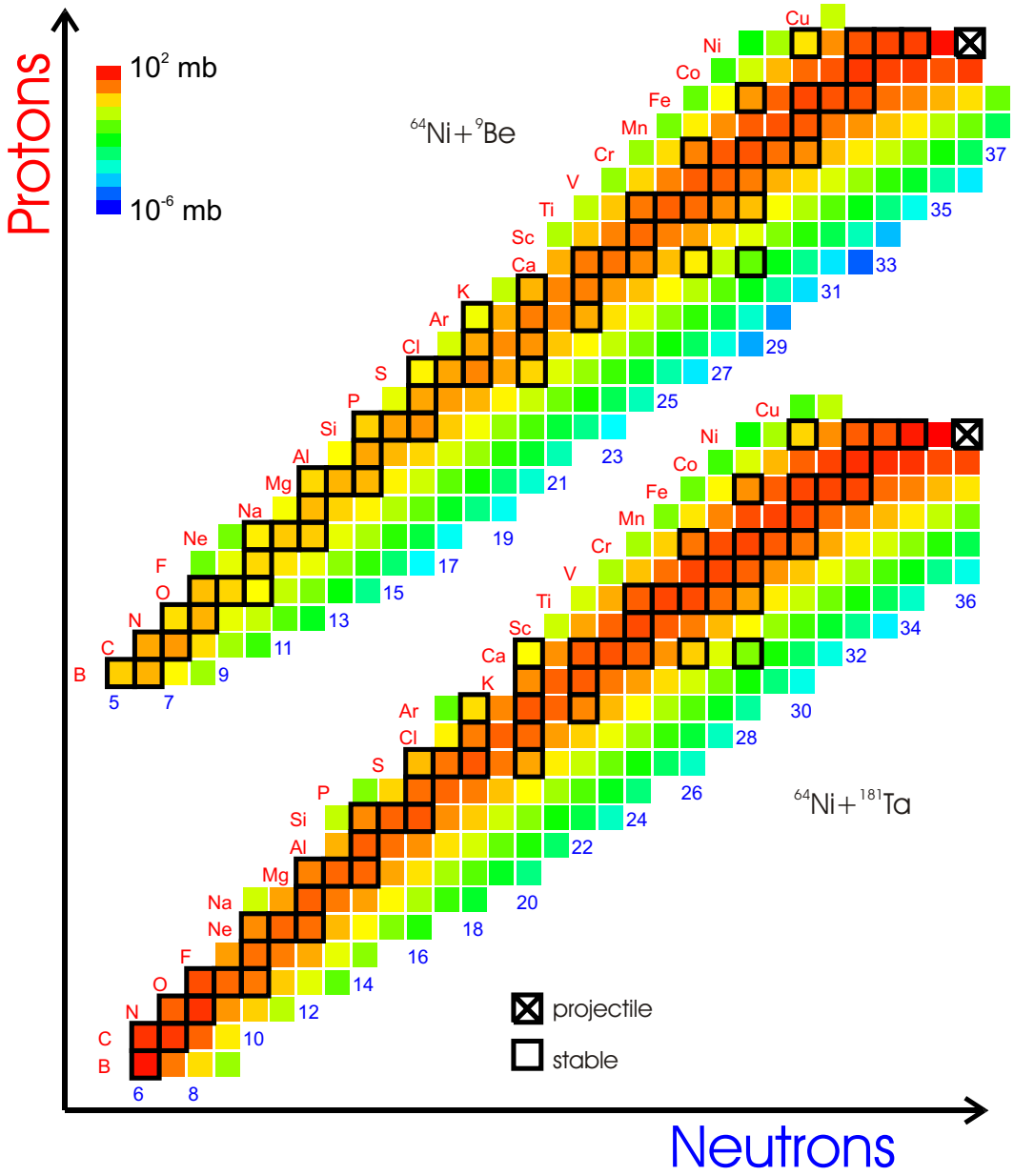

Figure 4.11: Nuclides identified in the fragmentation of ^{64}Ni projectile on two targets. There are 246 and 234 isotopes shown for ^{9}Be and ^{181}Ta targets respectively.

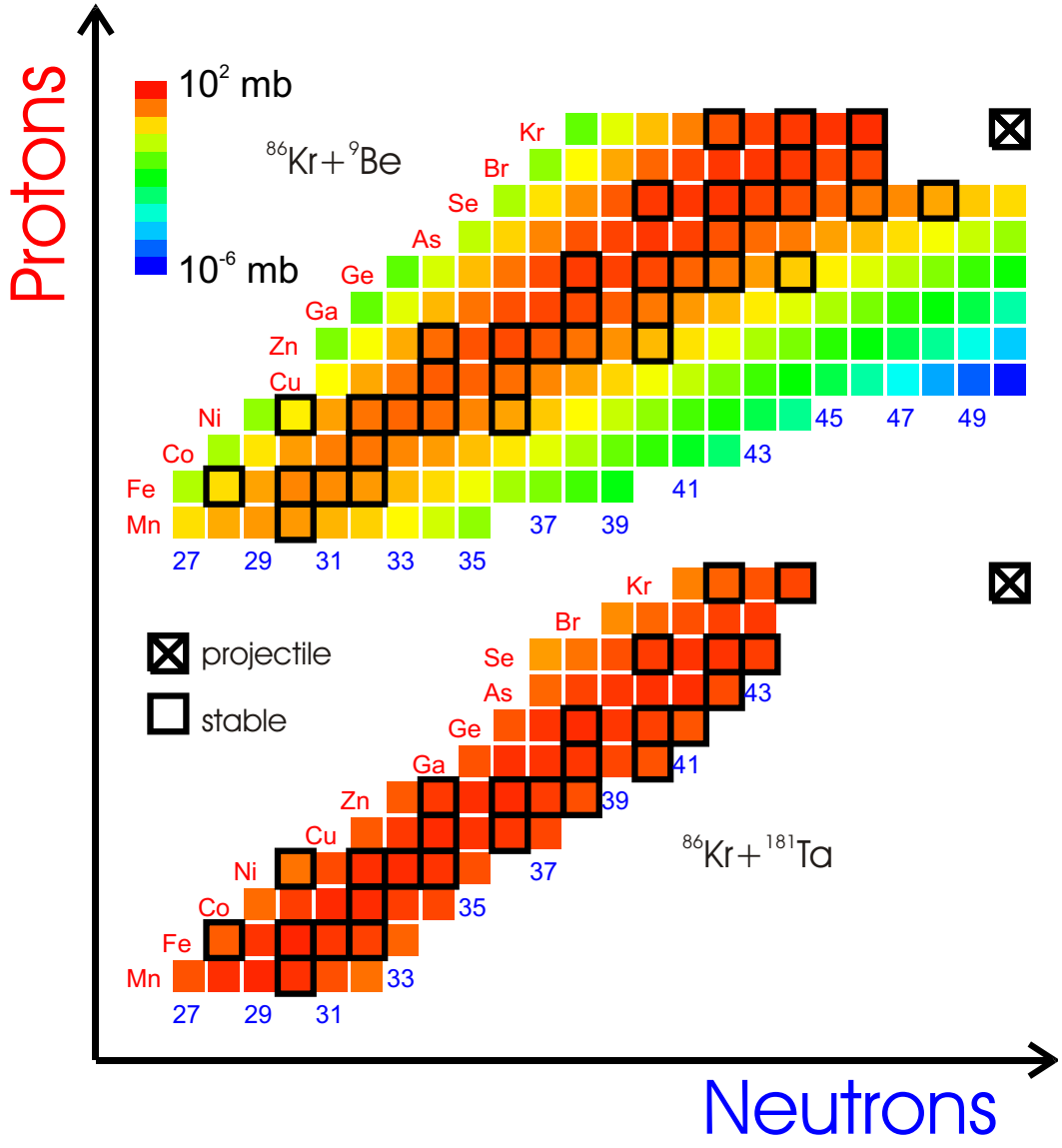

Figure 4.12: Nuclides identified in the fragmentation of ^{86}Kr projectile on two targets. There are 180 and 70 fragments shown for ^{9}Be and ^{181}Ta targets respectively.

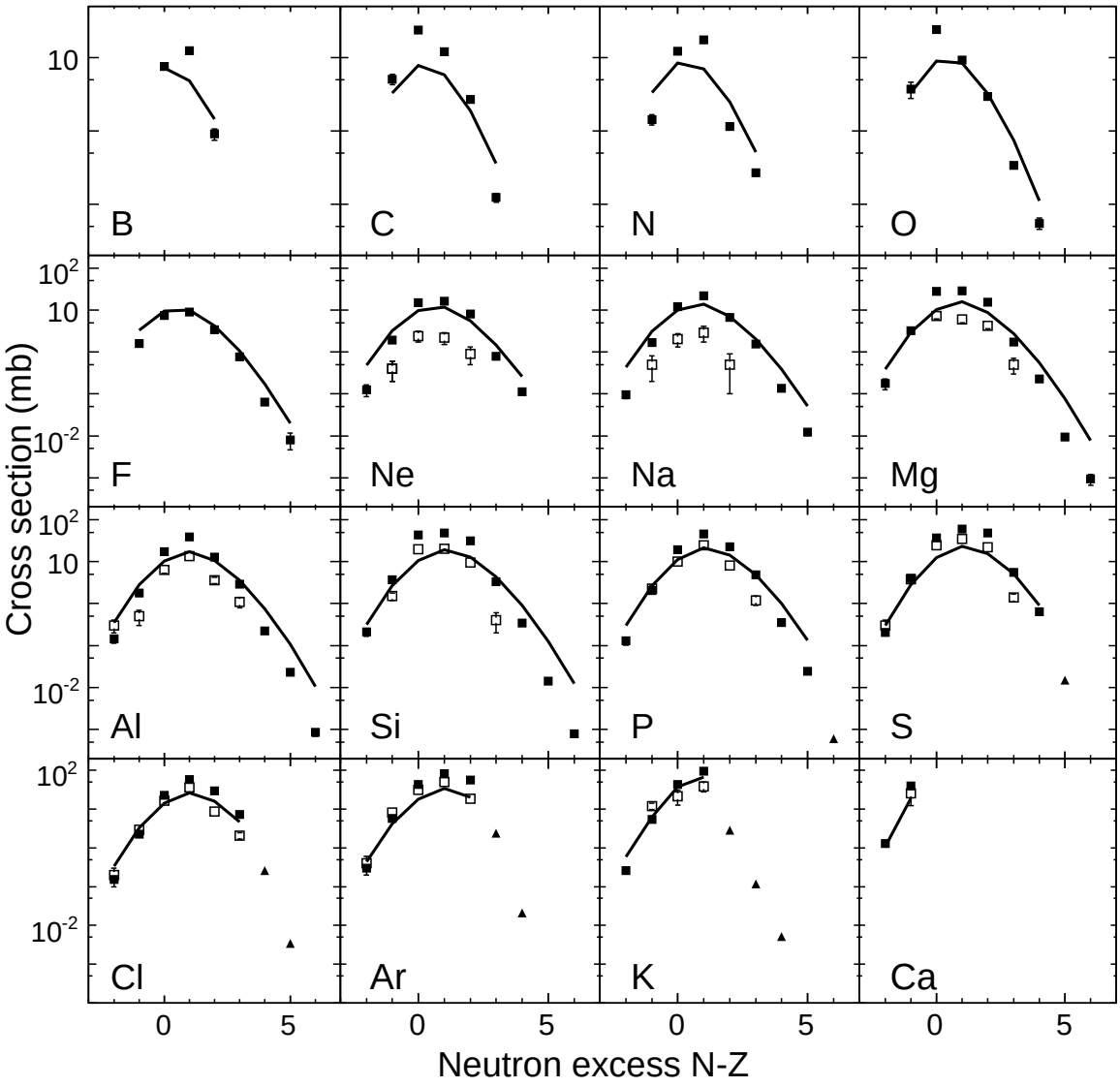

Figure 4.13: Isotopic distributions of measured cross sections plotted as a function of neutron excess for $5 \leq Z \leq 20$ elements detected in the ^{40}Ca+^{9}Be reaction at 140 MeV/u. The experimental fragmentation data are shown as filled squares, cross sections of pick-up reactions are depicted with filled triangles, the solid line shows the calculation by EPAX and open squares show ^{40}Ca+^{1}H data at 356 MeV/u [95].

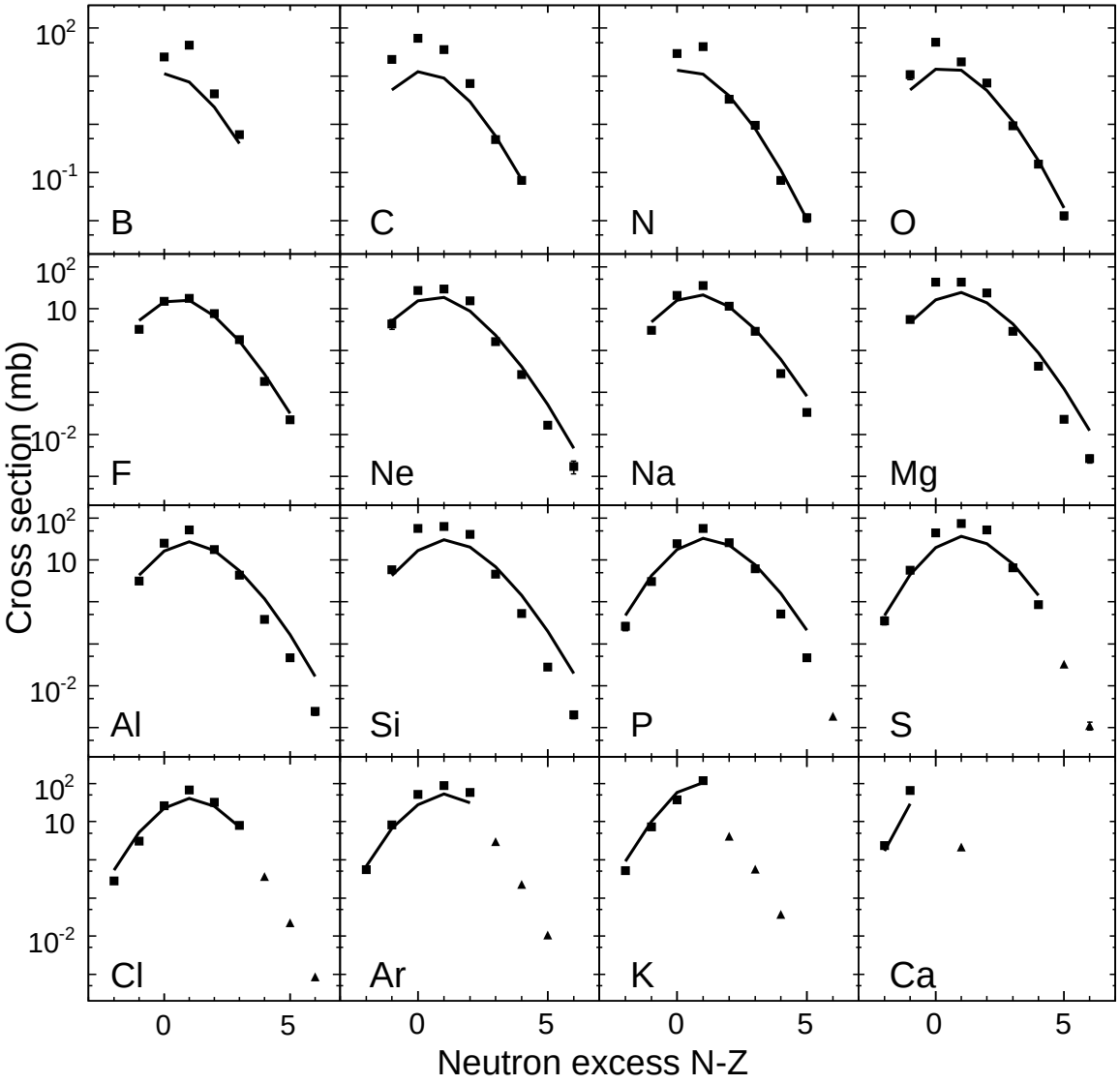

Figure 4.14: Isotopic distributions of measured cross sections plotted as a function of neutron excess for $5 \leq Z \leq 20$ elements detected in the ^{40}Ca+^{181}Ta reaction at 140 MeV/u. The experimental fragmentation data are shown as filled squares, cross sections of pick-up reactions are depicted with filled triangles and the solid line shows the calculation by EPAX.

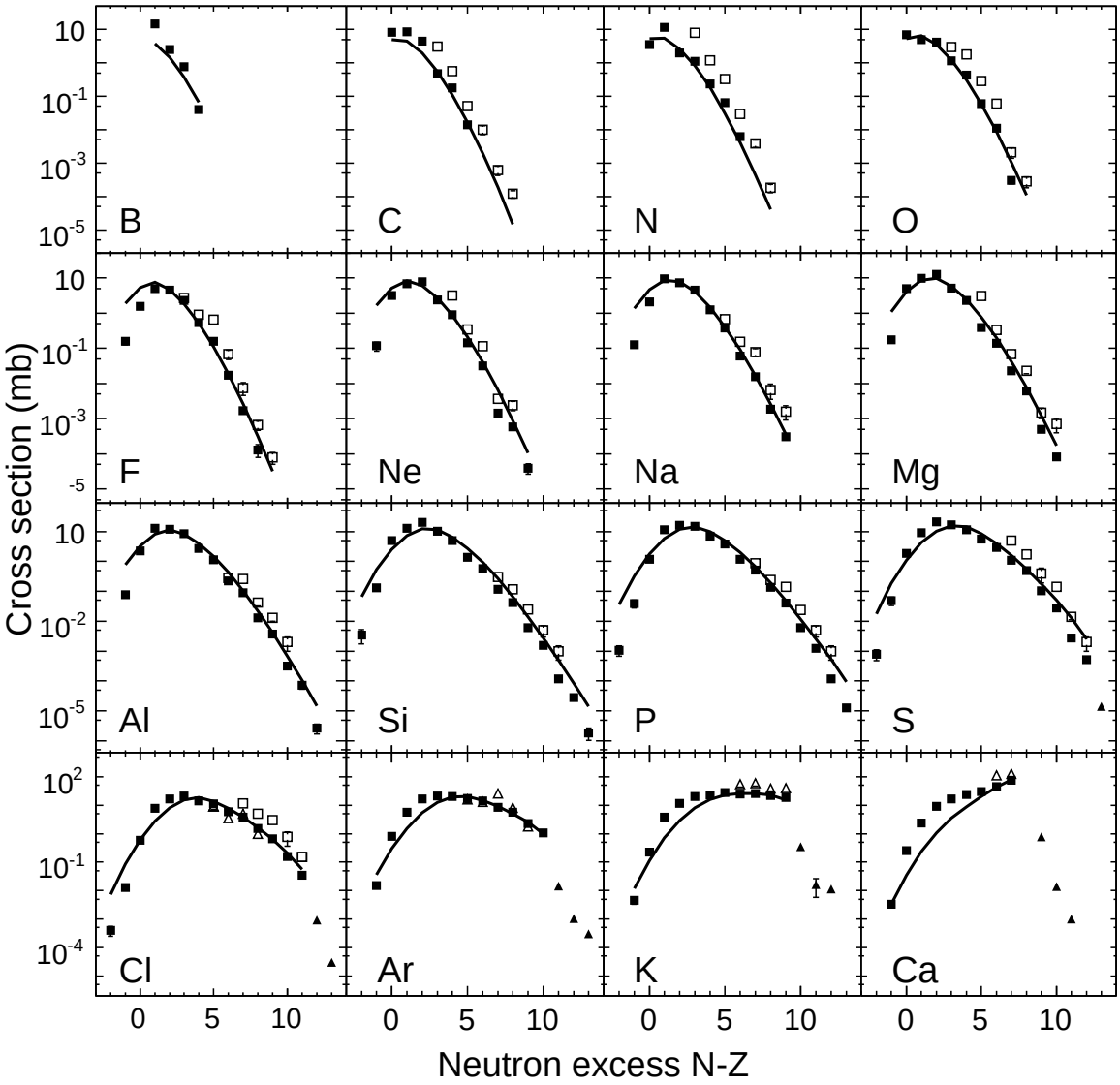

Figure 4.15: Isotopic distributions of measured cross sections plotted as a function of neutron excess for $5 \leq Z \leq 20$ elements detected in the ^{48}Ca+^{9}Be reaction at 140 MeV/u. The experimental fragmentation data are shown as filled squares, cross sections of pick-up reactions are depicted with filled triangles, the solid line shows the calculation by EPAX and open squares show ^{48}Ca+^{9}Be data at 212 MeV/u [42]. Open triangles depict the fragmentation data of ^{48}Ca on a ^{2}H target at 104 MeV/u [96].

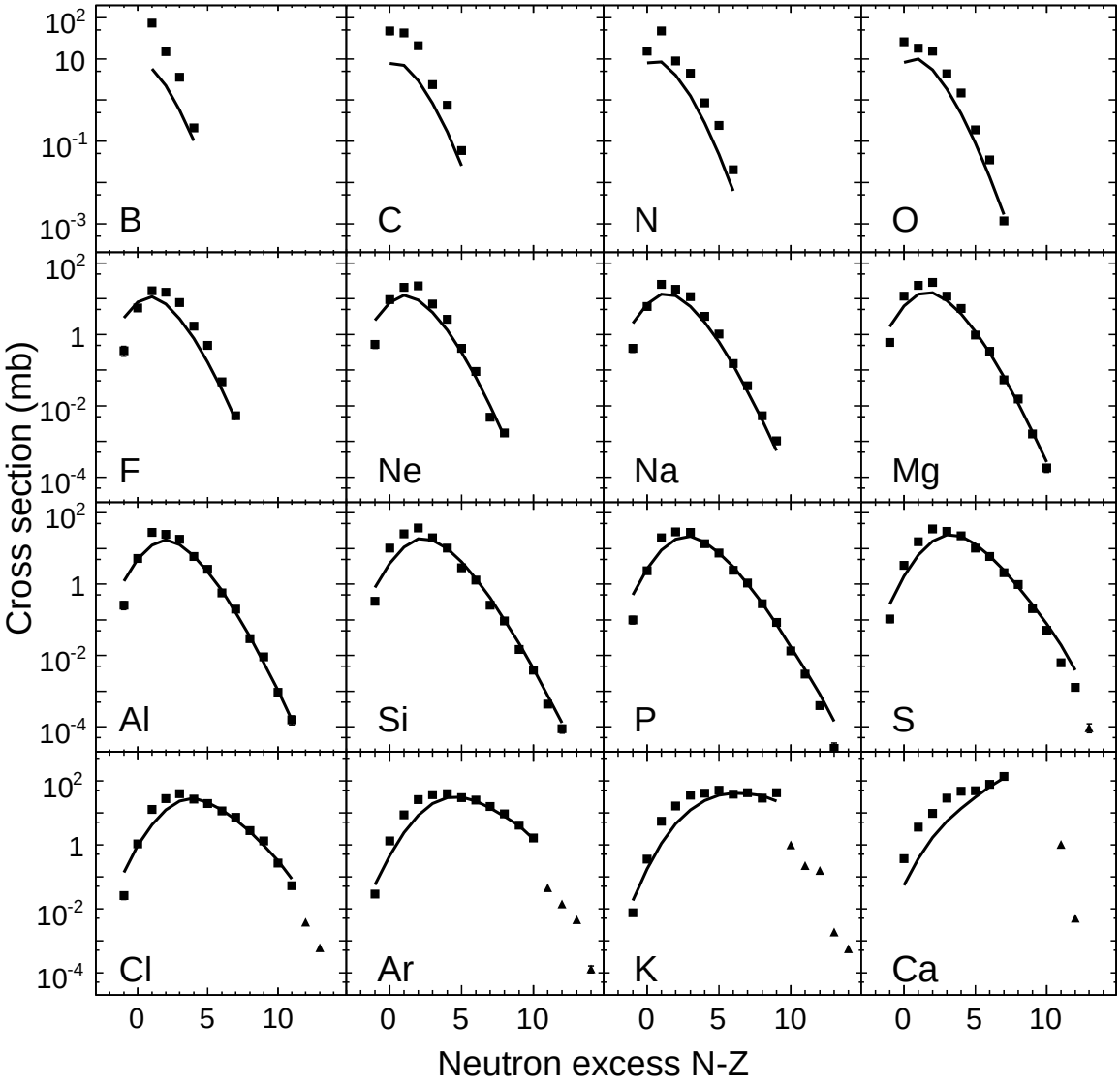

Figure 4.16: Isotopic distributions of measured cross sections plotted as a function of neutron excess for $5 \leq Z \leq 20$ elements detected in the ^{48}Ca+^{181}Ta reaction at 140 MeV/u. The experimental fragmentation data are shown as filled squares, cross sections of pick-up reactions are depicted with filled triangles and the solid line shows the calculation by EPAX.

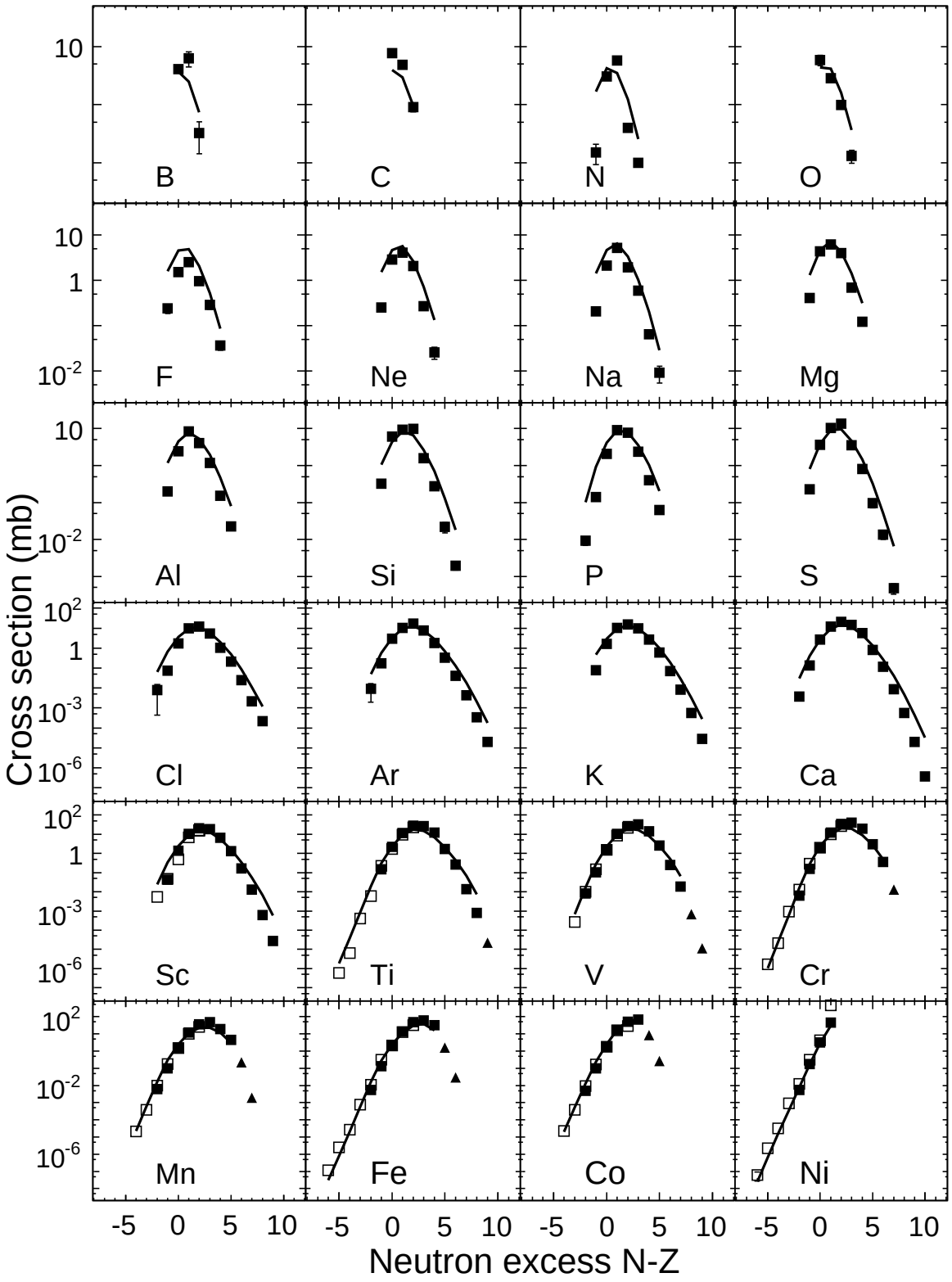

Figure 4.17: Isotopic distributions of measured cross sections plotted as a function of neutron excess for $5 \leq Z \leq 28$ elements detected in the ^{58}Ni+^{9}Be reaction at 140 MeV/u. The experimental fragmentation data are shown as filled squares, cross sections of pick-up reactions are depicted with filled triangles, the solid line shows the calculation by EPAX and open squares show ^{58}Ni+^{9}Be data at 650 MeV/u [89].

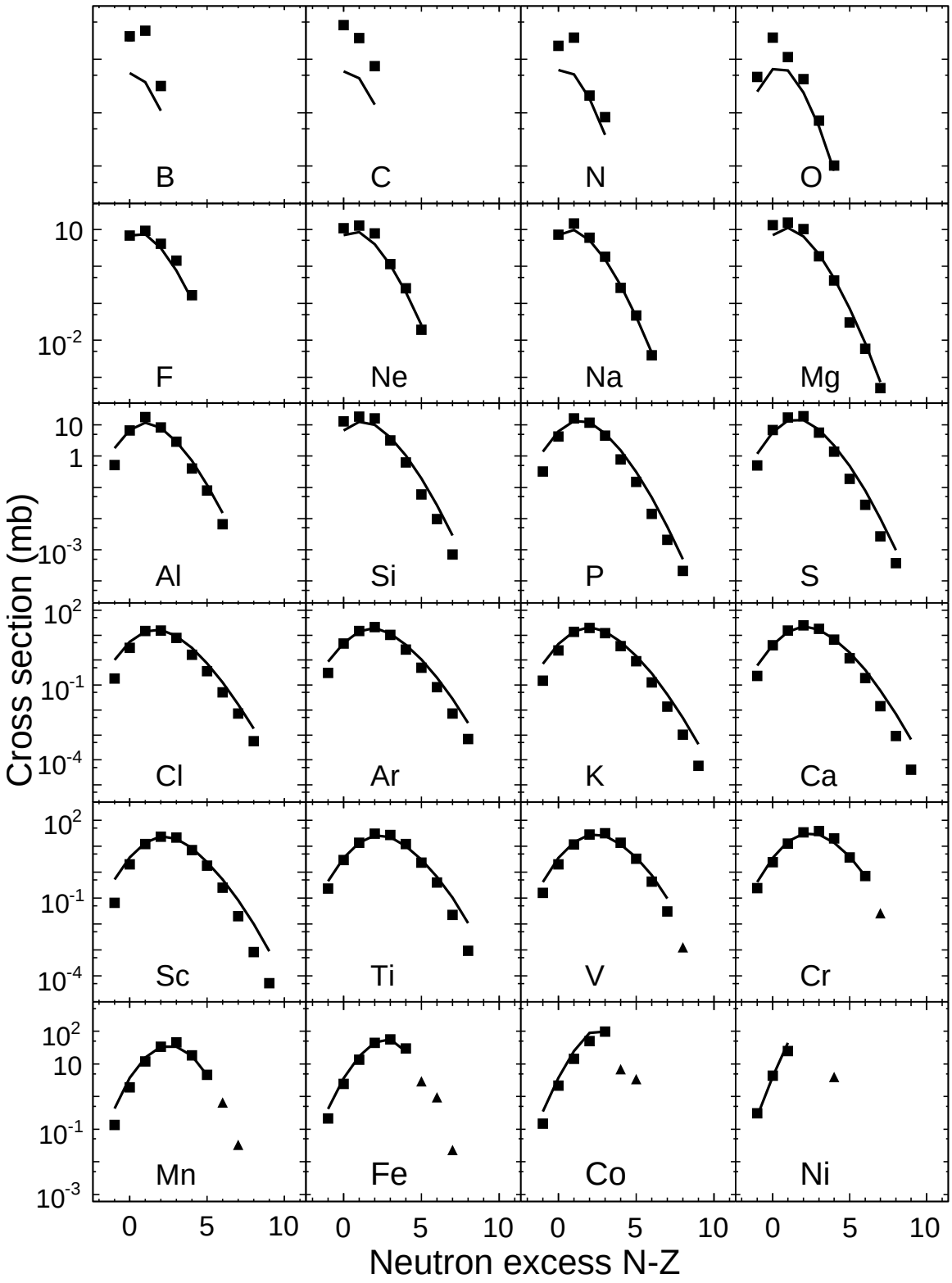

Figure 4.18: Isotopic distributions of measured cross sections plotted as a function of neutron excess for $5 \leq Z \leq 28$ elements detected in the ^{58}Ni+^{181}Ta reaction at 140 MeV/u. The experimental fragmentation are data shown as filled squares, cross sections of pick-up reactions are depicted with filled triangles and the solid line shows the calculation by EPAX.

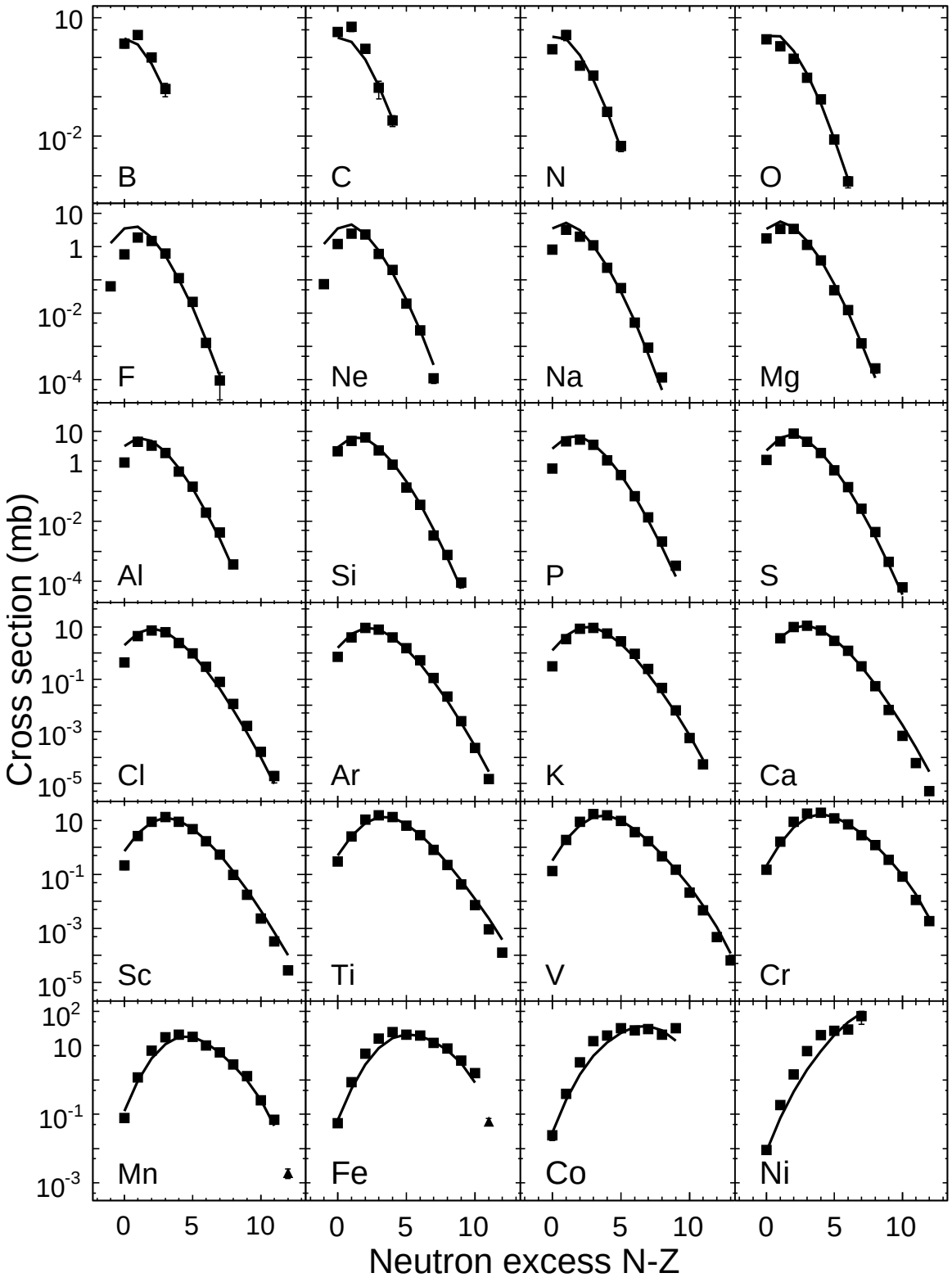

Figure 4.19: Isotopic distributions of measured cross sections plotted as a function of neutron excess for $5 \leq Z \leq 28$ elements detected in the ^{64}Ni+^{9}Be reaction at 140 MeV/u. The experimental fragmentation data are shown as filled squares, cross sections of pick-up reactions are depicted with filled triangles and the solid line shows the calculation by EPAX.

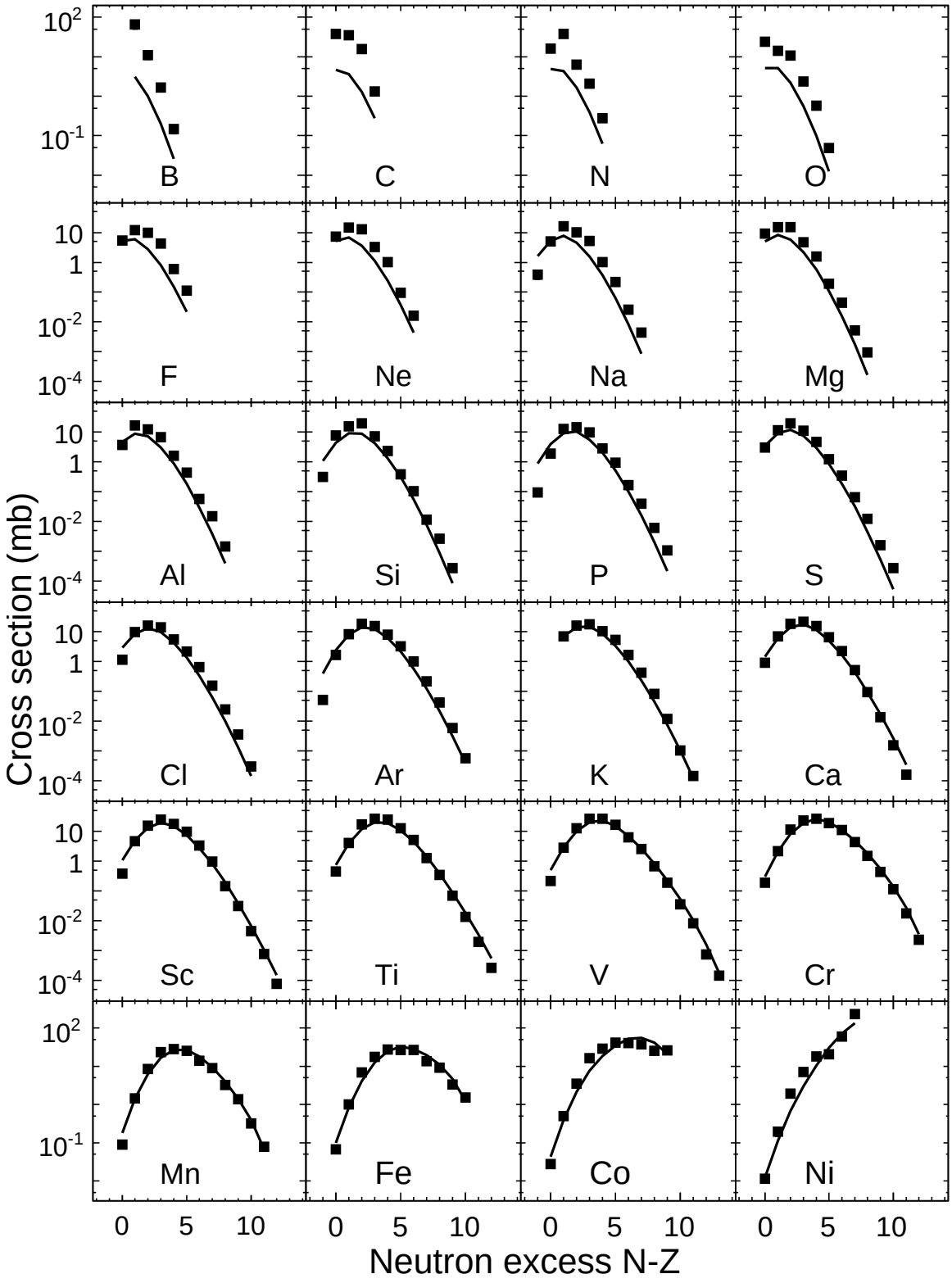

Figure 4.20: Isotopic distributions of measured cross sections plotted as a function of neutron excess for $5 \leq Z \leq 28$ elements detected in the ^{64}Ni+^{181}Ta reaction at 140 MeV/u. The experimental fragmentation data are shown as filled squares and the solid line shows the calculation by EPAX.

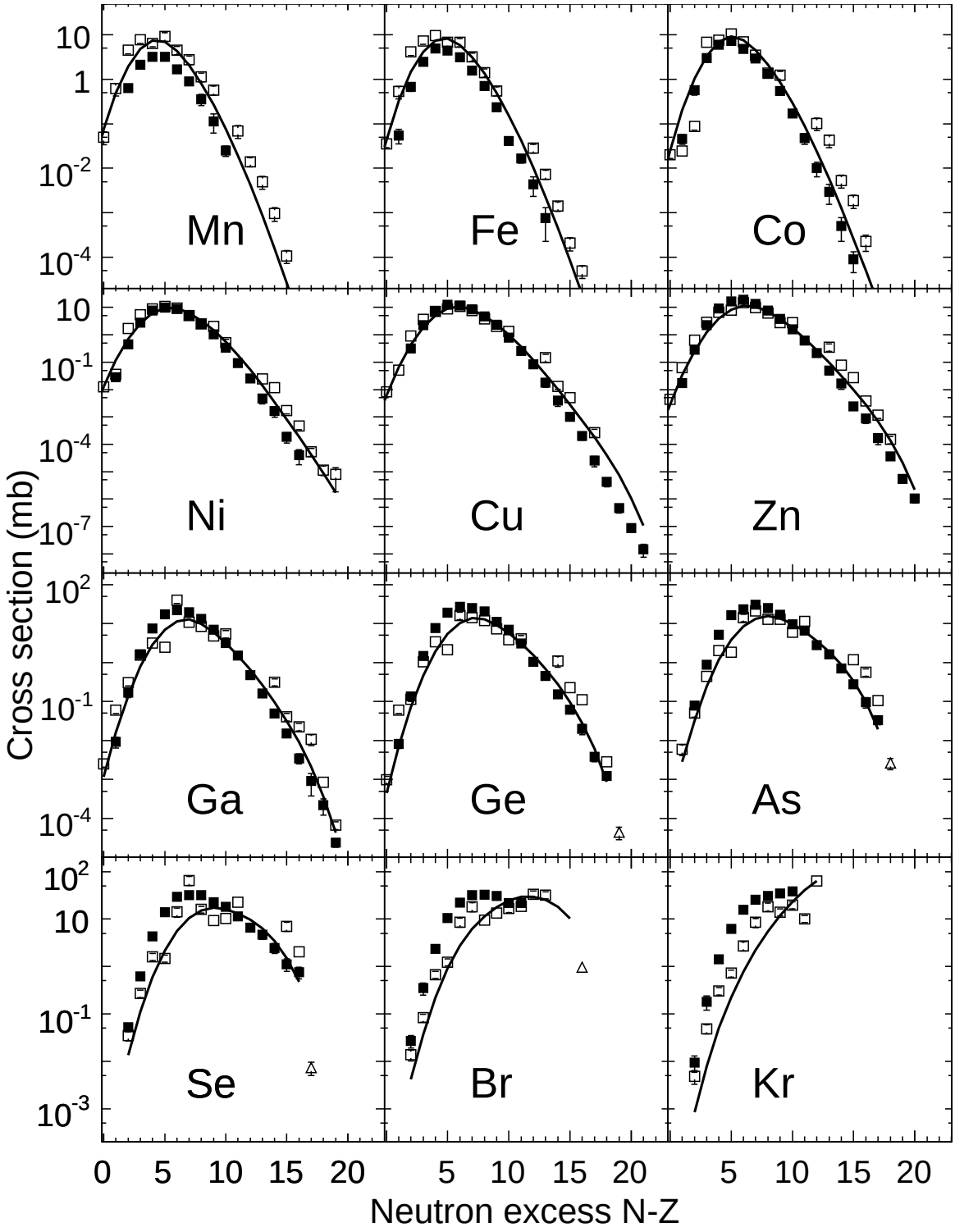

Figure 4.21: Isotopic distributions of measured cross sections plotted as a function of neutron excess for $25 \leq Z \leq 36$ elements detected in the ^{86}Kr+^{9}Be reaction at 64 MeV/u. The experimental fragmentation data are shown as filled squares, the solid line shows the calculation by EPAX and open squares show ^{86}Kr+^{9}Be fragmentation data at 500 MeV/u [75], the nucleon pick-up cross sections from this data set are shown as open triangles.

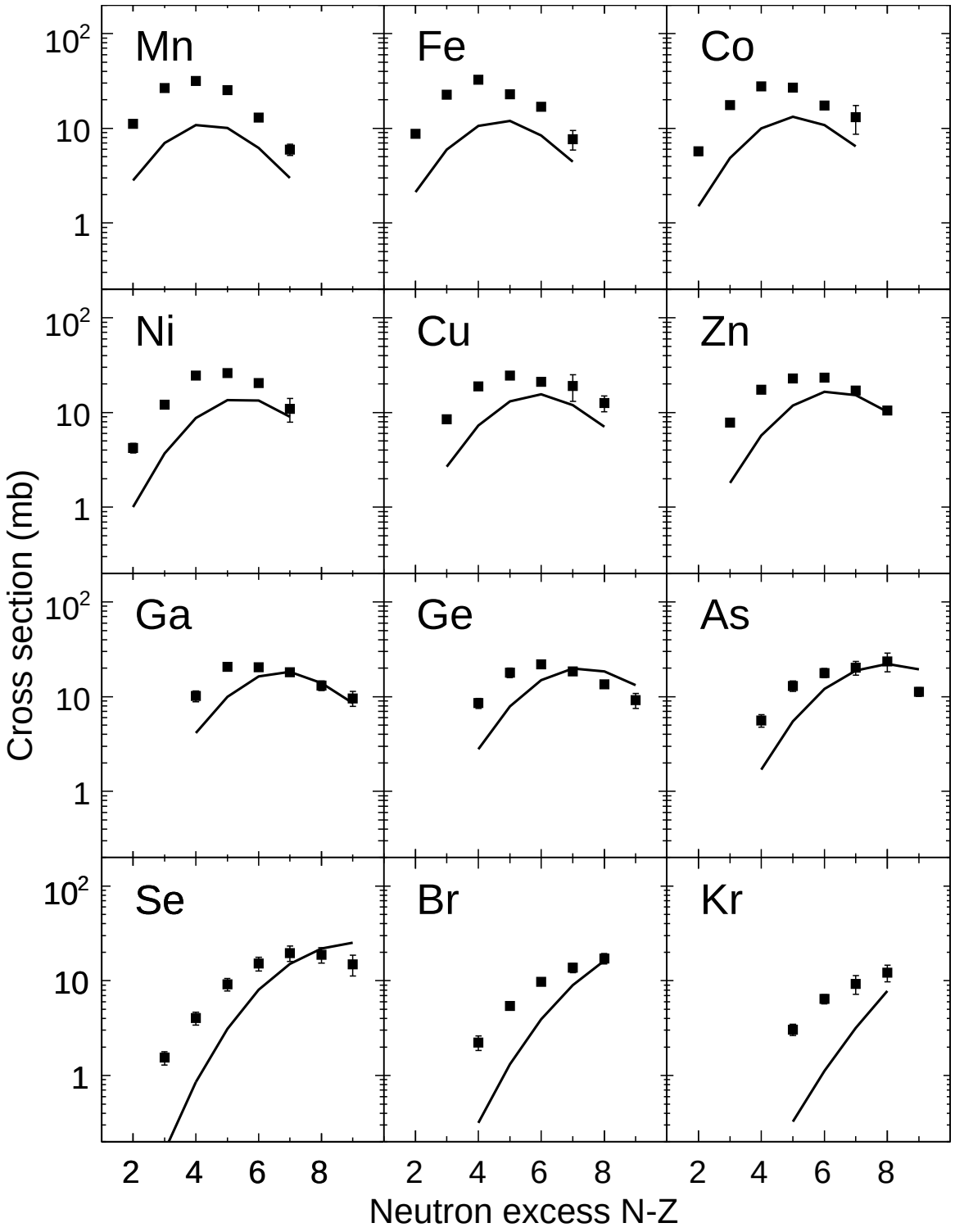

Figure 4.22: Isotopic distributions of measured cross sections plotted as a function of neutron excess for $25 \leq Z \leq 36$ elements detected in the ^{86}Kr+^{181}Ta reaction at 64 MeV/u. The experimental fragmentation data are shown as filled squares and the EPAX calculation is shown as a solid line.

4.3.4 Target dependence

In order to explore the target dependence of the fragmentation cross sections for a given projectile, we constructed target isotope ratios, $R_{tgt}(A,Z)$, for isotopes with mass, A, and proton number, Z. $R_{tgt}(A,Z) \equiv \sigma_{\rm Ta}(A,Z)/\sigma_{\rm Be}(A,Z)$, where $\sigma_{\rm Ta}(A,Z)$ and $\sigma_{\rm Be}(A,Z)$ are the fragmentation cross sections measured for reactions with ^{181}Ta and ^{9}Be target, respectively. The $R_{tgt}(A,Z)$ ratios were calculated for all projectiles in our study. By convention, fragment cross sections created in interactions with the more neutron-rich target (^{181}Ta) are used as numerators.

$R_{tgt}(A,Z)$ for elements $8 \leq Z \leq 18$ are plotted as a function of the fragment mass number, A, in Figure 4.23 for ^{40}Ca (left panel) and ^{48}Ca (right panel) beam. Figure 4.24 shows the $R_{tgt}(A,Z)$ as a function of fragment mass number, A, for elements $10 \leq Z \leq 26$ for ^{58}Ni (left panel) and ^{64}Ni (right panel) beam. The target isotope ratios, $R_{tgt}(A,Z)$ for elements $25 \leq Z \leq 36$ for the ^{86}Kr primary beam are plotted as a function of fragment mass number, A, in Figure 4.25.

The isotopes with even proton number, Z, are plotted with filled symbols and the isotopes with odd Z are plotted with open symbols in Figure 4.23–4.25. The lines connecting the isotopes of one element are drawn to guide the eye. Only ratios with errors smaller than 20% are plotted; for clarity we do not show the error bars of the $R_{tgt}(A,Z)$.

In the geometrical limit, the target isotope ratios, $R_{tgt}(A,Z)$, are given by the differences of the total reaction cross sections which are proportional to the sum of radii squared [98]. This leads to the expression:

$$R_{tgt} = \frac{\left(A_P^{1/3} + A_{\rm Ta}^{1/3}\right)^2}{\left(A_P^{1/3} + A_{\rm Be}^{1/3}\right)^2}, \tag{4.22}$$

where A_P is the mass number of the projectile, $A_{\rm Ta}$ and $A_{\rm Be}$ are mass numbers of ^{181}Ta and ^{9}Be. The horizontal dotted lines in Figure 4.23–4.25 indicate the R_{tgt}

values calculated by Equation (4.22). The target isotope ratios calculated using EPAX parameterization are shown as horizontal dashed lines in Figure 4.23–4.25. EPAX systematics assumes only peripheral interactions parameterizing the cross sections as a linear function of the sum of projectile and target radii. The experimental data, however, exhibit a complex dependence of the target isotope ratios as a function of the fragment mass number, A, for all investigated projectiles.

In the case of the ^{40}Ca primary beam, left panel of Figure 4.23, we can see the U-shaped curves for different elements suggesting enhanced production of neutron-rich as well as neutron-deficient isotopes of a given element with ^{181}Ta target. This is a direct consequence of the wider isotope distributions for reactions with the ^{181}Ta target compared to the ones with the ^{9}Be target. In the case of the ^{48}Ca projectile, right panel of Figure 4.23, the U-shaped curves are not as pronounced and smooth as those seen in the left panel of Figure 4.23 for the ^{40}Ca beam. The magnitude of the effect is small but larger than EPAX and geometrical limit predictions for light neutron-rich isotopes. Such differences may be interpreted as an effect of isospin transfer from the target to the projectile. The relatively steep increase of the production of neutron-rich fragments in the fragmentation of ^{40}Ca ($Z/A = 0.50$) on a ^{181}Ta ($Z/A = 0.40$) target may be due to the relatively large difference of the isospin asymmetry, whereas in the case of ^{48}Ca ($Z/A = 0.42$) projectile the asymmetry is similar to that of the ^{181}Ta target.

For the ^{58}Ni projectile, left panel of Figure 4.24, the enhanced production of neutron-rich as well as neutron-deficient isotopes is not as pronounced as in the case of ^{40}Ca, but the overall increase of the fragmentation cross sections with decreasing fragment number can be observed. The more neutron-rich ^{64}Ni projectile, right panel of Figure 4.24, exhibits less pronounced U-shaped curves. A clear enhancement, inversely proportional to the fragment mass number, A, of the production cross section using the ^{181}Ta target, can be observed for light elements ($10 \leq Z \leq 16$). Again, this behavior may be interpreted as an effect of the isospin transfer from the target to

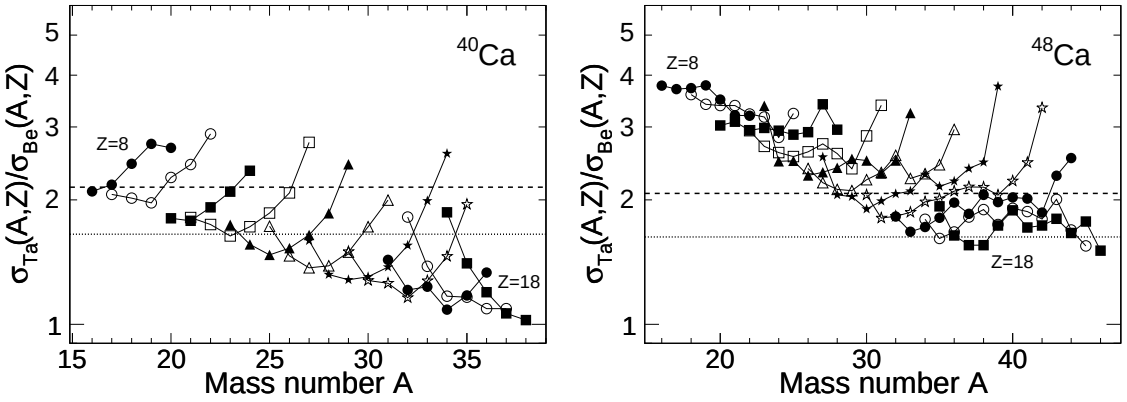

Figure 4.23: Target ratios of the fragmentation cross sections $\sigma_{\mathrm{Ta}}(A,Z)/\sigma_{\mathrm{Be}}(A,Z)$, of fragments $8 \leq \mathrm{Z} \leq 18$ for two projectiles ^{40}Ca (left panel) and ^{48}Ca (right panel). The horizontal dashed and dotted lines indicate the ratio calculated by the EPAX formula and Equation (4.22), respectively.

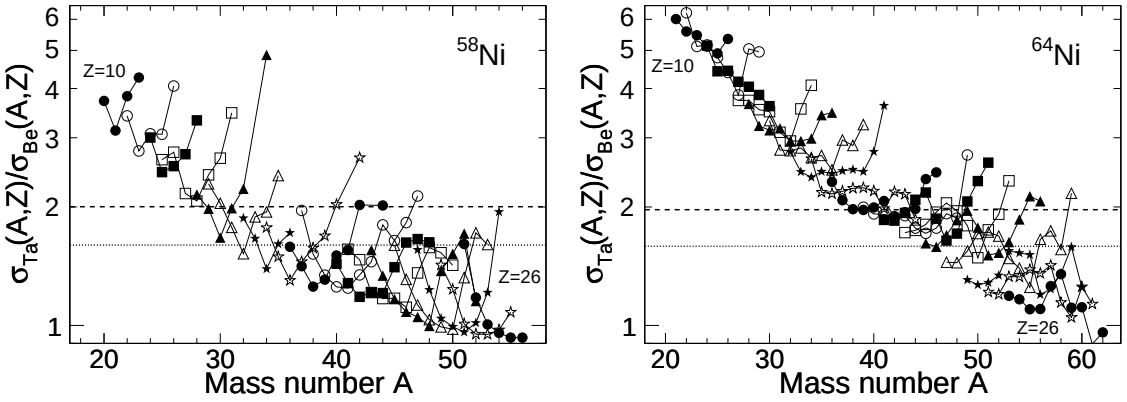

Figure 4.24: Target ratios of the fragmentation cross sections $\sigma_{\mathrm{Ta}}(A,Z)/\sigma_{\mathrm{Be}}(A,Z)$ of fragments $10 \leq \mathrm{Z} \leq 26$ for two projectiles ^{58}Ni (left panel) and ^{64}Ni (right panel). The horizontal dashed and dotted lines indicate the ratio calculated by the EPAX formula and Equation (4.22), respectively.

the projectile. For the ^{58}Ni ($Z/A = 0.48$) projectile, however, the isospin asymmetry is larger than in the case of the ^{40}Ca beam, which may account for the less pronounced enhancement of cross sections for neutron-rich fragments. In the case of the ^{64}Ni ($Z/A = 0.44$) beam, we do not observe strong enhancement of the production cross sections for the neutron-rich fragments because of a rather similar asymmetry between the target and the projectile.

The overall trend of the target isotope ratios, $R_{tgt}(A,Z)$, for the ^{86}Kr projectile measured at 64 MeV/u is similar to the projectiles measured at 140 MeV/u, but with

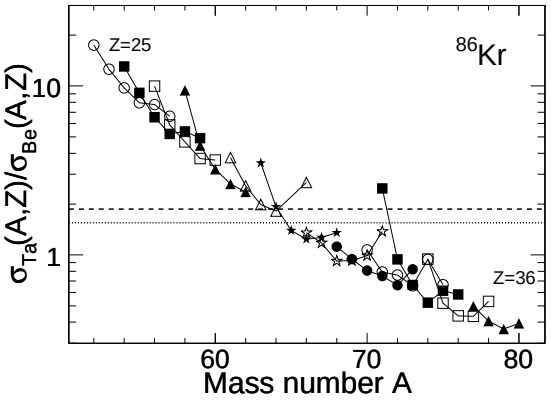

Figure 4.25: Target ratios of the fragmentation cross sections $\sigma_{\mathrm{Ta}}(A,Z)/\sigma_{\mathrm{Be}}(A,Z)$ of fragments $25 \leq \mathrm{Z} \leq 36$ for ^{86}Kr projectile. The horizontal dashed and dotted lines indicate the ratio calculated by the EPAX formula and Equation (4.22), respectively.

steeper overall slope. The experimental cross section data set for the ^{86}Kr+^{181}Ta reaction is much smaller than the one for the ^{86}Kr+^{9}Be reaction, not allowing us to investigate the enhancement of the production cross section of neutron-rich isotopes for individual elements.

There are many differences in the shape of the target isotope ratios for different projectiles. One common feature is that the overall slope of the target isotope ratios, $R_{tgt}(A,Z)$, seems to get steeper with increasing mass of the projectile.

Unfortunately, the observed small enhancement of the fragmentation cross sections using ^{181}Ta target is offset by the large difference in atomic mass of the two target materials (approximately a factor of 20). The ^{181}Ta target must be more than 20 times thicker in order to have the same number of target nucleons per cm^2 as ^{9}Be. Furthermore, effects like the energy loss and angular straggling must be considered when using thick targets for production of rare isotopes. In the case of the ^{86}Kr projectile at 64 MeV/u a relatively broad charge state distribution for ^{181}Ta target makes it undesirable to us. However, if the rising trend of the R_{tgt} for the ^{86}Kr primary beam in Figure 4.25 continues for fragments of lighter elements, it may overcome the above mentioned handicaps of the ^{181}Ta target material. Unfortunately, our limited set of the fragmentation cross sections does not allow us to make this conclusion.

4.3.5 Projectile dependence

The ratios of the fragmentation cross sections for a given fragment with neutron, N, and proton number, Z, $R_{proj}(N,Z)$, from different projectiles were calculated to address the projectile dependence. $R_{proj}(N,Z) \equiv \sigma_{48}(N,Z)/\sigma_{40}(N,Z)$ in the case of the Ca primary beams and $R_{proj}(N,Z) \equiv \sigma_{64}(N,Z)/\sigma_{58}(N,Z)$ for the Ni projectiles. By convention, fragment cross sections from the more neutron-rich projectile (^{48}Ca or ^{64}Ni) are used as numerators.

Figure 4.26 displays the ratios, $R_{proj}(N,Z)$, for the reactions of the ^{48}Ca and ^{40}Ca with ^{9}Be and ^{181}Ta targets. The $R_{proj}(N,Z)$ ratios calculated for even and odd Z elements are shown as filled and open symbols, respectively. Similarly, Figure 4.27 shows the $R_{proj}(N,Z)$, for the reactions of the ^{64}Ni and ^{58}Ni primary beams with ^{9}Be and ^{181}Ta targets. Ratios obtained with the ^{9}Be and ^{181}Ta targets are plotted in the top and bottom panels, respectively, of Figure 4.26 and 4.27 as a function of fragment neutron number, N.

Peripheral projectile fragmentation reactions are mostly responsible for production of fragments with mass $A > A_P/2$. Most likely, lighter fragments are produced by more central collisions with different reaction mechanisms including multifragmentation. Indeed, light fragments ($Z \leq 9$ and $Z \leq 12$ for Ca and Ni systems, respectively) exhibit the linear isoscaling behavior as observed in multifragmentation [99]

$$R_{proj}(N,Z) = R_{21}(N,Z) = C\exp\left(\alpha N + \beta Z\right), \tag{4.23}$$

where the isoscaling ratio $R_{21}(N,Z)$ is factored into two fugacity terms α and β, which contain the differences of the chemical potentials for neutrons and protons of the two reaction systems. C is a normalization factor of the isoscaling ratio. The lines in Figure 4.26 and 4.27 for elements $Z \leq 9$ and $Z \leq 12$, respectively, are the best fits of the data to Equation (4.23). The best fit values of α and β parameters for all investigated reaction systems are listed in Table 4.3.

For heaviest fragments ($Z \geq 15$ and $Z \geq 22$ for Ca and Ni systems, respectively), longer chains of isotopes were measured. The data no longer exhibit the linear isoscaling behavior of Equation (4.23). Instead, the data are better represented by a function which contains second order terms in neutron, N, and proton number, Z,

$$R_{proj}(N,Z) = C\exp\left(\alpha N + \alpha_1 N^2 + \beta Z + \beta_1 Z^2\right), \tag{4.24}$$

where C is the normalization factor, α, α_1, β, and β_1 are parameters of the proposed function. The curves in Figure 4.26 for elements $15 \leq Z \leq 19$ are the best fits of the data to Equation (4.24). In the case of the Ni reaction systems we fitted the R_{proj} ratios for elements $22 \leq Z \leq 26$ by function of Equation (4.24).

It may seem that this second order function may be in contradiction with the findings of the deeply inelastic scattering of Kr isotopes on Ni isotopes. However, close examinations of previous data [100] show that the observed isoscaling is more similar to Equation (4.24) than to Equation (4.23). Furthermore, closer examination of the $10 \leq Z \leq 14$ and $13 \leq Z \leq 21$ regions for the Ca and Ni reaction systems, respectively, revealed that they cannot be described by a single set of parameters of Equation (4.23) or (4.24). Instead we noticed a gradual change of the α, α_1, β, and β_1 parameters with every isotope chain of $10 \leq Z \leq 14$ and $13 \leq Z \leq 21$ elements for Ca and Ni systems, respectively. This observation suggests that the isotopes of these elements contain contributions from both projectile fragmentation as well as multifragmentation. Unlike multifragmentation which can be assumed to be statistical and thermal the large prefragment residues are most likely formed in non-equilibrium processes and there is no a priori reason to assume that the fragments would observe isoscaling. Impact parameter event selection detector in future experiments should allow better distinction between the above described processes.

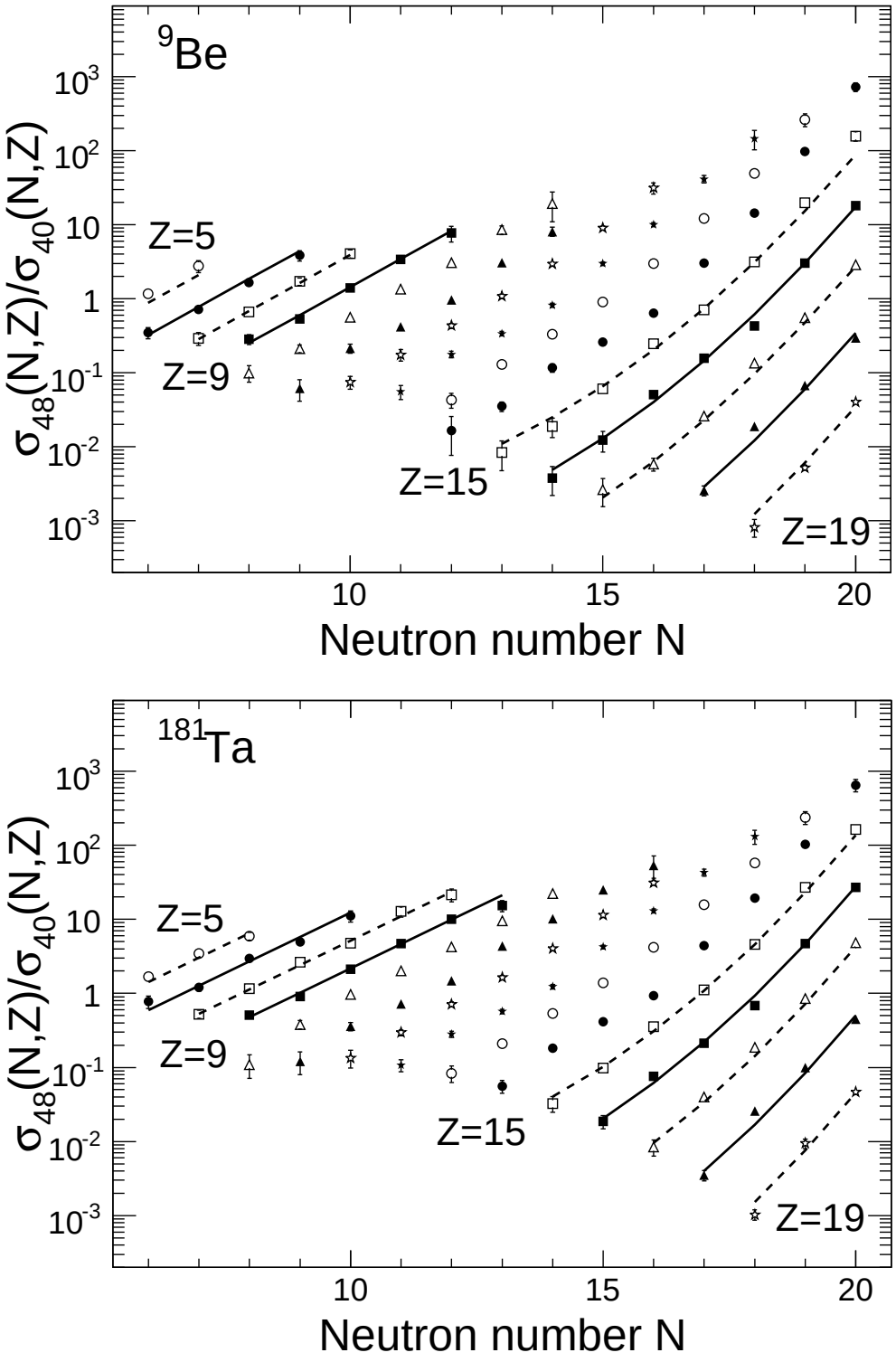

Figure 4.26: Ratios of cross sections $\sigma_{48}(N,Z)/\sigma_{40}(N,Z)$ of fragments created in ^{48}Ca and ^{40}Ca reactions on ^{9}Be (top panel) and ^{181}Ta (bottom panel) targets. The projectile ratios for even and odd Z elements are denoted by filled and open symbols, respectively. Solid and dashed lines show the fit by Equation (4.23) for $5 \leq Z \leq 9$. Curved solid and dashed lines denote fits by Equation (4.24) for $15 \leq Z \leq 19$.

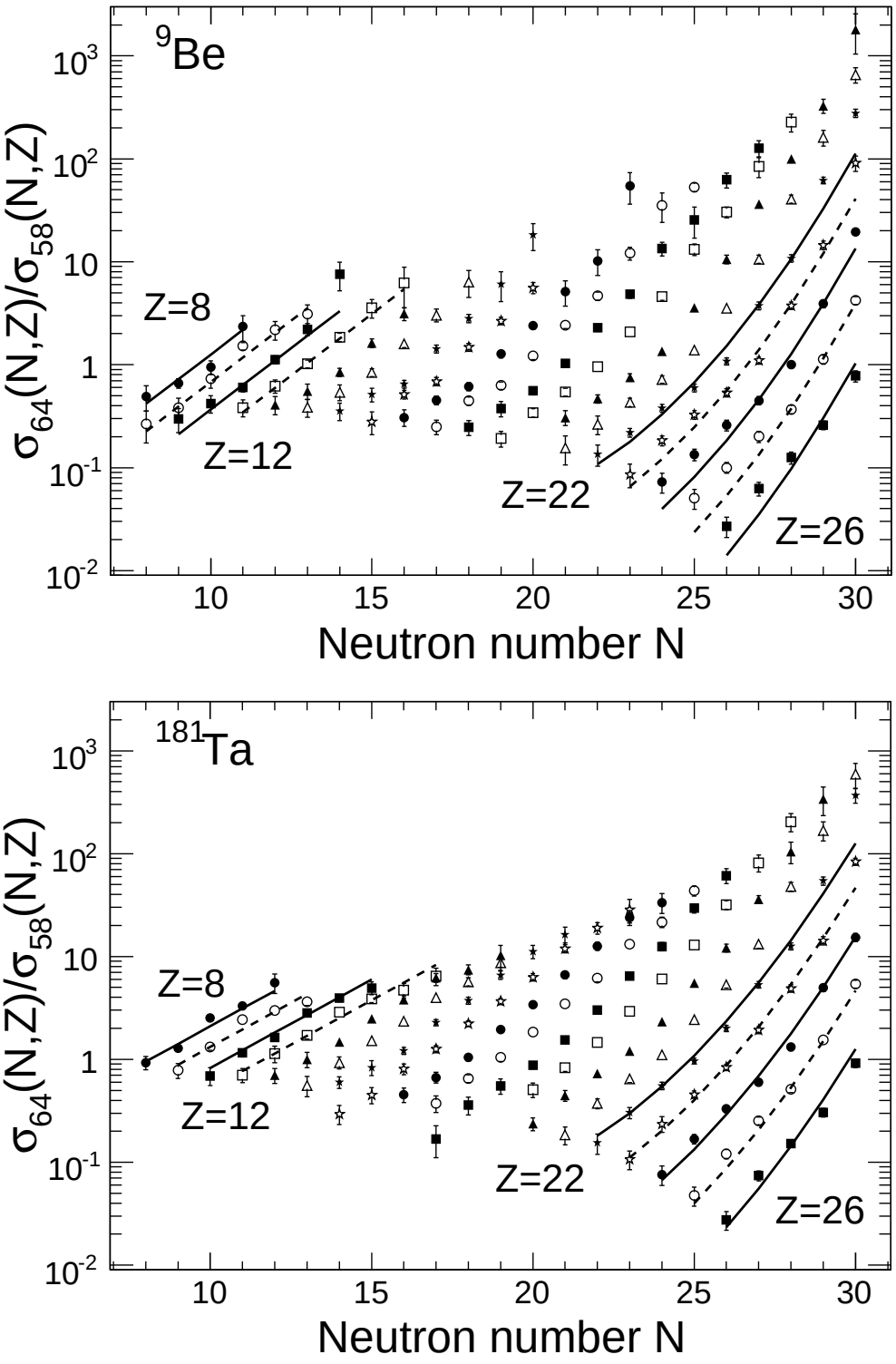

Figure 4.27: Ratios of cross sections $\sigma_{64}(N,Z)/\sigma_{58}(N,Z)$ of fragments created in ^{64}Ni and ^{58}Ni reactions on ^{9}Be (top panel) and ^{181}Ta (bottom panel) targets. The projectile ratios for even and odd Z elements are denoted by filled and open symbols, respectively. Solid and dashed lines show the fit by Equation (4.23) for $8 \leq Z \leq 12$. Curved solid and dashed lines denote fits by Equation (4.24) for $22 \leq Z \leq 26$.

Table 4.3: Best fit values of the α, α_1, β, and β_1 parameters of the isoscaling function of Equation (4.23) and the second order function of Equation (4.24) for Ca and Ni systems. Z_{min} and Z_{max} values indicate the range of elements for which the best fit values were obtained.

Projectiles	Target material	Range Z_{min}	Range Z_{max}	α	α_1	β	β_1
Ca	^{9}Be	5	9	0.8714	0.0	−0.9971	0.0
		15	19	−1.2764	0.0776	1.8367	−0.1116
	^{181}Ta	5	9	0.7586	0.0	−0.8706	0.0
		12	19	−1.5350	0.0850	2.5532	−0.1340
Ni	^{9}Be	8	12	0.5503	0.0	−0.6142	0.0
		22	26	−1.8047	0.0514	1.4966	−0.0556
	^{181}Ta	8	12	0.3961	0.0	−0.4670	0.0
		22	26	−1.4904	0.0444	1.4062	−0.0533

Chapter 5

Comparison to models

In order to get a physical understanding of the underlying fragmentation processes and the reaction mechanism, three reaction models, varying in complexity and sophistication, were used to understand the results of our experimental measurements. Calculations by the macroscopic Abrasion-Ablation (AA) model, the macroscopic-microscopic Heavy Ion Phase Space Exploration (HIPSE) model and the sophisticated fully microscopic Antisymmetrized Molecular Dynamics (AMD) model were compared to the experimental data of this study. The AA model used in the present work is a modified version of the geometrical AA model implemented in LISE++ [56]. In all described theoretical models the nuclear reactions are simulated in two stages: primary (fast nuclear reaction dynamics) and secondary (slow decay of excited primary fragments).

First the three reaction models are discussed, introducing the main assumptions and the theoretical concepts. Then the primary fragments generated by these models are compared with each other. The discussion continues with the description of evaporation codes used to de-excite the residues obtained by the reaction models. At the end of the chapter the calculated properties of the final fragments are compared to the experimental data.

5.1 Reaction models

5.1.1 Abrasion Ablation model

In the fully macroscopic Abrasion-Ablation (AA) model, the projectile and target nuclei are assumed to be spherical. The Coulomb deflection of the projectile trajectory is neglected. In the case of a peripheral reaction, at a given impact parameter, b, the projectile and target nucleons which lie in the overlap region (participant nucleons) are removed from the original nuclei, while the remainder nucleons do not participate (spectator nucleons). This first stage of the reaction, called abrasion, is very fast; the timescale is given by the relative velocity of projectile and target (see Figure 1.3). The AA model does not describe the ultimate fate of the participant nucleons, since they are not necessary to model the fragmentation of projectile or target nuclei.

Analytic formulas relating the impact parameter, b, to the number of removed nucleons, ΔA, have been derived [101]. Unfortunately the expression of impact parameter, b, as a function of number of removed nucleons must be obtained numerically. The cross section, $\sigma_{pre}(A)$, for producing a primary fragment with mass, A, from a projectile, A_P, is calculated from the obtained $b(\Delta A)$ function:

$$\sigma_{pre}(A) = \pi \left\{ [b(\Delta A - 0.5)]^2 - [b(\Delta A + 0.5)]^2 \right\}. \tag{5.1}$$

Assuming there are no proton-neutron correlations in the reaction system, the probability to form a residue with a given mass number, A, and nuclear charge, Z, is given by a hypergeometric distribution. Hence the total cross section, $\sigma_{pre}(A, Z)$, to form a primary fragment (A, Z) is

$$\sigma_{pre}(A, Z) = \left[\binom{Z_p}{\Delta Z} \binom{N_p}{\Delta N} / \binom{A_p}{\Delta A} \right] \sigma_{pre}(A). \tag{5.2}$$

Where A_p, Z_p, and N_p are mass, charge and neutron numbers of the projectile and ΔA,

ΔZ, and ΔN are numbers of nucleons, protons, and neutrons, respectively, removed in the interaction. The projectile and target dependence is contained in the $b(\Delta A)$ dependence.

The highly excited and deformed spectators de-excite in the second stage, called ablation, by evaporating light clusters and nucleons (see Figure 1.3). This evaporation stage of the reaction is taken to be slower ($\approx 10^{-21}$–10^{-16} s) compared to the abrasion step ($\approx 10^{-22}$–10^{-23} s) and results in the formation of the de-excited nuclei detected in the experiments. In the original AA model [45] the excitation energy of the primary fragments is determined from the surface energy (typical value $\approx$ 1 MeV/fm^2). This value of the excitation energy, however, must be regarded as a lower limit, because the energy of the primary fragment can be altered by other processes (such as transfer of energetic participant nucleons into the projectile prefragment).

To increase the excitation energy, many different mechanisms have been proposed, such as scattered nucleons from the participant zone to the spectators [102] or inclusion of the frictional energy in the target-projectile interaction [103]. Gaimard *et al.* [104] calculated the excitation energy based on vacancies created in the Fermi distribution of the nucleons in the spectator nucleus. This simple statistical "hole-energy" model yields an average excitation energy of 13.3 MeV per hole (abraded nucleon). Another investigation by Schmidt *et al.* [105] resulted in an average excitation energy of 27 MeV per abraded nucleon for fragments of heavy projectiles ($A > 100$) in the most peripheral collisions. The above mentioned estimates of the mean excitation energy per nucleon illustrate the level of uncertainties in determination of the excitation energy in the AA model.

In our calculations we used a modified version of geometrical Abrasion-Ablation model that has been implemented in the LISE++ code [56]. The mean excitation energy, $E^\star$, of the primary fragment is expressed as a linear function of the number of abraded nucleons, ΔA:

$$E^\star = K \cdot \Delta A. \tag{5.3}$$

Table 5.1: Best fit values for the K and S parameters of the excitation energy in the Abrasion-Ablation model for all investigated reaction systems. Uncertainties estimated from the minima in the two-dimensional K versus S space.

Beam	Target	K (MeV/u)	S (MeV/$\sqrt{u}$)
^{40}Ca	^{9}Be	11 ± 2	6 ± 1
	^{181}Ta	9 ± 1	4 ± 1
^{48}Ca	^{9}Be	11 ± 2	6 ± 1
	^{181}Ta	11 ± 2	6 ± 1
^{58}Ni	^{9}Be	13 ± 2	7 ± 1
	^{181}Ta	13 ± 2	8 ± 1
^{64}Ni	^{9}Be	13 ± 2	7 ± 1
	^{181}Ta	15 ± 2	8 ± 1
^{86}Kr	^{9}Be	19 ± 2	10 ± 2
	^{181}Ta	18 ± 2	10 ± 2

The fluctuations around this mean value are described by a Gaussian distribution with a variance, $\sigma_{E^\star}$, parameterized as:

$$\sigma_{E^\star} = S \cdot \sqrt{\Delta A}. \tag{5.4}$$

The K and S are taken as fitting parameters of the model. The excitation energy is assigned to prefragments according to Equations (5.3) and (5.4). These excited primary fragments decay as described in the analytical LisFus evaporation code [106].

The K and S parameters are determined by fitting the measured cross sections of projectile-like fragments ($A > A_P/2$) for a given reaction system. The obtained best fit values of the K and S parameters for all our reaction systems are listed in Table 5.1. This approach has been applied in the case of the ^{78}Kr+^{9}Be reactions at 140 MeV/u by Stolz *et al.* [107]. The measurement focused on proton-rich fragments in Ge–Se region and obtained $K = 12$ MeV/ΔA and $S = 3$ MeV/$\sqrt{\Delta A}$.

The obtained values for the K and S parameters in our analysis as listed in Table 5.1, do not depend on the target for all investigated projectiles within the quoted uncertainties. Both Ni projectiles seem to require a slightly larger values for the K

parameter than the Ca beams, but the differences are still within the large uncertainties. The ^{86}Kr reactions, however, require much steeper slopes of the excitation energy as a function of the number of removed nucleons in order to describe the fragmentation data.

The LISE++ implementation of the AA model [104] provides fast calculations over a wide dynamic range of final fragment cross sections. With only two parameters, the excitation energy and its fluctuations, the predictions reproduce the experimental data extremely well as will be discussed in Section 5.5. Currently it requires fitting of principal parameters to the experimental data for each reaction, its predictive power is rather limited. However, it may be used to extrapolate the production cross sections, in the case of one reaction system, for very exotic fragment species when a systematic set of fragmentation cross sections becomes available.

5.1.2 Heavy Ion Phase Space Exploration

The Heavy Ion Phase Space Exploration (HIPSE) model has been implemented to bridge the gap between the statistical models, which reduce the description of the reaction to a few important parameters, and fully microscopic models which require a large amount of CPU time to describe the motion of individual nucleons. Based on a macroscopic-microscopic "phenomenology," it accounts for both dynamical and statistical aspects of nuclear collisions.

The nuclear reaction, as described by HIPSE [108], can be separated into three stages: approach of projectile and target nuclei, partition formation and the cluster propagation phase (ending with an in-flight statistical decay). In the entrance channel at a given beam energy, E_B, a classical two-body dynamics of the center of masses of the target and the projectile nuclei is assumed. For projectile and target nuclei with mass numbers, A_P and A_T, and positions, $\mathbf{r}_P$ and $\mathbf{r}_T$, respectively, the dynamical

evolution associated with the following Hamiltonian is considered:

$$\frac{A_T}{A_T + A_P} E_B = \frac{\mathbf{p}^2}{2\mu} + V_{A_T A_P}(|\mathbf{r}_T - \mathbf{r}_P|), \tag{5.5}$$

where $V_{A_T A_P}$ is the nucleus-nucleus potential, $\mathbf{p}$ is the relative momentum and $\mu = m_T m_P/(m_T+m_P)$ is the reduced mass with m_P and m_T being the projectile and target mass, respectively. The proximity potential [109] is used to express the nucleus-nucleus potential $V_{A_T A_P}$ at large distances $r > (R_T + R_P)$, with R_T and R_P radii of the target and the projectile nuclides, respectively. This potential is unambiguously defined when the two nuclei are well separated. For small relative distances $r \leq (R_T + R_P)$, a simple third order polynomial extrapolation is used, assuming continuity of the derivative of the potential at each point. The value at $r = 0$ is expressed as:

$$V_{A_T A_P}(0) = \alpha_a V^{Froz}_{A_T A_P}(r = 0) \tag{5.6}$$

where the potential hardness parameter, α_a, is an adjustable parameter of the model, and $V^{Froz}_{A_T A_P}(r = 0)$ is the energy of the system assuming that the two nuclei overlap completely in the frozen density approximation. This energy corresponds *a priori* to the maximal value of $V_{A_T A_P}(0)$, leading to $\alpha_a \leq 1$. Figure 5.1 shows a dependence of $V_{A_T A_P}$ on relative distance between target and projectile nuclei for different values of the α_a parameter. The frozen density or "sudden" approximation assumes that the internal degrees of freedom do not have time to reorganize themselves and the system has a strong memory of the initial conditions. At energies close to the fusion barrier, the α_a parameter represents a measure of the degree of reorganization of the internal degrees of freedom during the reaction. Since the model does not treat the internal reorganization of nucleons explicitly, α_a is taken as a free parameter, depending only on the beam energy, representing the absence of knowledge of the nucleus-nucleus potential at large overlaps.

The trajectories of the projectile and the target nuclides are determined by the

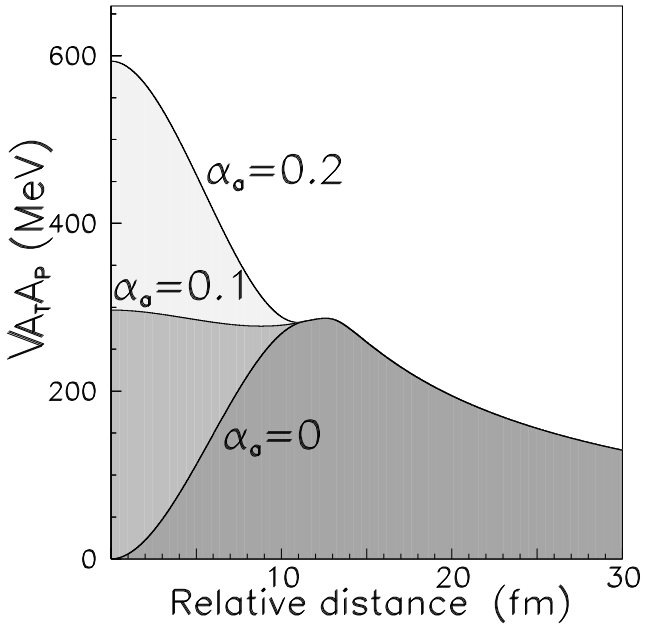

Figure 5.1: Nucleus-nucleus potential $V_{A_T A_P}$ as a function of the relative distance for the ^{129}Xe+^{120}Sn system with $\alpha_a = 0$, 0.01, and 0.2 [108].

Hamiltonian in Equation (5.5). At the minimum distance of approach, the two reacting nuclei overlap according to the impact parameter and the potential hardness parameter, α_a. The frozen density approximation is applied again, explicitly, to sample the positions and the momenta of the nucleons in the center of mass of each of the reaction partners. The semiclassical Thomas-Fermi theory is used to get realistic ground state density distributions for each of the reaction partners. The nucleons are sampled according to a Metropolis algorithm where the Pauli principle is taken into account in each nucleus by requiring that $\Delta r_\tau \cdot \Delta p_\tau \geq \hbar$, where Δr_τ and Δp_τ are the relative position and momentum of two nucleons with the same isospin, τ. This procedure ensures a uniform arrangement of the nucleons in each of the reaction partners. At the end of the first stage of the reaction positions $(x, y, z)_i$ and momenta $(p_x, p_y, p_z)_i$ for a set of $A_T + A_P$ nucleons are obtained.

Before the clusters are defined, the overlap region is determined based on the following consideration: a nucleon initially in the target at position $\mathbf{r}_i$, is assumed to

be in the overlap region if $|\mathbf{r}_i - \mathbf{r}_P| \leq R_P$, where $\mathbf{r}_P$ is the position of the projectile in the center of mass frame, and R_P is the radius of the projectile. For the nucleons initially in the projectile analogous criteria are required $|\mathbf{r}_i - \mathbf{r}_T| \leq R_T$, where $\mathbf{r}_T$ is the position of the target in the center of mass frame, and R_T is the radius of the target. This approach corresponds to the so-called "participant-spectator" picture. However, experimentally it is observed that the quasi-projectile fragments have a slightly reduced kinetic energy with respect to that of the initial projectile. This effect is taken into account by introducing the exchange of particles between the two partners during the reaction. In the HIPSE model it is introduced *ad hoc* by assuming that a fraction, x_{tr}, of the nucleons coming initially from the target (projectile) are transferred to the projectile (target). It is expected that the number of exchanged nucleons decreases with the beam energy, and thus x_{tr} depends only on the initial kinetic energy.

A simplified procedure is applied to treat nucleon-nucleon collisions inside the overlap region characterized by a mass number, A_{over}. Only a fraction of the nucleons in the participant region experiences a collision. Thus the number of collisions is defined by $N_{coll} = A_{over} \cdot x_{coll}$. The fraction of the nucleon-nucleon collisions, x_{coll}, is the third free parameter of the HIPSE model. It is expected to depend only on the energy of the beam. A two-body nucleon-nucleon collision is simulated only in the momentum space. The final spatial positions of the two nucleons are randomly distributed inside a sphere with radius

$$R_{coll} = 1.2A_{over}^{1/3} + r_{coll}, \tag{5.7}$$

where parameter r_{coll} is taken to be 4 fm which reproduces the low energy multifragmentation data [30]. It must be noted that due to the Pauli exclusion principle not all the volume of the sphere with radius, R_{coll}, is accessible.

After nucleon-nucleon collisions take place, the clusters are defined according to

a straight-forward coalescence algorithm. First, one of the nucleons is chosen at random, constituting a starting point from which the fragment is built. Then, another nucleon, i, from the participant region is chosen. Since the exact conditions when a nucleon in the nuclear medium can be absorbed by a cluster are not known, a simple phenomenological criterion is used. In particular, the nucleon with relative position, r_i, and relative momentum, p_i, with respect to fragment is assumed to be absorbed by it if

$$\frac{p_i^2}{2m} + \frac{V_{cut}}{1 + \exp\left[\frac{r_i - d_f}{a}\right]} < 0, \tag{5.8}$$

where m is the nucleon mass and the parameters d_f and V_{cut} correspond to limits in position, r, and momentum, p, space, respectively. The distance, d_f, is expressed as $R_f + r_{cut}$, where R_f is the radius of the fragment and r_{cut} is 7 fm for all nucleons undergoing a collision and 2.5 fm for all others. Using $V_{cut} = -p^2/2m$, p_{cut}=500 MeV/c was obtained and the diffuseness parameter, a, has been fixed to be 0.6 fm. If the phase space condition of Equation (5.8) is fulfilled the nucleon is absorbed by the fragment and a new cluster is formed provided that it exists in the mass table. If the above mentioned requirements are not fulfilled the simulated event is discarded as unphysical.

The whole procedure is repeated until all nucleons in the participant region are exhausted. The position, momentum, mass and charge of the clusters are then updated at each step. If there is more than one possibility for aggregation at a given step, the nucleon is absorbed by one of the fragments at random.

Once all the residues are defined with mass number, position, momentum and angular momentum (A_i, $\mathbf{R}_i$, $\mathbf{P}_i$, $\mathbf{L}_i$), deduced from the nucleon properties in every cluster, a clock is started corresponding to $t = 0$ fm/c for the forthcoming dynamics. The fragments are propagated according to the Hamiltonian

$$H = \sum_i \frac{P_i^2}{2mA_i} + \sum_{i<j} V_{A_iA_j}(|\mathbf{R}_i - \mathbf{R}_j|). \tag{5.9}$$

In order to ensure the consistency of the calculation, the same nucleus-nucleus potential of Equation (5.5) is used as in the entrance channel. The dynamical propagation of the clusters is stopped at $t = 150$ fm/c, when a rather significant reorganization in the phase space may have occurred. The relative energy of any of the combinations of two fragments is calculated, and if it is lower than the fusion barrier, the corresponding clusters fuse and the properties of the fused systems are calculated. It is then assumed that the thermalization occurs on a time scale of tens of fm/c, which is not described on the microscopic level in the model, the excitation energy is obtained from the overall energy balance of the reaction in the Center of Mass System (CMS):

$$E_0 = Q + E_K + E_{pot} + E^* + E_{rot}, \tag{5.10}$$

where E_K and E_{pot} are, respectively, the sum of the kinetic and potential energies of all primary fragments, E_{rot} is total rotational energy and Q is the energy balance between the entrance channel and the final distribution of residues. Finally, E^* represents the total excitation energy available for all the primary fragments. The excitation energy is distributed among the residues according to their mass number:

$$E_i^* = \frac{E^* A_i}{A}, \tag{5.11}$$

where A_i and A are the mass numbers of the fragment and the whole system, respectively. At the end of the third phase of the reaction in the HIPSE model, a distribution of residues defined by their mass number, charge, position, momentum, angular momentum and excitation energy (A_i, Z_i, $\mathbf{R}_i$, $\mathbf{P}_i$, $\mathbf{L}_i$, E_i^*) is defined. The secondary decays on the set of primary fragments are performed by the statistical sequential evaporation code GEMINI [110].

The HIPSE model has three freely adjustable parameters: α_a, x_{tr}, and x_{coll}, which depend only on the incident beam energy. Their energy dependence and the resulting values for beam energy, $E_B = 10$, 25, 50 and 80 MeV/u are listed in Table 5.2 [111].

Table 5.2: Values of HIPSE adjustable parameters as determined by Lacroix [111] for energy 10, 25, 50 and 80 MeV/u. Extrapolated values to 140 MeV/u and interpolated values for 64 MeV/u used in our calculations are also shown.

Beam energy (MeV/u)	α_a	x_{tr}	x_{coll}
10	-0.10	0.60	0.00
25	0.10	0.45	0.02
50	0.20	0.30	0.05
80	0.25	0.25	0.10
140	0.55	0.09	0.18
64	0.22	0.27	0.06

The parameter values used in our calculations for ^{86}Kr at 64 MeV/u were interpolated using a second order polynomial function and the results are listed also in Table 5.2. For the ^{40,48}Ca and ^{58,64}Ni projectiles at 140 MeV/u, we used the extrapolation by second order polynomial (α_a and x_{coll}) and the exponential decay function (x_{tr}) resulting in values listed in Table 5.2.

The results of the HIPSE calculations at 140 and 64 MeV/u for ^{40,48}Ca, ^{58,64}Ni and ^{86}Kr projectiles on Be and Ta targets, are insensitive to the choice of α_a parameter because the energy available in the center of mass frame is always much larger than the value $V^{Froz}_{A_T A_P}(r = 0)$ in Equation (5.6). The nucleon exchange rate, x_{tr}, and fraction of nucleon-nucleon collisions, x_{coll}, parameters, on the other hand, set the overall distribution of the excitation energy of the residues.

Since the HIPSE model requires three adjustable parameters whose values are beam energy dependent, its predictive power is considerably larger as compared to that of the geometrical AA model. It has been applied to the multifragmentation data from central collisions of ^{129}Xe+$^{\rm nat}$Sn measured at 32, 39, 45 and 50 MeV/u [112], ^{58}Ni+^{58}Ni measured at 32 to 90 MeV/u [113]. Until this study the HIPSE model had not been applied extensively to the peripheral collisions at beam energy higher than 100 MeV/u [114]. This investigation provided a test of the HIPSE model, which uncovered some unexpected deficiencies of the model, as will be discussed in Section

5.3 and 5.6.

5.1.3 Antisymmetrized Molecular Dynamics

From the many microscopic models available today to simulate the nuclear collisions, the Antisymmetrized Molecular Dynamics (AMD) model was used to compare to our experimental projectile fragmentation data. As the most sophisticated model used in our study it describes the nuclear reaction at the microscopic level of interactions of individual nucleons. The AMD model has a potential to mimic all reaction processes involved in the complex heavy-ion collisions. This investigation also represents one of the first attempts to use the AMD model in a study of projectile fragmentation reactions at 140 MeV/u [115].

The AMD model developed by A. Ono and H. Horiuchi [116] is, an antisymmetrized version of a molecular dynamics model. The original version of AMD [117] contains some quantum features, like the use of the wave functions and a correct treatment of antisymmetrization, plus the effect of nucleon-nucleon collisions. The version of the AMD used in this work has been improved by incorporating the advantages of other microscopic models such as the time-dependent Hartree-Fock (TDHF) theory and the Boltzman-Uehling-Uhlenbeck (BUU) equation [116]. Implementation of a mean field theory in a nuclear reaction model usually results in the improvement of the single particle description [118, 119], but the fragment formation description gets worse [116]. The authors of AMD attempt to overcome this conceptual difficulty by incorporating quantum branching [120].

AMD is a special case of the time-dependent variational theory [121]. The AMD wave function is given by a Slater determinant of Gaussian wave packets for individual nucleons [116]:

$$\langle \mathbf{r}_1 \cdots \mathbf{r}_A | \Phi(Z) \rangle = \det \left[\varphi_{\mathbf{Z}_i}(\mathbf{r}_j) \chi_{\alpha_i}(j) \right], \tag{5.12}$$

where the wave functions in spatial coordinates are expressed as:

$$\langle \mathbf{r}|\varphi_{\mathbf{Z}}\rangle = \left(\frac{2\nu}{\pi}\right)^{3/4} \exp\left\{-\nu\left(\mathbf{r} - \frac{\mathbf{Z}}{\sqrt{\nu}}\right)^2 + \frac{1}{2}\mathbf{Z}^2\right\} \tag{5.13}$$

and χ_α is the spin and isospin part of the wave function. The many-body state, $|\Phi(Z)\rangle$, is parameterized by a set of complex variables $Z \equiv \{\mathbf{Z}_1, \cdots, \mathbf{Z}_A\}$, with A being the total number of nucleons in the system. The width parameter, ν, is treated as a constant parameter in AMD, while the complex centroid, $\mathbf{Z}$, is treated as a dynamical variable. The real part and the imaginary part of $\mathbf{Z}$ correspond to the centroids of the position and the momentum respectively [116], therefore the ν parameter defines the balance of the uncertainties of the position and the momentum, having a minimum given by the Heisenberg uncertainty principle. In the AMD calculations $\nu = 0.16$ fm^{-2} was chosen in order to reproduce the ground state energy of the light nuclei.

An effective two-body nuclear interaction is utilized in the AMD Hamiltonian:

$$H = \sum_{i=1}^{A} \frac{\mathbf{p}_i^2}{2m} + \sum_{i<j} v_{ij}, \tag{5.14}$$

where m is the nucleon mass and v_{ij} is the effective two-body force. For our calculations a modified Gogny-type force (GOGNY-AS [122]) has been used with parameters listed in Ref. [116].

The time evolution of the centroids, Z, which parameterize the many-body wave function $|\Phi(Z)\rangle$, is determined by the time-dependent variational principle

$$\delta \int dt \frac{\langle \Phi(Z)|i\hbar\frac{d}{dt} - H|\Phi(Z)\rangle}{\langle \Phi(Z)|\Phi(Z)\rangle} = 0, \tag{5.15}$$

from which the classical Hamiltonian equation of motion for Z is derived. The equation of motion in AMD can be regarded as a generalization of the time-dependent cluster model (e. g., [123]). The frictional cooling method, derived from the equation of motion [116], is utilized to calculate the ground states of colliding nuclei.

The AMD wave function of Equation (5.12), as a single Slater determinant, does not contain any two-body correlations, except the implicit correlations given by the mean field and the antisymmetrization. In order to describe nuclear collision, correlation beyond mean field is included in a more explicit way by considering nucleon-nucleon scattering in the dynamically evolving system. The two-nucleon scattering was introduced in order to improve description of the (multi) fragmentation reactions in the intermediate energy regime. It is simulated by changing the momenta of two nucleons when their centroids approach in spatial coordinates. The implementation of the nucleon-nucleon scattering in AMD is non-trivial because the wave packet centroids, Z, do not have a physical meaning due to the antisymmetrization procedure. In order to overcome this difficulty, physical coordinates $W \equiv \{\mathbf{W}_1, \cdots, \mathbf{W}_A\}$ are introduced, which have a physical meaning as the centroids of the nucleon wave packets [116]. The transformation from Z coordinates to W space is chosen such that it respects the Pauli exclusion principle (i. e., the inverse transformation from W to Z exists only if the Pauli principle is obeyed).

A typical two-nucleon scattering event is calculated as follows. Any two nucleons, i and j, in the system are scattered with a probability based on the differential cross section, $\mathrm{d}\sigma_{\mathrm{NN}}/\mathrm{d}\Omega$, of nucleon-nucleon collisions. The cross section, σ_{NN}, depends on the relative kinetic energy of the nucleons, the isospin and the environment surrounding the two scattering nucleons. Then, at every time step in solving the equation of motion for AMD, it is examined whether each pair of nucleons should make a stochastic collision based on the real part, $\mathbf{R}_i$ and $\mathbf{R}_j$, of the physical coordinates, W, and the probability of the scattering is determined by the overlap of the Gaussian wave packets of the two nucleons and their relative velocity. Once the two nucleons are allowed to collide based on the probability described above, their physical momenta, $\mathbf{P}_i$ and $\mathbf{P}_j$, are changed in the following way. First, the unit vector, $\mathbf{n}$, representing the scattering angle is chosen randomly based on the differential cross section, $\mathrm{d}\sigma_{\mathrm{NN}}/\mathrm{d}\Omega$. The spatial positions, $\mathbf{R}_i$ and $\mathbf{R}_j$, of the nucleons are not changed and the first guess

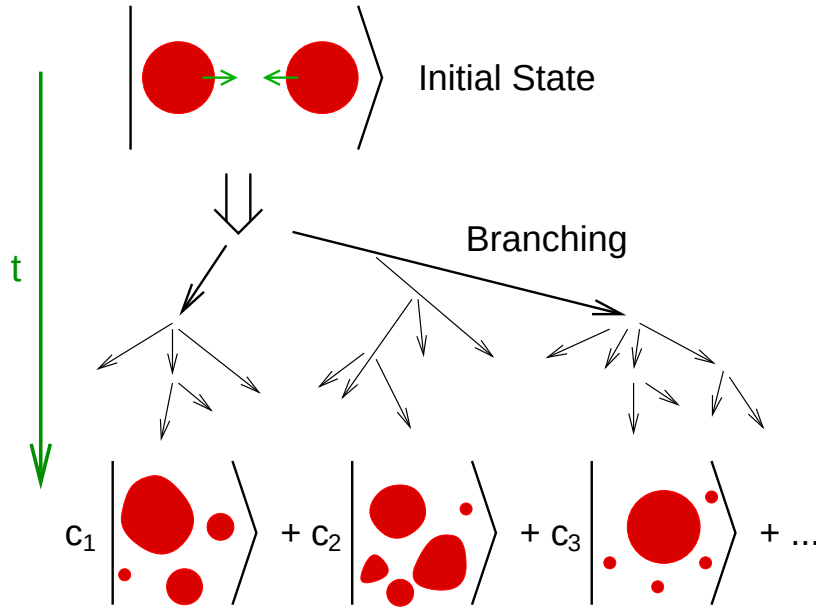

Figure 5.2: A schematic representation of the quantum branching for multichannel reactions [115].

of the final momenta in the final state, W', is calculated:

$$\mathbf{P}'_i = \frac{1}{2}\mathbf{P}_{CM} + P'_{rel}\mathbf{n}, \tag{5.16}$$

$$\mathbf{P}'_j = \frac{1}{2}\mathbf{P}_{CM} - P'_{rel}\mathbf{n}, \tag{5.17}$$

where $\mathbf{P}_{CM} = \mathbf{P}_i + \mathbf{P}_j$ and P'_{rel} is the relative momentum $(1/2)|\mathbf{P}_i - \mathbf{P}_j|$. Next, the final state W' is transformed to Z' coordinates. If the corresponding Z' solution does not exist, it means the calculated final state is Pauli blocked and the collision is discarded. If the corresponding Z' solution exists, the total energy, E', of the state, $|\Phi(Z')\rangle$, is calculated. Then energy conservation between the initial and the final states is required. If not fulfilled the next guess of the relative momentum P''_{rel} is taken from

$$\frac{P''^2_{rel}}{m} - \frac{P'^2_{rel}}{m} = E - E'. \tag{5.18}$$

The procedure is iterated until energy conservation is satisfied.

It is necessary to go beyond fluctuations introduced via nucleon-nucleon collisions

in order to better describe the multifragmentation data. Although a single Slater determinant is sufficient for the initial two nuclei and the fragments in each reaction channel, it is far from sufficient for the superposition of the final channel wave functions (see Figure 5.2). In such cases, one can expect that by solving the deterministic time evolution, one gets a final state which resembles one of the possible channels. In other cases, however, the obtained final state does not look like any of the channels. By introducing the quantum branching to AMD, the many-body state wave function, $|\Psi(t)\rangle$, which is evolving from the initial to the final state according to the Shrödinger equation, is expressed as an ensemble of AMD wave functions, $|\Phi(Z)\rangle$:

$$|\Psi(t)\rangle\langle\Psi(t)| \approx \int \frac{|\Phi(Z)\rangle\langle\Phi(Z)|}{\langle\Phi(Z)|\Phi(Z)\rangle} w(Z,t)\mathrm{d}t, \tag{5.19}$$

where the right hand side is the statistical density operator of the ensemble and $w(Z,t)$ represents the weight of the state, $|\Phi(Z)\rangle$, at time, t. The approximation in Equation (5.19) neglects the off-diagonal terms which are expected to have negligible contributions [116]. Although different channels may interfere, it is impossible to perform the numerical calculations by keeping all of the interference. It should be noted that the time evolution is solved independently for each channel. Namely, the state is decomposed into independent branches of channels, which is called quantum branching.

The ground states of ^{40,48}Ca, ^{58,64}Ni, and ^{86}Kr projectiles and ^{9}Be target were prepared by applying the frictional cooling method to the AMD wave function [115]. The time evolution of the system in the AMD model is governed by the equation of motion, together with the stochastic nucleon-nucleon scattering. In order to compare the results of the AMD calculation to our inclusive experimental data, it is necessary to perform many collisions with different impact parameters, b. The range of impact parameters chosen for our AMD simulations was $0 \leq b \leq 14$ fm. The system dynamical evolution was followed up to time, $t = 150$ fm/c, when the produced clusters

of nucleons are spatially well separated. Then a simple coalescence algorithm applied to the physical positions of the centroids of the Gaussian wave packets can be used to define the primary fragments. The cut-off radius was chosen to be $r_{cut} = 5$ fm, meaning that if the centroids of two Gaussian wave packets are closer than 5 fm, they belong to one cluster. After applying this algorithm, all primary fragments i are defined with mass and charge number, momentum, angular momentum and total kinetic energy (A_i, Z_i, $\mathbf{P}_i$, $\mathbf{L}_i$, E_i). The excitation energy of a given residue is then defined with respect to the experimental binding energy taken from the Audi-Wapstra atomic mass evaluation [124]. These residues were then de-excited using the statistical decay code GEMINI [110].

Since the AMD calculation is extremely CPU-intensive, all calculations have been carried out at the High Performance Computing Center (HPC) at Michigan State University using a 64-processor cluster [125] running under OS Linux. For the ^{40}Ca+^{9}Be reaction one event requires approximately 6 CPU minutes. The computing time scales as A^3, where A is the total number of nucleons in the reaction. For the ^{40,48}Ca, ^{58,64}Ni, and ^{86}Kr projectiles on ^{9}Be target we gathered approximately 20,000 events/reaction. The AMD calculations have not been performed for the ^{181}Ta target, because the large number of nucleons, $A > 200$, results in an impractically long execution time to gather enough statistics.

A time evolution of four sample events (in center of mass frame of reference) with different impact parameters is shown in Figure 5.3 in the case of ^{86}Kr+^{9}Be reaction. The nuclear collision is represented by the nuclear density projection onto the reaction plane (labeled as 'Y' versus 'Z' in the bottom left pane of Figure 5.3). Each row of snapshots in Figure 5.3 represents the state of the reaction, simulated by the AMD model, at different time, $t = 0$, 30, 60, 90, 120, and 150 fm/c. The snapshots are grouped in four vertical columns representing events with four different impact parameters, $b = 0.57$, 4.14, 7.47, and 10.97 fm, from left to right. The area of each snapshot shown in Figure 5.3 is 40×40 fm^2. The projectile ^{86}Kr (large density

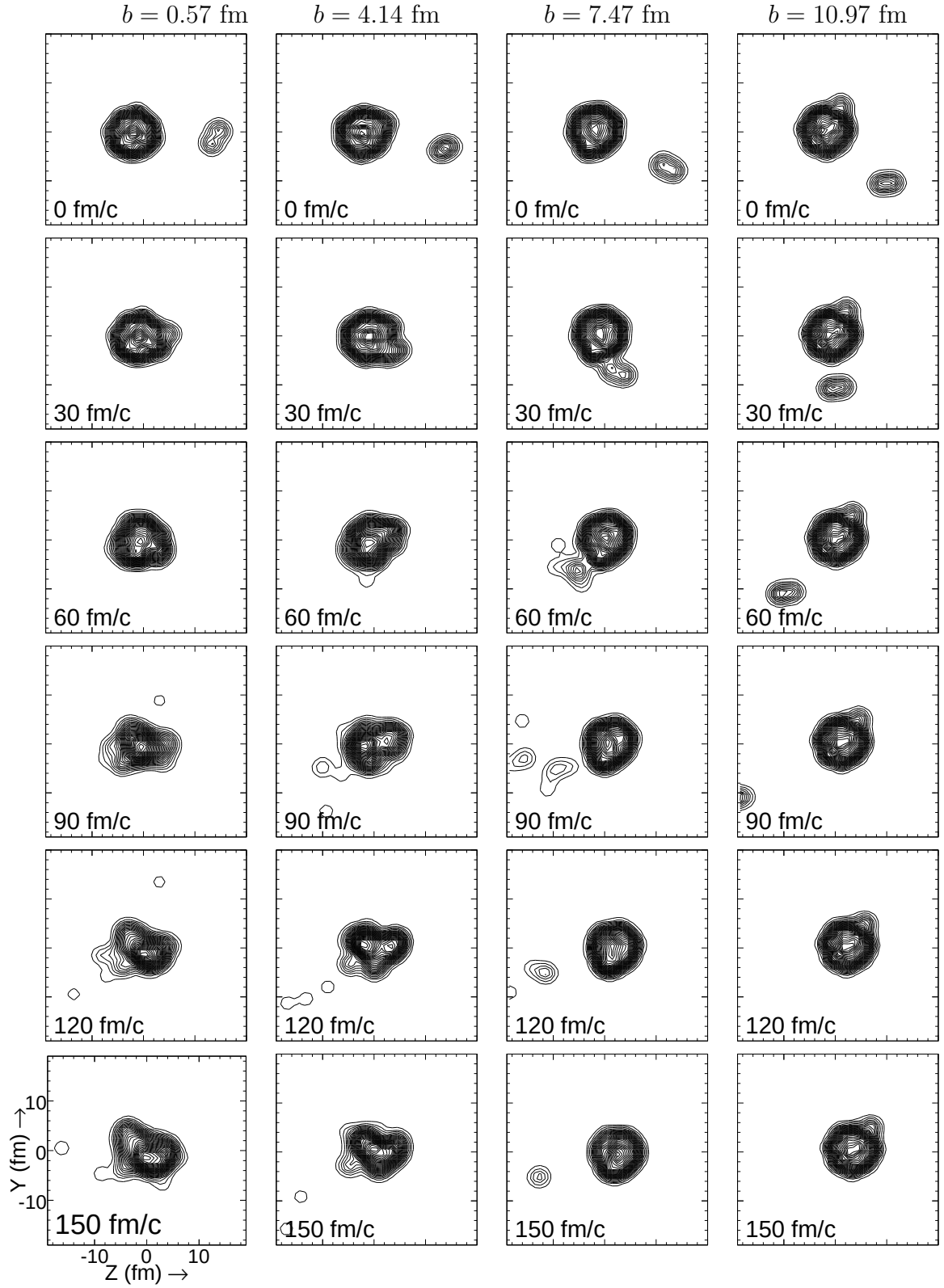

Figure 5.3: Examples of the time evolution of the density projected onto the reaction plane Y versus Z, where the projectile (from left) collides with the target (from right) nucleus along the Z axis. Snapshots from $t = 0$ to $t = 150$ fm/c for ^{86}Kr+^{9}Be collisions at 64 MeV/u are shown in vertical columns for impact parameters $b = 0.57$, 4.14, 7.47 and 10.97 fm. The area shown for each time step corresponds to 40×40 fm^2.

contours) and the target ^{9}Be (small density contours) nuclei are well separated for all impact parameters at $t = 0$ fm (first row in Figure 5.3). In the case of central collisions (2 leftmost columns) the target nucleus is absorbed by the projectile with few prompt nucleons emitted. For more peripheral reaction, $b = 7.47$ fm (third column from left), we see the abrasion of the projectile nucleus by the target. For extremely large impact parameter, $b = 10.97$ fm, (rightmost column) we observe no overlap of the projectile and target nuclei. Events of all impact parameters are summed up and normalized to the maximum impact parameter in order to be compared to the inclusive experimental data.

5.2 Primary fragment distributions

In order to directly compare the results of all three calculations (AA, HIPSE, and AMD) one must examine the properties of the primary fragments before sequential decays occur. Excitation energy of the residues will be discussed in Section 5.3. Here we compare the isotopic distributions of the primary fragments.

Figure 5.4 and 5.5 display the primary fragment distributions obtained in three different models for ^{40,48}Ca and ^{58,64}Ni primary beams on ^{9}Be target. The AA, HIPSE, and AMD model calculations are shown as dotted, solid, and dashed lines, for $13 \leq Z \leq 20$ isotopes for the Ca beams and $21 \leq Z \leq 28$ isotopes for Ni beams, respectively. In the case of projectile-like primary fragments of (up to approximately 10 nucleons removed), all three models predict very similar isotopic distributions. The Abrasion-Ablation model (dotted lines) calculates the primary residue distributions according to geometrical assumptions (Equation (5.2)), resulting in smooth and broad distributions, calculated over an extremely wide range of isotopes. The HIPSE and AMD models based on Monte Carlo techniques, on the other hand, create fragments over a limited range of cross sections proportional to the number of simulated events. The disagreements of the three reaction models grow with the number of removed

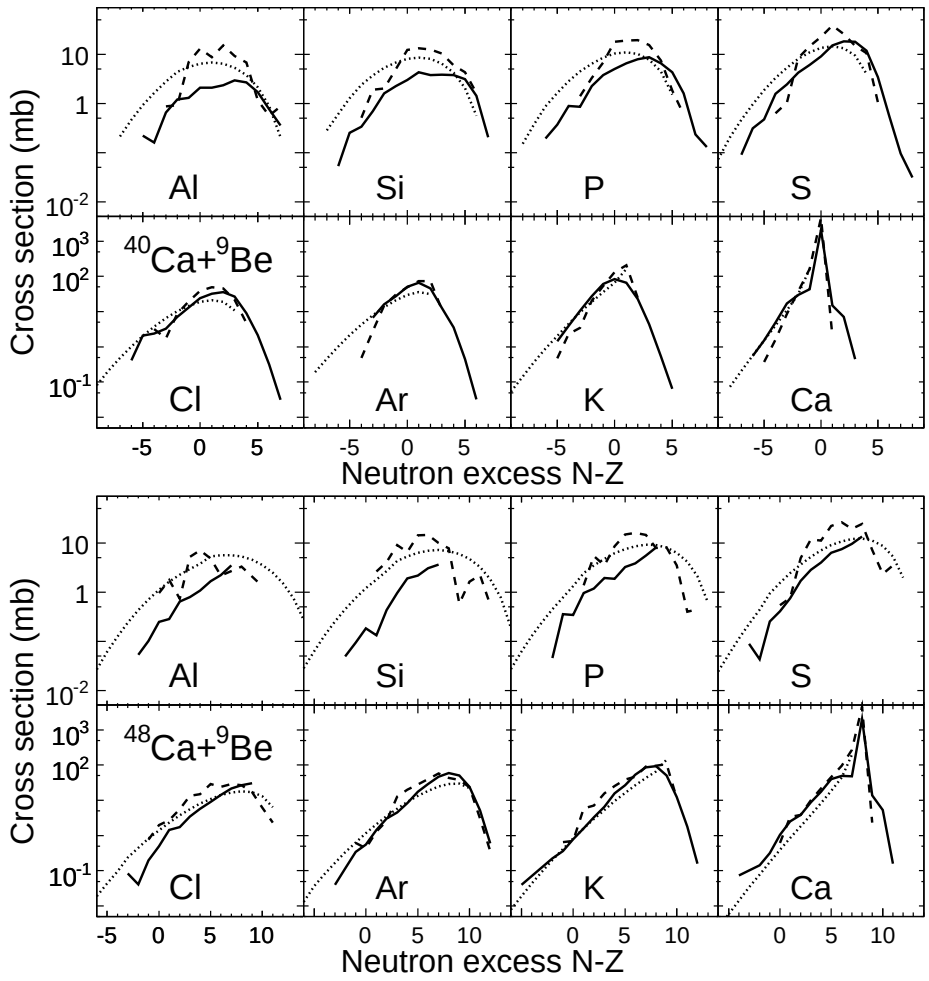

Figure 5.4: Primary fragment isotopic distributions for ^{40}Ca+^{9}Be (top) and ^{48}Ca+^{9}Be (bottom) reaction system plotted as a function of neutron excess, $N-Z$. Dotted, solid and dashed lines show calculations by AA, HIPSE and AMD models, respectively.

nucleons for all investigated reaction systems. Overall the isotopic distributions of primary fragments in the HIPSE calculation are wider than the ones obtained by the AMD model. Furthermore, clear trends of deviations between the HIPSE and AMD models are observed for the lightest primary fragments shown in Figure 5.4 and 5.5, when the AMD predicts systematically larger cross sections than the HIPSE calculation.

One should note that unlike the HIPSE or AMD models which follow the dynamics up to $t = 150$ fm/c, the AA model does not describe the dynamical evolution of the fragments in the collision. Since the primary fragments are created in an instantaneous

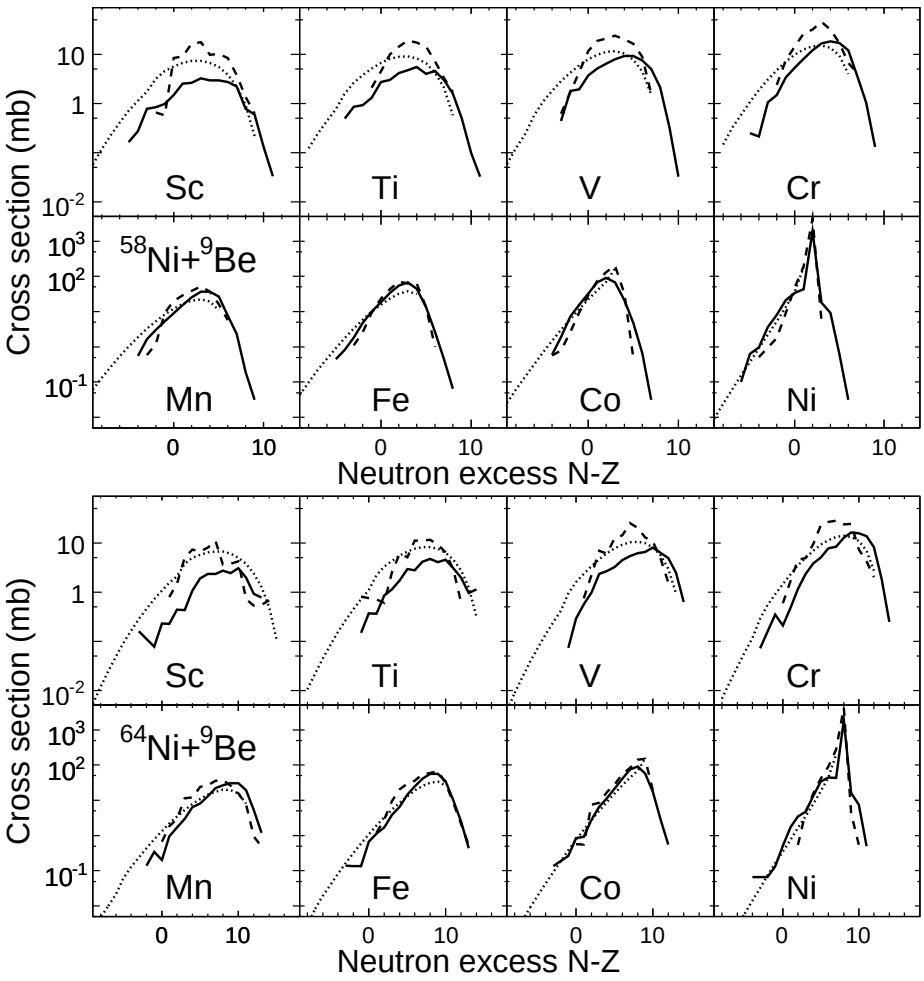

Figure 5.5: Primary fragment isotopic distributions for ^{58}Ni+^{9}Be (top) and ^{64}Ni+^{9}Be (bottom) reaction systems plotted as a function of neutron excess, $N-Z$. Dotted, solid and dashed lines show calculations by AA, HIPSE and AMD models, respectively.

geometrical abrasion the prefragments from the AA model could be formed at much earlier times.

5.3 Excitation energy

The excitation energy is one of the principal parameters describing the nuclear collisions, but it is very difficult to measure experimentally. These difficulties stem from the technical issues during experiments like: incomplete measurement of all particles in an experiment or problems associated with detection of neutrons, one of the most

dominant evaporation/de-excitation channels. In the case of our experimental data, we did not detect the entire spectrum of emitted particles, rather only the nuclides with velocity close to that of the projectile were measured. The mean excitation energy must be determined from the theoretical calculations by comparing measured observables.

In the case of the Abrasion-Ablation model the excitation energy and its fluctuations are parameterized with respect to the number of removed nucleons by Equations (5.3) and (5.4), respectively. The excitation energy of primary fragments used in our AA calculations is determined by fitting the K and S parameters to our experimental cross section data (Section 5.1.1).

The dynamical calculations used in our analysis (HIPSE and AMD), on the other hand, define all the residues with their excitation energies. The mean excitation energy for a given prefragment mass number, A_i, was calculated as an average over all events resulting in primary fragments with A_i for both the HIPSE and AMD models.

The average excitation energy per nucleon for prefragments produced in the fragmentation of ^{40,48}Ca and ^{58,64}Ni primary beams on ^{9}Be target is shown in Figure 5.6 as a function of the primary fragment mass number. The mean excitation energy used in the AA calculations is plotted as a dashed line. The mean excitation energy for a given prefragment mass number, A_i, calculated by the HIPSE and AMD models is shown by the black and cyan-shaded curves in Figure 5.6. The shaded regions represent the variance of the excitation energy distribution in all simulated events. In addition to these three models, we show a calculation by a single-particle, microscopic Boltzman-Uehling-Uhlenbeck (BUU) equation [126] (solid line).

The excitation energy per nucleon, $E^{\star}/A$, used in the AA model calculations (dashed line) has a monotonically increasing trend determined by the K parameter of Equation (5.3) and the number of removed nucleons from the projectile, ΔA. It results in extremely large $E^{\star}/A$ for lighter primary fragments (> 10 MeV), but the excitation energy for primary fragments in the vicinity of the projectile is lower than predicted

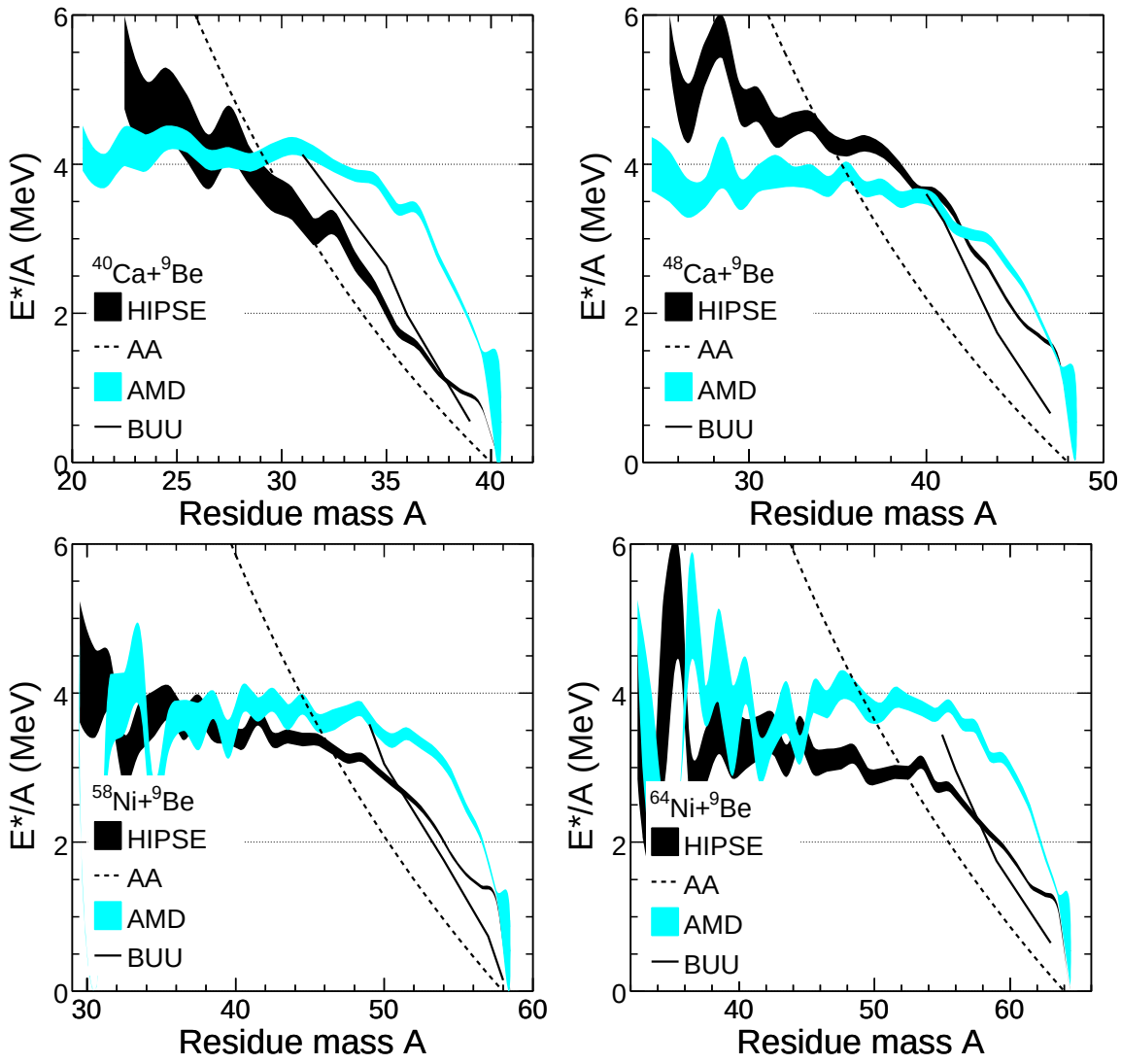

Figure 5.6: The mean excitation energy per nucleon, $E^{\star}/A$, as a function of the mass number of the primary fragments in different models. HIPSE and AMD calculations are shown for reactions of ^{40,48}Ca and ^{58,64}Ni projectiles on ^{9}Be target. The mean excitation energy used in our Abrasion-Ablation calculations is shown as a dashed line.

by all other models (HIPSE, BUU, AMD). In the case of dynamical models (HIPSE and AMD) we notice a rather sharp rise of the $E^{\star}/A$ with the number of removed nucleons up to approximately 4–5 MeV, when it remains roughly constant. The $E^{\star}/A$ calculated in the BUU model exhibits very similar trend as the HIPSE results for all reaction systems shown in Figure 5.6. The HIPSE and AMD model calculations differ mainly for residues close to the projectile ($\approx$ 0–10 abraded nucleons). The AMD calculation produces systematically higher excitation energy for this region of primary

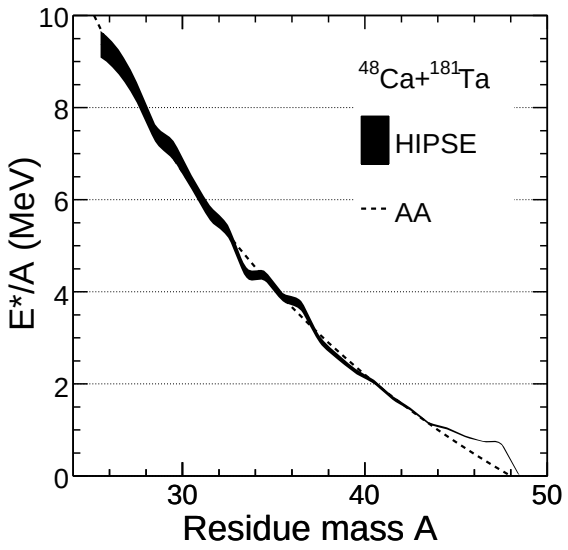

Figure 5.7: The mean excitation energy per nucleon, $E^{\star}/A$, as a function of the mass number of the primary fragments in different models. HIPSE calculation is shown for the ^{48}Ca+^{181}Ta reaction system. The mean excitation energy used in our Abrasion-Ablation calculations is shown as a dashed line.

fragments.

Plotting the $E^{\star}/A$ as a function of the primary fragment mass number inevitably mixed events with different impact parameters. The deterministic BUU calculations result in the mean mass and charge numbers of the primary fragment for a given impact parameter. This procedure makes the direct comparison with the AA, HIPSE and AMD models difficult. Nevertheless, we conclude that the BUU result in terms of average excitation energy per nucleon is similar to that of the HIPSE model for all reaction systems shown in Figure 5.6.

Figure 5.7 shows the mean excitation energy of primary fragments, created in the ^{48}Ca+^{181}Ta reaction, as a function of their mass number. Results of the HIPSE calculations are shown along with the excitation energy used in the AA model. Optimum excitation energy determined using the AA calculation in the case of ^{181}Ta and ^{9}Be target is the same. On the other hand, the $E^{\star}/A$ profile obtained by the HIPSE calculation is very different for the two target materials. In the case of ^{181}Ta target, the excitation energy saturates at much higher values ($\approx$10 MeV/u), not shown in

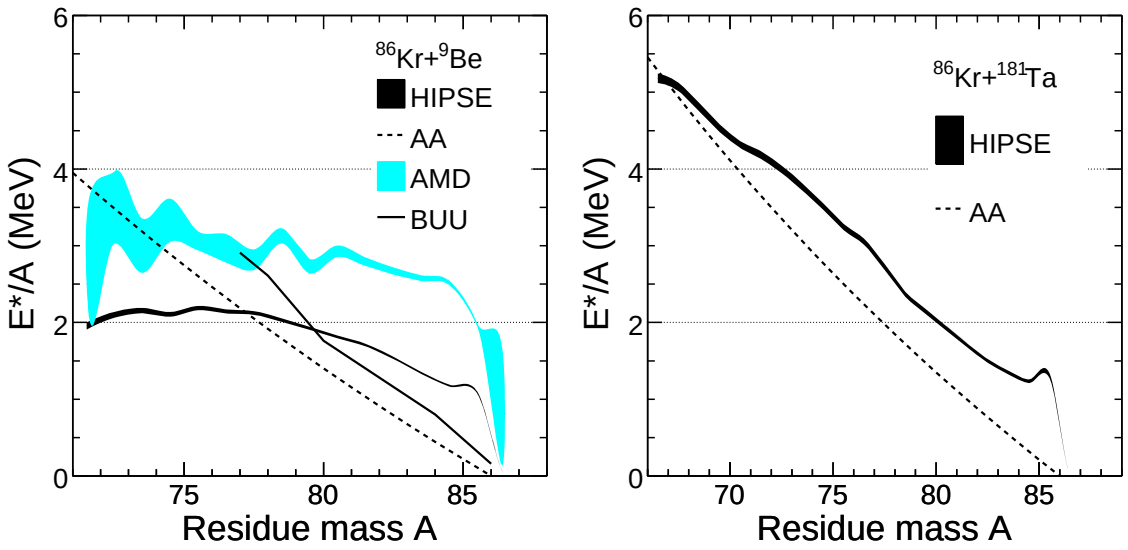

Figure 5.8: The mean excitation energy per nucleon, $E^{\star}/A$, as a function of the mass number of the primary fragment different models for ^{86}Kr beam and ^{9}Be and ^{181}Ta target materials. The HIPSE calculations are shown in black, the AMD results are presented in cyan and the mean excitation energy used in our AA model calculation is shown as a dashed line.

the plot because of poor statistics for the intermediate mass range fragments. The HIPSE calculation suggests a rather big difference between the excitation energy of primary fragments when using ^{9}Be and ^{181}Ta targets for ^{40}Ca and ^{58,64}Ni projectiles as well.

The mean excitation energy per nucleon calculated for ^{86}Kr projectile is compared to the values used by the AA model in Figure 5.8. Results for the ^{86}Kr+^{9}Be are shown in the left and ^{86}Kr+^{181}Ta in the right panel. The $E^{\star}/A$ used for the AA calculation (dashed line) is very similar (K = 18 and 19 MeV/ΔA, respectively) for both targets (^{9}Be and ^{181}Ta). Such K values are larger than those obtained in the lighter projectile systems ($K \approx$ 11–15 MeV/ΔA). On the other hand, the $E^{\star}/A$ predicted by the dynamical models is lower for ^{86}Kr reaction systems in Figure 5.8 than that of the NSCL reaction systems due to lower beam energy (64 MeV/u). The HIPSE simulation of ^{86}Kr+^{9}Be reaction produces very low excitation energy ($\approx$ 2 MeV) as compared to the AMD result ($\approx$ 3 MeV). The $E^{\star}/A$ calculated using the HIPSE model in the case of ^{86}Kr+^{181}Ta reaction is higher than the assumptions

used in the AA model calculations (especially for the heaviest prefragments). The saturation excitation energy per nucleon is approximately 6 MeV, which is lower than in the case of the NSCL reaction systems.

The HIPSE model predicts rather different excitation energy for reactions of all investigated projectiles with ^{9}Be and ^{181}Ta targets, which is in strict contrast with the AA model where we do not observe any differences in the excitation energy necessary to reproduce the final cross section distributions. Unfortunately, the AMD calculations could not be carried out for the reaction systems involving ^{181}Ta target, because of excessive CPU-time required.

5.4 Evaporation codes

The calculated primary fragment distributions (Section 5.2) cannot be compared directly to the experimental data, because the experimental observation of fragment is performed after hundreds of nanoseconds — orders of magnitude later than the prompt step, simulated by the nuclear reaction models (geometrical-cut Abrasion, HIPSE, and AMD). The (hot) primary fragments prepared by these three nuclear reaction models must be de-excited before comparing to the experimental data.

In our study, two different evaporation codes were used to calculate the final states. The analytic LisFus [106] code was used in conjunction with the AA model, and the GEMINI [110] code was applied to primary fragments generated by the HIPSE and AMD calculations.

5.4.1 LisFus evaporation code

LisFus [106] is a fusion-evaporation code developed in the framework of LISE++ [56]. The evaporation stage of the LisFus is treated in a macroscopic way on the basis of a master equation which leads to diffusion equations as proposed by Campi and Hüfner [127]. For each i-th point of excitation energy, E_i, distribution, P, of

parent nucleus, the LisFus model calculates the probabilities, W_k, for 8 possible decay channels (n, 2n, p, 2p, d, t, ^{3}He, α) and a daughter excitation energy distribution function, $D_k(E_i)$. With the above mentioned definitions the i-th segment of the parent excitation function is expressed as:

$$\int_{E_i}^{E_{i+1}} P(E)\mathrm{d}E = \sum_{k=1}^{8} W_k(E_i) D_k(E_i). \tag{5.20}$$

Masses of all parent and daughter nuclei are taken from Audi-Wapstra atomic mass evaluation [124]. Level density, $\rho(E^\star)$, is calculated by the phenomenological level density systematics based on the Fermi-gas model [128]:

$$\rho(E^\star) = \frac{1}{12}\sqrt{\pi} a^{-1/4} (E^\star - \Delta)^{-5/4} \exp\left[2\sqrt{a(E^\star - \Delta)}\right], \tag{5.21}$$

where a is the level density parameter and $E^\star$ is the excitation energy of the nucleus with mass number, A. Δ is the pairing energy correction expressed as $\Delta = \chi\frac{12}{\sqrt{A}}$, where $\chi = 0$, 1, or 2, for odd-odd, odd-even or even-even nuclei, respectively. The level density parameter, a, is expressed as:

$$a(E^\star, Z, N) = \left(\alpha A + \beta A^{2/3}\right) \cdot \left[1 + \delta W(Z,N) \frac{1 - \mathrm{e}^{-\gamma(E^\star - \Delta)}}{E^\star - \Delta}\right], \tag{5.22}$$

where $\delta W(Z,N)$ is a shell correction in the liquid drop model and α, β and γ are parameters taken to be 0.111, 0.107, and 0.46, respectively [128].

The analytical approach of this code allows one to calculate the cross sections of nuclei far from stability. Currently, the LisFus code [106] does not take into account the contributions of the angular momentum.

To demonstrate the importance of the evaporation code we show two Abrasion-Ablation calculations in Figure 5.9 for projectile-like fragments created in ^{40}Ca+^{9}Be and ^{48}Ca+^{9}Be reactions. The experimental fragmentation and pick-up cross sections are shown as open squares and triangles, respectively. The Abrasion-Ablation model

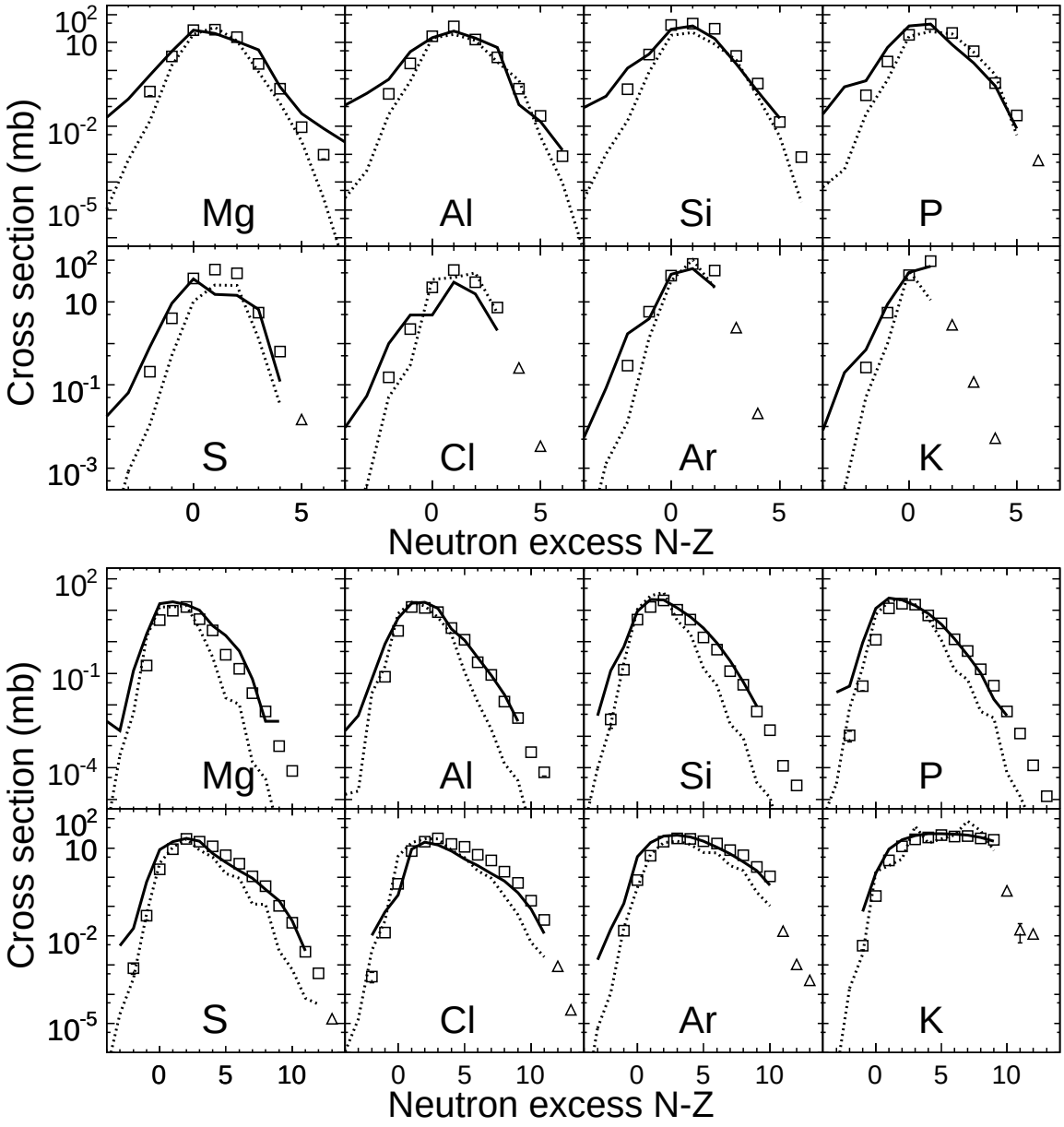

Figure 5.9: Measured isotopic cross section (open squares) distributions for ^{40}Ca+^{9}Be (top panel) and ^{48}Ca+^{9}Be (bottom panel) for $12 \leq Z \leq 19$ elements are compared to two Abrasion-Ablation calculations with the same excitation energy assumptions. Solid line shows a calculation by the ABRABLA code [104] and a dotted line displays LISE++ AA calculation. The average excitation energy is determined by Equation (5.3) with $K = 27$ MeV/u in both calculations.

calculation by the ABRABLA [104] code is shown as a solid line. The average excitation energy in this code is calculated with slope parameter of Equation (5.3), $K = 27$ MeV/ΔA which reproduces the high energy projectile fragmentation cross sections very well [129]. This calculation is compared to LISE++ AA code with $K = 27$ MeV/ΔA shown as a dotted line in Figure 5.9. We observe a fairly good reproduction of the experimental cross sections (especially in the peak of isotopic distributions) for the ABRABLA calculation (solid lines) for both reaction systems in Figure 5.9. The description of the isotopic distributions in the case of the ^{40}Ca+^{9}Be reaction system by LISE++ AA calculation with changed excitation energy assumptions ($K = 27$ MeV/u) is also reasonable. However, in the case of the ^{48}Ca+^{9}Be reaction system the LISE++ AA model shows large deficiencies for the more neutron-rich fragments ($N - Z > 5$) of $12 \leq Z \leq 17$ elements. The proton-rich ($N - Z < 0$) fragments, on the other hand, are described rather well. It must be noted that the Abrasion stage of the two models is identical and the evaporation code is based on the same principles (Campi and Hüfner [127]). The discrepancy between the two AA models is clearly pronounced in the case of neutron-rich projectiles (^{48}Ca and ^{64}Ni), while calculated isotopic distributions for the projectiles closer to the line of stability (^{40}Ca and ^{58}Ni) are comparable. Based on our previous discussion we conclude that the differences in the final cross section distributions between the LISE++ AA and HIPSE (AMD) models are caused by the very different decay codes used.

5.4.2 Statistical evaporation code GEMINI

The GEMINI code calculates the decay of a primary fragment by sequential binary decays. All possible binary decays from light-particle emission to symmetric division are considered. Monte Carlo technique is employed to follow all decay chains until the resulting products are unable to undergo further decay. For the purposes of the sequential decay calculations the excited primary fragments generated by the HIPSE and AMD calculations are taken as the compound nucleus [130] input of the GEM-

INI code. Every primary fragment is decayed as a separate event in the GEMINI calculation.

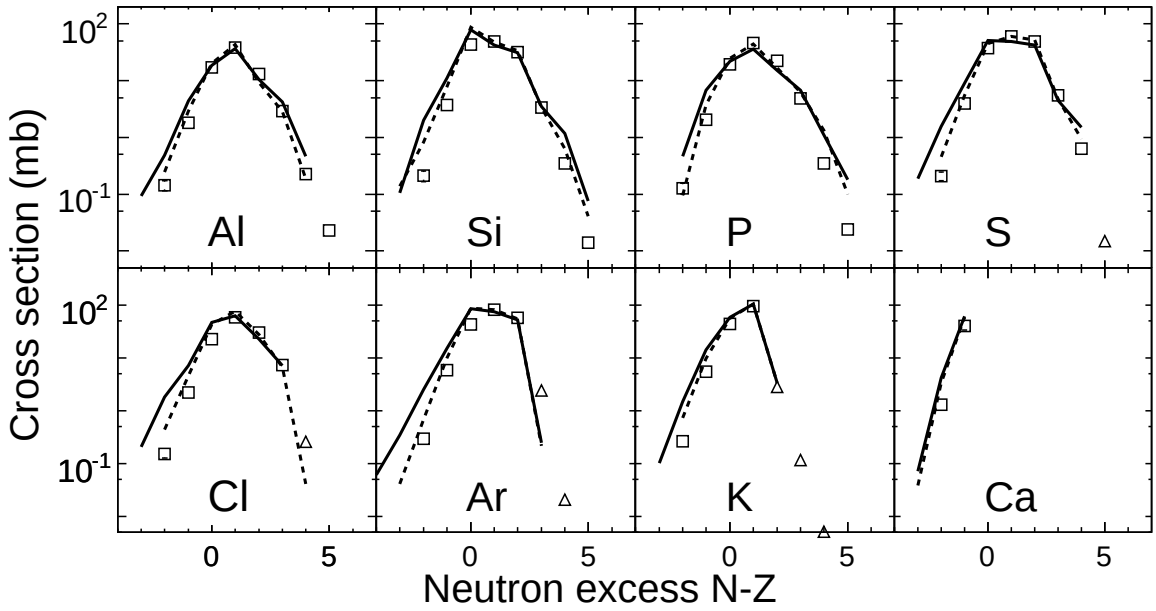

Figure 5.10: Influence of the level density parameterization on the final isotope distributions in ^{40}Ca+^{9}Be reaction. Open squares show the experimental fragmentation data and open triangles depict the pick-up reaction products. The AMD primary fragment distributions are decayed using GEMINI with level density parameter $a = A/8$ MeV^{-1} (dashed line) and $a = A/12$ MeV^{-1} (solid line).

For the evaporation of particles lighter than α-particle, the Hauser-Feshbach [131] formalism is applied. For binary divisions corresponding to emission of heavier fragments, the decay width is calculated using the formalism of Morretto [132]. The liquid drop model with shell corrections [133] was used to calculate the masses of all parent and daughter nuclei in the calculation. For all level densities, the Fermi gas [134] expression is assumed in the GEMINI calculation:

$$\rho(E^\star, J) = (2J+1)\left[\frac{\hbar^2}{2I}\right]^{3/2} \frac{\sqrt{a}}{12}\frac{\exp\left(2\sqrt{aE^\star}\right)}{E^{\star 2}}, \tag{5.23}$$

where J, I, and $E^\star$ are the spin, moment of inertia and excitation energy of the residual nucleus or saddle-point configuration, respectively.

The final isotope distributions are sensitive to the level density parameter, a.

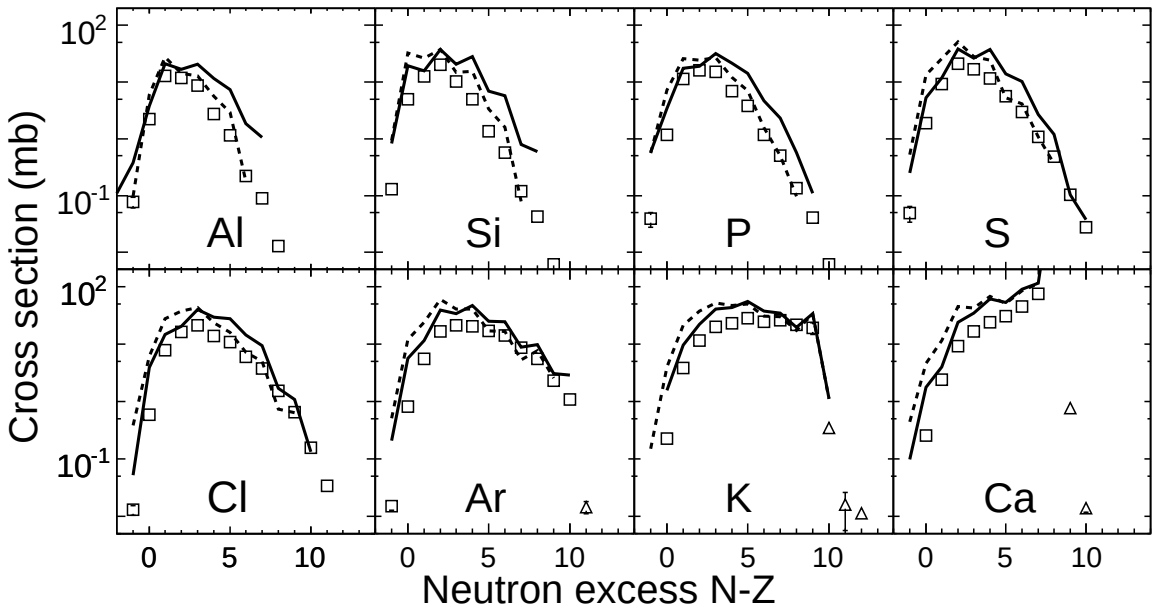

Figure 5.11: Influence of the level density parameterization on the final isotope distributions in ^{48}Ca+^{9}Be reaction. Open squares show the experimental fragmentation data and open triangles depict the pick-up reaction products. The AMD primary fragment distributions are decayed using GEMINI with level density parameter $a = A/8$ MeV^{-1} (dashed line) and $a = A/12$ MeV^{-1} (solid line).

To demonstrate this effect, two different primary fragment decay calculations for ^{40}Ca and ^{48}Ca beams and ^{9}Be target are shown as solid and dashed lines in Figure 5.10 and 5.11. The only difference between the two calculations is the level density parameterization. The solid lines are calculated using $a = A/12$ MeV^{-1} and the dashed lines depict calculations using $a = A/8$ MeV^{-1}. In the case of ^{40}Ca+^{9}Be reaction we see the two calculations with different level density parameter assumptions are nearly identical in the peaks of the isotopic distributions shown in Figure 5.10. Differences can be observed only in the tails of the distributions. On the contrary, calculations with different level density parameter assumptions for the ^{48}Ca+^{9}Be system, shown in Figure 5.11, differ much more. We clearly see a shift of the peak of the isotopic distributions for elements shown in Figure 5.11 towards the more neutron-rich isotopes in the case of $a = A/12$ MeV^{-1} as compared to $a = A/8$ MeV^{-1} calculation. The same conclusions are reached in the case of the ^{58}Ni projectile, where no shift of the isotopic distributions is observed. For the ^{64}Ni beam, shifts towards

the neutron-rich isotopes are clearly visible.

In the following discussions we choose $a = A/10$ MeV^{-1} for all GEMINI sequential decay calculations as a reasonable compromise between the two investigated cases ($a = A/8$ and $A/12$ MeV^{-1}).

5.5 Cross section distributions

The fragmentation production cross section is by far the most important experimental observable in the present experiments. In this section we are going to compare the experimentally determined reaction cross sections with the final fragment cross sections calculated by the AA, HIPSE and AMD reaction models in conjunction with the LisFus and GEMINI evaporation codes.

Figures 5.12–5.16 present the comparisons of the measured isotope cross section distributions with ^{40,48}Ca, ^{58,64}Ni and ^{86}Kr primary beams and the ^{9}Be target. Experimental fragmentation cross sections and pick-up (nucleon exchange) cross sections are shown as open squares and triangles, respectively. The calculations are shown with dotted, solid and dashed lines for AA, HIPSE, and AMD models respectively in Figure 5.12–5.16.

The Abrasion-Ablation model in LISE++ reproduces the experimental fragmentation cross sections extremely well, which is not surprising for the projectile-like fragments, because the excitation energy dependence on the number of abraded nucleons and its fluctuations have been adjusted for each reaction system individually. The cross sections calculated by the AA model for fragments lighter than half of the mass of the projectile describe the experimental data very well too. This feature is not expected because the AA model based on the geometrical cut of the projectile by the target nucleus, has clear deficiencies when describing more central collisions, and the excitation energy used for the intermediate mass prefragments ($\approx A_P/2$) is rather large (> 10 MeV/u). The simple geometrical AA model is very good at reproducing

the tails of the isotope distributions — this is especially clear in the case of ^{48}Ca and ^{64}Ni projectiles, where the experimental data extend to very neutron-rich isotopes.

The HIPSE and AMD are stochastic calculations, so the final cross section dynamical range depends on the number of simulated events, which was approximately 100,000 and 20,000 for the HIPSE and AMD models, respectively. Hence we are restricted to compare the final cross sections only in the peak region of the isotope distribution. For reference the total number of events detected for ^{64}Ni+^{9}Be reaction system was of the order of 10^7!

The isotope cross section distributions calculated using the HIPSE model are generally wider than the experimental ones for all investigated projectiles on ^{9}Be target (Figure 5.12–5.16). This effect is especially pronounced in the case of ^{86}Kr primary beam (Figure 5.16), when the excitation energy is clearly not sufficient to decay the residues on the neutron-rich side of the isotope distributions, resulting in cross section deficit in the peak regions (Ga–Se). Overall the peaks of the isotope distributions are described well for reactions of ^{40,48}Ca, ^{58,64}Ni and ^{9}Be by the HIPSE calculations. The overestimation of the experimental cross section in the tails of the isotope distributions may be caused by large fluctuations of the excitation energy in the HIPSE model. Unfortunately, the calculated cross sections of proton or neutron-rich fragments are very important when considering the predictive power of a model.

The experimental fragmentation cross sections of ^{40}Ca, ^{58}Ni, and ^{86}Kr primary beams (Figure 5.12, 5.14, and 5.16) are described rather well in the AMD model. The AMD model has larger deficiencies when describing the cross section distributions of fragments created in the reactions of more neutron-rich projectiles ^{48}Ca and ^{64}Ni plotted in Figure 5.13 and 5.15. These problems may be caused by problems of AMD describing the ground states of these projectiles [115]. The successful application of the AMD for the ^{40}Ca and ^{58}Ni projectiles is important, because the calculations were done without adjustments of the parameters. This finding is encouraging for the development of the AMD model to describe projectile fragmentation phenomena. AMD

has been known for its successful applications in more central, multifragmentation reactions [117].

Measured fragment isotope cross section distributions with ^{40,48}Ca, ^{58,64}Ni and ^{86}Kr primary beams and ^{181}Ta target are presented as open squares in Figure 5.17–5.21, along with the nucleon pick-up and exchange cross sections depicted by open triangles. The AA and HIPSE calculations are shown as dotted and solid lines, respectively.

The Abrasion-Ablation calculation reproduces the experimental fragmentation cross sections extremely well, as a consequence of the adjustment of the mean excitation energy and its fluctuations. We notice a surprisingly good description of the isotope distributions even for the lightest elements (B–O) for ^{40,48}Ca and ^{58}Ni projectiles. It should be noted that the light elements (B–Ne) for the ^{64}Ni primary beam (Figure 5.20) are described very poorly, as expected in a simple geometrical AA model.

The isotope cross section distributions calculated by the HIPSE model are overall broader than the experimental ones for both reaction systems involving ^{9}Be and ^{181}Ta target. The experimental cross sections for the lightest elements (B–O) are reproduced well for all projectile measured at the NSCL (Figure 5.17–5.20). The intermediate mass fragment ($\approx A_P/2$) cross sections in HIPSE, on the other hand, show rather large deficits (almost a factor of 10) with respect to the experimental data. This might be a direct consequence of the large excitation energy produced by the HIPSE model for the intermediate mass residues (as shown in Figure 5.7). The overall description of the isotope distributions gradually improves for higher Z isotopes. The projectile-like fragment cross sections are reproduced rather well by HIPSE, especially in the case of the ^{48}Ca and ^{64}Ni projectiles (Figure 5.18 and 5.20). Cross sections of fragments near the peak of the isotope distributions for all measured elements (Mn–Kr) in the ^{86}Kr+^{181}Ta reaction are reproduced very well using the HIPSE model calculations (see Figure 5.21). However, the experimental distributions measured in the case of

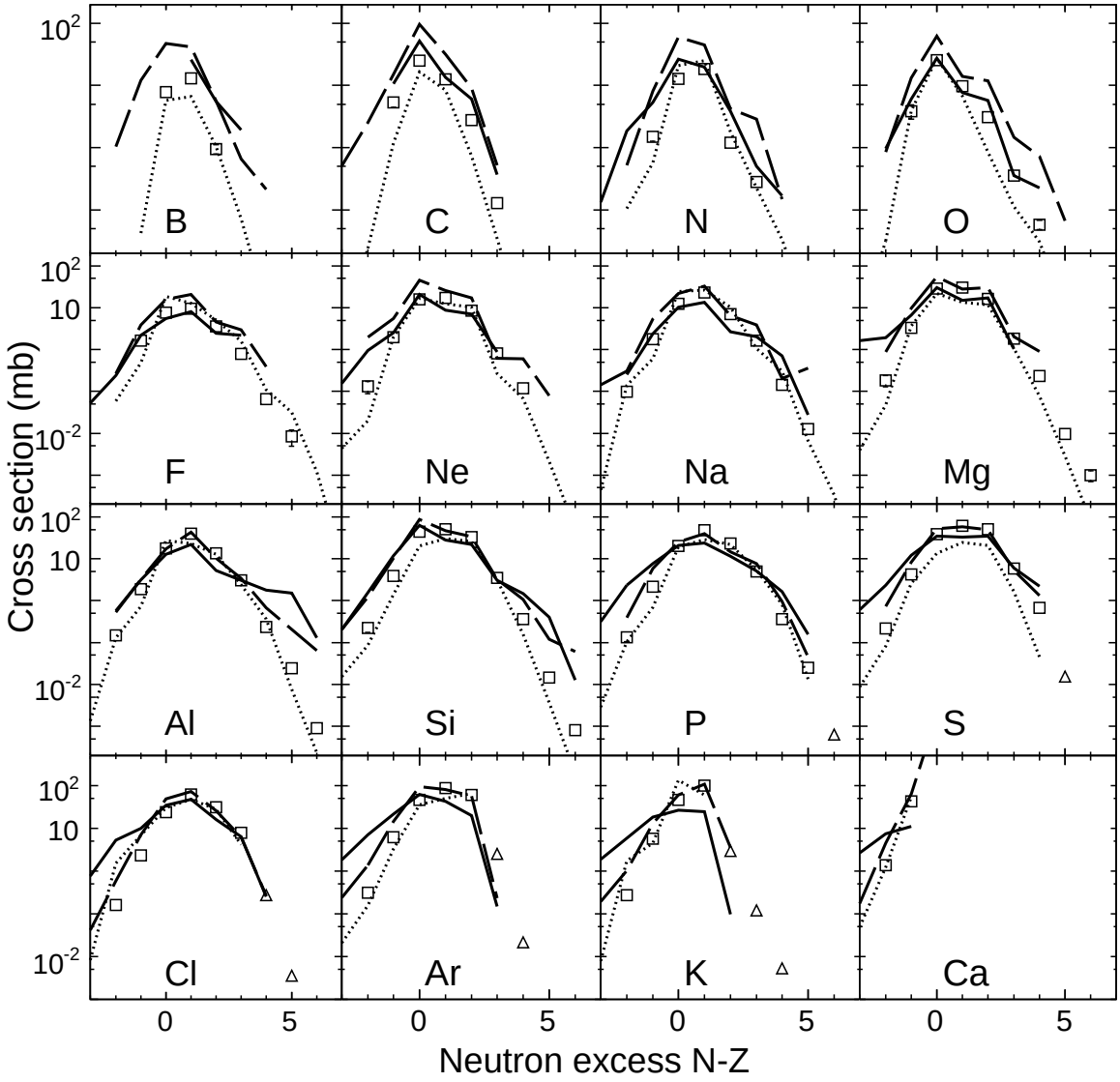

Figure 5.12: Fragmentation (open squares) and nucleon pick-up (open triangles) cross section isotopic distributions of ^{40}Ca+^{9}Be reaction are compared to the calculations by HIPSE (solid line), AMD (dashed line) and Abrasion-Ablation (dotted line) models.

^{86}Kr+^{181}Ta system contain only approximately 6 isotopes per element versus 12–16 for the ^{86}Kr+^{9}Be reaction. The dynamic range in cross section is only a factor of 10 versus many orders of magnitude (3–9) in the case of the ^{86}Kr+^{9}Be reaction. It is therefore impossible to draw conclusions about the tails of the isotope distributions. Nevertheless, the HIPSE calculation describes the cross sections of fragments in the peak of isotope distributions much better for the ^{86}Kr+^{181}Ta than the ^{86}Kr+^{9}Be reaction.

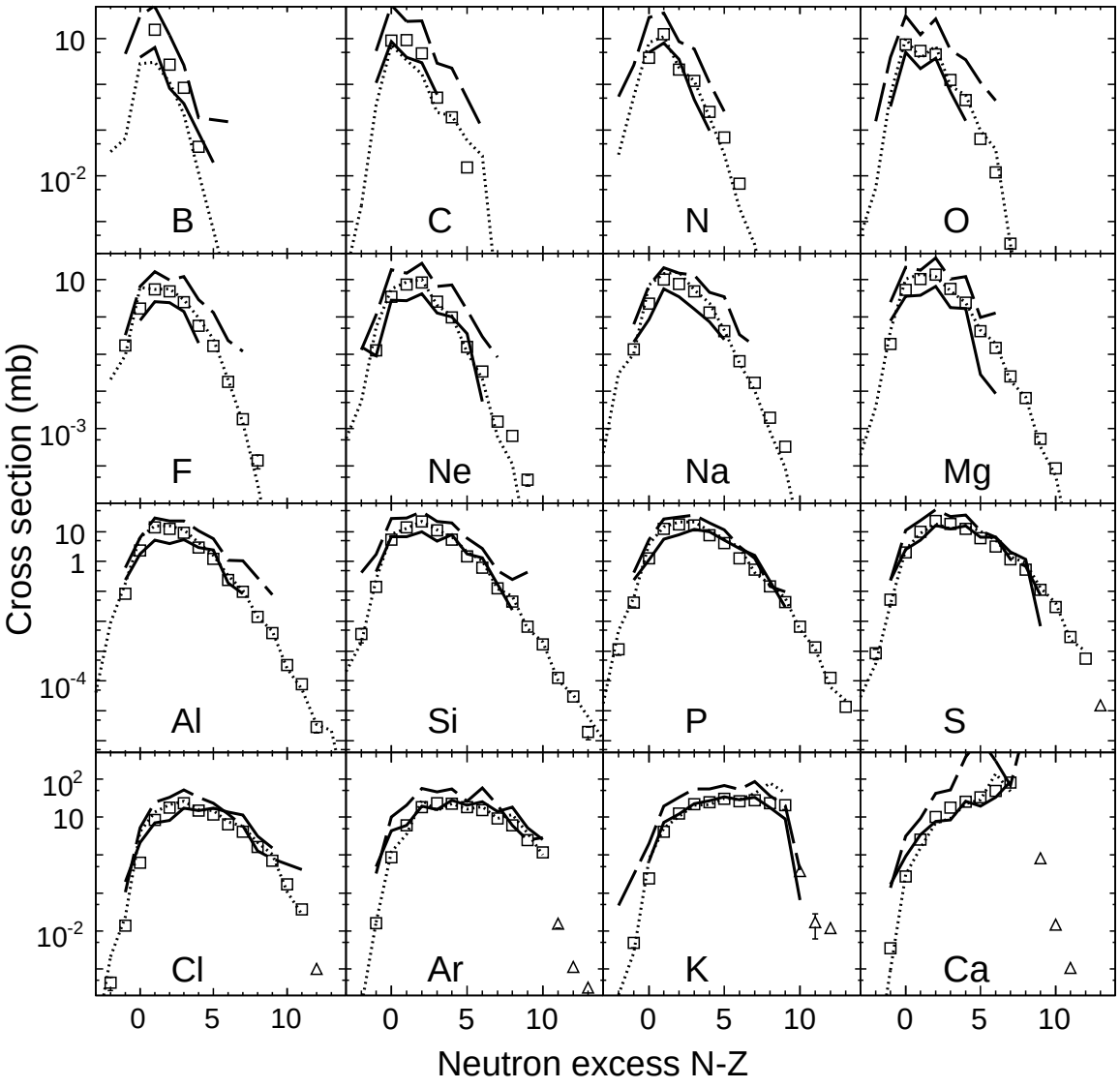

Figure 5.13: Fragmentation (open squares) and nucleon pick-up (open triangles) cross section isotopic distributions of ^{48}Ca+^{9}Be reaction are compared to the calculations by HIPSE (solid line), AMD (dashed line) and Abrasion-Ablation (dotted line) models.

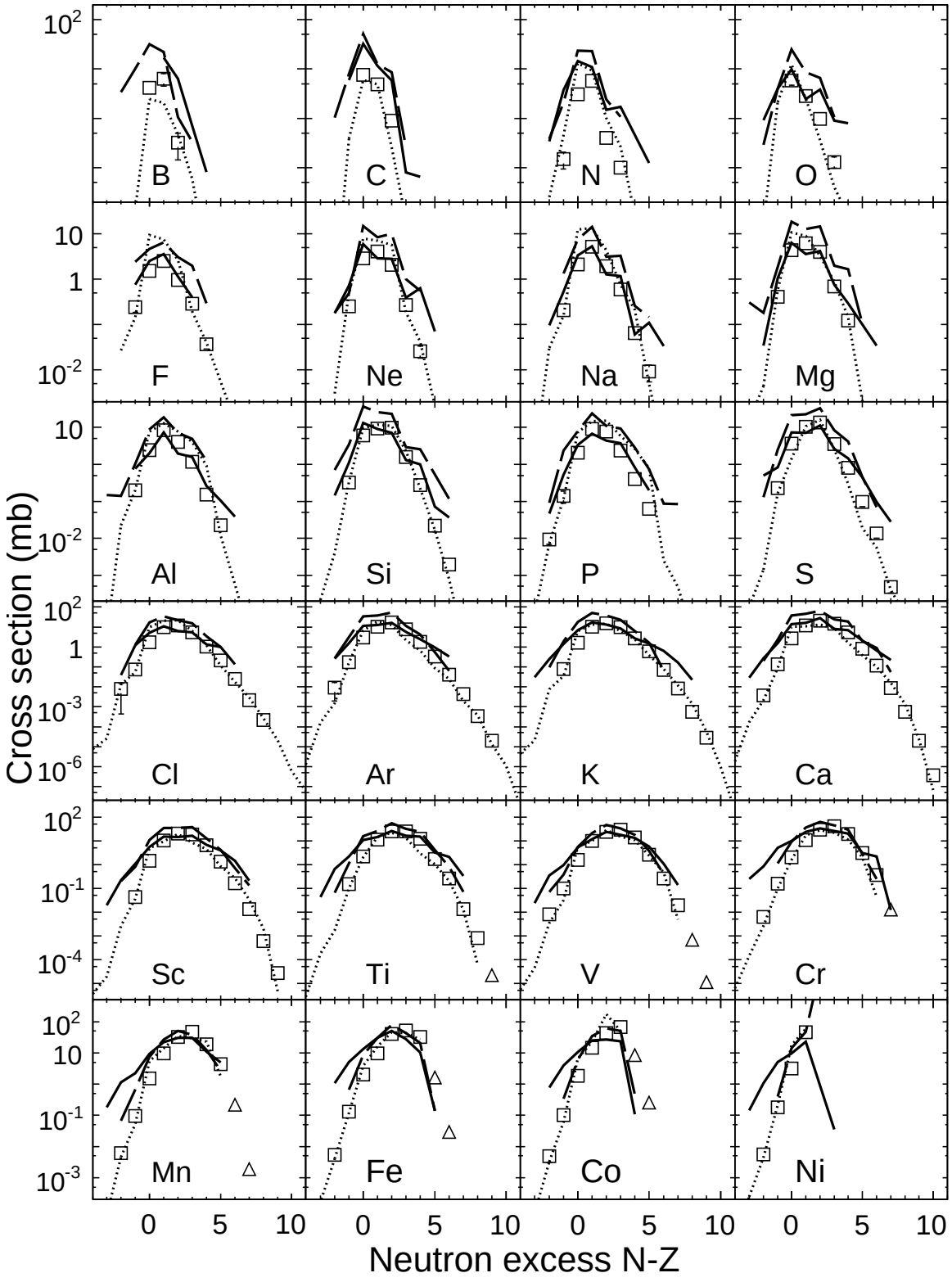

Figure 5.14: Fragmentation (open squares) and nucleon pick-up (open triangles) cross section isotopic distributions of ^{58}Ni+^{9}Be reaction are compared to the calculations by HIPSE (solid line), AMD (dashed line) and Abrasion-Ablation (dotted line) models.

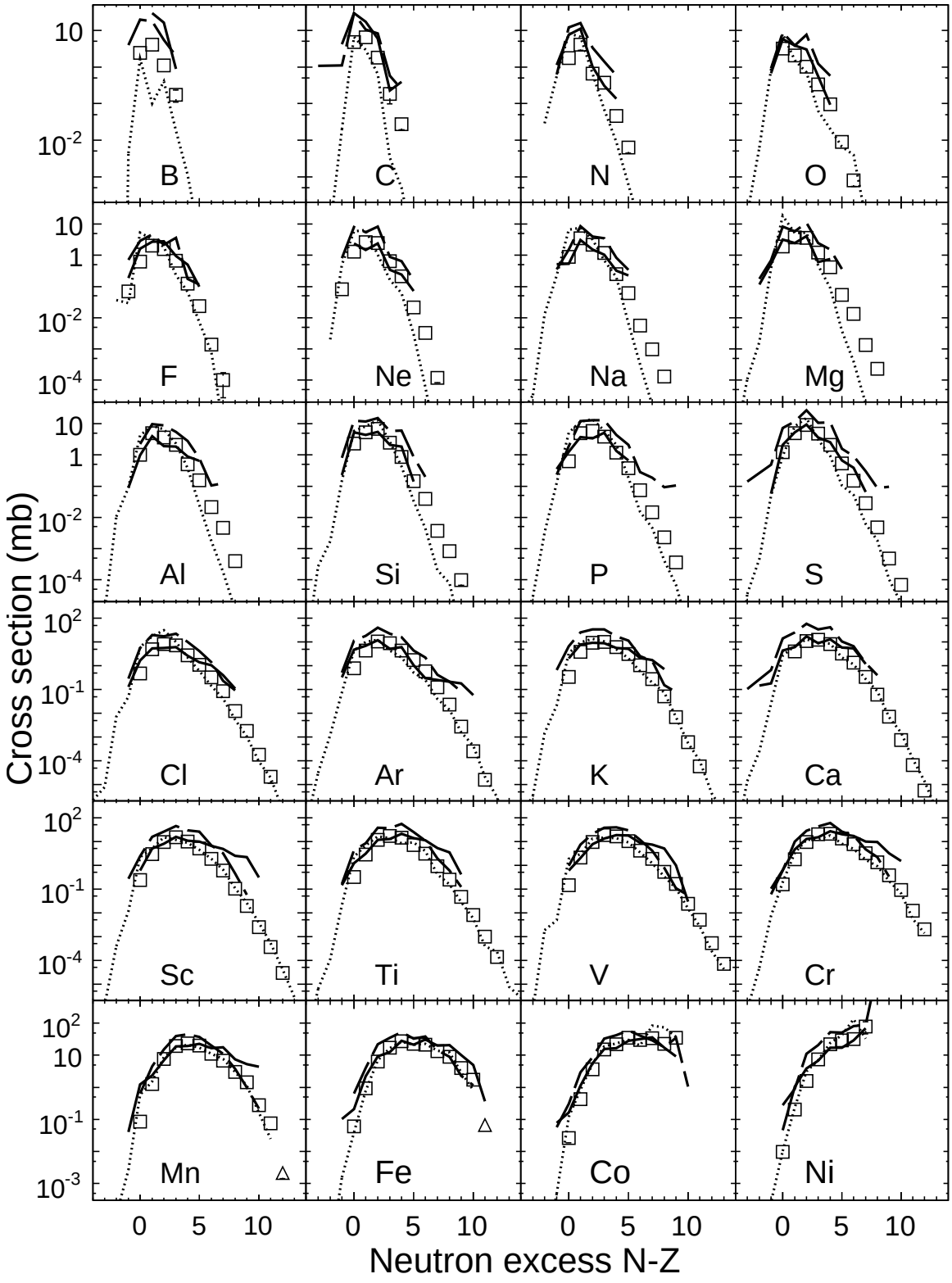

Figure 5.15: Fragmentation (open squares) and nucleon pick-up (open triangles) cross section isotopic distributions of ^{64}Ni+^{9}Be reaction are compared to the calculations by HIPSE (solid line), AMD (dashed line) and Abrasion-Ablation (dotted line) models.

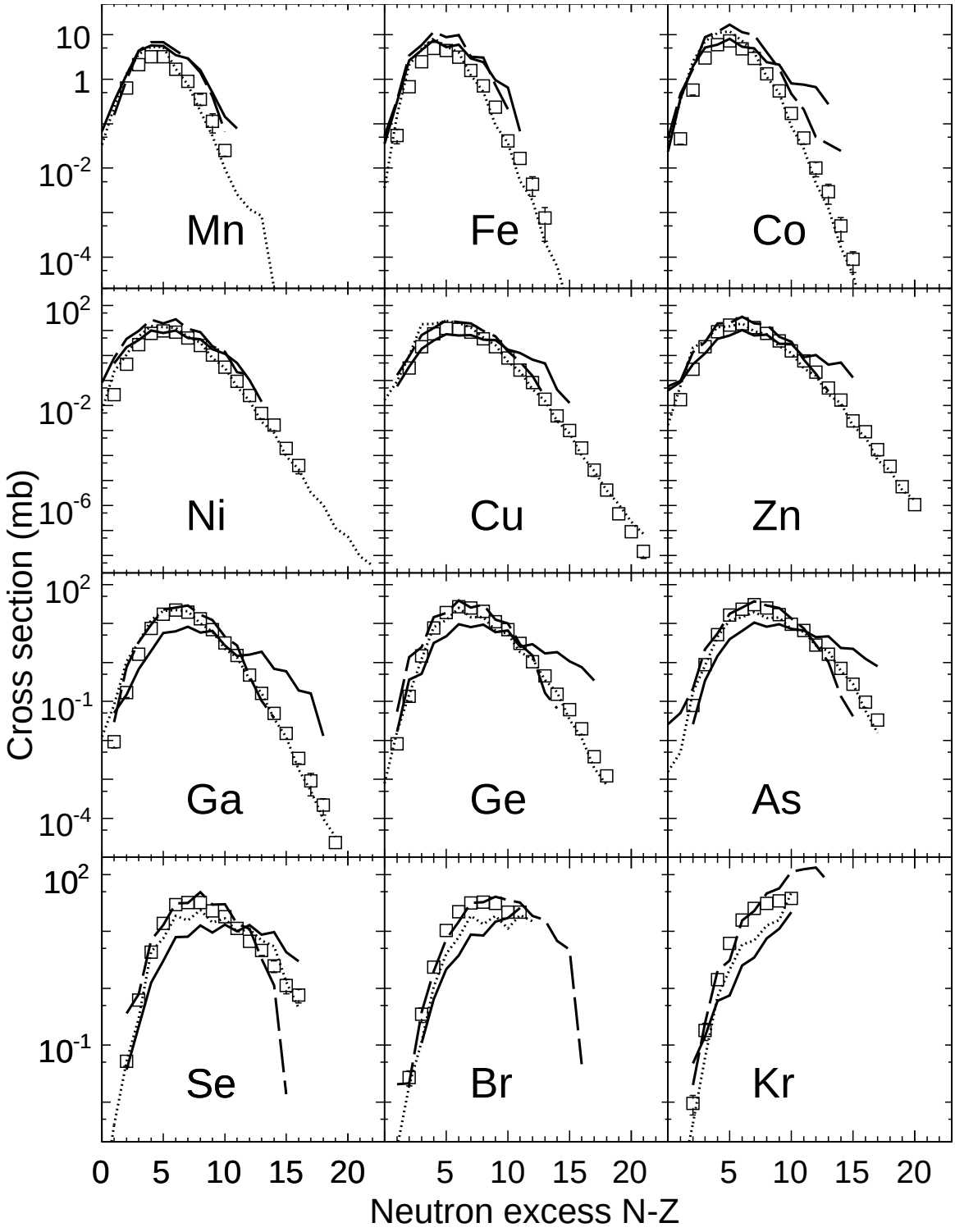

Figure 5.16: Fragmentation (open squares) cross section isotopic distributions of ^{86}Kr+^{9}Be reaction are compared to the calculations by HIPSE (solid line), AMD (dashed line) and Abrasion-Ablation (dotted line) models.

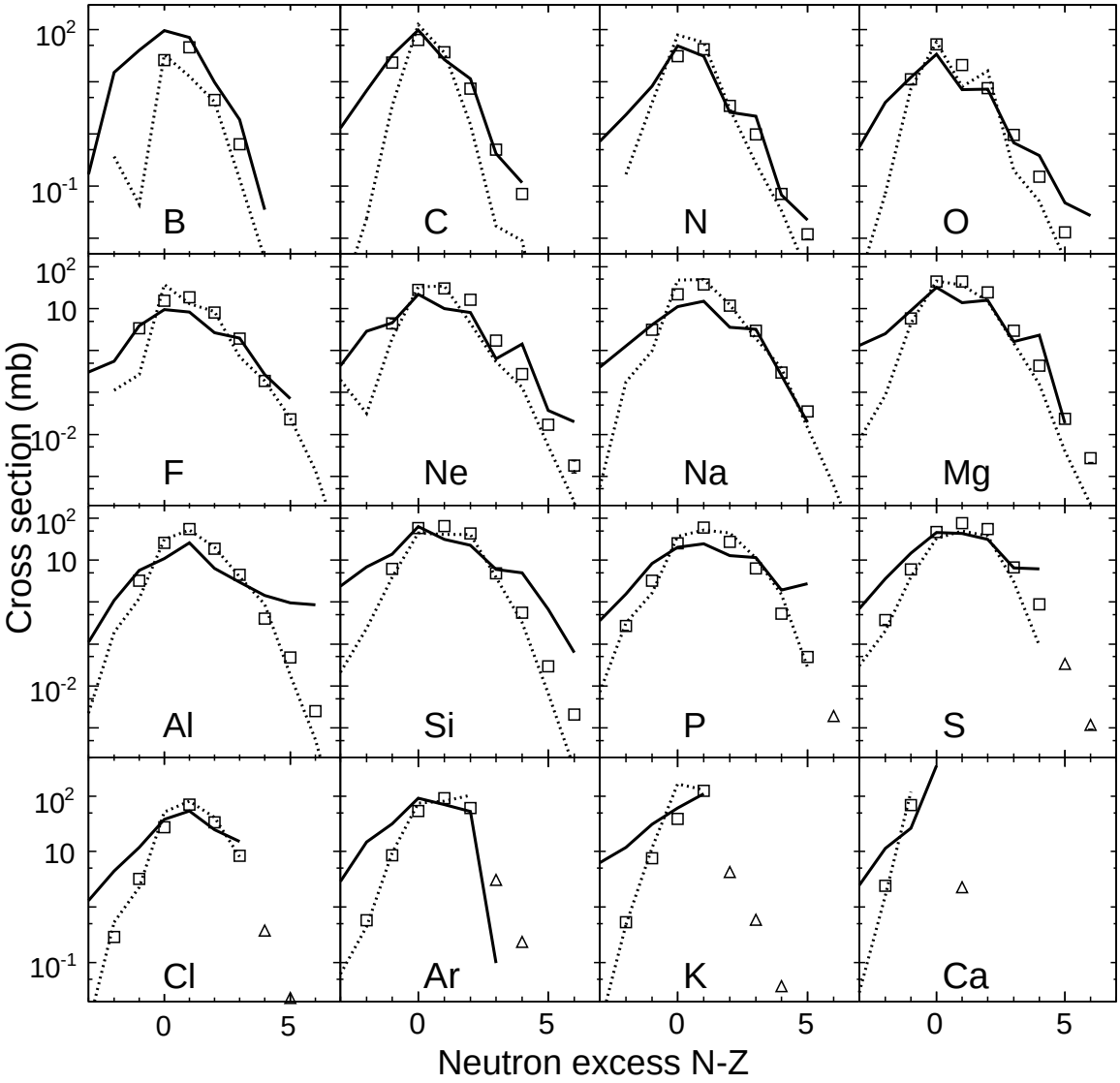

Figure 5.17: Fragmentation (open squares) and nucleon pick-up (open triangles) cross sections of ^{40}Ca+^{181}Ta are compared to the calculations by HIPSE (solid line) and Abrasion-Ablation (dotted line) models.

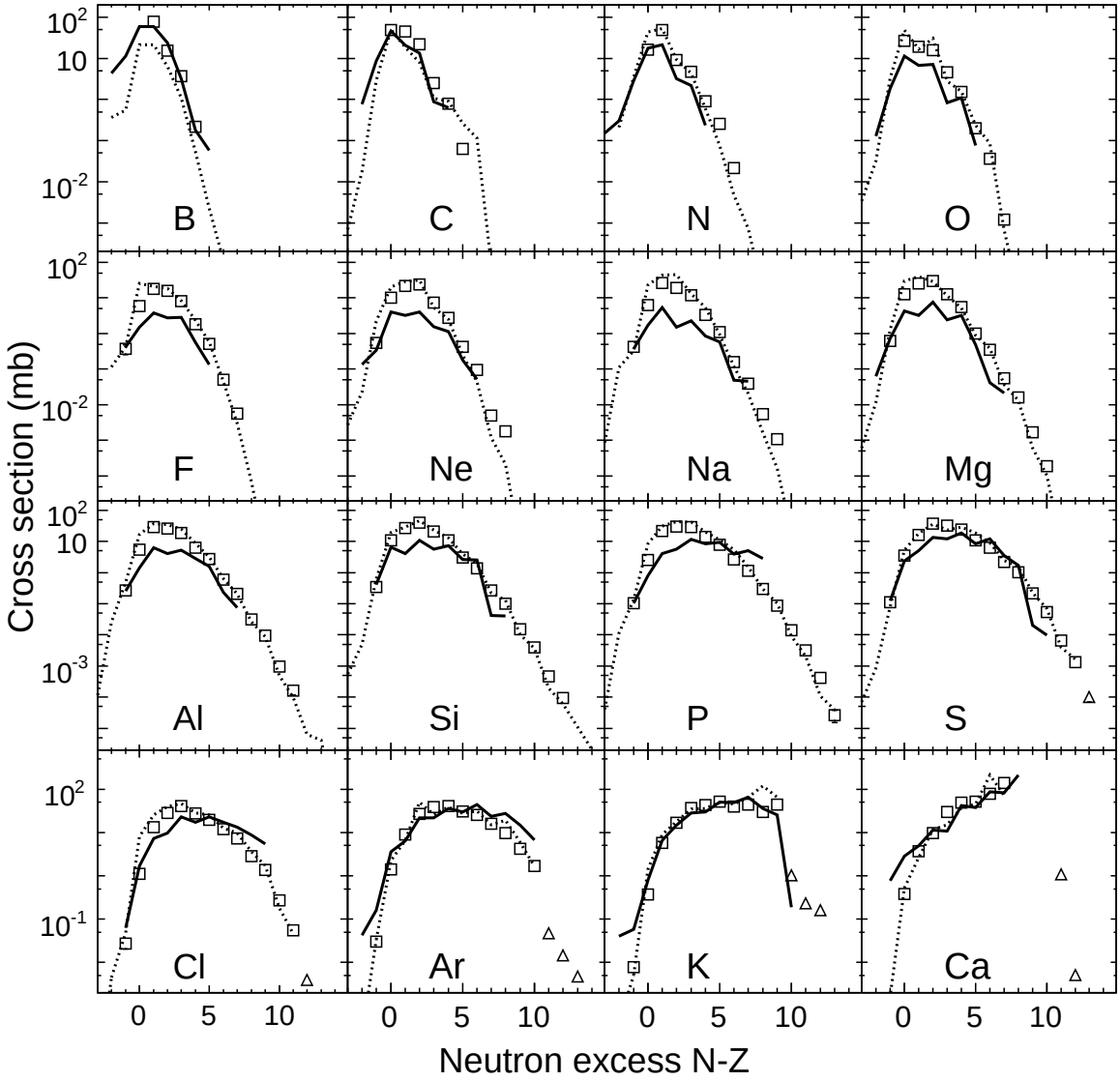

Figure 5.18: Fragmentation (open squares) and nucleon pick-up (open triangles) cross section isotopic distributions of ^{48}Ca+^{181}Ta reaction are compared to the calculations by HIPSE (solid line) and Abrasion-Ablation (dotted line) models.

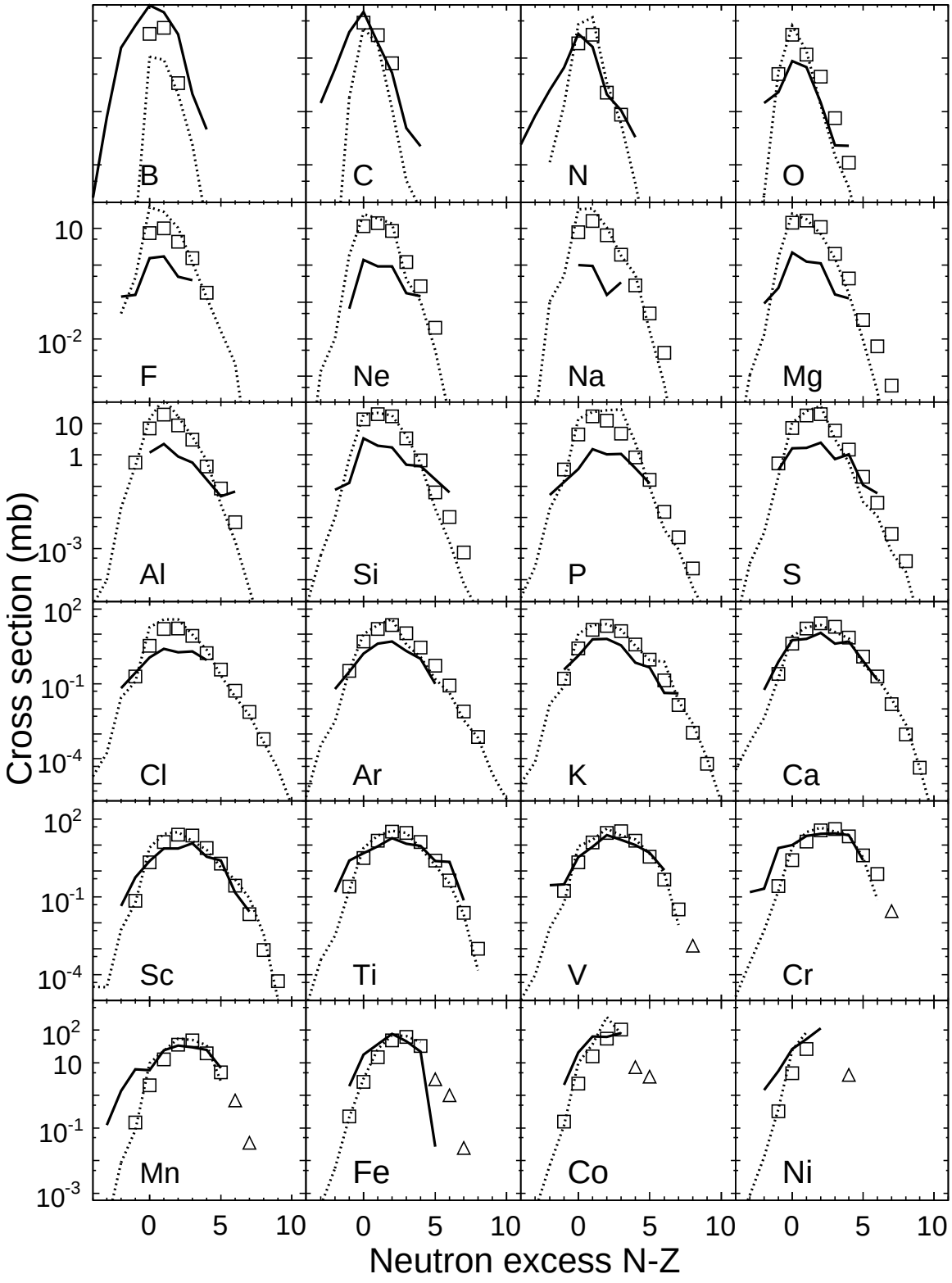

Figure 5.19: Fragmentation (open squares) and nucleon pick-up (open triangles) cross section isotopic distributions of ^{58}Ni+^{181}Ta reaction are compared to the calculations by HIPSE (solid line) and Abrasion-Ablation (dotted line) models.

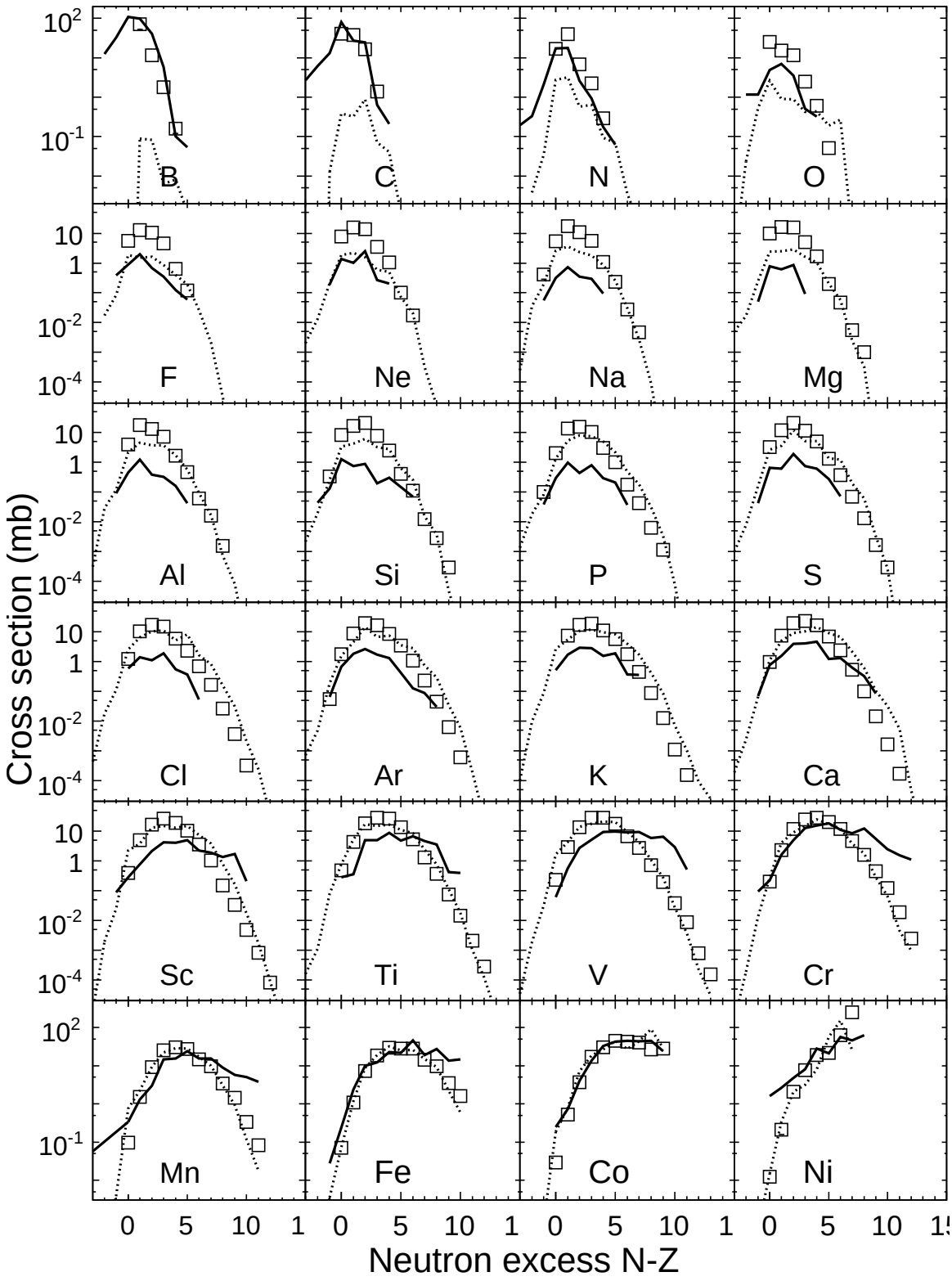

Figure 5.20: Fragmentation (open squares) cross section isotopic distributions of ^{64}Ni+^{181}Ta reaction are compared to the calculations by HIPSE (solid line) and Abrasion-Ablation (dotted line) models.

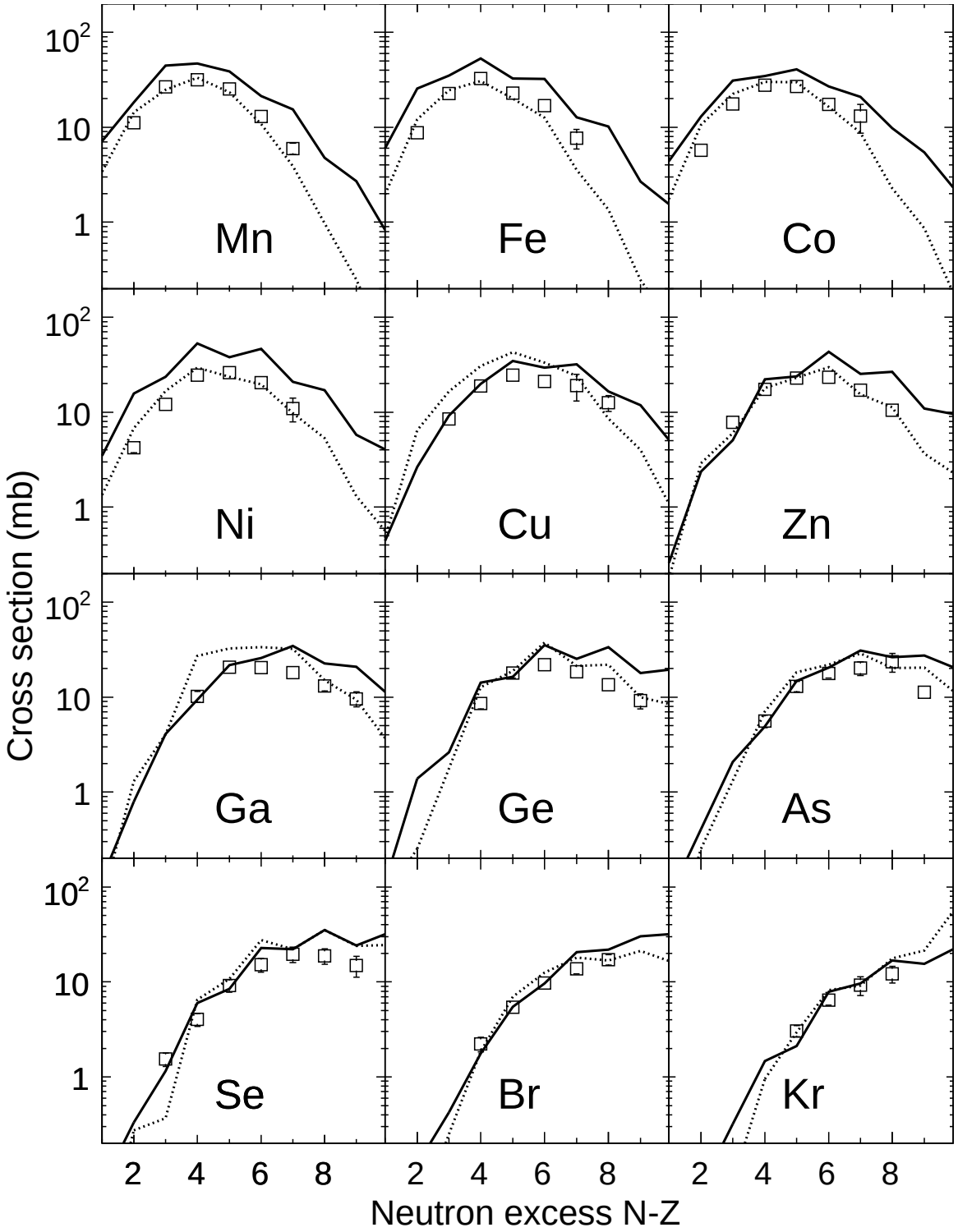

Figure 5.21: Fragmentation (open squares) cross section isotopic distributions of ^{86}Kr+^{181}Ta reaction are compared to the calculations by HIPSE (solid line) and Abrasion-Ablation (dotted line) models.

It must be noted that the overall shape and the peak position of the isotope distributions are not only influenced by the simulation of the fast part of the reaction — done by the geometrical cut of projectile by the target nucleus in AA, or dynamical evolution in HIPSE and AMD models, but also by the statistical cascade decay code, LisFus in the case of AA and GEMINI for HIPSE and AMD calculations. The results of the HIPSE and AMD calculations can be compared directly, because identical sequential decay code (GEMINI) has been used. The fragment cross sections calculated by the AA model, on the other hand, used a different decay code (LisFus).

5.6 Velocity distributions

The fragment velocity is one of the experimental observables sensitive to the dynamics of the nuclear collision. It allows one to disentangle (to a certain degree) the fast reaction dynamics from the long in-flight decay of the excited primary fragments. The final fragment velocity distributions contain a significant imprint of the nuclear collision as described by a particular nuclear reaction model.

The Abrasion-Ablation model used in our calculations does not treat the dynamical evolution of the abrasion stage, it produces only one relevant observable — the fragmentation production cross section. More sophisticated models like the HIPSE and AMD, on the other hand, describe the dynamics of the nuclear collision, and can predict more observables (e. g., excitation energy, momentum), to be compared to experimental data.

The experimental fragment velocity is defined as the velocity of the weighted mean of the momentum distribution for every fragment measured with complete momentum distribution. The fragment velocity has been extracted from the HIPSE and AMD calculations by taking the mean of the calculated velocity distribution for every fragment after decay using GEMINI with more than 100 events simulated.

The final fragment velocity deviations with respect to the projectile, in percent, are presented in Figure 5.22 and 5.24 for ^{40,48}Ca, ^{58,64}Ni and ^{86}Kr primary beams on ^{9}Be target, respectively. The experimental fragment velocities are shown as open circles, the HIPSE and AMD calculation results are displayed as filled triangles and squares, respectively. The fragment velocity results from the fully microscopic BUU [126] calculation are also available for ^{9}Be target for all NSCL experiments (Figure 5.22) and are shown as solid lines.

The HIPSE calculation reproduces the velocities for all ^{40,48}Ca and ^{58,64}Ni primary beams and ^{9}Be target, as can be seen in Figure 5.22. It must be noted that the experimental velocity deviations are slightly lower for lighter fragments for ^{48}Ca,

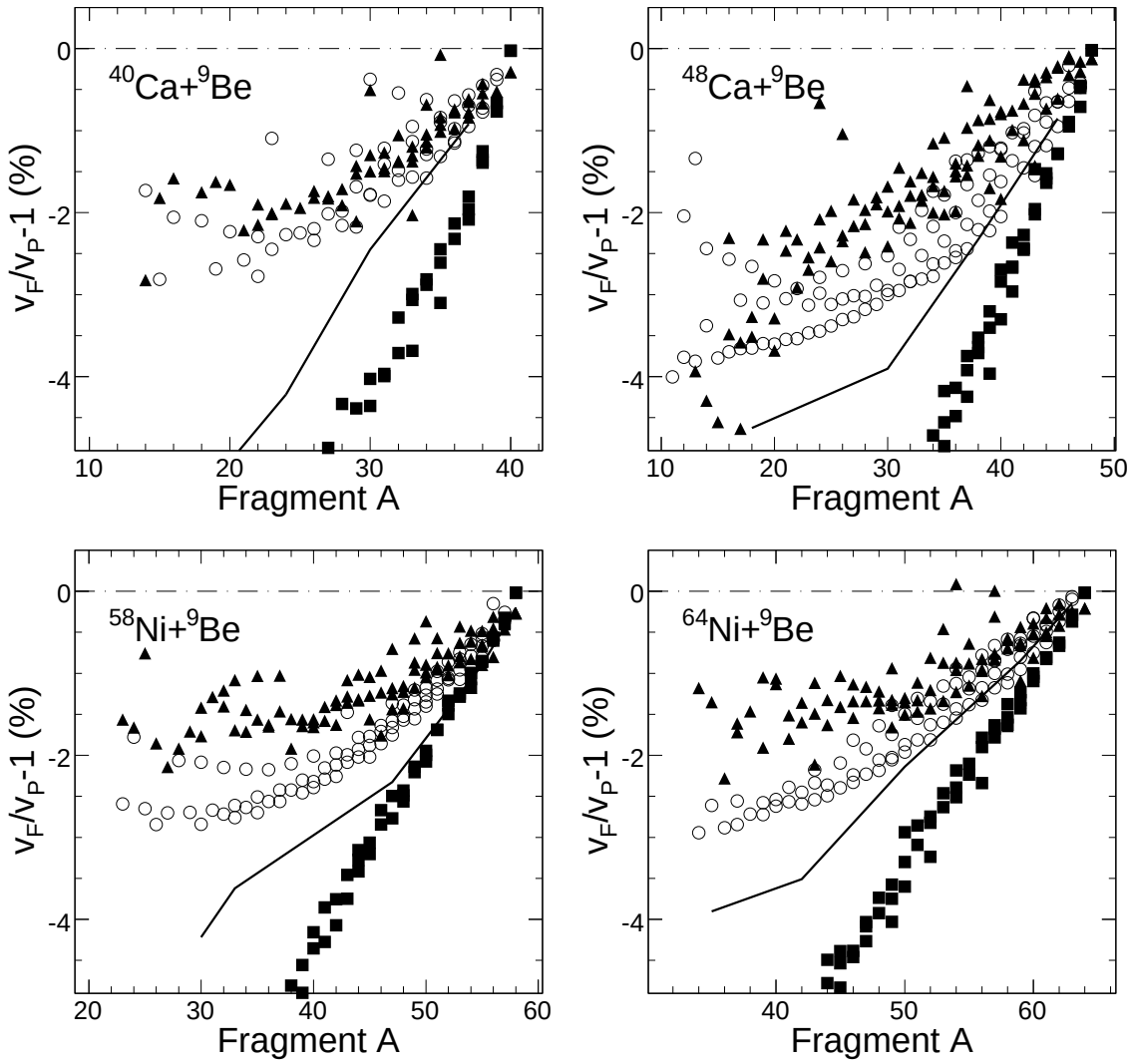

Figure 5.22: Deviation from the projectile velocity ($v_F/v_P - 1$) in percent for fragments in the ^{40,48}Ca and ^{58,64}Ni projectile on ^{9}Be target collisions shown as open circles. Filled triangles and squares depict the HIPSE and AMD calculations, respectively. BUU calculation is also shown as a solid line.

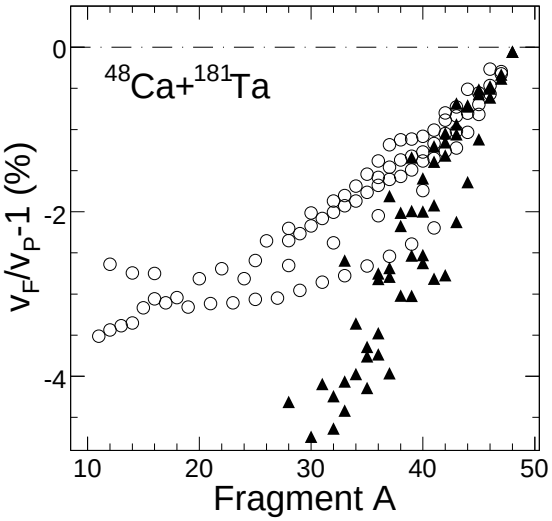

Figure 5.23: Deviation from the projectile velocity ($v_F/v_P - 1$) in percent for fragments in the ^{48}Ca projectile and ^{181}Ta target collisions shown as open circles. Filled triangles depict the HIPSE calculation.

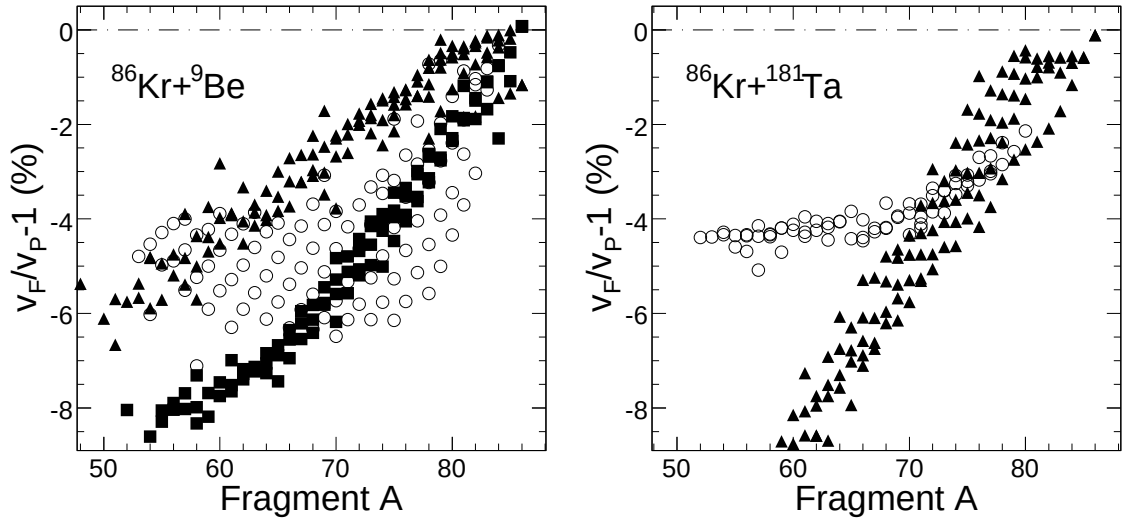

Figure 5.24: Deviation from the projectile velocity ($v_F/v_P - 1$) in percent for fragments in the ^{86}Kr projectile and ^{9}Be, ^{181}Ta target collisions shown as open circles. Filled triangles depict the HIPSE calculation and filled squares show the AMD simulation results.

^{58}Ni, and ^{64}Ni beams (Figure 5.22). It must be emphasized that the free parameters (see Section 5.1.2) of the HIPSE model have not been adjusted to reproduce this observable. The velocities predicted by the AMD model are lower and have smaller spread, probably due to insufficient fluctuations in the AMD theory. The BUU model velocity predictions are located between the HIPSE and AMD calculations. The BUU is a deterministic model, such that it predicts average values of observables for a given impact parameter, hence one must be careful when comparing the velocity as a function of the fragment mass.

In the case of the ^{86}Kr+^{9}Be reaction, the final fragment velocity deviations with respect to the projectiles shown in Figure 5.24, we see a rather good reproduction of the fragment velocities by the HIPSE model and very steep decline of the velocities calculated by the AMD. The fragment velocity comparison prefers the HIPSE model, which in turn results in rather low excitation energies. These calculated excitation energies are not sufficient to decay the neutron-rich primary fragments resulting in unsatisfactory fragmentation cross section values.

For the reactions involving the ^{181}Ta target material, there are no AMD and BUU calculations available, hence Figure 5.23 presents the experimental velocities for the ^{48}Ca+^{181}Ta reaction system compared to the HIPSE model only. We can see the HIPSE model is no longer able to describe the fragment velocities as in the case of ^{9}Be target material presented in Figure 5.22. This is another indication that the excitation energy for ^{181}Ta systems is overestimated (see Section 5.3).

For the nuclear collisions involving the target nuclei of ^{181}Ta, the HIPSE calculated fragment velocities show a clear deviation from the experimental data. The origin of the deficiencies for all reactions involving ^{181}Ta target is not fully understood. A series of benchmark calculations were carried out to understand the underestimation of the fragment velocities. Alterations of the three adjustable parameters α_a, x_{tr}, and x_{coll} did not show significant changes in the velocity distributions. The excitation energy, on the other hand, varied significantly as expected when changing the nucleon

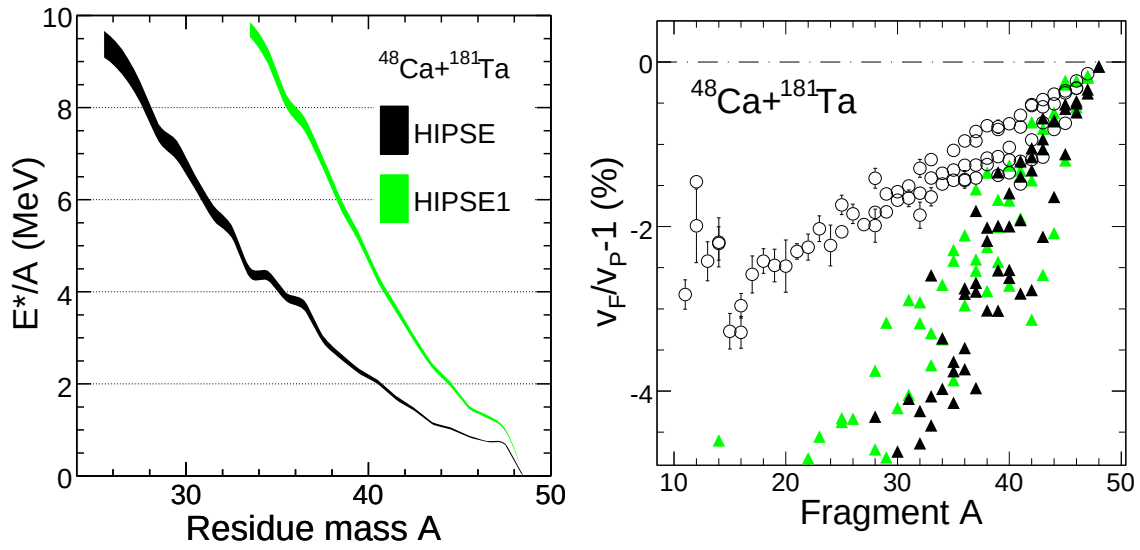

Figure 5.25: Results of the HIPSE calculations in terms of the excitation energy per nucleon, $E^\star/A$, (left) and the fragment velocity (right) for the ^{48}Ca+^{181}Ta reaction system. The calculation with changed distribution of the excitation energy among the final fragments is labeled as HIPSE1. The deviations from the projectile velocity ($v_F/v_P - 1$) for fragments in the ^{86}Kr+^{181}Ta collisions, shown as open circles, are compared to the HIPSE (filled triangles) and the HIPSE1 (green triangles).

exchange parameter, x_{tr}.

For the calculations using the ^{9}Be target the maximum number of nucleons able to collide and exchange with the quasi-projectile is 9. The ^{181}Ta nucleus offers much larger pool of available nucleons for the interactions with the quasi-projectile. The rather small number of nucleons of the ^{9}Be target nucleus is reflected in the saturation of the mean excitation energy per nucleon as shown in Figure 5.6, while in the case of ^{181}Ta target the mean excitation energy saturates at much larger values (Figure 5.7), when using the same set of HIPSE parameters. By comparing two profiles of the mean excitation energy for the ^{9}Be and ^{181}Ta target, respectively, we see a very different evolution as a function of the fragment mass number (Figure 5.6 versus 5.7).

Beside the change of input parameters, several tests have been done, by direct modifications of the HIPSE code to improve the description of the fragment velocity. One of the ways to improve the description of the velocities is to increase the excitation energy, $E^\star$, of the projectile-like primary fragments for our reaction systems

with ^{181}Ta target. In order to achieve this change, the algorithm of total excitation energy distribution among the prefragments was modified. In the new algorithm the total excitation energy, obtained from the energy balance of Equation (5.10), is equally distributed among all the residues. This new approach assigns relatively larger excitation energy (per nucleon) to lighter projectile-like fragments as compared to (much) heavier target-like fragments. The results of this changed energy distribution algorithm (labeled HIPSE1) are shown in Figure 5.25 for the ^{48}Ca+^{181}Ta reaction. The left panel of Figure 5.25 displays the excitation energy per nucleon as a function of fragment mass number obtained by the modified calculation (green) compared to the previously shown result (black). The right panel of Figure 5.25 shows the results of the HIPSE1 with changed excitation energy (green filled triangles) compared to the experimental data (open circles) and the previously shown HIPSE calculation (black filled triangles). It is clear that the excitation energy per nucleon for the heaviest projectile-like primary fragments has increased. But in terms of fragment velocities, the change of the calculation of the excitation energy is not sufficient to bring a significant increase of the calculated velocities. In the extreme case, when all the excitation energy is deposited in the quasi-projectile, the fragment velocities get closer to the experimental data. However, even this increase of the excitation energy is not sufficient to reproduce the experimental fragment velocities. Not to mention that such unequal sharing of the $E^\star$ among the primary fragments is very hard to justify.

However, these tests illustrate that the HIPSE calculation may become consistent with the experimental data if larger amount of the excitation energy is deposited in the quasi-projectile compared to the one originally produced by the model. The experimental fragment velocity distributions prefer the overall shape of the mean excitation energy per nucleon as a function of the fragment mass to be similar to that of the reactions with ^{9}Be target (Figure 5.6). Such an increase of the $E^\star$ can only be obtained by additional dissipative processes for very peripheral collisions with heavy targets, which does not seem to be treated properly in the current version of the

HIPSE model.

Chapter 6

Summary and conclusions

An extensive study of projectile fragmentation reactions is presented in this dissertation. A series of systematic measurements have been undertaken to extend the available data sets for projectile fragmentation at intermediate energies. The experimental work has been done at two laboratories. Experiments with primary beams of ^{40}Ca, ^{48}Ca, ^{58}Ni, and ^{64}Ni at 140 MeV/u were done at the NSCL using the A1900 fragment separator. The experiment using ^{86}Kr primary beam at 64 MeV/u was done at RIKEN using the RIPS fragment separator. Two targets ^{9}Be and ^{181}Ta, were used in experiments with all primary beams in order to investigate the target dependence of the fragmentation production cross sections. The experiments with a total of 10 reaction systems resulted in 1740 measured cross sections and momentum distributions.

The fragment momentum distributions were asymmetric unlike those measured in projectile fragmentation reactions at high energy ($\gg$ 200 MeV/u). The fitting of the experimental parallel momentum distributions was done using a modified Gaussian function consisting of two half Gaussians in Equation (3.2). We found that the right side of the momentum distribution described by the width parameter, σ_R (high momentum), is reproduced well by the Goldhaber systematics derived for high energy fragmentation phenomena. The reduced width parameters, σ_0^R, of the Goldhaber

model are lower than those calculated from the measured Fermi momenta for all NSCL reaction systems. This deficit is consistent with other intermediate and high energy fragmentation experiments. σ_0^R deduced from the experimental momentum distributions of ^{86}Kr fragments are larger than the values obtained for the NSCL reaction systems. This difference may be caused by the lower energy of the projectile (64 MeV/u).

The left side of the experimental momentum distributions, described by the width parameter σ_L (low momentum), also follows the behavior of the simple Goldhaber model, but requires higher values for the reduced width, σ_0^L, for all the NSCL reaction systems. The ^{86}Kr fragmentation experiment at 64 MeV/u results in even larger σ_L values and we noticed that the experimental data of σ_L began to deviate from the Goldhaber description. This was especially pronounced in ^{86}Kr+^{9}Be reaction. The data for the ^{86}Kr+^{181}Ta reaction are not so conclusive because of the small number of fragments with completely measured momentum distributions. The left side (low momentum) of the momentum distribution likely includes contributions from different reaction mechanisms (more important at lower energy like 64 MeV/u) which are clearly outside of the Goldhaber model assumptions.

The fragment velocities, defined by the maximum of the momentum distribution, p_0 parameter of the fitting function of Equation (3.2), were compared to momentum transfer systematics and parameterizations of Borrel, Kaufman and Morrissey. These parameterizations have their foundation in target spallation. All the above parameterizations provide similar predictions in terms of fragment velocity for the heaviest projectile-like fragments, close to the experimental data. They all fail to describe the overall shape of the experimental velocity distributions for all investigated systems. This fact is not surprising as all of the above mentioned parameterizations were derived and fitted only for the projectile or target-like fragments.

The experimental cross sections have been obtained by integration of the parallel momentum distribution fitting function of Equation (3.2) over the whole interval of

parallel momentum. All extracted fragmentation cross sections were compared to the empirical code EPAX [48]. This parameterization is based on the limiting fragmentation assumptions (Section 4.3.1), when the fragmentation production cross sections do not depend on primary beam energy and very weakly on the target material. The observed cross sections for the projectile-like fragments are in agreement with the EPAX formula for all NSCL reaction systems, however, some discrepancies remain. A clear shift of the peak of the isotope distributions between the EPAX values and the experimental data was observed for the fragments of neutron-rich projectiles (^{48}Ca, ^{64}Ni and ^{86}Kr) for elements in the vicinity of the projectile. This effect can be attributed to the memory parameter in the EPAX. It is much more pronounced for the fragmentation of ^{86}Kr primary beam, which might indicate a stronger dependence of the memory parameter on the incident energy. The enhanced production of neutron-deficient fragments for elements close to the neutron-rich projectiles is probably caused by transfer-type reactions, which play a more dominant role at lower beam energies [97]. The experimental isotope distributions tend to be narrower than the EPAX calculated distributions. This discrepancy is clearly pronounced for the intermediate mass fragments ($\approx A_P/2$) in the case of the ^{40}Ca beam, and a smaller effect is still visible for the rest of the reaction systems.

The target dependence of fragmentation cross section has been investigated by calculating the target cross section ratios, R_{tgt}. It is shown that the R_{tgt} dependence on the fragment mass number is much more complicated than suggested by the limiting fragmentation framework (EPAX). A clear enhancement of cross sections for neutron-rich as well as neutron-deficient fragments was observed for the ^{40}Ca projectile when using a ^{181}Ta versus a ^{9}Be target. However, the effect is small, around a factor of 3–4. Other investigated projectiles did not show the cross section enhancement for very neutron-rich fragments. An overall cross section enhancement trend was noticed for lighter fragments in the case of all investigated projectiles when using ^{181}Ta target. Unfortunately, the observed enhancement of fragmentation production cross section

does not translate into yields (Section 4.3.4).

Projectile dependence of the fragmentation cross section was addressed by calculating the projectile cross section ratios, R_{proj}, for the Ca and Ni projectiles in our study. These ratios for isotopes of the lightest elements are equivalent to isoscaling ratios studied in central multifragmentation reactions. For isotopes of heavier elements the ratios for isotopes of one element formed a slightly curved line. A modified isoscaling-like function with second order terms has been used to reproduce the trends for individual elements. Study of R_{proj} allows one to see the difference between two dominating reaction mechanisms — projectile fragmentation (heaviest fragments with curved R_{proj} trends) and multifragmentation (lightest fragments with straight R_{proj} trends).

In order to get a better understanding of the physical processes involved in the studied reactions, calculations using different theoretical models were carried out. The geometrical Abrasion-Ablation, the macroscopic-microscopic Heavy Ion Phase Space Exploration (HIPSE) and the microscopic Antisymmetrized Molecular Dynamics (AMD) models have been used in our studies. The above mentioned calculations were done for all investigated reaction systems, but the AMD calculations were carried out only for the five reaction systems using ^{9}Be target, because of unrealistically long execution time for systems involving ^{181}Ta.

A revised version of a simple geometrical Abrasion-Ablation model in conjunction with the LisFus evaporation code [106] as implemented in LISE++ [56] has been used. After adjusting the excitation energy as a function of the number of removed nucleons and its fluctuations for each system independently we get an extremely good description of the experimental fragmentation cross sections. The excitation energies required to reproduce the cross section distributions for all NSCL reaction systems are $\approx$ 11–13 MeV per removed nucleon, indicating a very slow rising trend with the mass of the projectile in the studied beam mass range of $40 < A < 64$. For the ^{86}Kr primary beam a little higher excitation energy of 18 MeV per removed

nucleon is required. There is no target dependence of the excitation energy observed for all the investigated reaction systems. Small differences in terms of the excitation energy for individual projectiles are well within the errors of its determination. Even though the simple linear dependence of the excitation energy produces extremely large excitation energy for lighter primary fragments, which is unphysical, we observe very good reproduction of the isotope distributions for the lightest elements (except for ^{64}Ni+^{181}Ta reaction). Since the AA model assumes that the fragment velocity is equivalent to that of the projectile and it requires adjustment of the excitation energy with experimental data, its predictive power is severely limited. More sophisticated nuclear reaction models are needed to get a clearer picture of the excitation energy and the fragment velocity.

The HIPSE and AMD models have been used to get more insight into the reaction mechanisms involved in the investigated nuclear collisions by treating the collisions dynamically. Aside from the fragment cross sections we compared the primary fragment excitation energies and the final fragment velocities. For all reaction systems involving the ^{9}Be target material, we noticed the excitation energy for the primary fragments close to the projectile determined by the dynamical models (HIPSE and AMD) was higher than the one required by the AA model. For lighter prefragments, however, the dynamical models saturate around 4–5 MeV/u while the AA model uses large values of the excitation energy (>10 MeV/u). For all reaction systems involving the ^{181}Ta target, the excitation energy obtained from the HIPSE model was qualitatively and quantitatively equal to the one used in the AA calculation (Figure 5.7). The excitation energy in the HIPSE model, however, saturates at approximately 10 MeV/u for all primary beams measured at the NSCL and at approximately 6 MeV/u for the ^{86}Kr+^{181}Ta reaction.

The excitation energy of the primary fragments obtained from the HIPSE and AMD models for all reaction systems involving ^{9}Be target showed rather similar profiles close to the fully microscopic BUU calculations. Calculations by the HIPSE

model for all reaction systems containing ^{181}Ta target, on the other hand, produced very low excitation energies for primary fragments close to the projectile and very large values for the lighter fragments (Figure 5.7).

The comparisons of the relative fragment velocity to the calculated values strictly preferred the HIPSE model for all reaction systems containing ^{9}Be target. The AMD fragment velocities plotted as a function of the fragment mass number are lower and the overall trend is much steeper than the experimental data exhibit. The HIPSE model not only reproduced the overall trend of the fragment velocity as a function of the fragment mass, but also more or less successfully described the spread of the experimental values. On the contrary, for the reaction systems containing ^{181}Ta target the HIPSE model was not able to reproduce the fragment velocities. Our study with the HIPSE model showed that the fragment velocity description was improved slightly when we increased the excitation energy for the heaviest primary fragments. Most probably the description of peripheral nuclear collisions with heavy targets like ^{181}Ta at 140 MeV/u is beyond the scope of the current HIPSE model.

The failure to describe the fragment velocities and probably the excitation energies by the HIPSE, resulted in a rather poor description of the fragmentation cross section for reaction systems that include a ^{181}Ta target. The experimental isotope cross section distributions involving a ^{9}Be target, on the other hand, were described fairly well by the results of both dynamical calculations (HIPSE and AMD). It should be noted that calculated cross section isotope distributions in the HIPSE model were slightly broader than the experimental ones. It would suggest that the excitation energy was not large enough to decay the neutron and proton-rich primary fragments. This conclusion is consistent with the AMD calculated isotope distributions which appeared to be narrower, keeping in mind that we used the same statistical cascade evaporation code GEMINI for the two calculations.

It must be noted that the calculated final cross section distributions are the results, not only of the primary (fast) step of the nuclear reaction (modeled by HIPSE or

AMD), but also of the secondary (slow) step modeled by the statistical evaporation code (GEMINI). Hence, if we want to put the dynamical nuclear collision calculations to a more stringent test, it is imperative to fully understand the de-excitation part of the nuclear collision — the evaporation process.

Appendix A

Fitting results

The fitting results of the experimental momentum distributions of the reaction products identified in projectile fragmentation reactions using all primary beam and target combinations are presented in this appendix. Values of p_0, σ_L and σ_R parameters of the fitting function of Equation (3.2), plus the value of the final production cross section, σ_{prod}, are given for all measured nuclides in reactions of ^{40}Ca, ^{48}Ca, ^{58}Ni, ^{64}Ni and ^{86}Kr beams with ^{9}Be and ^{181}Ta targets. Values of p_0, σ_L and σ_R quoted without errors were extrapolated according to the procedure described in Section 3.4.3. All entries in *italics* are products of nucleon exchange or pick-up reactions.

A.1 Results for ^{40}Ca projectile

Table A.1: Fitting results for the reaction system ^{40}Ca+^{9}Be.

A	Z	p_0 (MeV/c)	σ_L (MeV/c)	σ_R (MeV/c)	σ_{prod} (mb)
10	5	5232	371	247	7.52E+00 ± 6.43E−01
11	5	5719 ± 2	462 ± 4	244 ± 1	1.24E+01 ± 8.19E−01
12	5	6148	476	275	9.03E−01 ± 1.54E−01
11	6	5692	363	258	5.10E+00 ± 8.27E−01
12	6	6228 ± 2	436 ± 13	250 ± 1	2.39E+01 ± 1.61E+00
13	6	6728 ± 2	454 ± 3	256 ± 1	1.20E+01 ± 7.51E−01
14	6	7118 ± 6	405 ± 9	353 ± 5	2.66E+00 ± 1.66E−01
15	6	7662	371	311	1.23E−01 ± 1.73E−02
13	7	6740	423	346	1.43E+00 ± 2.29E−01
14	7	7234 ± 10	441 ± 17	280 ± 4	1.21E+01 ± 8.00E−01
15	7	7692 ± 2	385 ± 1	274 ± 1	1.74E+01 ± 1.02E+00
16	7	8123 ± 4	376 ± 2	362 ± 9	1.14E+00 ± 1.12E−01
17	7	8632	436	365	2.70E−01 ± 2.93E−02
15	8	7757	371	301	3.70E+00 ± 9.27E−01
16	8	8248 ± 8	436 ± 13	283 ± 3	2.43E+01 ± 1.47E+00
17	8	8717 ± 6	407 ± 4	295 ± 2	9.23E+00 ± 5.16E−01

continued on next page

Table A.1: continued from previous page

A	Z	p_0 (MeV/c)	σ_L (MeV/c)	σ_R (MeV/c)	σ_{prod} (mb)
18	8	9152 ± 8	395 ± 4	351 ± 3	2.96E+00 ± 1.60E−01
19	8	9674 ± 9	471 ± 14	369 ± 14	3.40E−01 ± 1.94E−02
20	8	10340	384	273	5.50E−02 ± 9.36E−03
17	9	8812	513	296	1.57E+00 ± 2.59E−01
18	9	9264 ± 11	452 ± 14	311 ± 5	7.34E+00 ± 4.23E−01
19	9	9721 ± 6	411 ± 3	313 ± 2	8.98E+00 ± 4.66E−01
20	9	10254 ± 6	512 ± 4	323 ± 2	3.39E+00 ± 1.69E−01
21	9	10700 ± 5	467 ± 9	369 ± 4	7.57E−01 ± 3.71E−02
22	9	11185	434	368	6.30E−02 ± 7.51E−03
23	9	11875	513	318	8.06E−03 ± 3.42E−03
18	10	9300	449	313	1.25E−01 ± 3.95E−02
19	10	9833	518	305	1.90E+00 ± 2.74E−01
20	10	10272 ± 9	421 ± 10	315 ± 4	1.49E+01 ± 7.74E−01
21	10	10746 ± 5	411 ± 3	320 ± 2	1.64E+01 ± 7.79E−01
22	10	11287 ± 5	474 ± 3	318 ± 2	8.05E+00 ± 3.65E−01
23	10	11727 ± 10	449 ± 10	358 ± 5	7.82E−01 ± 3.56E−02
24	10	12267	485	362	1.12E−01 ± 1.42E−02
20	11	10485	406	289	9.44E−02 ± 1.75E−02
21	11	10840	518	305	1.67E+00 ± 2.23E−01
22	11	11287 ± 10	424 ± 9	331 ± 4	1.20E+01 ± 5.73E−01
23	11	11802 ± 5	433 ± 3	313 ± 2	2.17E+01 ± 9.37E−01
24	11	12310 ± 5	466 ± 3	318 ± 2	6.62E+00 ± 2.72E−01
25	11	12807 ± 7	466 ± 7	333 ± 3	1.55E+00 ± 6.19E−02
26	11	13304 ± 7	465 ± 10	353 ± 7	1.36E−01 ± 5.50E−03
27	11	13840	458	256	1.22E−02 ± 1.96E−03
22	12	11391	449	326	1.76E−01 ± 5.21E−02
23	12	11878	514	314	3.17E+00 ± 3.81E−01
24	12	12346 ± 8	424 ± 7	314 ± 3	2.75E+01 ± 1.17E+00
25	12	12863 ± 5	438 ± 3	304 ± 2	2.89E+01 ± 1.12E+00
26	12	13385 ± 5	456 ± 3	302 ± 2	1.53E+01 ± 5.56E−01
27	12	13873 ± 7	456 ± 7	315 ± 2	1.73E+00 ± 6.21E−02
28	12	14370 ± 11	451 ± 11	328 ± 5	2.25E−01 ± 8.17E−03
29	12	14880	427	325	9.28E−03 ± 9.58E−04
30	12	15439	449	278	9.42E−04 ± 2.71E−04
24	13	12381	442	362	1.43E−01 ± 2.86E−02
25	13	12914	426	304	1.80E+00 ± 1.52E−01
26	13	13404 ± 9	427 ± 6	304 ± 4	1.71E+01 ± 6.52E−01
27	13	13936 ± 5	438 ± 2	290 ± 2	3.85E+01 ± 1.31E+00
28	13	14430 ± 5	439 ± 3	294 ± 2	1.30E+01 ± 4.14E−01
29	13	14949 ± 6	440 ± 6	293 ± 2	2.90E+00 ± 8.99E−02
30	13	15472 ± 9	441 ± 10	293 ± 3	2.25E−01 ± 7.22E−03
31	13	15938 ± 20	424 ± 19	312 ± 15	2.31E−02 ± 1.01E−03

continued on next page

Table A.1: continued from previous page

A	Z	p_0 (MeV/c)	σ_L (MeV/c)	σ_R (MeV/c)	σ_{prod} (mb)
32	13	16405	415	296	8.50E−04 ± 1.60E−04
26	14	13482	431	306	2.11E−01 ± 4.53E−02
27	14	13976	442	294	3.71E+00 ± 1.91E−01
28	14	14484 ± 7	403 ± 4	281 ± 3	4.29E+01 ± 1.41E+00
29	14	15031 ± 5	428 ± 2	267 ± 2	4.88E+01 ± 1.44E+00
30	14	15554 ± 4	424 ± 3	258 ± 1	3.16E+01 ± 8.60E−01
31	14	16026 ± 6	403 ± 5	271 ± 2	3.36E+00 ± 9.00E−02
32	14	16565 ± 7	407 ± 7	262 ± 3	3.45E−01 ± 9.64E−03
33	14	17036 ± 16	378 ± 17	278 ± 8	1.41E−02 ± 6.18E−04
34	14	17542	332	252	7.79E−04 ± 1.00E−04
28	15	14550	401	279	1.28E−01 ± 2.70E−02
29	15	15108 ± 14	426 ± 14	247 ± 8	2.06E+00 ± 8.31E−02
30	15	15556 ± 7	393 ± 3	269 ± 3	1.92E+01 ± 5.53E−01
31	15	16127 ± 4	418 ± 2	241 ± 2	4.56E+01 ± 1.15E+00
32	15	16536 ± 3	330 ± 1	266 ± 1	2.25E+01 ± 5.14E−01
33	15	17117 ± 6	372 ± 5	243 ± 2	4.83E+00 ± 1.25E−01
34	15	17577 ± 5	317 ± 1	259 ± 2	3.48E−01 ± 8.46E−03
35	15	18115	325	244	2.40E−02 ± 3.25E−03
36	*15*	*18639 ± 17*	*311 ± 9*	*222 ± 8*	*6.02E−04 ± 5.10E−05*
30	16	15594	449	283	2.07E−01 ± 3.57E−02
31	16	16169 ± 5	398 ± 6	228 ± 5	4.00E+00 ± 1.20E−01
32	16	16671 ± 5	373 ± 2	234 ± 2	3.72E+01 ± 9.28E−01
33	16	17222 ± 4	394 ± 2	214 ± 2	5.95E+01 ± 1.48E+00
34	16	17683 ± 3	309 ± 1	218 ± 1	4.85E+01 ± 1.12E+00
35	16	18193 ± 5	330 ± 4	216 ± 2	5.54E+00 ± 1.46E−01
36	16	18758 ± 4	311 ± 16	191 ± 2	6.39E−01 ± 2.62E−02
37	*16*	*19212 ± 5*	*273 ± 2*	*195 ± 1*	*1.48E−02 ± 4.64E−04*
38	*16*	*19758 ± 31*	*226 ± 12*	*161 ± 5*	*1.81E−04 ± 3.49E−05*
32	17	16705	413	234	1.53E−01 ± 2.63E−02
33	17	17256 ± 4	342 ± 3	208 ± 2	2.23E+00 ± 5.98E−02
34	17	17742 ± 2	354 ± 2	218 ± 1	2.26E+01 ± 5.66E−01
35	17	18293 ± 2	343 ± 1	188 ± 1	5.81E+01 ± 1.40E+00
36	17	18772 ± 5	311 ± 6	193 ± 2	2.99E+01 ± 8.42E−01
37	17	19309 ± 3	273 ± 1	169 ± 1	7.38E+00 ± 1.80E−01
38	*17*	*19777 ± 2*	*226 ± 1*	*161 ± 1*	*2.58E−01 ± 6.54E−03*
39	*17*	*20271 ± 25*	*336 ± 59*	*277 ± 12*	*3.41E−03 ± 3.79E−04*
34	18	17772	293	204	2.96E−01 ± 1.43E−02
35	18	18328 ± 3	318 ± 2	181 ± 3	5.84E+00 ± 1.55E−01
36	18	18861 ± 3	311 ± 1	167 ± 2	4.33E+01 ± 1.19E+00
37	18	19347 ± 3	273 ± 1	164 ± 1	8.22E+01 ± 2.11E+00
38	18	19895 ± 3	226 ± 1	135 ± 1	5.71E+01 ± 1.47E+00
39	*18*	*20301 ± 1*	*191 ± 1*	*141 ± 1*	*2.40E+00 ± 6.01E−02*

continued on next page

Table A.1: continued from previous page

A	Z	p_0 (MeV/c)	σ_L (MeV/c)	σ_R (MeV/c)	σ_{prod} (mb)
40	*18*	*20997 ± 10*	*217 ± 2*	*170 ± 6*	*2.09E−02 ± 9.02E−04*
36	19	18859 ± 12	274 ± 10	165 ± 11	2.62E−01 ± 1.20E−02
37	19	19428 ± 2	273 ± 1	144 ± 1	5.49E+00 ± 1.32E−01
38	19	19901 ± 4	226 ± 1	144 ± 2	4.36E+01 ± 1.50E+00
39	19	20488 ± 1	162 ± 1	85 ± 1	9.56E+01 ± 2.42E+00
40	*19*	*20787 ± 12*	*187 ± 6*	*137 ± 5*	*2.84E+00 ± 1.18E−01*
41	*19*	*21468 ± 7*	*297 ± 2*	*178 ± 4*	*1.17E−01 ± 1.44E−02*
42	*19*	*21772 ± 73*	*338 ± 17*	*228 ± 32*	*5.18E−03 ± 5.93E−04*
38	20	19959 ± 3	221 ± 2	119 ± 4	1.29E+00 ± 4.18E−02
39	20	20470	162	115	4.00E+01 ± 6.53E+00
41	*21*	*21262 ± 6*	*134 ± 4*	*165 ± 1*	*2.10E−01 ± 3.39E−02*

Table A.2: Fitting results for the reaction system ^{40}Ca+^{181}Ta.

A	Z	p_0 (MeV/c)	σ_L (MeV/c)	σ_R (MeV/c)	σ_{prod} (mb)
10	5	5198 ± 6	343 ± 1	249 ± 3	2.52E+01 ± 2.03E+00
11	5	5623 ± 3	365 ± 1	257 ± 1	4.43E+01 ± 3.47E+00
12	5	6107 ± 7	429 ± 11	305 ± 1	4.29E+00 ± 3.37E−01
13	5	6662	357	287	6.06E−01 ± 6.10E−02
11	6	5651	440	243	2.25E+01 ± 2.60E+00
12	6	6167	344	261	6.13E+01 ± 5.52E+00
13	6	6648 ± 3	391 ± 1	275 ± 1	3.57E+01 ± 2.66E+00
14	6	7178 ± 1	363 ± 1	284 ± 2	7.12E+00 ± 5.18E−01
15	6	7688 ± 7	391 ± 1	293 ± 6	4.83E−01 ± 3.51E−02
16	6	8215	373	252	6.85E−02 ± 1.11E−02
14	7	7160	374	309	2.97E+01 ± 2.38E+00
15	7	7712 ± 5	430 ± 4	272 ± 1	4.08E+01 ± 2.90E+00
16	7	8133 ± 8	397 ± 6	326 ± 4	3.35E+00 ± 2.33E−01
17	7	8597 ± 12	415 ± 9	356 ± 6	9.51E−01 ± 6.48E−02
18	7	9132	379	346	6.77E−02 ± 1.02E−02
19	7	9593	381	257	1.14E−02 ± 2.09E−03
15	8	7756	391	264	1.07E+01 ± 2.13E+00
16	8	8195 ± 4	351 ± 1	293 ± 2	5.08E+01 ± 3.49E+00
17	8	8710 ± 3	407 ± 1	291 ± 1	2.01E+01 ± 1.33E+00
18	8	9135 ± 6	379 ± 3	339 ± 3	7.25E+00 ± 4.66E−01
19	8	9670 ± 6	456 ± 8	333 ± 11	9.29E−01 ± 5.99E−02
20	8	10188 ± 9	403 ± 1	331 ± 9	1.47E−01 ± 9.30E−03
21	8	10675	439	348	1.25E−02 ± 2.05E−03

continued on next page

Table A.2: continued from previous page

A	Z	p_0 (MeV/c)	σ_L (MeV/c)	σ_R (MeV/c)	σ_{prod} (mb)
17	9	8774	340	304	3.24E+00 ± 5.25E−01
18	9	9203 ± 9	391 ± 12	333 ± 4	1.48E+01 ± 9.98E−01
19	9	9720 ± 6	417 ± 4	309 ± 2	1.77E+01 ± 1.10E+00
20	9	10198 ± 4	446 ± 1	327 ± 1	7.68E+00 ± 4.54E−01
21	9	10684 ± 9	451 ± 9	353 ± 6	1.84E+00 ± 1.07E−01
22	9	11177 ± 17	454 ± 14	363 ± 12	1.82E−01 ± 1.08E−02
23	9	11720 ± 14	399 ± 4	329 ± 3	2.22E−02 ± 1.45E−03
19	10	9840	477	285	4.31E+00 ± 1.15E+00
20	10	10256 ± 8	402 ± 9	317 ± 3	2.69E+01 ± 1.65E+00
21	10	10769 ± 5	423 ± 3	307 ± 2	2.92E+01 ± 1.66E+00
22	10	11247 ± 3	429 ± 1	317 ± 1	1.54E+01 ± 8.29E−01
23	10	11740 ± 9	453 ± 8	335 ± 4	1.64E+00 ± 8.67E−02
24	10	12251 ± 12	471 ± 12	336 ± 9	2.64E−01 ± 1.40E−02
25	10	12787	515	326	1.64E−02 ± 1.43E−03
26	10	13200	492	245	1.71E−03 ± 5.57E−04
21	11	10827	372	303	3.03E+00 ± 4.80E−01
22	11	11283 ± 9	410 ± 9	327 ± 4	2.09E+01 ± 1.18E+00
23	11	11806 ± 5	435 ± 3	307 ± 2	3.56E+01 ± 1.84E+00
24	11	12280 ± 4	440 ± 1	321 ± 1	1.14E+01 ± 5.51E−01
25	11	12791 ± 5	435 ± 1	321 ± 2	2.87E+00 ± 1.31E−01
26	11	13299 ± 14	467 ± 13	334 ± 9	2.84E−01 ± 1.37E−02
27	11	13772	450	347	3.35E−02 ± 2.03E−03
23	12	11876	392	301	5.52E+00 ± 4.05E−01
24	12	12348 ± 7	412 ± 7	307 ± 3	4.29E+01 ± 2.16E+00
25	12	12868 ± 5	438 ± 3	296 ± 2	4.25E+01 ± 1.96E+00
26	12	13347 ± 3	421 ± 1	304 ± 1	2.34E+01 ± 9.95E−01
27	12	13840 ± 4	417 ± 1	310 ± 2	2.85E+00 ± 1.14E−01
28	12	14356 ± 6	442 ± 4	314 ± 3	4.17E−01 ± 1.58E−02
29	12	14834	439	350	2.26E−02 ± 2.22E−03
30	12	15334	446	301	2.60E−03 ± 5.58E−04
25	13	12930	395	295	3.11E+00 ± 1.72E−01
26	13	13402 ± 8	417 ± 6	299 ± 4	2.50E+01 ± 1.12E+00
27	13	13922 ± 3	431 ± 1	287 ± 1	5.27E+01 ± 2.09E+00
28	13	14394 ± 3	411 ± 1	295 ± 2	1.80E+01 ± 6.59E−01
29	13	14901 ± 4	405 ± 1	296 ± 2	4.34E+00 ± 1.46E−01
30	13	15409 ± 6	406 ± 3	298 ± 3	3.87E−01 ± 1.23E−02
31	13	15912 ± 19	429 ± 17	309 ± 13	4.60E−02 ± 2.05E−03
32	13	16430	412	279	2.43E−03 ± 4.66E−04
27	14	13970	385	286	5.91E+00 ± 2.98E−01
28	14	14471 ± 7	394 ± 4	278 ± 3	5.67E+01 ± 2.18E+00
29	14	14993 ± 2	413 ± 1	269 ± 1	6.25E+01 ± 2.10E+00
30	14	15476 ± 3	374 ± 1	269 ± 1	4.11E+01 ± 1.25E+00
31	14	15975 ± 4	381 ± 1	274 ± 2	4.62E+00 ± 1.28E−01

continued on next page

Table A.2: continued from previous page

A	Z	p_0 (MeV/c)	σ_L (MeV/c)	σ_R (MeV/c)	σ_{prod} (mb)
32	14	16496 ± 5	380 ± 19	277 ± 2	5.35E−01 ± 2.06E−02
33	14	17025 ± 6	392 ± 4	265 ± 1	2.79E−02 ± 8.67E−04
34	14	17481	301	254	2.01E−03 ± 3.76E−04
28	15	14574	349	259	2.59E−01 ± 5.47E−02
29	15	15072 ± 13	368 ± 25	251 ± 8	3.09E+00 ± 1.72E−01
30	15	15537 ± 7	383 ± 4	268 ± 3	2.45E+01 ± 8.04E−01
31	15	16048 ± 3	385 ± 1	253 ± 1	5.73E+01 ± 1.58E+00
32	15	16534 ± 3	358 ± 1	254 ± 2	2.61E+01 ± 6.38E−01
33	15	17047 ± 4	351 ± 1	249 ± 2	6.16E+00 ± 1.44E−01
34	15	17543 ± 5	353 ± 3	256 ± 3	5.09E−01 ± 1.29E−02
35	15	18034 ± 14	351 ± 14	283 ± 7	4.68E−02 ± 1.92E−03
36	*15*	*18535 ± 34*	*359 ± 31*	*245 ± 22*	*1.84E−03 ± 1.61E−04*
30	16	15604	330	261	3.58E−01 ± 7.47E−02
31	16	16128 ± 5	354 ± 5	237 ± 4	5.73E+00 ± 1.80E−01
32	16	16646 ± 5	366 ± 3	226 ± 2	4.50E+01 ± 1.20E+00
33	16	17122 ± 3	350 ± 1	229 ± 1	7.33E+01 ± 1.72E+00
34	16	17636 ± 3	310 ± 1	216 ± 1	5.25E+01 ± 1.23E+00
35	16	18121 ± 4	323 ± 1	223 ± 2	6.50E+00 ± 1.57E−01
36	16	18670 ± 4	308 ± 4	216 ± 3	8.52E−01 ± 2.25E−02
37	*16*	*19088 ± 17*	*294 ± 16*	*289 ± 7*	*3.24E−02 ± 1.58E−03*
38	*16*	*19950 ± 8*	*215 ± 3*	*119 ± 24*	*1.12E−03 ± 2.36E−04*
32	17	16695	310	220	2.77E−01 ± 3.93E−02
33	17	17223 ± 4	319 ± 4	197 ± 7	3.08E+00 ± 9.61E−02
34	17	17712 ± 2	348 ± 2	214 ± 1	2.65E+01 ± 6.77E−01
35	17	18198 ± 3	309 ± 1	198 ± 1	6.76E+01 ± 1.63E+00
36	17	18690 ± 3	289 ± 1	198 ± 1	3.26E+01 ± 7.85E−01
37	17	19215 ± 3	260 ± 1	179 ± 1	8.05E+00 ± 2.00E−01
38	*17*	*19665 ± 8*	*254 ± 7*	*224 ± 4*	*3.61E−01 ± 1.28E−02*
39	*17*	*20357 ± 12*	*268 ± 1*	*206 ± 6*	*2.22E−02 ± 8.48E−04*
40	*17*	*20865 ± 62*	*209 ± 43*	*244 ± 33*	*8.45E−04 ± 1.42E−04*
34	18	17771	259	182	5.53E−01 ± 3.03E−02
35	18	18290 ± 3	297 ± 4	178 ± 1	8.21E+00 ± 2.23E−01
36	18	18786 ± 1	289 ± 1	173 ± 1	5.18E+01 ± 1.19E+00
37	18	19277 ± 3	261 ± 1	163 ± 1	8.75E+01 ± 2.19E+00
38	18	19814 ± 1	223 ± 1	134 ± 1	5.85E+01 ± 1.36E+00
39	*18*	*20243 ± 2*	*233 ± 3*	*146 ± 1*	*2.98E+00 ± 8.85E−02*
40	*18*	*20943 ± 5*	*188 ± 1*	*150 ± 3*	*2.26E−01 ± 6.78E−03*
41	*18*	*21419 ± 6*	*190 ± 3*	*141 ± 3*	*1.07E−02 ± 5.18E−04*
36	19	18839 ± 6	231 ± 6	149 ± 4	5.14E−01 ± 1.92E−02
37	19	19345 ± 2	245 ± 2	161 ± 1	7.28E+00 ± 2.07E−01
38	19	19848 ± 1	243 ± 1	146 ± 1	3.75E+01 ± 9.00E−01
39	19	20381 ± 2	126 ± 1	93 ± 1	1.18E+02 ± 3.46E+00
40	*19*	*20692 ± 8*	*188 ± 4*	*186 ± 5*	*4.11E+00 ± 1.56E−01*

continued on next page

Table A.2: continued from previous page

A	Z	p_0 (MeV/c)	σ_L (MeV/c)	σ_R (MeV/c)	σ_{prod} (mb)
41	*19*	*21497 ± 2*	*148 ± 1*	*109 ± 1*	*5.69E−01 ± 1.64E−02*
42	*19*	*22000 ± 10*	*301 ± 2*	*180 ± 3*	*3.66E−02 ± 1.64E−03*
38	20	19897 ± 2	185 ± 2	113 ± 1	2.34E+00 ± 7.35E−02
39	20	20416 ± 2	114 ± 1	73 ± 1	6.54E+01 ± 1.96E+00
41	*20*	*21394 ± 4*	*210 ± 1*	*155 ± 51*	*2.17E+00 ± 3.10E−01*
40	*21*	*20818 ± 3*	*110 ± 1*	*76 ± 2*	*2.14E−01 ± 9.04E−03*
41	*21*	*21259 ± 11*	*158 ± 9*	*158 ± 4*	*2.22E−01 ± 4.74E−02*

A.2 Results for ^{48}Ca projectile

Table A.3: Fitting results for the reaction system ^{48}Ca+^{9}Be.

A	Z	p_0 (MeV/c)	σ_L (MeV/c)	σ_R (MeV/c)	σ_{prod} (mb)
11	5	5617 ± 10	516 ± 3	349 ± 2	1.45E+01 ± 9.95E−01
12	5	6249 ± 6	532 ± 15	266 ± 1	2.51E+00 ± 1.77E−01
13	5	6786	480	273	7.75E−01 ± 7.01E−02
14	5	7106	460	378	4.01E−02 ± 3.43E−03
12	6	6069	393	344	8.31E+00 ± 1.30E+00
13	6	6667 ± 18	482 ± 17	298 ± 6	8.58E+00 ± 6.27E−01
14	6	7095 ± 19	440 ± 14	376 ± 7	4.40E+00 ± 3.08E−01
15	6	7811 ± 21	324 ± 18	318 ± 7	4.73E−01 ± 3.67E−02
16	6	8333 ± 11	494 ± 29	290 ± 8	1.77E−01 ± 1.34E−02
17	6	8739	434	398	1.41E−02 ± 1.45E−03
14	7	7213	558	279	3.53E+00 ± 6.57E−01
15	7	7602 ± 22	479 ± 20	352 ± 9	1.16E+01 ± 8.40E−01
16	7	8212 ± 7	428 ± 1	329 ± 3	1.96E+00 ± 1.24E−01
17	7	8825 ± 15	556 ± 13	328 ± 4	1.10E+00 ± 7.36E−02
18	7	9381	615	339	2.31E−01 ± 3.47E−02
19	7	9862	555	356	6.45E−02 ± 7.56E−03
20	7	10518	606	356	6.22E−03 ± 1.12E−03
16	8	8139	438	332	6.86E+00 ± 9.44E−01
17	8	8629 ± 28	474 ± 21	352 ± 13	4.93E+00 ± 3.55E−01
18	8	9154 ± 20	486 ± 10	369 ± 8	4.14E+00 ± 2.63E−01
19	8	9683 ± 18	453 ± 8	390 ± 6	1.15E+00 ± 7.03E−02
20	8	10265	461	378	4.23E−01 ± 7.19E−02
21	8	10920 ± 34	516 ± 43	328 ± 15	5.95E−02 ± 4.91E−03
22	8	11440	614	390	1.10E−02 ± 1.79E−03
23	8	11825	614	361	3.04E−04 ± 6.58E−05
17	9	8669	511	398	1.56E−01 ± 2.98E−02
18	9	9237	567	307	1.56E+00 ± 1.69E−01
19	9	9667 ± 28	499 ± 21	358 ± 13	5.02E+00 ± 3.48E−01
20	9	10206 ± 24	504 ± 11	359 ± 11	4.55E+00 ± 2.81E−01
21	9	10742 ± 8	450 ± 1	376 ± 4	2.31E+00 ± 1.31E−01
22	9	11341 ± 18	517 ± 14	364 ± 5	5.37E−01 ± 3.31E−02
23	9	11878 ± 25	491 ± 41	367 ± 9	1.56E−01 ± 1.26E−02
24	9	12540	621	312	1.69E−02 ± 2.43E−03
25	9	12935	496	368	1.66E−03 ± 2.83E−04
26	9	13496	452	360	1.29E−04 ± 5.10E−05
19	10	9792	444	301	1.16E−01 ± 3.35E−02
20	10	10282	595	298	3.19E+00 ± 4.17E−01
21	10	10722 ± 27	517 ± 20	337 ± 11	6.82E+00 ± 4.52E−01

continued on next page

Table A.3: continued from previous page

A	Z	p_0 (MeV/c)	σ_L (MeV/c)	σ_R (MeV/c)	σ_{prod} (mb)
22	10	11193 ± 23	486 ± 9	376 ± 10	7.78E+00 ± 4.53E−01
23	10	11755 ± 21	499 ± 7	370 ± 9	2.39E+00 ± 1.35E−01
24	10	12328 ± 20	534 ± 13	381 ± 6	9.09E−01 ± 5.38E−02
25	10	12888 ± 31	495 ± 41	372 ± 11	1.44E−01 ± 1.17E−02
26	10	13509 ± 29	452 ± 36	336 ± 10	3.15E−02 ± 2.44E−03
27	10	14087	572	314	1.42E−03 ± 1.91E−04
28	10	14590	553	364	5.88E−04 ± 7.81E−05
29	10	15262	575	354	3.94E−05 ± 1.32E−05
21	11	10719	609	373	1.24E−01 ± 1.83E−02
22	11	11267	587	335	2.10E+00 ± 3.67E−01
23	11	11747 ± 26	513 ± 18	340 ± 10	9.40E+00 ± 5.95E−01
24	11	12225 ± 23	490 ± 9	368 ± 10	7.18E+00 ± 4.01E−01
25	11	12818 ± 21	515 ± 7	356 ± 9	4.56E+00 ± 2.45E−01
26	11	13368 ± 21	518 ± 11	364 ± 8	1.23E+00 ± 6.89E−02
27	11	13947 ± 27	519 ± 20	358 ± 9	3.82E−01 ± 2.33E−02
28	11	14531 ± 31	483 ± 43	345 ± 10	5.96E−02 ± 5.22E−03
29	11	15111	596	335	1.57E−02 ± 1.87E−03
30	11	15560	532	412	1.84E−03 ± 1.83E−04
31	11	16113	535	294	3.05E−04 ± 5.07E−05
23	12	11719	614	389	1.75E−01 ± 3.09E−02
24	12	12310	578	318	4.87E+00 ± 4.80E−01
25	12	12782 ± 24	514 ± 16	338 ± 9	9.74E+00 ± 5.88E−01
26	12	13275 ± 21	493 ± 8	358 ± 8	1.26E+01 ± 6.62E−01
27	12	13873 ± 20	524 ± 7	342 ± 9	5.16E+00 ± 2.67E−01
28	12	14455 ± 23	536 ± 10	340 ± 10	2.26E+00 ± 1.20E−01
29	12	14984 ± 29	517 ± 18	356 ± 10	3.84E−01 ± 2.23E−02
30	12	15668 ± 28	572 ± 31	304 ± 9	1.37E−01 ± 9.59E−03
31	12	16194	633	317	2.30E−02 ± 2.61E−03
32	12	16741 ± 34	585 ± 54	320 ± 14	6.20E−03 ± 5.07E−04
33	12	17173	478	333	4.98E−04 ± 8.35E−05
34	12	17704	558	279	8.06E−05 ± 1.42E−05
25	13	12719	454	410	7.75E−02 ± 1.65E−02
26	13	13282 ± 37	540 ± 50	354 ± 13	2.21E+00 ± 1.92E−01
27	13	13822 ± 23	512 ± 15	334 ± 8	1.28E+01 ± 7.33E−01
28	13	14353 ± 20	515 ± 8	341 ± 8	1.17E+01 ± 5.98E−01
29	13	14931 ± 19	530 ± 7	340 ± 8	8.63E+00 ± 4.23E−01
30	13	15543 ± 22	543 ± 10	316 ± 9	2.72E+00 ± 1.36E−01
31	13	16034 ± 21	497 ± 12	341 ± 7	1.14E+00 ± 5.74E−02
32	13	16669 ± 30	516 ± 22	318 ± 10	2.24E−01 ± 1.35E−02
33	13	17224 ± 26	484 ± 29	313 ± 8	8.89E−02 ± 6.36E−03
34	13	17731 ± 30	491 ± 41	337 ± 10	1.28E−02 ± 9.53E−04
35	13	18339 ± 32	539 ± 35	310 ± 14	3.78E−03 ± 2.51E−04
36	13	18847 ± 46	496 ± 42	360 ± 8	3.18E−04 ± 3.96E−05

continued on next page

Table A.3: continued from previous page

A	Z	p_0 (MeV/c)	σ_L (MeV/c)	σ_R (MeV/c)	σ_{prod} (mb)
37	13	19412	420	304	7.33E−05 ± 1.92E−05
38	13	19797	369	250	2.64E−06 ± 9.27E−07
26	14	13139	532	372	3.50E−03 ± 1.73E−03
27	14	13775	609	370	1.31E−01 ± 1.81E−02
28	14	14318	511	344	5.00E+00 ± 6.27E−01
29	14	14855 ± 24	497 ± 13	333 ± 9	1.27E+01 ± 7.00E−01
30	14	15424 ± 18	513 ± 7	323 ± 6	2.02E+01 ± 9.82E−01
31	14	16013 ± 18	529 ± 7	318 ± 7	1.02E+01 ± 4.88E−01
32	14	16628 ± 21	536 ± 9	296 ± 8	4.98E+00 ± 2.45E−01
33	14	17128 ± 23	486 ± 13	318 ± 9	1.37E+00 ± 7.28E−02
34	14	17769 ± 22	520 ± 16	287 ± 7	5.67E−01 ± 3.06E−02
35	14	18307 ± 25	449 ± 31	292 ± 8	1.19E−01 ± 9.81E−03
36	14	18839 ± 23	443 ± 25	296 ± 7	4.28E−02 ± 2.90E−03
37	14	19424 ± 31	502 ± 32	287 ± 11	6.19E−03 ± 4.20E−04
38	14	19970 ± 24	463 ± 24	284 ± 8	1.57E−03 ± 9.83E−05
39	14	20513	406	240	1.18E−04 ± 1.63E−05
40	14	21010	458	310	2.79E−05 ± 4.06E−06
41	14	21671	371	255	1.84E−06 ± 8.25E−07
28	15	14418	527	303	1.08E−03 ± 4.07E−04
29	15	14781	395	361	3.89E−02 ± 1.14E−02
30	15	15272 ± 37	449 ± 29	397 ± 15	1.17E+00 ± 8.11E−02
31	15	15921 ± 22	498 ± 12	322 ± 8	1.13E+01 ± 5.93E−01
32	15	16491 ± 18	515 ± 7	309 ± 6	1.60E+01 ± 7.64E−01
33	15	17090 ± 17	524 ± 6	297 ± 7	1.51E+01 ± 6.90E−01
34	15	17686 ± 19	526 ± 9	291 ± 7	6.90E+00 ± 3.31E−01
35	15	18243 ± 20	488 ± 10	286 ± 8	3.79E+00 ± 1.87E−01
36	15	18852 ± 20	486 ± 13	266 ± 7	1.19E+00 ± 6.11E−02
37	15	19433 ± 19	477 ± 14	258 ± 6	5.04E−01 ± 2.76E−02
38	15	19947 ± 22	451 ± 20	271 ± 7	1.34E−01 ± 9.08E−03
39	15	20478 ± 21	421 ± 20	273 ± 7	4.11E−02 ± 2.43E−03
40	15	21016 ± 23	425 ± 18	278 ± 9	6.12E−03 ± 3.45E−04
41	15	21583 ± 23	400 ± 17	256 ± 7	1.25E−03 ± 7.36E−05
42	15	22130 ± 27	395 ± 27	252 ± 10	1.19E−04 ± 1.08E−05
43	15	22659	375	254	1.26E−05 ± 2.21E−06
30	16	15246	517	402	7.85E−04 ± 3.02E−04
31	16	15772	469	390	4.95E−02 ± 1.53E−02
32	16	16335 ± 33	439 ± 24	377 ± 13	1.88E+00 ± 1.21E−01
33	16	16960 ± 22	484 ± 10	320 ± 8	9.31E+00 ± 4.74E−01
34	16	17551 ± 17	500 ± 7	304 ± 6	2.08E+01 ± 9.87E−01
35	16	18170 ± 17	517 ± 6	281 ± 6	1.69E+01 ± 7.71E−01
36	16	18757 ± 18	506 ± 8	270 ± 7	1.16E+01 ± 5.47E−01
37	16	19328 ± 20	474 ± 9	267 ± 7	5.62E+00 ± 2.79E−01
38	16	19874 ± 21	436 ± 11	270 ± 8	2.96E+00 ± 1.57E−01

continued on next page

Table A.3: continued from previous page

A	Z	p_0 (MeV/c)	σ_L (MeV/c)	σ_R (MeV/c)	σ_{prod} (mb)
39	16	20443 ± 20	412 ± 11	272 ± 6	1.08E+00 ± 5.37E−02
40	16	21015 ± 20	403 ± 15	254 ± 6	4.89E−01 ± 3.07E−02
41	16	21571 ± 21	385 ± 17	246 ± 7	1.04E−01 ± 6.78E−03
42	16	22132 ± 19	379 ± 15	233 ± 6	2.76E−02 ± 1.56E−03
43	16	22663 ± 14	375 ± 9	228 ± 7	2.78E−03 ± 1.43E−04
44	16	23227 ± 22	333 ± 16	210 ± 8	5.14E−04 ± 3.43E−05
45	*16*	*23590 ± 18*	*297 ± 53*	*201 ± 34*	*1.42E−05 ± 2.97E−06*
32	17	16326	504	392	4.04E−04 ± 1.53E−04
33	17	16898	484	334	1.30E−02 ± 2.50E−03
34	17	17375 ± 15	442 ± 17	378 ± 8	5.91E−01 ± 3.52E−02
35	17	18060 ± 20	486 ± 9	288 ± 7	7.85E+00 ± 3.88E−01
36	17	18620 ± 17	493 ± 7	288 ± 6	1.65E+01 ± 7.91E−01
37	17	19238 ± 18	497 ± 7	271 ± 7	2.14E+01 ± 1.04E+00
38	17	19804 ± 19	478 ± 8	266 ± 7	1.39E+01 ± 7.33E−01
39	17	20376 ± 20	441 ± 9	259 ± 7	1.10E+01 ± 5.70E−01
40	17	20904 ± 18	402 ± 9	273 ± 7	5.98E+00 ± 3.38E−01
41	17	21498 ± 18	380 ± 10	252 ± 6	3.78E+00 ± 2.01E−01
42	17	22091 ± 21	367 ± 11	237 ± 6	1.54E+00 ± 9.02E−02
43	17	22659 ± 17	347 ± 11	221 ± 5	6.53E−01 ± 4.36E−02
44	17	23164 ± 19	311 ± 12	228 ± 7	1.56E−01 ± 9.20E−03
45	17	23752 ± 10	297 ± 1	183 ± 4	3.43E−02 ± 1.70E−03
46	*17*	*24183 ± 9*	*245 ± 1*	*166 ± 1*	*9.16E−04 ± 4.79E−05*
47	*17*	*24719 ± 32*	*307 ± 77*	*227 ± 60*	*2.95E−05 ± 6.25E−06*
35	18	17872	390	343	1.50E−02 ± 2.28E−03
36	18	18471 ± 31	425 ± 17	340 ± 14	8.15E−01 ± 5.03E−02
37	18	19110 ± 21	469 ± 9	284 ± 8	5.57E+00 ± 2.88E−01
38	18	19711 ± 17	474 ± 7	263 ± 7	1.68E+01 ± 8.95E−01
39	18	20311 ± 18	474 ± 7	249 ± 7	2.13E+01 ± 1.13E+00
40	18	20907 ± 18	452 ± 8	234 ± 7	2.07E+01 ± 1.18E+00
41	18	21432 ± 19	395 ± 8	250 ± 7	1.71E+01 ± 9.62E−01
42	18	22026 ± 19	370 ± 8	231 ± 8	1.42E+01 ± 8.77E−01
43	18	22549 ± 19	322 ± 9	247 ± 7	8.61E+00 ± 5.03E−01
44	18	23170 ± 24	309 ± 10	210 ± 10	5.60E+00 ± 3.81E−01
45	18	23719 ± 4	297 ± 6	201 ± 1	2.30E+00 ± 1.01E−01
46	18	24299 ± 10	245 ± 3	147 ± 4	1.08E+00 ± 6.61E−02
47	*18*	*24668 ± 5*	*203 ± 1*	*150 ± 4*	*1.45E−02 ± 3.40E−03*
48	*18*	*25164 ± 14*	*230 ± 5*	*185 ± 7*	*1.06E−03 ± 8.83E−05*
49	*18*	*25736 ± 23*	*239 ± 50*	*190 ± 15*	*3.01E−04 ± 5.42E−05*
37	19	19015	499	302	4.51E−03 ± 1.21E−03
38	19	19493 ± 34	407 ± 17	345 ± 20	2.28E−01 ± 1.54E−02
39	19	20191 ± 19	448 ± 8	262 ± 8	3.83E+00 ± 2.12E−01
40	19	20782 ± 18	451 ± 7	241 ± 7	1.15E+01 ± 6.80E−01
41	19	21372 ± 18	431 ± 7	230 ± 7	2.01E+01 ± 1.15E+00

continued on next page

Table A.3: continued from previous page

A	Z	p_0 (MeV/c)	σ_L (MeV/c)	σ_R (MeV/c)	σ_{prod} (mb)
42	19	21953 ± 16	402 ± 7	220 ± 6	2.31E+01 ± 1.41E+00
43	19	22518 ± 17	356 ± 8	213 ± 6	2.82E+01 ± 1.88E+00
44	19	23092 ± 24	323 ± 9	211 ± 12	2.46E+01 ± 2.07E+00
45	19	23644 ± 7	276 ± 5	201 ± 6	2.61E+01 ± 1.78E+00
46	19	24245 ± 4	245 ± 1	166 ± 1	2.19E+01 ± 9.44E−01
47	19	24775	175	119	1.91E+01 ± 4.30E+00
48	*19*	*25230 ± 20*	*293 ± 11*	*208 ± 5*	*3.50E−01 ± 3.55E−02*
49	*19*	*25405 ± 81*	*121 ± 25*	*121 ± 25*	*1.59E−02 ± 1.02E−02*
50	*19*	*26222 ± 7*	*185 ± 8*	*140 ± 3*	*1.13E−02 ± 8.88E−04*
39	20	20170	483	212	3.29E−03 ± 5.61E−04
40	20	20659 ± 28	400 ± 13	276 ± 15	2.56E−01 ± 1.74E−02
41	20	21294 ± 18	424 ± 8	223 ± 8	2.40E+00 ± 1.49E−01
42	20	21876 ± 9	406 ± 4	205 ± 5	9.32E+00 ± 5.28E−01
43	20	22433 ± 10	375 ± 3	204 ± 6	1.67E+01 ± 1.09E+00
44	20	23018 ± 12	340 ± 3	192 ± 7	2.39E+01 ± 1.98E+00
45	20	23599 ± 9	297 ± 4	176 ± 5	3.06E+01 ± 2.04E+00
46	20	24181 ± 10	245 ± 1	157 ± 5	4.57E+01 ± 3.28E+00
47	20	24777 ± 10	175 ± 1	105 ± 4	7.59E+01 ± 6.11E+00
49	*20*	*25836 ± 24*	*290 ± 11*	*209 ± 10*	*7.68E−01 ± 7.71E−02*
50	*20*	*26367 ± 44*	*192 ± 27*	*166 ± 15*	*1.40E−02 ± 2.13E−03*
51	*20*	*26969 ± 19*	*230 ± 46*	*178 ± 42*	*1.02E−03 ± 1.82E−04*
41	*21*	*21238 ± 67*	*320 ± 91*	*293 ± 73*	*3.99E−04 ± 1.09E−04*
42	*21*	*21664 ± 37*	*369 ± 19*	*270 ± 59*	*3.67E−02 ± 4.56E−03*
43	*21*	*22315 ± 12*	*375 ± 3*	*205 ± 8*	*5.82E−01 ± 3.70E−02*
44	*21*	*22892 ± 11*	*340 ± 2*	*181 ± 6*	*2.58E+00 ± 1.68E−01*
45	*21*	*23450 ± 13*	*297 ± 1*	*169 ± 7*	*5.53E+00 ± 4.39E−01*
46	*21*	*24016 ± 5*	*245 ± 1*	*166 ± 4*	*6.38E+00 ± 3.15E−01*
47	*21*	*24619 ± 6*	*175 ± 1*	*119 ± 1*	*8.38E+00 ± 4.76E−01*
48	*21*	*25442 ± 17*	*331 ± 11*	*131 ± 6*	*5.26E+00 ± 5.68E−01*
49	*21*	*25995 ± 40*	*396 ± 20*	*485 ± 79*	*1.14E+00 ± 2.17E−01*
44	*22*	*22707 ± 23*	*340 ± 8*	*230 ± 9*	*5.41E−03 ± 4.37E−04*
45	*22*	*23247 ± 15*	*297 ± 2*	*201 ± 2*	*3.56E−02 ± 2.18E−03*
46	*22*	*23848 ± 10*	*345 ± 18*	*255 ± 8*	*1.05E−01 ± 6.43E−03*
47	*22*	*24406 ± 13*	*398 ± 8*	*294 ± 18*	*1.08E−01 ± 6.53E−03*
48	*22*	*25051 ± 17*	*473 ± 10*	*350 ± 4*	*7.18E−02 ± 4.41E−03*

Table A.4: Fitting results for the reaction system ^{48}Ca+^{181}Ta.

A	Z	p_0 (MeV/c)	σ_L (MeV/c)	σ_R (MeV/c)	σ_{prod} (mb)
11	5	5591 ± 13	450 ± 4	319 ± 6	7.47E+01 ± 4.18E+00
12	5	6212 ± 1	482 ± 14	263 ± 1	1.48E+01 ± 8.19E−01
13	5	6645 ± 13	365 ± 19	319 ± 7	3.59E+00 ± 2.10E−01
14	5	7124	445	370	2.11E−01 ± 2.48E−02
12	6	6168	499	298	4.75E+01 ± 7.93E+00
13	6	6644 ± 21	438 ± 34	319 ± 7	4.28E+01 ± 3.17E+00
14	6	7175 ± 19	457 ± 14	328 ± 6	2.11E+01 ± 1.22E+00
15	6	7674 ± 16	366 ± 13	345 ± 5	2.38E+00 ± 1.44E−01
16	6	8277 ± 18	525 ± 5	306 ± 11	7.57E−01 ± 3.69E−02
17	6	8645	393	390	5.99E−02 ± 7.25E−03
14	7	7177	408	285	1.56E+01 ± 1.56E+00
15	7	7579 ± 22	432 ± 19	362 ± 10	4.75E+01 ± 3.08E+00
16	7	8118 ± 16	376 ± 6	348 ± 5	8.80E+00 ± 4.64E−01
17	7	8623 ± 13	458 ± 12	383 ± 4	4.51E+00 ± 2.49E−01
18	7	9192 ± 15	398 ± 23	377 ± 5	8.64E−01 ± 5.04E−02
19	7	9828	579	366	2.45E−01 ± 1.76E−02
20	7	10254	488	402	2.07E−02 ± 2.86E−03
16	8	8083 ± 21	388 ± 26	358 ± 10	2.59E+01 ± 1.79E+00
17	8	8669 ± 26	472 ± 20	334 ± 12	1.83E+01 ± 1.19E+00
18	8	9199 ± 18	499 ± 10	345 ± 7	1.54E+01 ± 8.37E−01
19	8	9708 ± 11	504 ± 7	367 ± 4	4.36E+00 ± 2.12E−01
20	8	10181 ± 14	405 ± 19	384 ± 5	1.48E+00 ± 8.27E−02
21	8	10832 ± 19	468 ± 8	345 ± 8	1.91E−01 ± 8.66E−03
22	8	11360	538	394	3.52E−02 ± 3.46E−03
23	8	11735	532	389	1.17E−03 ± 1.80E−04
17	9	8882	202	147	3.54E−01 ± 1.10E−01
18	9	9132	399	371	5.61E+00 ± 6.66E−01
19	9	9703 ± 26	492 ± 42	343 ± 11	1.71E+01 ± 1.33E+00
20	9	10238 ± 24	515 ± 11	342 ± 11	1.54E+01 ± 8.39E−01
21	9	10722 ± 17	502 ± 11	371 ± 5	7.79E+00 ± 4.00E−01
22	9	11265 ± 18	500 ± 12	365 ± 7	1.73E+00 ± 9.44E−02
23	9	11820 ± 20	451 ± 31	357 ± 6	4.94E−01 ± 3.25E−02
24	9	12419 ± 20	493 ± 5	351 ± 10	4.79E−02 ± 1.99E−03
25	9	12974	549	303	5.37E−03 ± 7.51E−04
19	10	9853	369	278	5.22E−01 ± 1.09E−01
20	10	10213	446	339	9.65E+00 ± 1.10E+00
21	10	10749 ± 13	493 ± 14	334 ± 7	2.11E+01 ± 1.15E+00
22	10	11269 ± 24	507 ± 10	340 ± 10	2.29E+01 ± 1.21E+00
23	10	11828 ± 22	522 ± 9	331 ± 9	7.13E+00 ± 3.56E−01
24	10	12321 ± 13	516 ± 4	367 ± 5	2.67E+00 ± 1.27E−01
25	10	12940 ± 19	427 ± 5	316 ± 7	4.13E−01 ± 2.10E−02

continued on next page

Table A.4: continued from previous page

A	Z	p_0 (MeV/c)	σ_L (MeV/c)	σ_R (MeV/c)	σ_{prod} (mb)
26	10	13414 ± 19	462 ± 11	354 ± 7	9.17E−02 ± 4.21E−03
27	10	13942	552	394	4.82E−03 ± 5.79E−04
28	10	14502	493	314	1.74E−03 ± 1.96E−04
21	11	10801	462	364	4.06E−01 ± 8.69E−02
22	11	11266	474	345	6.15E+00 ± 4.43E−01
23	11	11816 ± 24	518 ± 18	326 ± 9	2.53E+01 ± 1.54E+00
24	11	12340 ± 23	530 ± 10	332 ± 9	1.87E+01 ± 9.59E−01
25	11	12893 ± 20	547 ± 8	341 ± 8	1.16E+01 ± 5.53E−01
26	11	13382 ± 13	518 ± 6	353 ± 6	3.22E+00 ± 1.50E−01
27	11	13933 ± 15	471 ± 3	337 ± 6	1.04E+00 ± 4.72E−02
28	11	14480 ± 17	443 ± 20	340 ± 6	1.54E−01 ± 8.32E−03
29	11	15008 ± 20	477 ± 7	359 ± 8	3.73E−02 ± 1.42E−03
30	11	15583 ± 26	545 ± 24	356 ± 22	5.25E−03 ± 2.88E−04
31	11	16015	462	390	1.03E−03 ± 1.93E−04
23	12	11762	497	397	5.92E−01 ± 9.72E−02
24	12	12296	486	344	1.21E+01 ± 9.82E−01
25	12	12838 ± 13	495 ± 5	328 ± 6	2.42E+01 ± 1.19E+00
26	12	13390 ± 21	523 ± 14	325 ± 8	2.87E+01 ± 1.47E+00
27	12	13940 ± 21	535 ± 8	317 ± 9	1.20E+01 ± 5.67E−01
28	12	14503 ± 23	533 ± 11	307 ± 9	5.41E+00 ± 2.66E−01
29	12	14985 ± 15	471 ± 3	335 ± 6	9.66E−01 ± 4.50E−02
30	12	15578 ± 18	424 ± 3	312 ± 7	3.41E−01 ± 1.61E−02
31	12	16032 ± 29	430 ± 40	351 ± 10	5.34E−02 ± 4.13E−03
32	12	16614 ± 18	482 ± 17	354 ± 10	1.54E−02 ± 6.25E−04
33	12	17161	516	378	1.61E−03 ± 2.20E−04
34	12	17422	449	274	1.82E−04 ± 4.22E−05
25	13	12784	500	390	2.59E−01 ± 6.31E−02
26	13	13343	507	357	5.26E+00 ± 4.30E−01
27	13	13881 ± 12	495 ± 5	324 ± 6	2.81E+01 ± 1.38E+00
28	13	14423 ± 9	519 ± 2	327 ± 4	2.48E+01 ± 1.14E+00
29	13	14983 ± 8	535 ± 5	327 ± 3	1.82E+01 ± 8.14E−01
30	13	15505 ± 13	496 ± 2	326 ± 6	6.09E+00 ± 2.62E−01
31	13	16047 ± 14	476 ± 3	322 ± 6	2.66E+00 ± 1.21E−01
32	13	16604 ± 16	441 ± 3	315 ± 6	5.73E−01 ± 2.54E−02
33	13	17145 ± 15	418 ± 5	319 ± 6	2.00E−01 ± 8.46E−03
34	13	17622 ± 26	431 ± 39	353 ± 10	2.97E−02 ± 1.94E−03
35	13	18245 ± 16	470 ± 7	331 ± 10	9.18E−03 ± 3.46E−04
36	13	18806 ± 29	413 ± 13	297 ± 13	9.41E−04 ± 5.51E−05
37	13	19150	346	253	1.58E−04 ± 4.34E−05
27	14	13902	552	333	3.31E−01 ± 6.30E−02
28	14	14392	487	342	1.03E+01 ± 7.64E−01
29	14	14940 ± 12	488 ± 3	313 ± 6	2.58E+01 ± 1.24E+00
30	14	15484 ± 9	509 ± 2	317 ± 5	3.84E+01 ± 1.70E+00

continued on next page

Table A.4: continued from previous page

A	Z	p_0 (MeV/c)	σ_L (MeV/c)	σ_R (MeV/c)	σ_{prod} (mb)
31	14	16037 ± 5	515 ± 3	309 ± 2	2.03E+01 ± 7.15E−01
32	14	16601 ± 24	502 ± 11	310 ± 11	1.03E+01 ± 5.14E−01
33	14	17144 ± 14	481 ± 4	309 ± 8	2.88E+00 ± 1.35E−01
34	14	17656 ± 13	426 ± 3	306 ± 5	1.30E+00 ± 5.72E−02
35	14	18219 ± 16	395 ± 8	300 ± 6	2.56E−01 ± 1.27E−02
36	14	18704 ± 14	376 ± 14	315 ± 6	9.48E−02 ± 4.17E−03
37	14	19276 ± 18	447 ± 29	326 ± 10	1.47E−02 ± 7.65E−04
38	14	19894 ± 16	410 ± 11	273 ± 11	3.86E−03 ± 1.79E−04
39	14	20382	447	243	4.43E−04 ± 7.66E−05
40	14	20924	403	298	9.01E−05 ± 2.20E−05
29	15	14874	433	361	1.00E−01 ± 2.33E−02
30	15	15410 ± 42	480 ± 33	401 ± 16	2.40E+00 ± 1.64E−01
31	15	16005 ± 21	496 ± 43	316 ± 8	2.04E+01 ± 1.54E+00
32	15	16535 ± 9	502 ± 2	314 ± 5	2.92E+01 ± 1.27E+00
33	15	17093 ± 5	509 ± 2	306 ± 13	2.82E+01 ± 1.05E+00
34	15	17624 ± 12	468 ± 2	308 ± 6	1.36E+01 ± 5.85E−01
35	15	18210 ± 12	459 ± 1	289 ± 6	7.63E+00 ± 3.43E−01
36	15	18759 ± 13	421 ± 2	284 ± 6	2.49E+00 ± 1.17E−01
37	15	19309 ± 14	385 ± 1	277 ± 5	1.08E+00 ± 4.81E−02
38	15	19833 ± 12	378 ± 6	284 ± 5	2.88E−01 ± 1.23E−02
39	15	20359 ± 12	388 ± 10	290 ± 5	8.44E−02 ± 3.04E−03
40	15	20942 ± 13	400 ± 2	277 ± 7	1.36E−02 ± 4.80E−04
41	15	21484 ± 28	377 ± 21	263 ± 15	3.08E−03 ± 1.88E−04
42	15	22004	365	269	3.98E−04 ± 7.33E−05
43	15	22261	261	216	2.54E−05 ± 1.07E−05
31	16	15900	453	384	1.07E−01 ± 2.19E−02
32	16	16476 ± 35	460 ± 25	365 ± 13	3.42E+00 ± 2.13E−01
33	16	17041 ± 25	483 ± 11	316 ± 11	1.56E+01 ± 9.32E−01
34	16	17594 ± 9	487 ± 1	305 ± 5	3.58E+01 ± 1.63E+00
35	16	18152 ± 9	489 ± 1	296 ± 5	3.05E+01 ± 1.31E+00
36	16	18686 ± 11	439 ± 1	294 ± 5	2.29E+01 ± 9.95E−01
37	16	19280 ± 11	453 ± 2	287 ± 6	1.04E+01 ± 4.73E−01
38	16	19850 ± 13	409 ± 2	259 ± 6	6.08E+00 ± 3.16E−01
39	16	20369 ± 22	402 ± 17	279 ± 8	2.13E+00 ± 1.29E−01
40	16	20932 ± 12	336 ± 2	254 ± 4	9.91E−01 ± 4.42E−02
41	16	21444 ± 10	347 ± 11	257 ± 4	2.09E−01 ± 8.58E−03
42	16	22009 ± 9	343 ± 2	241 ± 5	5.14E−02 ± 1.63E−03
43	16	22524 ± 12	357 ± 5	245 ± 7	6.36E−03 ± 2.70E−04
44	16	23086 ± 11	308 ± 7	225 ± 7	1.30E−03 ± 6.32E−05
45	*16*	*23555 ± 120*	*353 ± 76*	*292 ± 99*	*9.64E−05 ± 2.79E−05*
33	17	17007	500	364	2.59E−02 ± 6.38E−03
34	17	17576	506	370	1.06E+00 ± 5.00E−02
35	17	18122 ± 9	479 ± 7	293 ± 12	1.27E+01 ± 7.23E−01

continued on next page

Table A.4: continued from previous page

A	Z	p_0 (MeV/c)	σ_L (MeV/c)	σ_R (MeV/c)	σ_{prod} (mb)
36	17	18639 ± 10	472 ± 1	294 ± 5	2.76E+01 ± 1.29E+00
37	17	19205 ± 9	463 ± 1	282 ± 4	3.88E+01 ± 1.73E+00
38	17	19746 ± 11	421 ± 2	283 ± 5	2.64E+01 ± 1.18E+00
39	17	20360 ± 5	432 ± 4	259 ± 12	1.91E+01 ± 7.76E−01
40	17	20901 ± 11	396 ± 3	262 ± 5	1.14E+01 ± 5.69E−01
41	17	21453 ± 11	370 ± 8	250 ± 6	7.08E+00 ± 3.97E−01
42	17	22014 ± 11	351 ± 31	242 ± 4	2.77E+00 ± 1.99E−01
43	17	22556 ± 8	296 ± 1	216 ± 3	1.31E+00 ± 5.47E−02
44	17	23073 ± 9	301 ± 3	220 ± 4	2.63E−01 ± 8.60E−03
45	17	23645 ± 8	281 ± 1	182 ± 4	5.30E−02 ± 1.91E−03
46	*17*	*24037 ± 13*	*320 ± 11*	*217 ± 9*	*3.83E−03 ± 2.05E−04*
47	*17*	*24478 ± 41*	*330 ± 8*	*288 ± 39*	*6.03E−04 ± 5.53E−05*
35	18	18066	427	311	2.89E−02 ± 4.54E−03
36	18	18643	472	353	1.34E+00 ± 8.14E−02
37	18	19165 ± 9	461 ± 7	290 ± 4	8.64E+00 ± 4.89E−01
38	18	19725 ± 5	457 ± 2	274 ± 4	2.61E+01 ± 9.80E−01
39	18	20271 ± 9	443 ± 2	269 ± 5	3.68E+01 ± 1.74E+00
40	18	20822 ± 10	387 ± 2	260 ± 5	3.89E+01 ± 1.83E+00
41	18	21412 ± 10	393 ± 2	250 ± 5	2.93E+01 ± 1.52E+00
42	18	22011 ± 8	372 ± 6	226 ± 3	2.46E+01 ± 1.43E+00
43	18	22530 ± 19	326 ± 8	233 ± 8	1.55E+01 ± 1.07E+00
44	18	23100 ± 17	318 ± 8	222 ± 6	9.31E+00 ± 6.30E−01
45	18	23638 ± 4	269 ± 2	197 ± 1	4.07E+00 ± 1.83E−01
46	18	24202 ± 6	222 ± 1	138 ± 2	1.63E+00 ± 6.56E−02
47	*18*	*24545 ± 13*	*236 ± 1*	*177 ± 6*	*4.50E−02 ± 1.74E−03*
48	*18*	*25046 ± 23*	*315 ± 14*	*201 ± 12*	*1.39E−02 ± 7.47E−04*
49	*18*	*25614 ± 5*	*220 ± 6*	*180 ± 1*	*4.55E−03 ± 1.96E−04*
50	*18*	*26050 ± 46*	*331 ± 82*	*249 ± 75*	*1.30E−04 ± 3.17E−05*
37	19	19093	394	342	7.48E−03 ± 1.18E−03
38	19	19614	424	331	3.53E−01 ± 5.06E−02
39	19	20210 ± 9	435 ± 7	281 ± 2	5.49E+00 ± 3.35E−01
40	19	20779 ± 5	442 ± 3	265 ± 3	1.61E+01 ± 6.35E−01
41	19	21216 ± 15	351 ± 1	282 ± 6	3.51E+01 ± 1.97E+00
42	19	21889 ± 9	359 ± 3	237 ± 4	4.14E+01 ± 2.08E+00
43	19	22472 ± 9	339 ± 1	216 ± 4	5.00E+01 ± 2.66E+00
44	19	23065 ± 17	330 ± 8	212 ± 7	3.85E+01 ± 2.77E+00
45	19	23630 ± 17	295 ± 8	224 ± 6	4.21E+01 ± 3.30E+00
46	19	24174 ± 7	272 ± 5	184 ± 4	2.89E+01 ± 2.09E+00
47	19	24757 ± 5	159 ± 1	116 ± 1	4.25E+01 ± 2.28E+00
48	*19*	*25020 ± 6*	*245 ± 6*	*181 ± 1*	*9.87E−01 ± 5.86E−02*
49	*19*	*25512 ± 9*	*208 ± 7*	*173 ± 4*	*2.23E−01 ± 1.08E−02*
50	*19*	*26118 ± 5*	*162 ± 1*	*120 ± 2*	*1.56E−01 ± 6.28E−03*
51	*19*	*26278 ± 40*	*225 ± 21*	*204 ± 18*	*1.86E−03 ± 1.85E−04*

continued on next page

Table A.4: continued from previous page

A	Z	p_0 (MeV/c)	σ_L (MeV/c)	σ_R (MeV/c)	σ_{prod} (mb)
52	*19*	*27048 ± 15*	*281 ± 52*	*207 ± 73*	*5.66E−04 ± 1.11E−04*
53	*19*	*27734 ± 24*	*196 ± 19*	*162 ± 56*	*4.47E−04 ± 1.13E−04*
40	20	20737	400	269	3.69E−01 ± 2.80E−02
41	20	21294 ± 13	416 ± 8	285 ± 6	3.52E+00 ± 2.31E−01
42	20	21820 ± 9	408 ± 8	257 ± 1	9.42E+00 ± 8.17E−01
43	20	22348 ± 16	301 ± 1	232 ± 6	2.90E+01 ± 1.64E+00
44	20	22969 ± 10	304 ± 1	197 ± 5	4.67E+01 ± 2.93E+00
45	20	23516 ± 10	273 ± 1	204 ± 5	4.93E+01 ± 3.58E+00
46	20	24174 ± 11	269 ± 2	202 ± 6	7.64E+01 ± 6.79E+00
47	20	24862 ± 6	270 ± 6	199 ± 1	1.34E+02 ± 9.62E+00
51	*20*	*26590 ± 22*	*165 ± 26*	*142 ± 7*	*1.04E+00 ± 1.58E−01*
52	*20*	*27496 ± 14*	*138 ± 12*	*126 ± 7*	*4.99E−03 ± 4.25E−04*
42	*21*	*21724 ± 22*	*375 ± 17*	*289 ± 16*	*4.99E−02 ± 3.96E−03*
43	*21*	*22331 ± 15*	*386 ± 11*	*299 ± 5*	*8.31E−01 ± 6.45E−02*
44	*21*	*22848 ± 20*	*386 ± 12*	*278 ± 5*	*1.87E+00 ± 2.13E−01*
45	*21*	*23377 ± 17*	*246 ± 41*	*201 ± 8*	*6.43E+00 ± 8.04E−01*
46	*21*	*23890 ± 40*	*276 ± 17*	*248 ± 19*	*4.80E+00 ± 9.36E−01*
47	*21*	*24368 ± 8*	*204 ± 4*	*269 ± 7*	*7.93E+00 ± 7.14E−01*
48	*21*	*25164 ± 12*	*250 ± 3*	*190 ± 5*	*3.23E+00 ± 2.10E−01*
49	*21*	*25669 ± 51*	*329 ± 29*	*281 ± 96*	*4.10E−01 ± 7.73E−02*
50	*21*	*25905 ± 1*	*410 ± 89*	*409 ± 42*	*2.56E−02 ± 6.21E−03*
44	*22*	*22694 ± 131*	*374 ± 142*	*342 ± 125*	*6.05E−03 ± 1.87E−03*
45	*22*	*23299 ± 74*	*354 ± 30*	*398 ± 84*	*6.01E−02 ± 2.36E−02*
46	*22*	*23822 ± 26*	*398 ± 22*	*314 ± 13*	*9.29E−02 ± 1.13E−02*
47	*22*	*24438 ± 59*	*296 ± 50*	*234 ± 45*	*1.45E−01 ± 2.93E−02*
48	*22*	*24995 ± 107*	*375 ± 47*	*426 ± 99*	*9.01E−02 ± 1.89E−02*
49	*22*	*25466 ± 16*	*209 ± 48*	*276 ± 13*	*3.53E−01 ± 5.47E−02*
50	*22*	*26207 ± 21*	*279 ± 10*	*206 ± 10*	*4.39E−02 ± 4.25E−03*
51	*22*	*26748 ± 17*	*128 ± 21*	*98 ± 8*	*4.04E−02 ± 6.54E−03*

A.3 Results for ^{58}Ni projectile

Table A.5: Fitting results for the reaction system ^{58}Ni+^{9}Be.

A	Z	p_0 (MeV/c)	σ_L (MeV/c)	σ_R (MeV/c)	σ_{prod} (mb)
10	5	5450	496	268	4.11E+00 ± 5.11E−01
11	5	5723	514	377	6.28E+00 ± 1.82E+00
12	5	5896	393	288	3.23E−01 ± 1.80E−01
12	6	6326	531	288	7.64E+00 ± 5.22E−01
13	6	6745	547	401	4.85E+00 ± 5.40E−01
14	6	7088	457	304	9.00E−01 ± 1.45E−01
13	7	6957	181	130	1.51E−01 ± 5.68E−02
14	7	7313	498	334	3.05E+00 ± 4.07E−01
15	7	7673 ± 21	472 ± 17	408 ± 12	5.77E+00 ± 3.26E−01
16	7	8208	501	317	4.01E−01 ± 5.64E−02
17	7	8467	441	380	1.00E−01 ± 1.64E−02
16	8	8305	586	330	5.85E+00 ± 1.17E+00
17	8	8696 ± 18	457 ± 14	388 ± 8	2.85E+00 ± 1.56E−01
18	8	9283	594	338	9.79E−01 ± 9.02E−02
19	8	9614	570	392	1.31E−01 ± 3.33E−02
17	9	8878	507	402	2.42E−01 ± 5.45E−02
18	9	9263	607	402	1.51E+00 ± 1.70E−01
19	9	9730 ± 17	490 ± 13	391 ± 7	2.54E+00 ± 1.31E−01
20	9	10269 ± 12	461 ± 4	411 ± 14	9.66E−01 ± 4.48E−02
21	9	10616	593	341	2.86E−01 ± 5.44E−02
22	9	11213	471	405	3.66E−02 ± 7.94E−03
19	10	9856	455	426	2.52E−01 ± 3.67E−02
20	10	10263	624	380	2.85E+00 ± 1.67E−01
21	10	10752 ± 14	499 ± 10	393 ± 5	4.07E+00 ± 1.88E−01
22	10	11307 ± 27	576 ± 15	403 ± 15	2.06E+00 ± 1.07E−01
23	10	11690	474	371	2.69E−01 ± 3.06E−02
24	10	11879	307	226	2.60E−02 ± 7.75E−03
21	11	10808	526	419	2.09E−01 ± 3.67E−02
22	11	11246	637	420	2.10E+00 ± 2.76E−01
23	11	11755 ± 13	503 ± 9	397 ± 5	5.21E+00 ± 2.25E−01
24	11	12214 ± 22	526 ± 13	443 ± 9	1.95E+00 ± 9.87E−02
25	11	12676	508	476	5.93E−01 ± 4.28E−02
26	11	13114	574	353	6.50E−02 ± 1.22E−02
27	11	13662	484	417	9.14E−03 ± 3.69E−03
23	12	11783	642	470	4.06E−01 ± 5.34E−02
24	12	12216	574	436	4.36E+00 ± 2.96E−01
25	12	12772 ± 14	540 ± 10	403 ± 5	6.15E+00 ± 2.54E−01
26	12	13252 ± 16	531 ± 9	427 ± 6	3.99E+00 ± 1.81E−01

continued on next page

Table A.5: continued from previous page

A	Z	p_0 (MeV/c)	σ_L (MeV/c)	σ_R (MeV/c)	σ_{prod} (mb)
27	12	13697 ± 45	524 ± 25	470 ± 25	6.91E−01 ± 3.96E−02
28	12	14156	559	355	1.23E−01 ± 1.46E−02
25	13	12849	650	405	1.99E−01 ± 1.93E−02
26	13	13240	562	416	2.41E+00 ± 1.47E−01
27	13	13802 ± 15	571 ± 10	400 ± 5	8.34E+00 ± 3.27E−01
28	13	14230 ± 13	514 ± 8	432 ± 4	4.01E+00 ± 1.68E−01
29	13	14730 ± 13	485 ± 3	454 ± 8	1.19E+00 ± 4.31E−02
30	13	15180	500	480	1.51E−01 ± 1.87E−02
31	13	15633	499	417	2.25E−02 ± 4.93E−03
27	14	13757	484	465	3.22E−01 ± 5.86E−02
28	14	14274	618	429	6.08E+00 ± 3.92E−01
29	14	14781 ± 20	566 ± 11	414 ± 6	9.45E+00 ± 3.70E−01
30	14	15250 ± 10	498 ± 5	420 ± 3	9.79E+00 ± 3.58E−01
31	14	15727 ± 25	504 ± 11	458 ± 9	1.60E+00 ± 7.52E−02
32	14	16218	482	465	2.78E−01 ± 1.85E−02
33	14	16694	547	425	2.19E−02 ± 6.85E−03
34	14	16934	480	412	1.94E−03 ± 4.49E−04
28	15	14375	570	480	9.21E−03 ± 2.24E−03
29	15	14739	485	477	1.39E−01 ± 2.16E−02
30	15	15284	599	440	2.09E+00 ± 3.58E−01
31	15	15826 ± 20	578 ± 11	402 ± 7	9.02E+00 ± 3.40E−01
32	15	16287 ± 11	507 ± 5	417 ± 4	7.72E+00 ± 2.76E−01
33	15	16840 ± 24	546 ± 13	421 ± 7	2.37E+00 ± 1.25E−01
34	15	17315 ± 34	589 ± 34	430 ± 21	4.03E−01 ± 2.08E−02
35	15	17742	575	387	6.20E−02 ± 5.50E−03
31	16	15767	484	475	2.28E−01 ± 4.94E−02
32	16	16279	549	449	3.65E+00 ± 1.82E−01
33	16	16821 ± 22	556 ± 10	420 ± 8	1.03E+01 ± 3.86E−01
34	16	17302 ± 10	492 ± 4	420 ± 3	1.36E+01 ± 4.58E−01
35	16	17852 ± 19	539 ± 10	419 ± 5	3.53E+00 ± 1.67E−01
36	16	18326 ± 28	531 ± 16	445 ± 14	7.99E−01 ± 3.20E−02
37	16	18855	646	393	9.71E−02 ± 2.55E−02
38	16	19448	596	397	1.36E−02 ± 3.58E−03
39	16	19294	455	392	4.82E−04 ± 1.50E−04
32	17	16139	567	478	7.92E−03 ± 7.48E−03
33	17	16908	480	403	7.25E−02 ± 1.49E−02
34	17	17266 ± 30	508 ± 32	468 ± 16	1.75E+00 ± 8.10E−02
35	17	17881 ± 22	560 ± 10	402 ± 9	9.94E+00 ± 3.63E−01
36	17	18339 ± 13	505 ± 5	416 ± 4	1.19E+01 ± 4.08E−01
37	17	18913 ± 15	548 ± 8	405 ± 4	5.32E+00 ± 2.36E−01
38	17	19367 ± 27	516 ± 15	432 ± 10	1.02E+00 ± 4.53E−02
39	17	19883	595	428	2.11E−01 ± 1.27E−02
40	17	20377	539	386	2.49E−02 ± 3.17E−03

continued on next page

Table A.5: continued from previous page

A	Z	p_0 (MeV/c)	σ_L (MeV/c)	σ_R (MeV/c)	σ_{prod} (mb)
41	17	20702	441	380	2.20E−03 ± 6.82E−04
42	17	21432	565	444	2.13E−04 ± 1.47E−05
34	18	17141	478	473	9.22E−03 ± 7.31E−03
35	18	17819	597	475	1.77E−01 ± 3.74E−02
36	18	18367 ± 24	546 ± 24	421 ± 13	2.94E+00 ± 1.13E−01
37	18	18918 ± 22	555 ± 9	403 ± 9	1.05E+01 ± 3.77E−01
38	18	19424 ± 13	517 ± 4	394 ± 4	1.69E+01 ± 5.83E−01
39	18	19974 ± 14	543 ± 7	389 ± 3	7.72E+00 ± 3.48E−01
40	18	20495 ± 22	548 ± 14	395 ± 7	1.77E+00 ± 7.89E−02
41	18	20893 ± 30	498 ± 28	448 ± 20	3.24E−01 ± 1.46E−02
42	18	21443	529	317	4.00E−02 ± 5.57E−03
43	18	22107	574	366	4.38E−03 ± 1.42E−03
44	18	22471	527	446	3.45E−04 ± 3.52E−05
45	18	23133	538	538	1.96E−05 ± 2.55E−06
37	19	19006	631	348	7.68E−02 ± 1.38E−02
38	19	19408 ± 26	540 ± 23	432 ± 15	1.63E+00 ± 6.24E−02
39	19	19955 ± 21	536 ± 8	406 ± 11	1.02E+01 ± 3.84E−01
40	19	20439 ± 16	510 ± 5	397 ± 6	1.57E+01 ± 6.39E−01
41	19	21029 ± 5	540 ± 7	379 ± 2	9.64E+00 ± 2.97E−01
42	19	21539 ± 12	521 ± 2	385 ± 3	2.68E+00 ± 8.80E−02
43	19	22006 ± 21	530 ± 23	411 ± 11	6.10E−01 ± 2.32E−02
44	19	22559	558	327	7.19E−02 ± 7.82E−03
45	19	23068	453	385	8.23E−03 ± 7.19E−04
46	19	23566	496	403	5.57E−04 ± 9.69E−05
47	19	24072	427	373	2.76E−05 ± 3.71E−06
38	20	19598	542	359	3.71E−03 ± 1.10E−03
39	20	19957	551	422	1.35E−01 ± 3.08E−02
40	20	20472 ± 21	512 ± 16	408 ± 12	2.71E+00 ± 8.97E−02
41	20	21026 ± 21	531 ± 7	391 ± 11	1.21E+01 ± 4.71E−01
42	20	21542 ± 15	510 ± 4	375 ± 5	2.12E+01 ± 8.66E−01
43	20	22083 ± 13	522 ± 6	372 ± 4	1.49E+01 ± 6.72E−01
44	20	22617 ± 12	478 ± 1	363 ± 3	5.54E+00 ± 1.99E−01
45	20	23103 ± 14	500 ± 5	378 ± 6	8.32E−01 ± 2.29E−02
46	20	23664	543	340	1.15E−01 ± 8.31E−03
47	20	24175 ± 9	415 ± 2	352 ± 3	8.57E−03 ± 2.16E−04
48	20	24678 ± 11	440 ± 9	362 ± 6	5.52E−04 ± 1.63E−05
49	20	25172 ± 21	458 ± 29	338 ± 19	2.03E−05 ± 2.77E−06
50	20	23863	176	176	3.76E−07 ± 1.47E−07
41	21	21022	594	437	4.28E−02 ± 6.55E−03
42	21	21512 ± 22	505 ± 15	405 ± 14	1.39E+00 ± 4.91E−02
43	21	22103 ± 23	521 ± 7	370 ± 13	1.02E+01 ± 4.48E−01
44	21	22652 ± 16	519 ± 5	356 ± 6	2.05E+01 ± 8.86E−01
45	21	23189 ± 15	520 ± 7	345 ± 4	1.89E+01 ± 9.63E−01

continued on next page

Table A.5: continued from previous page

A	Z	p_0 (MeV/c)	σ_L (MeV/c)	σ_R (MeV/c)	σ_{prod} (mb)
46	21	23668 ± 10	465 ± 1	355 ± 2	6.50E+00 ± 2.30E−01
47	21	24212 ± 11	443 ± 2	344 ± 4	1.34E+00 ± 3.67E−02
48	21	24766 ± 16	521 ± 12	318 ± 14	1.61E−01 ± 5.56E−03
49	21	25285 ± 8	377 ± 1	319 ± 3	1.33E−02 ± 3.40E−04
50	21	25744 ± 11	400 ± 10	335 ± 6	5.97E−04 ± 1.79E−05
51	21	26294	470	366	2.73E−05 ± 4.18E−06
43	22	22081	487	409	1.50E−01 ± 1.51E−02
44	22	22612 ± 20	483 ± 11	380 ± 11	2.20E+00 ± 7.06E−02
45	22	23213 ± 9	510 ± 4	336 ± 4	1.17E+01 ± 3.49E−01
46	22	23763 ± 7	507 ± 4	326 ± 1	2.83E+01 ± 9.87E−01
47	22	24293 ± 8	499 ± 3	315 ± 3	2.65E+01 ± 1.18E+00
48	22	24766 ± 8	428 ± 1	327 ± 2	1.23E+01 ± 4.38E−01
49	22	25330 ± 10	394 ± 1	311 ± 3	1.74E+00 ± 4.95E−02
50	22	25888 ± 10	449 ± 6	296 ± 7	2.64E−01 ± 7.39E−03
51	22	26363 ± 8	355 ± 1	297 ± 3	1.35E−02 ± 3.65E−04
52	22	26864 ± 10	352 ± 4	298 ± 4	8.14E−04 ± 2.27E−05
53	*22*	*27377 ± 30*	*378 ± 16*	*286 ± 20*	*2.20E−05 ± 1.58E−06*
44	23	22463	488	411	8.10E−03 ± 2.34E−03
45	23	23129	440	383	1.01E−01 ± 7.82E−03
46	23	23688 ± 20	467 ± 9	366 ± 11	1.56E+00 ± 5.13E−02
47	23	24296 ± 9	483 ± 3	320 ± 3	1.05E+01 ± 6.06E−01
48	23	24844 ± 9	474 ± 1	299 ± 5	2.71E+01 ± 1.32E+00
49	23	25379 ± 9	466 ± 2	294 ± 4	3.22E+01 ± 1.59E+00
50	23	25835 ± 8	408 ± 2	310 ± 2	1.40E+01 ± 5.24E−01
51	23	26450 ± 9	350 ± 1	277 ± 3	2.55E+00 ± 7.59E−02
52	23	26942 ± 8	393 ± 2	279 ± 4	2.56E−01 ± 6.59E−03
53	23	27494	356	238	1.91E−02 ± 2.69E−03
54	*23*	*27964 ± 10*	*294 ± 50*	*249 ± 5*	*6.71E−04 ± 6.75E−05*
55	*23*	*28400 ± 39*	*325 ± 65*	*249 ± 44*	*1.13E−05 ± 1.85E−06*
46	24	23783	393	288	6.19E−03 ± 1.19E−03
47	24	24222 ± 31	427 ± 29	382 ± 23	1.60E−01 ± 9.32E−03
48	24	24841 ± 20	450 ± 8	316 ± 12	2.02E+00 ± 7.39E−02
49	24	25411 ± 8	460 ± 3	303 ± 2	1.23E+01 ± 1.18E+00
50	24	25943 ± 10	433 ± 1	277 ± 6	3.45E+01 ± 2.94E+00
51	24	26455 ± 10	402 ± 1	267 ± 4	4.07E+01 ± 2.19E+00
52	24	26952 ± 7	361 ± 3	274 ± 2	1.98E+01 ± 8.28E−01
53	24	27515 ± 11	338 ± 1	257 ± 3	3.09E+00 ± 1.10E−01
54	24	28066 ± 6	327 ± 1	236 ± 2	3.69E−01 ± 9.34E−03
55	*24*	*28582 ± 7*	*291 ± 2*	*213 ± 1*	*1.28E−02 ± 8.53E−04*
48	25	24773	496	363	6.20E−03 ± 1.10E−03
49	25	25298 ± 33	386 ± 23	385 ± 26	9.56E−02 ± 5.71E−03
50	25	25955 ± 11	425 ± 4	279 ± 6	1.54E+00 ± 4.74E−02
51	25	26502 ± 8	413 ± 4	273 ± 2	1.17E+01 ± 4.04E−01

continued on next page

Table A.5: continued from previous page

A	Z	p_0 (MeV/c)	σ_L (MeV/c)	σ_R (MeV/c)	σ_{prod} (mb)
52	25	27014 ± 9	382 ± 1	257 ± 6	3.55E+01 ± 3.12E+00
53	25	27566 ± 11	360 ± 1	228 ± 4	4.84E+01 ± 2.91E+00
54	25	28062 ± 13	332 ± 5	237 ± 5	1.88E+01 ± 1.33E+00
55	25	28619 ± 9	289 ± 2	219 ± 3	4.36E+00 ± 1.68E−01
56	*25*	*29112 ± 16*	*264 ± 14*	*197 ± 7*	*2.15E−01 ± 1.01E−02*
57	*25*	*29600 ± 25*	*290 ± 9*	*235 ± 9*	*1.90E−03 ± 1.38E−04*
50	26	25914	334	286	5.31E−03 ± 1.55E−03
51	26	26484 ± 28	378 ± 14	302 ± 19	1.31E−01 ± 6.55E−03
52	26	27098 ± 8	380 ± 4	250 ± 2	2.05E+00 ± 6.55E−02
53	26	27621 ± 8	374 ± 4	251 ± 2	1.36E+01 ± 1.46E+00
54	26	28102 ± 14	318 ± 1	217 ± 7	4.70E+01 ± 4.92E+00
55	26	28651 ± 12	298 ± 1	216 ± 5	6.16E+01 ± 4.86E+00
56	26	29191 ± 12	239 ± 1	184 ± 4	3.23E+01 ± 2.33E+00
57	*26*	*29595 ± 16*	*249 ± 13*	*224 ± 4*	*1.60E+00 ± 1.29E−01*
58	*26*	*29996 ± 12*	*237 ± 2*	*312 ± 9*	*2.91E−02 ± 2.67E−03*
52	27	26994	323	285	4.86E−03 ± 1.71E−03
53	27	27548 ± 22	320 ± 11	313 ± 21	1.01E−01 ± 5.62E−03
54	27	28202 ± 21	324 ± 8	218 ± 12	1.82E+00 ± 1.01E−01
55	27	28694 ± 5	278 ± 1	204 ± 2	1.65E+01 ± 1.24E+00
56	27	29228 ± 17	267 ± 7	206 ± 6	5.15E+01 ± 4.57E+00
57	27	29808	174	146	6.67E+01 ± 1.08E+01
58	*27*	*30264 ± 19*	*219 ± 1*	*166 ± 9*	*8.45E+00 ± 1.92E+00*
59	*27*	*30920 ± 22*	*161 ± 35*	*161 ± 4*	*2.58E−01 ± 6.27E−02*
54	28	28117	251	243	5.60E−03 ± 6.27E−04
55	28	28770	291	157	1.79E−01 ± 2.20E−02
56	28	29407 ± 8	290 ± 3	198 ± 9	3.21E+00 ± 1.48E−01
57	28	29873	191	117	4.55E+01 ± 6.72E+00
56	*29*	*29244 ± 1*	*239 ± 11*	*140 ± 15*	*1.86E−03 ± 3.12E−04*
57	*29*	*29708 ± 25*	*216 ± 2*	*216 ± 2*	*1.41E−02 ± 4.79E−03*

Table A.6: Fitting results for the reaction system ^{58}Ni+^{181}Ta.

A	Z	p_0 (MeV/c)	σ_L (MeV/c)	σ_R (MeV/c)	σ_{prod} (mb)
10	5	5246	378	353	2.68E+01 ± 4.57E+00
11	5	5604 ± 6	333 ± 16	352 ± 3	3.43E+01 ± 4.64E+00
12	5	5938	344	280	3.17E+00 ± 3.55E−01
12	6	6104	459	354	4.33E+01 ± 2.54E+00
13	6	6646 ± 4	442 ± 1	325 ± 1	2.51E+01 ± 1.23E+00
14	6	7091 ± 6	482 ± 19	400 ± 1	7.48E+00 ± 3.94E−01

continued on next page

Table A.6: continued from previous page

A	Z	p_0 (MeV/c)	σ_L (MeV/c)	σ_R (MeV/c)	σ_{prod} (mb)
14	7	7121	500	385	1.78E+01 ± 2.83E+00
15	7	7719 ± 2	498 ± 4	303 ± 1	2.57E+01 ± 1.21E+00
16	7	8174 ± 9	366 ± 7	305 ± 3	2.10E+00 ± 1.01E−01
17	7	8573	452	333	8.24E−01 ± 4.04E−02
15	8	7727	438	343	4.67E+00 ± 6.76E−01
16	8	8124	474	367	2.56E+01 ± 1.88E+00
17	8	8599 ± 9	408 ± 7	382 ± 3	1.09E+01 ± 5.12E−01
18	8	9212 ± 8	418 ± 4	331 ± 3	4.24E+00 ± 1.90E−01
19	8	9547 ± 12	391 ± 17	384 ± 6	7.09E−01 ± 3.50E−02
20	8	10101	404	331	1.03E−01 ± 1.02E−02
18	9	9151	533	408	6.80E+00 ± 4.97E−01
19	9	9636 ± 9	450 ± 8	385 ± 3	9.20E+00 ± 4.11E−01
20	9	10210 ± 9	399 ± 4	364 ± 2	4.03E+00 ± 1.75E−01
21	9	10639 ± 8	510 ± 18	392 ± 4	1.42E+00 ± 6.42E−02
22	9	11048 ± 6	437 ± 5	434 ± 1	1.67E−01 ± 6.60E−03
20	10	10155	552	405	1.06E+01 ± 9.64E−01
21	10	10649 ± 8	452 ± 7	394 ± 2	1.27E+01 ± 5.29E−01
22	10	11210 ± 4	504 ± 1	377 ± 1	7.87E+00 ± 3.04E−01
23	10	11688 ± 8	515 ± 7	398 ± 3	1.15E+00 ± 4.53E−02
24	10	12080 ± 19	493 ± 28	468 ± 10	2.54E−01 ± 1.27E−02
25	10	12614	500	463	1.92E−02 ± 9.20E−04
22	11	11179	543	417	7.17E+00 ± 5.17E−01
23	11	11638 ± 8	450 ± 7	415 ± 3	1.45E+01 ± 5.66E−01
24	11	12175 ± 8	530 ± 6	410 ± 2	5.97E+00 ± 2.32E−01
25	11	12714 ± 9	498 ± 8	407 ± 3	1.81E+00 ± 6.94E−02
26	11	13124 ± 15	479 ± 23	461 ± 6	2.64E−01 ± 1.19E−02
27	11	13699 ± 8	574 ± 9	467 ± 10	4.66E−02 ± 1.69E−03
28	11	14169	575	467	3.98E−03 ± 5.88E−04
24	12	12194	540	414	1.31E+01 ± 8.14E−01
25	12	12651 ± 9	476 ± 7	424 ± 3	1.51E+01 ± 5.60E−01
26	12	13200 ± 7	521 ± 5	410 ± 2	1.01E+01 ± 3.61E−01
27	12	13700 ± 10	534 ± 11	421 ± 3	1.88E+00 ± 7.11E−02
28	12	14187 ± 12	566 ± 40	444 ± 4	4.08E−01 ± 2.19E−02
29	12	14734 ± 7	575 ± 7	468 ± 7	3.05E−02 ± 1.07E−03
30	12	15254	575	405	5.93E−03 ± 3.81E−04
31	12	15521	574	467	5.08E−04 ± 8.98E−05
25	13	12814	421	417	5.25E−01 ± 7.24E−02
26	13	13209	548	425	6.64E+00 ± 4.40E−01
27	13	13712 ± 10	534 ± 8	412 ± 4	1.80E+01 ± 6.33E−01
28	13	14195 ± 8	517 ± 5	421 ± 3	8.30E+00 ± 2.80E−01
29	13	14724 ± 10	533 ± 9	421 ± 3	2.87E+00 ± 1.01E−01
30	13	15197 ± 12	530 ± 21	444 ± 4	4.01E−01 ± 1.65E−02
31	13	15732 ± 15	608 ± 10	464 ± 6	7.79E−02 ± 2.70E−03

continued on next page

Table A.6: continued from previous page

A	Z	p_0 (MeV/c)	σ_L (MeV/c)	σ_R (MeV/c)	σ_{prod} (mb)
32	13	16278 ± 29	572 ± 10	453 ± 25	6.56E−03 ± 2.71E−04
28	14	14243	542	416	1.31E+01 ± 6.84E−01
29	14	14740 ± 10	543 ± 8	415 ± 4	1.87E+01 ± 6.16E−01
30	14	15207 ± 7	499 ± 4	425 ± 2	1.64E+01 ± 4.98E−01
31	14	15740 ± 10	517 ± 7	419 ± 3	3.18E+00 ± 1.04E−01
32	14	16242 ± 12	546 ± 17	431 ± 4	6.19E−01 ± 2.28E−02
33	14	16724 ± 15	570 ± 32	459 ± 5	5.93E−02 ± 2.79E−03
34	14	17292 ± 26	566 ± 11	455 ± 14	9.44E−03 ± 3.38E−04
35	14	17710	521	432	7.05E−04 ± 8.39E−05
29	15	14861	466	370	3.19E−01 ± 4.00E−02
30	15	15267	535	434	4.27E+00 ± 2.47E−01
31	15	15770 ± 10	549 ± 8	418 ± 4	1.60E+01 ± 4.96E−01
32	15	16235 ± 8	506 ± 4	427 ± 3	1.17E+01 ± 3.39E−01
33	15	16784 ± 9	538 ± 6	415 ± 3	4.47E+00 ± 1.33E−01
34	15	17248 ± 13	512 ± 14	431 ± 4	7.83E−01 ± 2.69E−02
35	15	17751 ± 14	579 ± 32	445 ± 5	1.49E−01 ± 6.81E−03
36	15	18294 ± 25	601 ± 16	458 ± 10	1.42E−02 ± 5.55E−04
37	15	18901	553	414	2.10E−03 ± 1.21E−04
38	15	19261	531	445	2.12E−04 ± 4.29E−05
31	16	15885	495	393	5.04E−01 ± 8.28E−02
32	16	16331	563	407	6.83E+00 ± 2.89E−01
33	16	16833 ± 10	556 ± 8	399 ± 4	1.71E+01 ± 4.92E−01
34	16	17298 ± 7	506 ± 4	411 ± 3	1.90E+01 ± 4.95E−01
35	16	17808 ± 9	535 ± 5	415 ± 3	5.69E+00 ± 1.52E−01
36	16	18330 ± 11	535 ± 11	410 ± 3	1.37E+00 ± 4.07E−02
37	16	18793 ± 12	556 ± 17	431 ± 4	1.84E−01 ± 6.15E−03
38	16	19324 ± 18	570 ± 8	442 ± 6	2.74E−02 ± 9.67E−04
39	16	19921 ± 29	568 ± 24	423 ± 16	2.71E−03 ± 1.21E−04
40	16	20348	532	433	3.66E−04 ± 4.35E−05
33	17	16850	570	445	1.82E−01 ± 2.61E−02
34	17	17351	538	416	3.10E+00 ± 1.64E−01
35	17	17867 ± 10	552 ± 7	399 ± 5	1.48E+01 ± 4.00E−01
36	17	18335 ± 8	515 ± 4	408 ± 3	1.55E+01 ± 3.77E−01
37	17	18837 ± 9	530 ± 5	414 ± 3	7.71E+00 ± 1.89E−01
38	17	19364 ± 8	539 ± 6	408 ± 3	1.61E+00 ± 4.14E−02
39	17	19852 ± 11	540 ± 24	416 ± 4	3.56E−01 ± 1.31E−02
40	17	20386 ± 13	538 ± 5	416 ± 5	5.05E−02 ± 1.60E−03
41	17	20917 ± 21	557 ± 33	426 ± 9	7.15E−03 ± 3.35E−04
42	17	21466 ± 19	514 ± 18	418 ± 12	5.67E−04 ± 2.89E−05
35	18	17940	478	373	3.08E−01 ± 6.72E−02
36	18	18402 ± 18	524 ± 21	396 ± 11	4.66E+00 ± 1.70E−01
37	18	18919 ± 10	546 ± 7	391 ± 5	1.49E+01 ± 3.73E−01
38	18	19404 ± 7	516 ± 3	392 ± 3	2.13E+01 ± 4.93E−01

continued on next page

Table A.6: continued from previous page

A	Z	p_0 (MeV/c)	σ_L (MeV/c)	σ_R (MeV/c)	σ_{prod} (mb)
39	18	19899 ± 8	530 ± 5	399 ± 3	1.01E+01 ± 2.44E−01
40	18	20420 ± 7	529 ± 2	398 ± 3	2.67E+00 ± 6.43E−02
41	18	20905 ± 10	518 ± 5	399 ± 3	5.03E−01 ± 1.34E−02
42	18	21400 ± 19	536 ± 36	414 ± 7	8.09E−02 ± 4.15E−03
43	18	21973 ± 24	532 ± 14	407 ± 9	7.37E−03 ± 3.17E−04
44	18	22508 ± 15	492 ± 21	400 ± 18	6.96E−04 ± 3.90E−05
37	19	18883	576	455	1.50E−01 ± 2.37E−02
38	19	19455 ± 22	543 ± 23	403 ± 13	2.47E+00 ± 9.51E−02
39	19	19960 ± 11	532 ± 6	390 ± 6	1.37E+01 ± 3.48E−01
40	19	20444 ± 7	513 ± 3	389 ± 3	1.97E+01 ± 4.61E−01
41	19	20927 ± 5	504 ± 1	394 ± 2	1.20E+01 ± 2.74E−01
42	19	21456 ± 10	506 ± 7	395 ± 4	3.59E+00 ± 9.61E−02
43	19	21985 ± 8	493 ± 3	377 ± 3	8.85E−01 ± 2.23E−02
44	19	22445 ± 14	527 ± 9	402 ± 5	1.30E−01 ± 3.92E−03
45	19	23038 ± 17	485 ± 8	374 ± 7	1.35E−02 ± 5.45E−04
46	19	23531	508	389	1.02E−03 ± 1.30E−04
47	19	24138	451	367	5.89E−05 ± 1.13E−05
39	20	20035	540	390	2.33E−01 ± 3.22E−02
40	20	20517 ± 17	505 ± 15	375 ± 10	3.88E+00 ± 1.27E−01
41	20	21030 ± 10	527 ± 5	368 ± 5	1.56E+01 ± 3.86E−01
42	20	21529 ± 7	511 ± 3	365 ± 3	2.50E+01 ± 5.85E−01
43	20	22051 ± 7	521 ± 4	360 ± 3	1.80E+01 ± 4.27E−01
44	20	22545 ± 8	495 ± 6	368 ± 3	6.69E+00 ± 1.71E−01
45	20	23039 ± 8	483 ± 7	365 ± 3	1.17E+00 ± 3.06E−02
46	20	23504 ± 12	500 ± 40	380 ± 4	1.87E−01 ± 1.01E−02
47	20	24080 ± 18	475 ± 8	362 ± 8	1.42E−02 ± 6.22E−04
48	20	24656	463	346	8.98E−04 ± 1.51E−04
49	20	25064	416	339	4.05E−05 ± 1.06E−05
41	21	21088	504	365	6.67E−02 ± 1.30E−02
42	21	21562 ± 19	500 ± 15	382 ± 11	2.04E+00 ± 6.97E−02
43	21	22079 ± 10	508 ± 5	362 ± 6	1.24E+01 ± 3.15E−01
44	21	22597 ± 7	503 ± 3	354 ± 3	2.40E+01 ± 5.70E−01
45	21	23115 ± 7	498 ± 4	346 ± 3	2.21E+01 ± 5.30E−01
46	21	23612 ± 5	479 ± 2	349 ± 3	7.22E+00 ± 1.70E−01
47	21	24135 ± 7	469 ± 4	343 ± 3	1.82E+00 ± 4.58E−02
48	21	24574 ± 13	437 ± 17	350 ± 4	2.54E−01 ± 9.63E−03
49	21	25195 ± 21	452 ± 3	323 ± 9	2.04E−02 ± 8.20E−04
50	21	25716 ± 26	397 ± 16	323 ± 9	8.49E−04 ± 9.74E−05
51	21	26210	375	305	5.27E−05 ± 1.33E−05
43	22	22149	407	354	2.34E−01 ± 2.66E−02
44	22	22650 ± 15	480 ± 11	360 ± 9	2.94E+00 ± 8.99E−02
45	22	23171 ± 9	493 ± 4	337 ± 5	1.36E+01 ± 3.40E−01
46	22	23707 ± 7	489 ± 3	319 ± 3	3.07E+01 ± 7.41E−01

continued on next page

Table A.6: continued from previous page

A	Z	p_0 (MeV/c)	σ_L (MeV/c)	σ_R (MeV/c)	σ_{prod} (mb)
47	22	24196 ± 4	474 ± 1	320 ± 2	2.78E+01 ± 6.38E−01
48	22	24708 ± 5	439 ± 1	315 ± 2	1.23E+01 ± 2.85E−01
49	22	25217 ± 6	431 ± 2	315 ± 3	2.40E+00 ± 5.88E−02
50	22	25703 ± 11	394 ± 12	314 ± 4	4.02E−01 ± 1.40E−02
51	22	26130 ± 23	465 ± 18	345 ± 9	2.30E−02 ± 1.11E−03
52	22	26809	350	285	9.38E−04 ± 1.33E−04
45	23	23251	463	313	1.62E−01 ± 1.52E−02
46	23	23720 ± 17	469 ± 10	338 ± 10	2.04E+00 ± 6.52E−02
47	23	24259 ± 8	478 ± 4	314 ± 5	1.18E+01 ± 3.00E−01
48	23	24782 ± 3	467 ± 2	300 ± 2	2.80E+01 ± 6.59E−01
49	23	25279 ± 4	444 ± 2	297 ± 2	3.19E+01 ± 7.43E−01
50	23	25776 ± 4	409 ± 1	294 ± 2	1.37E+01 ± 3.21E−01
51	23	26315 ± 5	391 ± 1	281 ± 3	3.37E+00 ± 8.27E−02
52	23	26769 ± 12	362 ± 13	275 ± 5	4.40E−01 ± 1.70E−02
53	23	27233 ± 21	399 ± 5	293 ± 8	3.07E−02 ± 1.26E−03
54	*23*	*27750 ± 20*	*373 ± 89*	*276 ± 63*	*1.25E−03 ± 3.22E−04*
47	24	24277	410	334	2.49E−01 ± 2.12E−02
48	24	24843 ± 17	450 ± 8	296 ± 9	2.49E+00 ± 7.69E−02
49	24	25349 ± 7	445 ± 4	290 ± 4	1.28E+01 ± 3.27E−01
50	24	25872 ± 3	421 ± 1	271 ± 2	3.43E+01 ± 8.12E−01
51	24	26361 ± 3	397 ± 1	267 ± 2	3.91E+01 ± 9.16E−01
52	24	26903 ± 4	360 ± 1	249 ± 2	2.00E+01 ± 4.81E−01
53	24	27393 ± 8	359 ± 6	263 ± 3	3.74E+00 ± 1.06E−01
54	24	27928 ± 5	310 ± 1	214 ± 3	7.17E−01 ± 1.95E−02
55	*24*	*28253 ± 11*	*255 ± 7*	*207 ± 1*	*2.63E−02 ± 2.08E−03*
49	25	25372	407	325	1.36E−01 ± 1.12E−02
50	25	25942 ± 7	428 ± 4	269 ± 10	1.90E+00 ± 5.76E−02
51	25	26437 ± 7	403 ± 4	259 ± 4	1.18E+01 ± 3.18E−01
52	25	26948 ± 3	375 ± 1	243 ± 2	3.37E+01 ± 8.13E−01
53	25	27457 ± 6	349 ± 3	235 ± 3	4.59E+01 ± 1.16E+00
54	25	27979 ± 3	323 ± 3	220 ± 2	1.83E+01 ± 4.69E−01
55	25	28469 ± 7	299 ± 5	239 ± 3	4.71E+00 ± 1.38E−01
56	*25*	*29029 ± 3*	*245 ± 1*	*181 ± 6*	*6.60E−01 ± 2.46E−02*
57	*25*	*29231 ± 11*	*155 ± 45*	*201 ± 7*	*3.30E−02 ± 6.16E−03*
51	26	26463	352	267	2.11E−01 ± 1.32E−02
52	26	27060 ± 6	387 ± 4	239 ± 4	2.41E+00 ± 6.69E−02
53	26	27526 ± 6	343 ± 4	238 ± 4	1.37E+01 ± 3.79E−01
54	26	28054 ± 3	311 ± 1	210 ± 2	4.50E+01 ± 1.18E+00
55	26	28565 ± 11	298 ± 4	181 ± 8	5.73E+01 ± 1.91E+00
56	26	29099 ± 2	253 ± 1	175 ± 1	3.01E+01 ± 7.56E−01
57	*26*	*29603 ± 9*	*304 ± 81*	*212 ± 4*	*2.92E+00 ± 4.64E−01*
58	*26*	*30188 ± 4*	*240 ± 4*	*198 ± 29*	*9.51E−01 ± 1.44E−01*
59	*26*	*30410 ± 18*	*200 ± 40*	*198 ± 28*	*2.30E−02 ± 3.31E−03*

continued on next page

Table A.6: continued from previous page

A	Z	p_0 (MeV/c)	σ_L (MeV/c)	σ_R (MeV/c)	σ_{prod} (mb)
53	27	27575 ± 28	339 ± 15	235 ± 16	1.48E−01 ± 8.62E−03
54	27	28157 ± 14	339 ± 6	212 ± 11	2.17E+00 ± 8.82E−02
55	27	28628 ± 4	282 ± 4	183 ± 2	1.46E+01 ± 4.73E−01
56	27	29090 ± 2	210 ± 1	171 ± 1	5.06E+01 ± 1.22E+00
57	27	29706	150	101	9.83E+01 ± 2.27E+01
58	*27*	*29953 ± 6*	*186 ± 3*	*249 ± 1*	*6.91E+00 ± 7.44E−01*
59	*27*	*30796 ± 2*	*154 ± 24*	*134 ± 2*	*3.46E+00 ± 3.05E−01*
55	28	28669	232	163	3.04E−01 ± 2.23E−02
56	28	29194 ± 4	210 ± 9	162 ± 3	4.42E+00 ± 1.86E−01
57	28	29689	150	122	2.47E+01 ± 2.85E+00
60	*28*	*31055 ± 7*	*151 ± 47*	*201 ± 3*	*3.94E+00 ± 6.38E−01*

A.4 Results for ^{64}Ni projectile

Table A.7: Fitting results for the reaction system ^{64}Ni+^{9}Be.

A	Z	p_0 (MeV/c)	σ_L (MeV/c)	σ_R (MeV/c)	σ_{prod} (mb)
10	5	5455	477	304	2.20E+00 ± 4.98E−01
11	5	6079	214	155	3.68E+00 ± 3.66E−01
12	5	6396	542	387	9.99E−01 ± 1.13E−01
13	5	6449	413	399	1.58E−01 ± 5.82E−02
12	6	6413	542	286	4.37E+00 ± 8.93E−01
13	6	6785	486	295	5.85E+00 ± 1.32E+00
14	6	7366 ± 12	550 ± 12	343 ± 6	1.64E+00 ± 1.43E−01
15	6	7765	588	420	1.69E−01 ± 7.94E−02
16	6	8104	444	373	2.52E−02 ± 7.69E−03
14	7	7434	574	355	1.60E+00 ± 2.58E−01
15	7	7816	435	310	3.67E+00 ± 1.06E+00
16	7	8397	444	330	6.07E−01 ± 6.04E−02
17	7	8826	613	438	3.40E−01 ± 3.18E−02
18	7	9223	624	446	4.19E−02 ± 6.75E−03
19	7	9484	469	394	5.73E−03 ± 1.64E−03
16	8	8369	575	322	2.87E+00 ± 5.45E−01
17	8	8706	540	403	1.89E+00 ± 1.72E−01
18	8	9509	401	314	9.27E−01 ± 1.16E−01
19	8	9931	634	371	3.06E−01 ± 3.63E−02
20	8	10328	643	459	8.67E−02 ± 1.39E−02
21	8	10679	652	465	8.17E−03 ± 1.43E−03
22	8	11041	487	409	7.21E−04 ± 2.27E−04
17	9	8908	533	324	6.41E−02 ± 1.67E−02
18	9	9358	505	376	5.78E−01 ± 1.17E−01
19	9	9720	608	439	1.86E+00 ± 3.52E−01
20	9	10379 ± 25	643 ± 2	369 ± 7	1.46E+00 ± 1.07E−01
21	9	10872 ± 27	540 ± 4	394 ± 10	6.23E−01 ± 4.66E−02
22	9	11263 ± 14	510 ± 37	471 ± 4	1.14E−01 ± 9.35E−03
23	9	11838	666	476	2.19E−02 ± 4.70E−03
24	9	12159	497	480	1.28E−03 ± 2.73E−04
25	9	12569	501	420	9.26E−05 ± 6.79E−05
19	10	9975	469	453	7.50E−02 ± 1.66E−02
20	10	10315	603	400	1.20E+00 ± 2.21E−01
21	10	10762 ± 34	652 ± 31	423 ± 13	2.45E+00 ± 2.00E−01
22	10	11384 ± 22	659 ± 3	382 ± 6	2.30E+00 ± 1.62E−01
23	10	11862 ± 21	666 ± 3	412 ± 7	5.95E−01 ± 4.20E−02
24	10	12334 ± 22	634 ± 32	442 ± 6	1.96E−01 ± 1.60E−02
25	10	12841	596	484	1.93E−02 ± 3.68E−03

continued on next page

Table A.7: continued from previous page

A	Z	p_0 (MeV/c)	σ_L (MeV/c)	σ_R (MeV/c)	σ_{prod} (mb)
26	10	13304	682	487	3.03E−03 ± 5.13E−04
27	10	13886	685	426	1.08E−04 ± 3.23E−05
22	11	11371	659	394	8.07E−01 ± 1.12E−01
23	11	11781	666	424	3.22E+00 ± 4.52E−01
24	11	12299 ± 18	633 ± 16	419 ± 3	1.98E+00 ± 1.48E−01
25	11	12905 ± 18	677 ± 3	401 ± 5	1.09E+00 ± 7.23E−02
26	11	13356 ± 18	618 ± 27	436 ± 3	2.32E−01 ± 1.79E−02
27	11	13861	685	474	5.67E−02 ± 7.69E−03
28	11	14386	600	492	5.10E−03 ± 9.35E−04
29	11	14866	691	493	8.98E−04 ± 1.71E−04
30	11	15648	641	430	1.17E−04 ± 3.05E−05
24	12	12315	598	430	1.79E+00 ± 3.40E−01
25	12	12787	677	429	3.41E+00 ± 5.74E−01
26	12	13345 ± 41	633 ± 29	411 ± 11	3.37E+00 ± 2.78E−01
27	12	13926 ± 31	655 ± 22	407 ± 8	1.12E+00 ± 8.58E−02
28	12	14415 ± 32	647 ± 27	427 ± 9	3.84E−01 ± 3.00E−02
29	12	14940	691	435	4.90E−02 ± 7.71E−03
30	12	15416	693	478	1.22E−02 ± 1.87E−03
31	12	15891	694	495	1.24E−03 ± 2.38E−04
32	12	16430	669	431	2.14E−04 ± 5.84E−05
26	13	13352	681	429	9.27E−01 ± 1.71E−01
27	13	13791	649	429	4.50E+00 ± 7.61E−01
28	13	14193 ± 49	542 ± 28	480 ± 17	3.37E+00 ± 2.67E−01
29	13	14936 ± 36	660 ± 19	411 ± 10	1.90E+00 ± 1.38E−01
30	13	15458 ± 30	660 ± 16	416 ± 8	4.56E−01 ± 3.21E−02
31	13	15958	691	434	1.43E−01 ± 2.74E−02
32	13	16404	694	478	1.93E−02 ± 2.74E−03
33	13	16944	694	495	4.29E−03 ± 6.50E−04
34	13	17463	658	495	3.60E−04 ± 5.95E−05
28	14	14329	637	428	2.15E+00 ± 3.90E−01
29	14	14771	595	437	4.84E+00 ± 6.94E−01
30	14	15263 ± 43	586 ± 29	452 ± 14	6.34E+00 ± 5.04E−01
31	14	15884 ± 38	622 ± 19	427 ± 10	2.28E+00 ± 1.64E−01
32	14	16486 ± 28	660 ± 14	413 ± 7	7.82E−01 ± 5.29E−02
33	14	16907 ± 39	570 ± 39	454 ± 10	1.33E−01 ± 1.18E−02
34	14	17489	693	446	3.53E−02 ± 6.34E−03
35	14	18014	691	459	3.38E−03 ± 4.95E−04
36	14	18497	689	492	7.65E−04 ± 1.23E−04
37	14	19290	637	426	9.03E−05 ± 2.98E−05
30	15	15302	607	450	5.81E−01 ± 1.05E−01
31	15	15815 ± 16	613 ± 45	430 ± 8	4.63E+00 ± 4.11E−01
32	15	16249 ± 53	582 ± 34	478 ± 22	5.30E+00 ± 4.36E−01
33	15	16861 ± 38	598 ± 17	444 ± 11	3.51E+00 ± 2.42E−01

continued on next page

Table A.7: continued from previous page

A	Z	p_0 (MeV/c)	σ_L (MeV/c)	σ_R (MeV/c)	σ_{prod} (mb)
34	15	17483 ± 33	643 ± 14	420 ± 9	1.08E+00 ± 7.09E−02
35	15	18033 ± 35	666 ± 35	420 ± 9	3.47E−01 ± 2.86E−02
36	15	18468	689	455	6.81E−02 ± 1.26E−02
37	15	19030	617	460	1.35E−02 ± 1.85E−03
38	15	19526	682	487	2.11E−03 ± 3.56E−04
39	15	20050	677	484	3.31E−04 ± 5.55E−05
32	16	16379	694	419	1.12E+00 ± 1.97E−01
33	16	16811 ± 33	590 ± 42	440 ± 7	4.64E+00 ± 4.00E−01
34	16	17275 ± 48	569 ± 30	465 ± 18	8.32E+00 ± 6.63E−01
35	16	17795 ± 41	565 ± 17	475 ± 14	4.49E+00 ± 3.02E−01
36	16	18490 ± 34	626 ± 14	423 ± 10	1.92E+00 ± 1.25E−01
37	16	19055 ± 34	668 ± 26	420 ± 9	4.96E−01 ± 3.68E−02
38	16	19524 ± 43	572 ± 38	436 ± 11	1.38E−01 ± 1.20E−02
39	16	20056	677	449	2.64E−02 ± 3.44E−03
40	16	20579	584	469	4.43E−03 ± 7.24E−04
41	16	21095	625	476	4.39E−04 ± 7.86E−05
42	16	21728	659	471	6.28E−05 ± 1.44E−05
34	17	17330	616	455	4.35E−01 ± 6.67E−02
35	17	17786 ± 36	541 ± 37	465 ± 7	4.44E+00 ± 3.75E−01
36	17	18305 ± 50	573 ± 31	462 ± 19	7.47E+00 ± 5.94E−01
37	17	18811 ± 38	554 ± 15	473 ± 14	6.46E+00 ± 4.19E−01
38	17	19468 ± 35	615 ± 13	445 ± 11	2.49E+00 ± 1.57E−01
39	17	20118 ± 37	666 ± 24	405 ± 10	9.82E−01 ± 7.13E−02
40	17	20554 ± 29	615 ± 30	432 ± 3	3.02E−01 ± 2.14E−02
41	17	21036 ± 31	534 ± 9	450 ± 9	7.79E−02 ± 4.78E−03
42	17	21574 ± 44	553 ± 15	460 ± 15	1.13E−02 ± 7.56E−04
43	17	22117	618	500	1.64E−03 ± 2.70E−04
44	17	22643	643	459	1.63E−04 ± 2.73E−05
45	17	23411	469	394	1.92E−05 ± 8.69E−06
36	18	18325	689	478	7.23E−01 ± 1.14E−01
37	18	18900	632	431	3.95E+00 ± 6.44E−01
38	18	19380 ± 46	582 ± 29	446 ± 16	9.43E+00 ± 7.46E−01
39	18	19849 ± 38	549 ± 14	472 ± 15	7.96E+00 ± 5.29E−01
40	18	20492 ± 36	607 ± 13	441 ± 13	4.05E+00 ± 2.55E−01
41	18	21110 ± 36	618 ± 19	409 ± 10	1.56E+00 ± 1.05E−01
42	18	21597 ± 7	594 ± 24	417 ± 3	5.37E−01 ± 3.69E−02
43	18	22135 ± 43	537 ± 36	421 ± 11	1.12E−01 ± 9.61E−03
44	18	22720	643	406	2.15E−02 ± 2.82E−03
45	18	23168	634	453	2.50E−03 ± 3.03E−04
46	18	23761	574	446	2.32E−04 ± 3.10E−05
47	18	24289	613	438	1.45E−05 ± 2.46E−06
38	19	19287	682	472	3.12E−01 ± 5.21E−02
39	19	19831 ± 39	558 ± 40	476 ± 9	3.49E+00 ± 2.99E−01

continued on next page

Table A.7: continued from previous page

A	Z	p_0 (MeV/c)	σ_L (MeV/c)	σ_R (MeV/c)	σ_{prod} (mb)
40	19	20470 ± 48	611 ± 29	423 ± 17	8.50E+00 ± 6.64E−01
41	19	20977 ± 38	587 ± 15	430 ± 15	9.19E+00 ± 6.19E−01
42	19	21561 ± 35	615 ± 12	424 ± 12	5.58E+00 ± 3.51E−01
43	19	22188 ± 37	635 ± 20	396 ± 11	2.80E+00 ± 1.92E−01
44	19	22673 ± 28	607 ± 19	406 ± 3	9.51E−01 ± 6.55E−02
45	19	23271 ± 39	611 ± 36	387 ± 10	2.50E−01 ± 2.16E−02
46	19	23769	624	397	4.69E−02 ± 6.22E−03
47	19	24301	613	409	6.26E−03 ± 9.02E−04
48	19	24806	601	429	5.53E−04 ± 6.43E−05
49	19	25336	451	420	5.34E−05 ± 8.62E−06
41	20	20900	561	438	3.72E+00 ± 6.05E−01
42	20	21464 ± 51	579 ± 37	422 ± 16	9.88E+00 ± 8.47E−01
43	20	21994 ± 40	581 ± 19	429 ± 14	1.12E+01 ± 7.90E−01
44	20	22599 ± 38	603 ± 16	412 ± 13	7.46E+00 ± 4.93E−01
45	20	23220 ± 39	626 ± 19	401 ± 13	2.97E+00 ± 2.11E−01
46	20	23729 ± 6	540 ± 16	387 ± 3	1.22E+00 ± 8.10E−02
47	20	24330 ± 23	613 ± 17	375 ± 7	3.11E−01 ± 1.82E−02
48	20	24872 ± 34	601 ± 27	373 ± 9	5.48E−02 ± 3.97E−03
49	20	25433 ± 31	588 ± 34	372 ± 9	6.64E−03 ± 5.24E−04
50	20	25959	518	386	6.76E−04 ± 1.08E−04
51	20	26481	558	399	6.14E−05 ± 1.17E−05
52	20	27125	542	387	5.01E−06 ± 9.38E−07
42	21	21400	659	451	2.15E−01 ± 6.74E−02
43	21	21964	573	421	2.69E+00 ± 5.35E−01
44	21	22474 ± 59	545 ± 37	434 ± 22	8.85E+00 ± 7.71E−01
45	21	23059 ± 40	572 ± 18	416 ± 14	1.36E+01 ± 9.61E−01
46	21	23642 ± 38	589 ± 15	411 ± 14	9.05E+00 ± 6.09E−01
47	21	24292 ± 40	607 ± 17	384 ± 15	4.73E+00 ± 3.35E−01
48	21	24866 ± 51	562 ± 32	371 ± 18	1.71E+00 ± 1.48E−01
49	21	25478 ± 39	571 ± 33	338 ± 10	5.42E−01 ± 4.94E−02
50	21	25957	574	354	9.60E−02 ± 1.61E−02
51	21	26543 ± 42	558 ± 25	343 ± 12	1.79E−02 ± 1.40E−03
52	21	27038 ± 29	425 ± 16	352 ± 11	2.33E−03 ± 1.66E−04
53	21	27576	485	374	3.29E−04 ± 4.64E−05
54	21	28066	556	403	2.75E−05 ± 4.72E−06
44	22	22446	643	459	2.96E−01 ± 6.74E−02
45	22	23044 ± 46	565 ± 50	396 ± 7	2.56E+00 ± 2.45E−01
46	22	23576 ± 51	544 ± 31	400 ± 17	1.07E+01 ± 9.02E−01
47	22	24150 ± 41	564 ± 17	390 ± 15	1.58E+01 ± 1.14E+00
48	22	24758 ± 33	582 ± 13	370 ± 11	1.33E+01 ± 9.01E−01
49	22	25335 ± 46	554 ± 25	371 ± 16	6.51E+00 ± 5.21E−01
50	22	25904 ± 10	521 ± 17	358 ± 5	2.86E+00 ± 2.20E−01
51	22	26528 ± 27	558 ± 20	324 ± 9	8.28E−01 ± 5.60E−02

continued on next page

Table A.7: continued from previous page

A	Z	p_0 (MeV/c)	σ_L (MeV/c)	σ_R (MeV/c)	σ_{prod} (mb)
52	22	27029 ± 46	515 ± 37	341 ± 4	2.26E−01 ± 2.05E−02
53	22	27626 ± 30	524 ± 14	312 ± 8	4.33E−02 ± 3.02E−03
54	22	28184 ± 31	406 ± 9	304 ± 9	7.34E−03 ± 5.26E−04
55	22	28652 ± 16	437 ± 23	324 ± 8	9.21E−04 ± 7.04E−05
56	22	29220	478	331	1.28E−04 ± 1.23E−05
46	23	23505	461	440	1.34E−01 ± 3.42E−02
47	23	24078 ± 45	514 ± 39	401 ± 8	1.92E+00 ± 1.81E−01
48	23	24672 ± 44	536 ± 26	368 ± 14	8.84E+00 ± 7.38E−01
49	23	25263 ± 36	553 ± 15	353 ± 12	1.72E+01 ± 1.28E+00
50	23	25842 ± 30	563 ± 11	352 ± 10	1.54E+01 ± 1.08E+00
51	23	26446 ± 39	532 ± 21	338 ± 12	9.57E+00 ± 7.80E−01
52	23	27036 ± 44	522 ± 28	329 ± 14	3.71E+00 ± 3.44E−01
53	23	27624 ± 38	509 ± 23	303 ± 10	1.74E+00 ± 1.51E−01
54	23	28129 ± 28	396 ± 8	301 ± 7	4.77E−01 ± 3.40E−02
55	23	28654 ± 26	417 ± 5	304 ± 7	1.49E−01 ± 9.78E−03
56	23	29319 ± 38	459 ± 26	266 ± 11	2.15E−02 ± 1.87E−03
57	23	29785 ± 25	393 ± 15	287 ± 9	4.69E−03 ± 3.54E−04
58	23	30268	390	295	4.77E−04 ± 7.88E−05
59	23	30846	434	290	6.59E−05 ± 1.43E−05
48	24	24700	601	324	1.47E−01 ± 3.16E−02
49	24	25187 ± 50	520 ± 33	356 ± 7	1.65E+00 ± 1.52E−01
50	24	25755 ± 45	510 ± 23	355 ± 16	8.91E+00 ± 7.42E−01
51	24	26380 ± 34	540 ± 13	323 ± 12	1.83E+01 ± 1.38E+00
52	24	26953 ± 16	542 ± 10	321 ± 8	1.97E+01 ± 1.33E+00
53	24	27547 ± 39	505 ± 19	304 ± 12	1.21E+01 ± 9.97E−01
54	24	28092 ± 20	446 ± 11	307 ± 7	7.21E+00 ± 5.11E−01
55	24	28657 ± 51	445 ± 24	305 ± 21	2.89E+00 ± 2.68E−01
56	24	29235 ± 27	416 ± 21	282 ± 12	1.24E+00 ± 1.06E−01
57	24	29749 ± 27	389 ± 7	277 ± 8	3.47E−01 ± 2.52E−02
58	24	30322 ± 28	377 ± 7	265 ± 9	8.41E−02 ± 6.31E−03
59	24	30888 ± 29	344 ± 24	248 ± 12	1.13E−02 ± 1.10E−03
60	24	31414 ± 27	333 ± 7	237 ± 8	1.87E−03 ± 1.45E−04
50	25	25657	574	410	7.77E−02 ± 1.66E−02
51	25	26230 ± 67	459 ± 45	360 ± 27	1.17E+00 ± 1.34E−01
52	25	26826 ± 46	482 ± 20	336 ± 20	7.12E+00 ± 6.30E−01
53	25	27500 ± 29	521 ± 10	290 ± 10	1.77E+01 ± 1.37E+00
54	25	27999 ± 13	481 ± 9	308 ± 13	2.12E+01 ± 1.61E+00
55	25	28622 ± 18	451 ± 11	281 ± 8	1.84E+01 ± 1.39E+00
56	25	29168 ± 22	410 ± 4	282 ± 8	1.02E+01 ± 7.72E−01
57	25	29728 ± 40	392 ± 10	292 ± 8	6.30E+00 ± 6.02E−01
58	25	30333 ± 30	377 ± 9	251 ± 13	2.80E+00 ± 2.47E−01
59	25	30886 ± 22	310 ± 4	223 ± 5	1.30E+00 ± 9.83E−02
60	25	31448 ± 29	305 ± 76	223 ± 12	2.53E−01 ± 4.34E−02

continued on next page

Table A.7: continued from previous page

A	Z	p_0 (MeV/c)	σ_L (MeV/c)	σ_R (MeV/c)	σ_{prod} (mb)
61	25	31989 ± 32	297 ± 4	200 ± 9	6.87E−02 ± 6.17E−03
62	*25*	*32519 ± 53*	*210 ± 47*	*164 ± 14*	*1.94E−03 ± 6.08E−04*
52	26	26783	485	343	5.53E−02 ± 1.21E−02
53	26	27354 ± 55	445 ± 34	311 ± 21	8.52E−01 ± 9.12E−02
54	26	28020 ± 38	481 ± 7	271 ± 5	5.89E+00 ± 4.97E−01
55	26	28552 ± 8	467 ± 8	280 ± 8	1.59E+01 ± 8.94E−01
56	26	29128 ± 16	441 ± 14	271 ± 5	2.51E+01 ± 2.55E+00
57	26	29709 ± 14	417 ± 10	265 ± 10	2.10E+01 ± 1.87E+00
58	26	30304 ± 21	347 ± 20	235 ± 9	1.96E+01 ± 1.85E+00
59	26	30852 ± 24	333 ± 6	228 ± 8	1.21E+01 ± 1.06E+00
60	26	31476 ± 25	331 ± 14	204 ± 13	8.22E+00 ± 8.53E−01
61	26	31991 ± 22	275 ± 12	191 ± 8	3.68E+00 ± 3.69E−01
62	26	32575 ± 27	246 ± 3	151 ± 8	1.56E+00 ± 1.59E−01
63	*26*	*33040 ± 8*	*172 ± 44*	*123 ± 20*	*6.09E−02 ± 1.41E−02*
54	27	27816	385	354	2.42E−02 ± 6.91E−03
55	27	28464 ± 24	433 ± 16	290 ± 17	3.94E−01 ± 4.56E−02
56	27	29021 ± 17	421 ± 10	280 ± 8	3.31E+00 ± 3.05E−01
57	27	29634 ± 14	396 ± 11	245 ± 11	1.38E+01 ± 1.32E+00
58	27	30204 ± 24	387 ± 15	265 ± 8	2.00E+01 ± 2.38E+00
59	27	30777 ± 17	313 ± 12	220 ± 6	3.25E+01 ± 2.83E+00
60	27	31394 ± 40	297 ± 10	199 ± 5	2.77E+01 ± 3.24E+00
61	27	31975 ± 21	288 ± 17	197 ± 13	3.10E+01 ± 6.47E+00
62	27	32549 ± 14	271 ± 17	175 ± 6	2.07E+01 ± 2.88E+00
63	27	33123	172	123	3.20E+01 ± 7.37E+00
56	28	28984	385	273	8.97E−03 ± 1.60E−03
57	28	29584	380	280	1.87E−01 ± 4.93E−02
58	28	30136 ± 14	381 ± 11	245 ± 3	1.45E+00 ± 1.64E−01
59	28	30704 ± 19	357 ± 10	252 ± 9	6.88E+00 ± 6.80E−01
60	28	31316 ± 12	298 ± 11	189 ± 7	2.01E+01 ± 2.32E+00
61	28	31922 ± 15	293 ± 9	162 ± 6	2.70E+01 ± 3.95E+00
62	28	32497 ± 19	271 ± 15	190 ± 14	2.94E+01 ± 4.13E+00
63	28	33069	131	119	7.19E+01 ± 2.97E+01
60	*29*	*31152 ± 22*	*268 ± 6*	*179 ± 15*	*3.29E−01 ± 4.96E−02*

Table A.8: Fitting results for the reaction system ^{64}Ni+^{181}Ta.

A	Z	p_0 (MeV/c)	σ_L (MeV/c)	σ_R (MeV/c)	σ_{prod} (mb)
11	5	5543	449	275	6.60E+01 ± 1.66E+01
12	5	6037	516	385	1.09E+01 ± 2.38E+00

continued on next page

Table A.8: continued from previous page

A	Z	p_0 (MeV/c)	σ_L (MeV/c)	σ_R (MeV/c)	σ_{prod} (mb)
13	5	6665	395	293	1.66E+00 ± 3.10E−01
14	5	6572	404	301	1.48E−01 ± 3.49E−02
12	6	6208	405	315	3.78E+01 ± 7.18E+00
13	6	6675 ± 15	422 ± 5	317 ± 4	3.50E+01 ± 2.05E+00
14	6	7070 ± 35	487 ± 22	379 ± 16	1.55E+01 ± 1.07E+00
15	6	7526	480	393	1.31E+00 ± 2.23E−01
14	7	7188	477	457	1.59E+01 ± 1.96E+00
15	7	7694 ± 19	453 ± 9	335 ± 6	3.73E+01 ± 2.22E+00
16	7	8132 ± 23	573 ± 9	380 ± 8	6.30E+00 ± 3.66E−01
17	7	8669 ± 18	432 ± 3	380 ± 17	2.10E+00 ± 1.42E−01
18	7	9108	440	408	2.76E−01 ± 3.85E−02
16	8	8233	573	352	2.38E+01 ± 3.09E+00
17	8	8664 ± 23	499 ± 17	376 ± 8	1.41E+01 ± 8.73E−01
18	8	9173 ± 18	595 ± 8	380 ± 5	1.07E+01 ± 5.89E−01
19	8	9620 ± 24	620 ± 23	422 ± 12	2.35E+00 ± 1.48E−01
20	8	10098	599	457	5.71E−01 ± 1.09E−01
21	8	10569	459	463	4.83E−02 ± 8.58E−03
18	9	9202	595	443	5.32E+00 ± 7.86E−01
19	9	9680 ± 25	523 ± 20	396 ± 9	1.21E+01 ± 7.60E−01
20	9	10175 ± 21	526 ± 2	393 ± 6	9.77E+00 ± 5.28E−01
21	9	10669 ± 24	621 ± 7	414 ± 9	4.25E+00 ± 2.34E−01
22	9	11128 ± 27	464 ± 21	454 ± 19	6.04E−01 ± 4.18E−02
23	9	11589	469	473	1.14E−01 ± 2.18E−02
20	10	10156	453	448	7.34E+00 ± 1.26E+00
21	10	10721 ± 19	596 ± 44	399 ± 4	1.47E+01 ± 1.14E+00
22	10	11253 ± 30	584 ± 26	393 ± 8	1.29E+01 ± 9.23E−01
23	10	11710 ± 16	635 ± 15	417 ± 5	3.25E+00 ± 1.76E−01
24	10	12172 ± 24	634 ± 18	441 ± 5	1.00E+00 ± 6.31E−02
25	10	12632	524	481	9.50E−02 ± 1.27E−02
26	10	13126	650	484	1.62E−02 ± 2.65E−03
21	11	10797	540	463	3.93E−01 ± 1.21E−01
22	11	11272	628	404	5.03E+00 ± 6.96E−01
23	11	11733	611	414	1.65E+01 ± 2.93E+00
24	11	12239 ± 33	606 ± 30	413 ± 9	1.02E+01 ± 7.27E−01
25	11	12766 ± 16	645 ± 7	409 ± 5	5.24E+00 ± 2.67E−01
26	11	13245 ± 21	650 ± 32	432 ± 8	1.02E+00 ± 6.31E−02
27	11	13671	492	476	2.18E−01 ± 3.43E−02
28	11	14176	656	489	2.57E−02 ± 3.29E−03
29	11	14720	654	491	4.45E−03 ± 6.30E−04
24	12	12256	618	421	9.17E+00 ± 1.43E+00
25	12	12759	612	412	1.51E+01 ± 2.48E+00
26	12	13251 ± 35	561 ± 24	417 ± 10	1.49E+01 ± 1.01E+00
27	12	13817 ± 17	653 ± 27	408 ± 6	4.67E+00 ± 2.68E−01

continued on next page

Table A.8: continued from previous page

A	Z	p_0 (MeV/c)	σ_L (MeV/c)	σ_R (MeV/c)	σ_{prod} (mb)
28	12	14260 ± 31	646 ± 22	437 ± 9	1.55E+00 ± 1.00E−01
29	12	14711 ± 49	568 ± 56	462 ± 16	1.89E−01 ± 1.72E−02
30	12	15237 ± 30	598 ± 58	484 ± 16	4.41E−02 ± 3.92E−03
31	12	15721	661	493	5.23E−03 ± 8.52E−04
32	12	16226	627	429	9.50E−04 ± 1.73E−04
26	13	13238	494	450	3.70E+00 ± 7.95E−01
27	13	13725	533	441	1.68E+01 ± 2.16E+00
28	13	14259 ± 38	544 ± 24	423 ± 11	1.25E+01 ± 8.55E−01
29	13	14827 ± 32	613 ± 19	416 ± 9	6.72E+00 ± 4.41E−01
30	13	15310 ± 32	646 ± 18	428 ± 10	1.59E+00 ± 9.83E−02
31	13	15811 ± 41	626 ± 40	443 ± 12	4.43E−01 ± 3.66E−02
32	13	16258	520	473	5.68E−02 ± 8.24E−03
33	13	16786 ± 30	661 ± 29	493 ± 23	1.52E−02 ± 9.96E−04
34	13	17304	590	492	1.47E−03 ± 2.49E−04
27	14	13768	568	477	3.12E−01 ± 5.31E−02
28	14	14322	656	413	7.86E+00 ± 9.27E−01
29	14	14804	600	421	1.56E+01 ± 2.48E+00
30	14	15300 ± 40	584 ± 28	423 ± 13	1.99E+01 ± 1.42E+00
31	14	15830 ± 34	605 ± 18	424 ± 10	7.23E+00 ± 4.55E−01
32	14	16412 ± 30	643 ± 17	404 ± 8	2.30E+00 ± 1.52E−01
33	14	16822 ± 44	592 ± 35	444 ± 12	3.91E−01 ± 3.26E−02
34	14	17306	600	462	1.05E−01 ± 1.48E−02
35	14	17790	658	491	1.16E−02 ± 1.48E−03
36	14	18344	656	489	2.66E−03 ± 4.56E−04
37	14	18797	483	360	2.75E−04 ± 6.68E−05
29	15	14816	573	490	9.39E−02 ± 1.56E−02
30	15	15298	594	451	1.93E+00 ± 3.28E−01
31	15	15819	592	431	1.29E+01 ± 1.47E+00
32	15	16336 ± 48	602 ± 32	424 ± 17	1.47E+01 ± 1.11E+00
33	15	16840 ± 33	569 ± 16	425 ± 10	9.93E+00 ± 5.96E−01
34	15	17413 ± 28	653 ± 13	419 ± 9	2.87E+00 ± 1.72E−01
35	15	17886 ± 37	599 ± 23	431 ± 10	9.38E−01 ± 6.33E−02
36	15	18367 ± 49	562 ± 42	441 ± 14	1.69E−01 ± 1.47E−02
37	15	18886	653	458	3.99E−02 ± 4.66E−03
38	15	19395	597	484	6.04E−03 ± 9.95E−04
39	15	19940	590	414	1.07E−03 ± 1.87E−04
32	16	16368	661	419	3.09E+00 ± 4.79E−01
33	16	16843	585	432	1.14E+01 ± 1.34E+00
34	16	17384 ± 43	603 ± 30	419 ± 14	1.98E+01 ± 1.47E+00
35	16	17869 ± 36	578 ± 15	423 ± 9	1.10E+01 ± 5.72E−01
36	16	18443 ± 34	623 ± 15	412 ± 11	4.66E+00 ± 2.94E−01
37	16	18954 ± 37	613 ± 25	412 ± 10	1.23E+00 ± 8.70E−02
38	16	19428 ± 48	633 ± 38	435 ± 14	3.45E−01 ± 2.95E−02

continued on next page

Table A.8: continued from previous page

A	Z	p_0 (MeV/c)	σ_L (MeV/c)	σ_R (MeV/c)	σ_{prod} (mb)
39	16	19921	645	455	6.50E−02 ± 1.05E−02
40	16	20402	521	477	1.22E−02 ± 2.25E−03
41	16	20922	635	473	1.59E−03 ± 2.03E−04
42	16	21315	628	468	2.75E−04 ± 6.19E−05
34	17	17402	660	427	1.15E+00 ± 2.00E−01
35	17	17873 ± 20	569 ± 39	433 ± 7	9.67E+00 ± 7.92E−01
36	17	18396 ± 51	595 ± 32	426 ± 20	1.61E+01 ± 1.24E+00
37	17	18913 ± 35	576 ± 15	421 ± 12	1.42E+01 ± 8.59E−01
38	17	19474 ± 37	627 ± 15	416 ± 14	5.56E+00 ± 3.54E−01
39	17	19989 ± 39	623 ± 23	419 ± 13	2.20E+00 ± 1.49E−01
40	17	20483 ± 29	613 ± 19	414 ± 4	6.63E−01 ± 4.22E−02
41	17	21003 ± 36	566 ± 30	416 ± 13	1.54E−01 ± 1.59E−02
42	17	21435 ± 50	524 ± 52	453 ± 15	2.46E−02 ± 2.48E−03
43	17	22026	621	463	3.53E−03 ± 4.60E−04
44	17	22550	453	457	3.04E−04 ± 5.39E−05
35	18	17885	573	491	5.18E−02 ± 1.36E−02
36	18	18441	656	402	1.67E+00 ± 3.21E−01
37	18	18936	613	416	8.21E+00 ± 1.35E+00
38	18	19473 ± 46	610 ± 30	410 ± 16	1.86E+01 ± 1.40E+00
39	18	19922 ± 40	566 ± 15	436 ± 17	1.56E+01 ± 1.01E+00
40	18	20563 ± 32	635 ± 14	388 ± 10	8.07E+00 ± 5.12E−01
41	18	21016 ± 36	592 ± 17	414 ± 12	3.23E+00 ± 2.06E−01
42	18	21547 ± 44	589 ± 27	406 ± 14	1.01E+00 ± 7.48E−02
43	18	22093 ± 50	602 ± 41	398 ± 15	2.17E−01 ± 1.90E−02
44	18	22516	556	435	4.25E−02 ± 6.49E−03
45	18	23004	604	450	5.87E−03 ± 9.91E−04
46	18	23731	595	399	5.67E−04 ± 9.19E−05
39	19	19972	603	418	6.97E+00 ± 1.11E+00
40	19	20508 ± 48	606 ± 30	406 ± 18	1.63E+01 ± 1.26E+00
41	19	21021 ± 36	581 ± 14	400 ± 13	1.76E+01 ± 1.11E+00
42	19	21555 ± 35	598 ± 13	410 ± 13	1.05E+01 ± 6.72E−01
43	19	22093 ± 36	593 ± 16	396 ± 12	5.33E+00 ± 3.45E−01
44	19	22609 ± 39	589 ± 21	395 ± 12	1.68E+00 ± 1.16E−01
45	19	23114 ± 52	514 ± 41	398 ± 15	4.29E−01 ± 4.12E−02
46	19	23617	595	406	8.28E−02 ± 1.17E−02
47	19	24157 ± 37	584 ± 34	409 ± 5	1.20E−02 ± 8.78E−04
48	19	24729	573	404	1.04E−03 ± 1.47E−04
49	19	25292	546	418	1.45E−04 ± 2.69E−05
40	20	20429	473	439	9.18E−01 ± 1.31E−01
41	20	21004	579	418	6.91E+00 ± 7.90E−01
42	20	21573 ± 44	599 ± 27	389 ± 15	1.82E+01 ± 1.39E+00
43	20	22093 ± 38	589 ± 15	386 ± 15	2.17E+01 ± 1.46E+00
44	20	22624 ± 30	589 ± 11	380 ± 10	1.55E+01 ± 9.76E−01

continued on next page

Table A.8: continued from previous page

A	Z	p_0 (MeV/c)	σ_L (MeV/c)	σ_R (MeV/c)	σ_{prod} (mb)
45	20	23135 ± 39	596 ± 18	385 ± 12	6.46E+00 ± 4.44E−01
46	20	23692 ± 37	583 ± 20	375 ± 12	2.27E+00 ± 1.65E−01
47	20	24209 ± 29	584 ± 30	382 ± 11	5.10E−01 ± 3.67E−02
48	20	24791	573	358	9.38E−02 ± 1.57E−02
49	20	25251	560	380	1.37E−02 ± 2.29E−03
50	20	25847	547	350	1.57E−03 ± 2.49E−04
51	20	26324	434	368	1.59E−04 ± 2.45E−05
42	21	21426	464	468	3.75E−01 ± 7.29E−02
43	21	22028 ± 73	562 ± 15	426 ± 26	4.63E+00 ± 5.02E−01
44	21	22589 ± 48	578 ± 26	401 ± 19	1.54E+01 ± 1.21E+00
45	21	23162 ± 37	588 ± 14	374 ± 15	2.46E+01 ± 1.70E+00
46	21	23686 ± 17	595 ± 9	375 ± 10	1.75E+01 ± 1.11E+00
47	21	24182 ± 42	561 ± 18	379 ± 14	9.69E+00 ± 7.15E−01
48	21	24714 ± 25	573 ± 11	376 ± 10	3.33E+00 ± 2.40E−01
49	21	25293 ± 47	548 ± 32	358 ± 14	9.71E−01 ± 8.93E−02
50	21	25840	480	357	1.43E−01 ± 2.52E−02
51	21	26367 ± 56	492 ± 42	350 ± 17	3.13E−02 ± 3.26E−03
52	21	26888	464	352	4.47E−03 ± 7.64E−04
53	21	27376 ± 47	499 ± 25	357 ± 17	7.67E−04 ± 6.19E−05
54	21	27891	387	358	7.58E−05 ± 1.69E−05
44	22	22547	472	400	4.53E−01 ± 1.00E−01
45	22	23080	544	413	4.14E+00 ± 5.03E−01
46	22	23663 ± 49	565 ± 24	380 ± 21	1.70E+01 ± 1.37E+00
47	22	24239 ± 17	584 ± 10	356 ± 8	2.67E+01 ± 1.64E+00
48	22	24767 ± 16	573 ± 19	349 ± 7	2.45E+01 ± 1.58E+00
49	22	25242 ± 34	542 ± 15	362 ± 11	1.27E+01 ± 9.01E−01
50	22	25820 ± 41	532 ± 18	344 ± 13	5.06E+00 ± 3.71E−01
51	22	26372 ± 42	522 ± 19	338 ± 4	1.25E+00 ± 9.67E−02
52	22	26903 ± 33	454 ± 10	330 ± 11	3.46E−01 ± 2.41E−02
53	22	27432 ± 37	471 ± 27	329 ± 6	7.04E−02 ± 6.25E−03
54	22	27973 ± 36	430 ± 39	324 ± 13	1.36E−02 ± 1.26E−03
55	22	28450	460	343	1.96E−03 ± 2.02E−04
56	22	29068	404	293	2.64E−04 ± 5.40E−05
46	23	23526	488	443	2.18E−01 ± 4.47E−02
47	23	24186	564	388	2.78E+00 ± 4.81E−01
48	23	24758 ± 43	563 ± 21	353 ± 16	1.28E+01 ± 1.02E+00
49	23	25307 ± 18	560 ± 5	337 ± 9	2.67E+01 ± 1.85E+00
50	23	25812 ± 35	544 ± 16	340 ± 13	2.63E+01 ± 1.98E+00
51	23	26315 ± 21	532 ± 14	358 ± 14	1.65E+01 ± 1.26E+00
52	23	26893 ± 30	544 ± 25	340 ± 16	6.26E+00 ± 5.14E−01
53	23	27465 ± 22	499 ± 10	313 ± 8	2.57E+00 ± 1.71E−01
54	23	27982 ± 37	449 ± 24	320 ± 16	6.67E−01 ± 5.55E−02
55	23	28576 ± 29	425 ± 21	292 ± 14	1.86E−01 ± 1.60E−02

continued on next page

Table A.8: continued from previous page

A	Z	p_0 (MeV/c)	σ_L (MeV/c)	σ_R (MeV/c)	σ_{prod} (mb)
56	23	29052 ± 35	420 ± 13	299 ± 13	3.56E−02 ± 2.83E−03
57	23	29582	413	300	8.15E−03 ± 1.29E−03
58	23	30141	386	287	7.43E−04 ± 1.36E−04
59	23	30673	355	265	1.43E−04 ± 1.35E−05
48	24	24690	533	366	1.89E−01 ± 4.08E−02
49	24	25240 ± 64	511 ± 40	345 ± 26	2.15E+00 ± 2.22E−01
50	24	25804 ± 39	526 ± 18	337 ± 14	1.13E+01 ± 9.02E−01
51	24	26348 ± 19	532 ± 4	335 ± 12	2.35E+01 ± 1.81E+00
52	24	26889 ± 14	530 ± 10	332 ± 3	2.64E+01 ± 2.03E+00
53	24	27423 ± 22	499 ± 8	316 ± 10	1.87E+01 ± 1.43E+00
54	24	27994 ± 26	471 ± 8	297 ± 10	1.10E+01 ± 9.64E−01
55	24	28502 ± 23	446 ± 5	298 ± 8	4.36E+00 ± 3.31E−01
56	24	29108 ± 32	395 ± 34	278 ± 14	1.48E+00 ± 1.44E−01
57	24	29619 ± 32	405 ± 10	278 ± 13	4.28E−01 ± 3.56E−02
58	24	30143 ± 15	386 ± 11	287 ± 16	1.14E−01 ± 1.24E−02
59	24	30662	382	272	1.79E−02 ± 3.78E−03
60	24	31242	306	243	2.33E−03 ± 5.44E−04
50	25	25729	473	343	9.02E−02 ± 1.89E−02
51	25	26304 ± 54	488 ± 32	330 ± 21	1.43E+00 ± 1.41E−01
52	25	26872 ± 40	504 ± 16	316 ± 15	8.53E+00 ± 7.10E−01
53	25	27444 ± 17	499 ± 3	293 ± 8	2.36E+01 ± 1.72E+00
54	25	27977 ± 8	494 ± 15	297 ± 5	2.81E+01 ± 1.57E+00
55	25	28514 ± 14	465 ± 10	292 ± 5	2.54E+01 ± 2.04E+00
56	25	29069 ± 23	477 ± 22	306 ± 15	1.39E+01 ± 1.36E+00
57	25	29651 ± 23	415 ± 4	253 ± 9	8.95E+00 ± 7.17E−01
58	25	30201 ± 29	386 ± 18	249 ± 15	3.20E+00 ± 3.08E−01
59	25	30730 ± 29	348 ± 9	237 ± 11	1.36E+00 ± 1.22E−01
60	25	31261 ± 27	335 ± 6	223 ± 10	3.17E−01 ± 2.79E−02
61	25	31812	280	208	7.78E−02 ± 1.23E−02
52	26	26780	414	350	6.61E−02 ± 1.34E−02
53	26	27358 ± 63	452 ± 29	331 ± 32	1.01E+00 ± 1.09E−01
54	26	27968 ± 17	475 ± 11	290 ± 9	6.86E+00 ± 5.40E−01
55	26	28492 ± 14	471 ± 10	297 ± 3	1.75E+01 ± 1.59E+00
56	26	29030 ± 12	463 ± 10	285 ± 1	2.76E+01 ± 2.60E+00
57	26	29571 ± 17	446 ± 12	299 ± 5	2.64E+01 ± 2.31E+00
58	26	30149 ± 23	386 ± 3	250 ± 13	2.65E+01 ± 2.58E+00
59	26	30717 ± 8	393 ± 15	236 ± 3	1.34E+01 ± 9.19E−01
60	26	31319 ± 11	336 ± 16	202 ± 19	9.14E+00 ± 7.89E−01
61	26	31839 ± 24	289 ± 10	194 ± 10	3.30E+00 ± 3.32E−01
62	26	32386 ± 13	230 ± 2	171 ± 4	1.50E+00 ± 1.26E−01
54	27	27816	389	358	2.77E−02 ± 4.90E−03
55	27	28496 ± 56	440 ± 11	264 ± 9	4.95E−01 ± 4.73E−02
56	27	29018 ± 14	443 ± 11	273 ± 4	3.46E+00 ± 3.32E−01

continued on next page

Table A.8: continued from previous page

A	Z	p_0 (MeV/c)	σ_L (MeV/c)	σ_R (MeV/c)	σ_{prod} (mb)
57	27	29589 ± 18	413 ± 2	242 ± 8	1.61E+01 ± 1.35E+00
58	27	30122 ± 22	386 ± 4	244 ± 12	2.87E+01 ± 2.88E+00
59	27	30677 ± 27	355 ± 1	221 ± 10	4.18E+01 ± 4.42E+00
60	27	31246 ± 23	320 ± 2	201 ± 7	4.00E+01 ± 3.48E+00
61	27	31824	280	208	3.76E+01 ± 4.65E+00
62	27	32380	230	171	2.49E+01 ± 3.26E+00
63	27	32961	164	100	2.62E+01 ± 5.33E+00
56	28	29038	437	267	1.15E−02 ± 2.40E−03
57	28	29538	373	251	1.96E−01 ± 4.88E−02
58	28	30104	371	247	1.93E+00 ± 3.28E−01
59	28	30641 ± 13	367 ± 13	227 ± 2	7.13E+00 ± 8.93E−01
60	28	31164 ± 22	353 ± 12	289 ± 9	1.78E+01 ± 1.86E+00
61	28	31672 ± 38	324 ± 25	234 ± 16	2.05E+01 ± 2.84E+00
62	28	32406 ± 7	170 ± 4	127 ± 10	5.94E+01 ± 5.85E+00
63	28	32943 ± 3	121 ± 5	90 ± 3	2.32E+02 ± 2.26E+01
59	*29*	*30526 ± 18*	*294 ± 54*	*217 ± 50*	*3.20E−02 ± 8.75E−03*
60	*29*	*31093 ± 33*	*310 ± 20*	*254 ± 71*	*2.90E−01 ± 5.46E−02*

A.5 Results for ^{86}Kr projectile

Table A.9: Fitting results for the reaction system ^{86}Kr+^{9}Be.

A	Z	p_0 (MeV/c)	σ_L (MeV/c)	σ_R (MeV/c)	σ_{prod} (mb)
52	25	16606	996	629	6.42E−01 ± 8.53E−02
53	25	16831 ± 32	884 ± 20	698 ± 18	2.11E+00 ± 1.42E−01
54	25	17239 ± 17	857 ± 11	528 ± 3	3.23E+00 ± 2.09E−01
55	25	17670 ± 46	847 ± 15	508 ± 23	3.18E+00 ± 2.18E−01
56	25	17928 ± 56	801 ± 17	609 ± 46	1.66E+00 ± 1.34E−01
57	25	18331 ± 63	803 ± 20	550 ± 48	9.05E−01 ± 7.44E−02
58	25	18729	981	468	3.57E−01 ± 1.01E−01
59	25	19096	726	627	1.13E−01 ± 5.19E−02
60	25	19001	718	459	2.49E−02 ± 6.49E−03
53	26	16505	880	653	5.49E−02 ± 1.95E−02
54	26	17140	917	682	6.71E−01 ± 1.40E−01
55	26	17529 ± 62	878 ± 28	552 ± 33	2.49E+00 ± 1.85E−01
56	26	17854 ± 49	830 ± 18	551 ± 24	4.97E+00 ± 3.46E−01
57	26	18213 ± 45	814 ± 15	541 ± 23	4.40E+00 ± 3.05E−01
58	26	18560 ± 45	786 ± 14	551 ± 24	3.13E+00 ± 2.19E−01
59	26	18818 ± 53	744 ± 17	611 ± 32	1.57E+00 ± 1.17E−01
60	26	19259 ± 78	804 ± 56	585 ± 43	7.04E−01 ± 6.46E−02
61	26	19588	797	614	2.38E−01 ± 4.37E−02
62	26	20374	356	295	4.06E−02 ± 6.09E−03
63	26	20383	692	442	1.65E−02 ± 3.52E−03
64	26	20745	682	473	4.36E−03 ± 2.02E−03
65	26	20957	790	429	7.63E−04 ± 5.37E−04
55	27	17410	951	480	4.54E−02 ± 1.09E−02
56	27	17712	858	644	5.71E−01 ± 1.27E−01
57	27	18119 ± 49	828 ± 23	530 ± 23	2.99E+00 ± 2.22E−01
58	27	18450 ± 44	803 ± 17	523 ± 21	5.94E+00 ± 4.17E−01
59	27	18824 ± 37	792 ± 13	512 ± 15	7.20E+00 ± 4.83E−01
60	27	19142 ± 43	752 ± 14	537 ± 19	4.80E+00 ± 3.28E−01
61	27	19516 ± 44	742 ± 14	535 ± 22	2.96E+00 ± 2.06E−01
62	27	19843 ± 49	717 ± 20	569 ± 25	1.32E+00 ± 9.64E−02
63	27	20231 ± 45	764 ± 45	598 ± 31	5.42E−01 ± 4.59E−02
64	27	20490 ± 80	725 ± 35	585 ± 33	1.69E−01 ± 1.45E−02
65	27	21143	909	581	4.74E−02 ± 1.31E−02
66	27	21512	660	483	1.00E−02 ± 3.65E−03
67	27	21854	684	415	2.96E−03 ± 1.43E−03
68	27	22126	748	406	5.05E−04 ± 2.79E−04
69	27	22485	623	398	8.90E−05 ± 4.39E−05
57	28	17907	847	472	2.77E−02 ± 5.26E−03
58	28	18288	806	633	4.49E−01 ± 6.96E−02

continued on next page

Table A.9: continued from previous page

A	Z	p_0 (MeV/c)	σ_L (MeV/c)	σ_R (MeV/c)	σ_{prod} (mb)
59	28	18696 ± 58	794 ± 24	538 ± 29	2.74E+00 ± 2.10E−01
60	28	19006 ± 44	761 ± 16	545 ± 23	7.62E+00 ± 5.49E−01
61	28	19407 ± 38	761 ± 13	516 ± 15	9.85E+00 ± 6.68E−01
62	28	19746 ± 39	730 ± 14	528 ± 14	8.69E+00 ± 5.82E−01
63	28	20105 ± 41	717 ± 14	541 ± 21	5.10E+00 ± 3.59E−01
64	28	20513 ± 45	728 ± 20	520 ± 18	2.53E+00 ± 1.77E−01
65	28	20800 ± 75	714 ± 46	591 ± 39	1.06E+00 ± 9.08E−02
66	28	21255 ± 42	670 ± 13	537 ± 18	3.43E−01 ± 2.53E−02
67	28	21894	797	415	9.34E−02 ± 2.11E−02
68	28	21899	636	550	2.50E−02 ± 6.50E−03
69	28	22793	842	445	4.75E−03 ± 1.81E−03
70	28	22940	608	389	1.65E−03 ± 6.80E−04
71	28	23470	593	379	1.88E−04 ± 7.82E−05
72	28	23777	781	499	4.01E−05 ± 2.20E−05
60	29	18936	804	579	3.13E−01 ± 4.28E−02
61	29	19201 ± 52	743 ± 21	559 ± 30	2.26E+00 ± 1.79E−01
62	29	19585 ± 42	739 ± 16	542 ± 23	7.35E+00 ± 5.37E−01
63	29	19978 ± 39	738 ± 13	541 ± 19	1.24E+01 ± 8.67E−01
64	29	20437 ± 37	747 ± 12	489 ± 15	1.16E+01 ± 7.86E−01
65	29	20740 ± 38	704 ± 13	519 ± 16	8.67E+00 ± 5.81E−01
66	29	21144 ± 42	713 ± 19	505 ± 16	4.68E+00 ± 3.24E−01
67	29	21457 ± 50	668 ± 26	542 ± 20	2.30E+00 ± 1.72E−01
68	29	22036 ± 62	815 ± 43	494 ± 22	7.90E−01 ± 6.53E−02
69	29	22347 ± 49	651 ± 15	515 ± 19	2.60E−01 ± 1.98E−02
70	29	22944	823	452	8.28E−02 ± 1.68E−02
71	29	23518	803	397	1.77E−02 ± 5.58E−03
72	29	23848	577	369	3.91E−03 ± 1.46E−03
73	29	24238	560	358	1.00E−03 ± 3.05E−04
74	29	24501	542	419	2.02E−04 ± 5.91E−05
75	29	24870	522	334	2.56E−05 ± 1.07E−05
76	29	25252	501	320	4.18E−06 ± 1.39E−06
77	29	25619	479	306	4.60E−07 ± 1.57E−07
78	29	25900	475	315	8.79E−08 ± 2.36E−08
79	29	26064	427	273	1.47E−08 ± 7.23E−09
61	30	19134	780	614	1.74E−02 ± 4.37E−03
62	30	19499	765	567	2.81E−01 ± 6.74E−02
63	30	19858 ± 23	731 ± 14	442 ± 14	2.23E+00 ± 1.63E−01
64	30	20212 ± 41	718 ± 15	530 ± 19	9.03E+00 ± 6.59E−01
65	30	20620 ± 36	721 ± 12	503 ± 16	1.65E+01 ± 1.14E+00
66	30	21033 ± 36	712 ± 12	483 ± 13	1.88E+01 ± 1.25E+00
67	30	21374 ± 38	689 ± 12	501 ± 14	1.34E+01 ± 8.87E−01
68	30	21725 ± 49	671 ± 20	531 ± 19	7.76E+00 ± 5.34E−01
69	30	22233 ± 45	700 ± 19	474 ± 16	3.83E+00 ± 2.68E−01

continued on next page

Table A.9: continued from previous page

A	Z	p_0 (MeV/c)	σ_L (MeV/c)	σ_R (MeV/c)	σ_{prod} (mb)
70	30	22623 ± 66	711 ± 34	510 ± 28	1.56E+00 ± 1.28E−01
71	30	22970 ± 35	628 ± 8	494 ± 13	6.21E−01 ± 4.31E−02
72	30	23559 ± 46	526 ± 4	408 ± 13	2.14E−01 ± 1.58E−02
73	30	24177	594	358	5.02E−02 ± 1.55E−02
74	30	24522	733	383	1.65E−02 ± 6.40E−03
75	30	24959	522	334	2.39E−03 ± 6.24E−04
76	30	25295	501	320	8.77E−04 ± 3.10E−04
77	30	25540	479	328	1.68E−04 ± 7.05E−05
78	30	25866	614	304	3.61E−05 ± 8.83E−06
79	30	26147	531	337	5.52E−06 ± 1.47E−06
80	30	26418	398	344	1.06E−06 ± 3.52E−07
63	31	19694	692	525	9.28E−03 ± 2.89E−03
64	31	20048	719	581	1.68E−01 ± 4.28E−02
65	31	20470 ± 58	722 ± 22	523 ± 43	1.64E+00 ± 1.41E−01
66	31	20840 ± 38	708 ± 14	478 ± 19	7.50E+00 ± 5.54E−01
67	31	21233 ± 37	700 ± 13	499 ± 16	1.75E+01 ± 1.22E+00
68	31	21633 ± 35	691 ± 12	482 ± 13	2.22E+01 ± 1.48E+00
69	31	22030 ± 40	679 ± 13	485 ± 17	1.96E+01 ± 1.32E+00
70	31	22413 ± 59	654 ± 9	486 ± 5	1.32E+01 ± 7.73E−01
71	31	22788 ± 25	647 ± 6	483 ± 4	6.98E+00 ± 4.28E−01
72	31	23378 ± 51	730 ± 27	430 ± 20	3.17E+00 ± 2.34E−01
73	31	23769 ± 27	694 ± 23	484 ± 24	1.53E+00 ± 1.18E−01
74	31	24093 ± 40	600 ± 4	453 ± 14	4.76E−01 ± 3.54E−02
75	31	24642 ± 45	502 ± 5	388 ± 14	1.61E−01 ± 1.26E−02
76	31	25179	401	335	4.87E−02 ± 6.55E−03
77	31	25625	338	288	1.50E−02 ± 2.02E−03
78	31	25974	303	280	3.49E−03 ± 1.00E−03
79	31	26152	282	332	9.06E−04 ± 5.30E−04
80	31	26427	479	344	2.21E−04 ± 9.77E−05
81	31	26841	366	284	2.38E−05 ± 5.43E−06
65	32	20413	754	527	8.12E−03 ± 1.84E−03
66	32	20687	707	571	1.34E−01 ± 3.35E−02
67	32	21154 ± 55	718 ± 21	484 ± 37	1.47E+00 ± 1.22E−01
68	32	21568 ± 38	716 ± 14	413 ± 16	7.62E+00 ± 5.42E−01
69	32	21882 ± 35	688 ± 12	456 ± 17	1.90E+01 ± 1.36E+00
70	32	22208 ± 16	659 ± 8	507 ± 4	2.71E+01 ± 1.78E+00
71	32	22612 ± 16	646 ± 8	499 ± 12	2.48E+01 ± 1.59E+00
72	32	23087 ± 10	634 ± 5	468 ± 23	2.03E+01 ± 1.19E+00
73	32	23498 ± 16	638 ± 9	488 ± 5	1.12E+01 ± 7.00E−01
74	32	23953 ± 11	585 ± 2	432 ± 6	6.95E+00 ± 3.85E−01
75	32	24400 ± 13	607 ± 11	449 ± 11	3.08E+00 ± 1.78E−01
76	32	24807 ± 13	584 ± 5	432 ± 3	1.04E+00 ± 6.19E−02
77	32	25518 ± 13	639 ± 27	306 ± 3	4.47E−01 ± 4.25E−02

continued on next page

Table A.9: continued from previous page

A	Z	p_0 (MeV/c)	σ_L (MeV/c)	σ_R (MeV/c)	σ_{prod} (mb)
78	32	25923	324	276	1.52E−01 ± 2.08E−02
79	32	26222	352	282	6.16E−02 ± 8.07E−03
80	32	26614	398	273	2.00E−02 ± 5.94E−03
81	32	26961	276	231	3.78E−03 ± 9.06E−04
82	32	27249	349	223	1.24E−03 ± 2.27E−04
68	33	21336	694	550	7.90E−02 ± 1.39E−02
69	33	21746 ± 52	695 ± 19	449 ± 33	8.70E−01 ± 7.15E−02
70	33	22045 ± 19	656 ± 10	517 ± 5	5.23E+00 ± 3.57E−01
71	33	22446 ± 18	648 ± 9	509 ± 4	1.64E+01 ± 1.11E+00
72	33	22719 ± 3	604 ± 5	454 ± 2	2.34E+01 ± 1.61E+00
73	33	23293 ± 13	632 ± 7	480 ± 2	3.07E+01 ± 1.92E+00
74	33	23720 ± 17	596 ± 3	444 ± 8	2.51E+01 ± 1.56E+00
75	33	24302 ± 34	643 ± 12	387 ± 11	1.69E+01 ± 1.09E+00
76	33	24725 ± 22	632 ± 11	433 ± 15	9.52E+00 ± 6.17E−01
77	33	25336 ± 20	647 ± 19	309 ± 8	6.69E+00 ± 4.56E−01
78	33	25708 ± 30	614 ± 10	371 ± 21	2.79E+00 ± 2.37E−01
79	33	26186 ± 13	574 ± 16	273 ± 3	1.62E+00 ± 1.46E−01
80	33	26585 ± 15	518 ± 18	255 ± 8	7.10E−01 ± 7.22E−02
81	33	26917 ± 9	469 ± 20	234 ± 2	2.80E−01 ± 2.98E−02
82	33	27006	327	356	9.64E−02 ± 2.88E−02
83	33	27474	218	249	3.33E−02 ± 7.87E−03
70	34	21932	667	526	5.19E−02 ± 9.66E−03
71	34	22336 ± 29	656 ± 19	518 ± 11	6.22E−01 ± 4.66E−02
72	34	22723 ± 21	641 ± 12	503 ± 11	4.30E+00 ± 3.05E−01
73	34	23110 ± 19	633 ± 9	500 ± 3	1.39E+01 ± 9.55E−01
74	34	23648 ± 39	651 ± 12	417 ± 21	2.92E+01 ± 2.12E+00
75	34	23962 ± 18	616 ± 9	489 ± 4	3.19E+01 ± 2.06E+00
76	34	24500 ± 27	608 ± 12	433 ± 18	3.23E+01 ± 2.17E+00
77	34	24965 ± 20	603 ± 9	414 ± 80	2.27E+01 ± 2.29E+00
78	34	25554 ± 22	614 ± 6	330 ± 16	1.81E+01 ± 1.34E+00
79	34	25954 ± 17	578 ± 4	370 ± 59	1.13E+01 ± 9.92E−01
80	34	26421 ± 23	539 ± 4	274 ± 10	6.62E+00 ± 5.36E−01
81	34	26900	495	234	4.65E+00 ± 8.77E−01
82	34	27083	347	257	2.46E+00 ± 5.88E−01
83	34	27468	375	286	1.12E+00 ± 3.22E−01
84	34	27933	319	181	7.53E−01 ± 2.04E−01
72	35	22687	689	381	2.71E−02 ± 8.00E−03
73	35	23093	678	465	3.50E−01 ± 9.94E−02
74	35	23363 ± 22	625 ± 12	497 ± 5	2.35E+00 ± 1.67E−01
75	35	23922 ± 41	648 ± 14	384 ± 24	1.04E+01 ± 8.16E−01
76	35	24330 ± 38	631 ± 12	385 ± 22	2.23E+01 ± 1.65E+00
77	35	24844 ± 38	640 ± 11	351 ± 21	3.18E+01 ± 2.30E+00
78	35	25269 ± 43	599 ± 15	341 ± 22	3.24E+01 ± 2.44E+00

continued on next page

Table A.9: continued from previous page

A	Z	p_0 (MeV/c)	σ_L (MeV/c)	σ_R (MeV/c)	σ_{prod} (mb)
79	35	25732 ± 19	578 ± 9	356 ± 27	3.09E+01 ± 2.63E+00
80	35	26163 ± 10	539 ± 8	255 ± 6	2.16E+01 ± 1.27E+00
81	35	26646 ± 15	495 ± 2	316 ± 12	2.17E+01 ± 1.46E+00
74	36	23276	651	346	9.44E−03 ± 3.57E−03
75	36	23742	639	410	1.79E−01 ± 5.95E−02
76	36	24256 ± 20	651 ± 13	320 ± 18	1.42E+00 ± 1.09E−01
77	36	24643 ± 41	629 ± 14	347 ± 26	6.15E+00 ± 4.89E−01
78	36	25058 ± 34	603 ± 11	355 ± 17	1.58E+01 ± 1.14E+00
79	36	25511 ± 50	571 ± 20	336 ± 27	2.55E+01 ± 2.13E+00
80	36	25948 ± 21	539 ± 2	329 ± 17	3.10E+01 ± 2.60E+00
81	36	26468	542	455	3.45E+01 ± 4.61E+00
82	36	26885	445	285	3.81E+01 ± 4.25E+00

Table A.10: Fitting results for the reaction system ^{86}Kr+^{181}Ta.

A	Z	p_0 (MeV/c)	σ_L (MeV/c)	σ_R (MeV/c)	σ_{prod} (mb)
52	25	16640 ± 30	816 ± 16	509 ± 20	1.12E+01 ± 7.85E−01
53	25	16805 ± 6	763 ± 16	587 ± 10	2.65E+01 ± 1.88E+00
54	25	17272 ± 21	852 ± 18	535 ± 4	3.15E+01 ± 2.17E+00
55	25	17738 ± 26	905 ± 16	484 ± 16	2.53E+01 ± 1.93E+00
56	25	18142 ± 56	952 ± 10	480 ± 35	1.29E+01 ± 9.01E−01
57	25	18378	924	652	5.98E+00 ± 8.07E−01
54	26	17271 ± 29	797 ± 19	518 ± 19	8.77E+00 ± 6.45E−01
55	26	17462 ± 6	748 ± 14	569 ± 9	2.27E+01 ± 1.56E+00
56	26	17957 ± 19	838 ± 16	518 ± 5	3.24E+01 ± 2.16E+00
57	26	18263 ± 26	858 ± 17	587 ± 6	2.29E+01 ± 1.54E+00
58	26	18732	911	673	1.68E+01 ± 1.43E+00
59	26	18979	908	621	7.69E+00 ± 1.81E+00
56	27	17963 ± 31	814 ± 30	519 ± 25	5.70E+00 ± 5.46E−01
57	27	18304 ± 12	804 ± 9	483 ± 32	1.76E+01 ± 1.14E+00
58	27	18619 ± 11	823 ± 20	494 ± 3	2.78E+01 ± 1.70E+00
59	27	18927 ± 22	840 ± 15	564 ± 4	2.68E+01 ± 1.74E+00
60	27	19430	904	463	1.75E+01 ± 1.59E+00
61	27	19628	887	598	1.31E+01 ± 4.39E+00
58	28	18639 ± 32	811 ± 32	511 ± 37	4.23E+00 ± 4.80E−01
59	28	18960 ± 22	815 ± 20	502 ± 12	1.21E+01 ± 8.42E−01
60	28	19269 ± 17	811 ± 15	499 ± 3	2.45E+01 ± 1.60E+00
61	28	19581 ± 19	818 ± 14	536 ± 3	2.59E+01 ± 1.67E+00
62	28	20015 ± 33	879 ± 17	630 ± 9	2.05E+01 ± 1.30E+00

continued on next page

Table A.10: continued from previous page

A	Z	p_0 (MeV/c)	σ_L (MeV/c)	σ_R (MeV/c)	σ_{prod} (mb)
63	28	20278	867	560	1.09E+01 ± 3.06E+00
61	29	19590 ± 25	780 ± 21	503 ± 11	8.51E+00 ± 5.68E−01
62	29	19907 ± 20	805 ± 18	510 ± 4	1.88E+01 ± 1.31E+00
63	29	20255 ± 21	815 ± 15	541 ± 5	2.45E+01 ± 1.55E+00
64	29	20784 ± 19	884 ± 13	440 ± 8	2.11E+01 ± 1.35E+00
65	29	21220	936	702	1.90E+01 ± 5.91E+00
66	29	21368	802	527	1.26E+01 ± 2.40E+00
63	30	20254 ± 73	757 ± 36	488 ± 38	7.81E+00 ± 6.21E−01
64	30	20599 ± 26	767 ± 20	510 ± 9	1.74E+01 ± 1.06E+00
65	30	20954 ± 19	783 ± 16	494 ± 6	2.29E+01 ± 1.39E+00
66	30	21279 ± 21	782 ± 15	520 ± 5	2.33E+01 ± 1.62E+00
67	30	21724 ± 39	831 ± 20	601 ± 17	1.71E+01 ± 1.08E+00
68	30	21994 ± 22	759 ± 17	481 ± 3	1.05E+01 ± 8.36E−01
66	31	21220 ± 77	744 ± 36	488 ± 38	1.02E+01 ± 1.33E+00
67	31	21592 ± 23	747 ± 16	496 ± 14	2.06E+01 ± 1.61E+00
68	31	21952 ± 24	766 ± 15	517 ± 7	2.04E+01 ± 1.18E+00
69	31	22339 ± 29	772 ± 18	537 ± 9	1.81E+01 ± 1.21E+00
70	31	22845	801	597	1.31E+01 ± 1.51E+00
71	31	23130 ± 28	747 ± 24	459 ± 7	9.61E+00 ± 1.71E+00
68	32	21903 ± 42	715 ± 27	501 ± 34	8.53E+00 ± 1.02E+00
69	32	22190 ± 21	707 ± 17	437 ± 4	1.79E+01 ± 2.06E+00
70	32	22657 ± 21	749 ± 17	469 ± 5	2.19E+01 ± 1.49E+00
71	32	23060 ± 37	751 ± 20	527 ± 12	1.86E+01 ± 1.67E+00
72	32	23260 ± 46	706 ± 22	525 ± 26	1.34E+01 ± 1.00E+00
73	32	23867	772	361	9.18E+00 ± 1.68E+00
70	33	22544	675	419	5.60E+00 ± 8.25E−01
71	33	22977	682	518	1.30E+01 ± 1.60E+00
72	33	23343 ± 46	690 ± 28	495 ± 47	1.78E+01 ± 1.97E+00
73	33	23843	735	554	2.02E+01 ± 3.33E+00
74	33	24570	843	843	2.36E+01 ± 5.28E+00
75	33	24412 ± 31	613 ± 18	337 ± 19	1.13E+01 ± 1.16E+00
71	34	23035	818	450	1.54E+00 ± 2.45E−01
72	34	23256	650	460	4.05E+00 ± 6.32E−01
73	34	23688	681	479	9.19E+00 ± 1.40E+00
74	34	24100	687	495	1.53E+01 ± 2.53E+00
75	34	24535	723	541	1.96E+01 ± 3.63E+00
76	34	24901	714	536	1.88E+01 ± 3.48E+00
77	34	25391	660	309	1.49E+01 ± 3.69E+00
74	35	23927	699	443	2.22E+00 ± 3.86E−01
75	35	24316 ± 35	648 ± 33	423 ± 49	5.40E+00 ± 4.88E−01
76	35	24699 ± 43	639 ± 25	460 ± 44	9.72E+00 ± 7.16E−01
77	35	25260	697	521	1.38E+01 ± 1.53E+00

continued on next page

Table A.10: continued from previous page

A	Z	p_0 (MeV/c)	σ_L (MeV/c)	σ_R (MeV/c)	σ_{prod} (mb)
78	35	25610	673	500	1.72E+01 ± 2.15E+00
77	36	25017	629	403	3.06E+00 ± 4.15E−01
78	36	25600	665	500	6.43E+00 ± 7.13E−01
79	36	25895	640	480	9.28E+00 ± 2.12E+00
80	36	26241	509	367	1.22E+01 ± 2.48E+00

Bibliography

[1] S. I. Glashow. *Nuclear Physics*, **22**:579–588, 1961.

[2] A. Salam. *Physical Review*, **127**:331–334, 1962.

[3] S. Weinberg. *Physical Review Letters*, **19**:1264–1266, 1967.

[4] M. Gell-Mann. *Physics Letters*, **8**:214–215, 1964.

[5] `http://www.phy.anl.gov/ria/figs/nl.jpg`.

[6] J. M. Blatt and V. F. Weisskopf. *Theoretical nuclear physics*. John Wiley & Sons, Inc., 1952.

[7] E. Rutherford and H. Geiger. *Proceedings of the Royal Society of London, Series A*, **81**:162–173, 1908.

[8] J. M. Robson. *Physical Review*, **78**:311–312, 1950.

[9] A. C. Mueller and B. M. Sherrill. *Annual Review Nuclear Particle Science*, **43**, 1993.

[10] D. F. Geesaman, C. K. Gelbke, R. V. F. Janssens, and B. M. Sherrill. *Annual Review Nuclear Particle Science*, **56**:53–92, 2006.

[11] M. Thoennessen. *Reports on Progress in Physics*, **67**:1187–1232, 2004.

[12] Kenneth S. Krane. *Introductory nuclear physics*. John Wiley & Sons, 1988.

[13] C. F. Weizsäcker. *Zeitung im Physics A*, **96**:431, 1935.

[14] I. Tanihata. *Nuclear Physics A*, **522**:275c–292c, 1991.

[15] I. Tanihata, D. Hirata, T. Kobayashi, S. Shimoura, K. Sugimoto, and H. Toki. *Physical Letters B*, **289**:261–266, 1992.

[16] N. Fukunishi, T. Otsuka, and I. Tanihata. *Physical Review C*, **48**:1648–1655, 1993.

[17] T. Motobayashi, Y. Ikeda, Y. Ando, K. Ieki, M. Inoue, N. Iwasa, T. Kikuchi, M. Kurokawa, W. Moryia, S. Ogawa, H. Murakami, S. Shimuoura, Y. Yanagisawa, T. Nakamura, Y. Watanabe, M. Ishihara, T. Teranishi, H. Okuno, and R. F. Casten. *Physical Letters B*, **346**:9–14, 1995.

[18] Scientific Opportunities with Fast Fragmentation Beams from RIA. 2000.

[19] G. Kraft. *Physica Medica*, **27**:13–20, 2001.

[20] `http://www.bnl.gov/medical/NASA/NSRL_description.asp`.

[21] G. Kraft. *Strahlentherapie und Okologie*, **166**:10, 1990.

[22] G. Taucher-Scholz, C. Wiese, and G. Kraft. *Radiation Research*, **148**:504–506, 1997.

[23] `http://www.gsi.de/portrait/Broschueren/Therapie/Krebstherapie_e.html`.

[24] J. Debus, K. D. Gross, and M. Pavlovic. Proposal for a dedicated Ion Beam Facility for cancer therapy. GSI, Darmstadt, 1998.

[25] C. L. Hebel, E. L. Christensen, F. A. Donath, W. E. Falconer, L. J. Lidofsky, E. J. Moniz, T. H. Moss, R. L. Pigford, T. H. Pigford, G. I. Rochlin, R. H. Silsbee, M. E. Wrenn, H. Frauenfelder, T. L. Cairns, W. K. H. Panofsky, and M. G. Simmons. *Rev. Mod. Phys.*, 50:S1–S176, 1978.

[26] C. D. Bowman, E. D. Arthur, P. W. Lisowski, G. P. Lawrence, R. J. Jensen, J. L. Anderson, B. Blind, M. Cappiello, J. W. Davidson, T. R. England, L. N. Engel, R. C. Haight, H. G. Hughes, J. R. Ireland, R. A. Krakowski, R. J. LaBauve, B. C. Letellier, R. T. Perry, G. J. Russell, K. P. Staudhammer, G. Versamis, and W. B. Wilson. *Nuclear Instruments and Methods A*, **320**:336–367, 1992.

[27] `http://aaa.lanl.gov`.

[28] H. Geissel, G. Münzenberg, and K. Rüsager. *Annual Review Nuclear Particle Science*, **45**:163–203, 1995.

[29] J. R. J. Bennett. *Nuclear Instruments and Methods B*, **126**:105–112, 1997.

[30] R. E. Laxdal. *Nuclear Instruments and Methods B*, **204**:400–409, 2003.

[31] W. Mittig. *Journal of Physics G*, **24**:1331–1339, 1998.

[32] M. Gaelens, M. Cogneau, M. Loiselet, and G. Ryckewaert. *Nuclear Instruments and Methods B*, **204**:48–52, 2003.

[33] O. Kester D. Habs, T. Sieber, H. Bongers, S. Emhofer, P. Reiter, P.G. Thirolf, G. Bollena, J. Aystö, O. Forstner, H. Ravn, T. Nilsson, M. Oinonen, H. Simon, J. Cederkal, F. Ames, P. Schmidt, G. Huber, L. Liljeby, O. Skeppstedt, K.G. Rensfelt, F. Wenander, B. Jonson, G. Nyman, R. von Hahn, H. Podlechf, R. Repnow f, C. Gund, D. Schwal, A. Schempp, K.-U. Kühnel, C. Welsch, U. Ratzinger, G. Walter, A. Huckiand K. Kruglov, M. Huyse, P. Van den Bergh jand P. Van Duppen, L. Weissman, A.C. Shotter, A.N. Ostrowski, T. Davinson, P.J. Woods, J. Cub, A. Richter, and G. Schrieder. *Hyperfine Interactions*, **129**:43–66, 2000.

[34] D. W. Stracener. *Nuclear Instruments and Methods B*, **204**:42–47, 2003.

[35] T. Kubo, M. Ishihara, N. Inabe, H. Kumagai, I. Tanihata, and K. Yoshida. *Nuclear Instruments and Methods B*, **70**:309–319, 1992.

[36] The K500 $\otimes$ K1200, A coupled cyclotron facility at the National Superconducting Cyclotron Laboratory. NSCL Report MSUCL-939, July 1994.

[37] C. Bertulani and P. Danielewicz. *Introduction to nuclear reactions*. Institute of Physics, 2004.

[38] H. W. Barz, J. P. Bondorf, R. Donangelo, and H. Schulz. *Physical Letters B*, **169**:318–322, 1986.

[39] H. A. Grunder, W. D. Hartsough, and E. J. Lofgren. *Science*, **174**:1128–1129, 1971.

[40] H. H. Heckman, D. E. Greiner, P. J. Lindstrom, and F. S. Bieser. *Science*, **174**:1130–1131, 1971.

[41] Y. P. Viyogi, T. J. M. Symons, P. Doll, D. E. Greiner, H. H. Heckman, D. L. Hednrie, P. J. Lindstrom, J. Mahoney, D. K. Scott, K. Van Bibber, G. D. Westfall, H. Wieman, H. J. Crawford, C. McParland, and C. K. Gelbke. *Physical Review Letters*, **42**:33–36, 1979.

[42] G. D. Westfall, T. J. M. Symons, D. E. Greiner, H. H. Heckman, P. J. Lindstrom, J. Mahoney, A. C. Shotter, D. K. Scott, H. J. Crawford, C. McParland, T. C. Awes, C. K. Gelbke, and J. M. Kidd. *Physical Review Letters*, **43**:1859–1862, 1979.

[43] B. M. Sherrill, D. J. Morrissey, J. A. Nolen, and J. A. Winger. *Nuclear Instruments and Methods B*, **56–57**:1106–1110, 1991.

[44] H. Geissel, P. Armbruster, K. H. Behr, A. Brünle, K. Burkard, M. Chen, H. Folger, B. Franczak, H. Keller, O. Klepper, B. Langenbeck, F. Nickel, E. Pfeng, M. Pfützner, E. Roeckl, K. Rykaczewski, I. Schall, D. Schardt, C. Scheidenberger, K.-H. Schmidt, A. Schröter, T. Schwab, K. Sümmerer, M. Weber, G. Münzenberg, T. Brohm, H.-G. Clerc, M. Fauerbach, J. J. Gaimard, A. Grewe, E. Hanelt, B. Knödler, M. Steiner, B. Voss, J. Weckenmann, C. Ziegler, A. Magel, H. Wollnik, J. P. Dufour, Y. Fujita, D. J. Vieira, and B. Sherrill. *Nuclear Instruments and Methods B*, **70**:286, 1992.

[45] J. D. Bowman, W. J. Swiatecki, and C. F. Tsang. Abrasion and Ablation of heavy ions. LBL Report, LBL-2908, 1973.

[46] The Science of the Rare Isotope Accelerator (RIA), 2005.

[47] K. Sümmerer, W. Brüchle, D. J. Morrissey, M. Schädel, B. Szweryn, and Y. Weifan. *Physical Review C*, **42**:2546–2561, 1990.

[48] K. Sümmerer and B. Blank. *Physical Review C*, **61**:034607, 2000.

[49] Glenn F. Knoll. *Radiation detection and measurement*. John Wiley & Sons, 2000.

[50] A. Stolz, T. Baumann, T. N. Ginter, D. J. Morrissey, M. Portillo, B. M. Sherrill, M. Steiner, and J. W. Stetson. *Nuclear Instruments and Methods B*, **241**:858–861, 2005.

[51] D. J. Morrissey. *Nuclear Physics A*, **616**:45c–55c, 1997.

[52] B. M. Sherrill. *Prog. Theor. Physics*, **146**:60–69, 2002.

[53] H. Koivisto, D. Cole, A. Fredell, C. Lyneis, P. Miller, J. Moskalik, B. Nurnberger, and J. Ottarson. *Proceedings of the Workshop on the Production of Intense Beams of Highly Charged ions (Italian Physical Society)*, **72**:83, 200.

[54] S. Gammino, G. Ciavola, T. Antaya, and K. Harrison. **67**:155–160, 1996.

[55] D. J. Morrissey, B. M. Sherrill, M. Steiner, A. Stolz, and I. Wiedenhoever. *Nuclear Instruments and Methods B*, **204**:90–96, 2003.

[56] D. Bazin, O. Tarasov, M. Lewitowicz, and O. Sorlin. *Nuclear Instruments and Methods A*, **482**:307–327, 2002.

[57] `http://sourceforge.net/projects/nscldaq/`.

[58] `http://docs.nscl.msu.edu/daq/spectcl/`.

[59] M. Notani. *Projectile Fragmentation Reactions and Production of Nuclei near the Neutron Drip-line*. PhD thesis, University of Tokyo, 2000.

[60] `http://www.rarf.riken.go.jp/rarf/exp/comp/daq/daq.html`.

[61] `http://www.ne.rikkyo.ac.jp/~takeuchi/`.

[62] `http://paw.web.cern.ch/paw/`.

[63] C. Scheidenberg, T. Stöhlker, W. E. Meyerhof, H. Geissel, P. H. Mokler, and B. Blank. *Nuclear Instruments and Methods B*, **142**:441, 1998.

[64] A. S. Goldhaber. *Physical Letters B*, **53**:306–308, 1974.

[65] D. Bazin, D. Guerreau, R. Anne, D. Guillemaud-Mueller, A. C. Mueller, and M. G. Saint-Laurent. *Nuclear Physics A*, **515**:349–364, 1990.

[66] N. Iwasa, H. Geissel, G. Münzenberg, C. Scheidenberger, T. Schwab, and H. Wollnik. *Nuclear Instruments and Methods B*, **126**:284–289, 1997.

[67] J. Stetson. private communications.

[68] N. Aoi. private communications.

[69] J. P. Conca. New approach to evaluate the angular transmission of the in-flight separator FRS at GSI. Master's thesis, Universidad de Santiago de Compostela, 1999.

[70] K. Van Bibber, D. L. Hendrie, D. K. Scott, H. H. Weiman, L. S. Schroeder, J. V. Geaga, S. A. Cessin, R. Treuhaft, Y. J. Grossiord, J. O. Rasmussen, and C. Y. Wong. *Physical Review Letters*, **43**:840–844, 1979.

[71] R. Dayras, A. Pagano, J. Barrette, B. Berther, D. M. De Castro Rizzo, E. Chavez, O. Cisse, R. Legrain, M. C. Mermaz, E. C. Pollacco, H. Delagrange, W. Mittig, B. Heusch, R. Coniglione, G. Lanzano, and A. Palmeri. *Nuclear Physics A*, **460**:299–323, 1986.

[72] S. Lukyanov. private communications.

[73] D. Bazin, J. A. Caggiano, B. M. Sherrill, J. Yurkon, and A. Zeller. *Nuclear Instruments and Methods B*, **204**:629, 2002.

[74] Ch. O. Bacri, P. Roussel, V. Borrel, F. Clapier, R. Anne, M. Bernas, Y. Blumenfeld, H. Gauvin, J. Herault, J. C. Jacmart, F. Pougheon, J. L. Sida, C. Stéphan, T. Suomijarvi, and L. Tassan-Got. *Nuclear Physics A*, **555**:477–498, 1993.

[75] M. Weber, C. Donzaud, J. P. Dufour, H. Geissel, A. Grewe, D. Guillemaud-Mueller, H. Keller, M. Lewitowicz, A. Magel, A. C. Mueller, G. Münzenberg, F. Nickel, M. Pfützner, A. Piechaczek, M. Pravikoff, E. Roeckl, K. Rykaczewski, M. G. Saint-Laurent, I. Schall, C. Stéphan, K. Sümmerer, L. Tassan-Got, D. J. Vieira, and B. Voss. *Nuclear Physics A*, **578**:659–672, 1994.

[76] R. Pfaff, D. J. Morrissey, M. Fauerbach, M. Hellström, J. H. Kelley, R. A. Kryger, B. M. Sherrill, M. Steiner, J. S. Winfield, J. A. Winger, S. J. Yennello, and B. M. Young. *Physical Review C*, **51**:1348–1355, 1995.

[77] D. J. Morrissey. *Physical Review C*, **39**:460–470, 1989.

[78] E. J. Moniz, I. Sick, R. R. Whitney, J. R. Ficenec, R. D. Kephart, and W. P. Trower. *Physical Review Letters*, **26**:445–448, 1971.

[79] L. Tassan-Got and C. Stéphan. *Nuclear Physics A*, **524**:121–140, 1991.

[80] G. Souliotis. *Study of projectile fragmentation reactions at intermediate energies*. PhD thesis, Michigan State University, 1992.

[81] R. Pfaff. *Projectile fragmentation of krypton isotopes at intermediate energies*. PhD thesis, Michigan State University, 1996.

[82] G. Bertsch. *Physical Review Letters*, **46**:472–473, 1981.

[83] V. Borrel, D. Guerreau, J. Galin, B. Gatty, D. Jacquet, and X. Tarrago. *Zeitschrift für Physik A*, **314**:191–197, 1983.

[84] J. B. Cumming, P. E. Haustein, and H.-C. Hseuh. *Physical Review C*, **24**:2162–2173, 1981.

[85] S. B. Kaufman, M. S. Freedman, D. J. Henderson, E. P. Steinberg, B. D. Wilkins, A. Baden, H. H. Gutbrod, M. R. Haier, J. Peter, H. G. Ritter, H. Stelzer, A. I. Warwick, H. H. Wieman, and F. Weik. *Physical Review C*, **26**:2694–2697, 1982.

[86] E. M. Friedlander and H. H. Heckmann. *Treatise on Heavy Ion Science*. Plenum, 1985.

[87] G. Rudstam. *Zeitschrift für Naturforschung A*, **21**:1027, 1966.

[88] W. R. Webber, J. C. Kish, and D. A. Schier. *Physical Review C*, **41**:547–565, 1990.

[89] B. Blank, S. Andriamonje, R. Del Moral, J. P. Dufour, A. Fleury, T. Josso, M. S. Pravikoff, S. Czajkowski, Z. Janas, A. Piechaczek, E. Roeckl, K. H. Schmidt, K. Sümmerer, W. Trinder, M. Weber, T. Brohm, A. Grewe, E. Hanelt, A. Heinz, A. Junghans, C. Röhl, S. Steinhäuser, B. Voss, and M. Pfützer. *Physical Review C*, **50**:2398–2407, 1994.

[90] J. Reinhold, J. Friese, H.-J. Körner, R. Schneider, K. Zeitelhack, H. Geissel, A. Magel, G. Münzenberg, and K. Sümmerer. *Physical Review C*, **58**:247–255, 1998.

[91] M. de Jong, K.-H. Schmidt, B. Blank, C. Böckstiegel, T. Brohm, H.-G. Clerc, S. Czajkowski, M. Dornik, H. Geissel, A. Grewe, E. Hanelt, A. Heinz, H. Irnich, A. R. Junghans, A. Magel, G. Münzenberg, F. Nickel, M. Pfützner, A. Piechaczek, C. Scheidenberger, W. Schwab, S. Steinhäuser, K. Sümmerer, W. Trinder, B. Voss, and C. Ziegler. *Nuclear Physics A*, **628**:479–492, 1998.

[92] B. M. Sherrill. *Nuclear Instruments and Methods B*, **204**:765–770, 2003.

[93] GSI. An international accelerator facility for beams of ions and antiprotons.

[94] T. Motobayashi. *Nuclear Instruments and Methods B*, **204**:736–738, 2003.

[95] C.-X. Chen, S. Albergo, Z. Caccia, S. Costa, H. J. Crawford, M. Cronqvist, J. Engelage, L. Greiner, T. G. Guzik, A. Insolia, C. N. Knott, P. J. Lindstrom, M. McMahon, J. W. Mitchell, R. Potenza, G. V. Russo, A. Soutoul, O. Testard, C. E. Tull, C. Tuve, C. J. Waddington, W. R. Webber, and J. P. Wefel. *Physical Review C*, **56**:1536–1543, 1997.

[96] B. T. Roeder, K. W. Kemper, N. Aoi, D. Bazin, M. Bowen, C. M. Campbell, J. M. Cook, D.-C. Dinca, A. Gade, T. Glasmacher, H. Iwasaki, S. Kanno, T. Motobayashi, W. F. Mueller, T. Nakamura, H. Sakurai, H. Suzuki, S. Takeuchi, J. R. Terry, K. Yoneda, and H. Zwahlen. *Physical Review C*, in press.

[97] K. Sümmerer. *Nuclear Instruments and Methods B*, **204**:278–281, 2003.

[98] S. Kox, A. Gamp, P. Cherkaoui, A. J. Cole, N. Longequeue, J. Menet, C. Perrin, and J. B. Viano. *Nuclear Physics A*, **420**:162–172, 1984.

[99] M. B. Tsang, C. K. Gelbke, X. D. Liu, W. G. Lynch, W. P. Tan, G. Verde, and H. S. Xu. *Physical Review C*, **64**:054615, 2001.

[100] G. A. Souliotis, M. Veselsky, D. V. Shetty, and S. J. Yennello. *Physical Letters B*, **588**:35–42, 2004.

[101] D. J. Morrissey, W. R. Marsh, R. J. Otto, W. Loveland, and G. T. Seaborg. *Physical Review C*, **18**:1267–1274, 1978.

[102] J. Hüfner, K. Schäfer, and B. Schürmann. *Physical Review C*, **12**:1888–1898, 1975.

[103] J. W. Wilson and L. W. Townsend. *Nuclear Instruments and Methods B*, **18**:225–231, 1987.

[104] J.-J. Gaimard and K.-H. Schmidt. *Nuclear Physics A*, **531**:709–745, 1991.

[105] K.-H. Schmidt, M. V. Ricciardi, A. S. Botvina, and T. Enqvist. *Nuclear Physics A*, **710**:157–179, 2002.

[106] O. Tarasov and D. Bazin. *Nuclear Instruments and Methods B*, **204**:174–178, 2003.

[107] A. Stolz, T. Baumann, N. H. Frank, T. N. Ginter, G. W. Hitt, E. Kwan, M. Mocko, W. Peters, A. Schiller, C. S. Sumithrarachchi, and M. Thoennessen. *Physical Letters B*, **627**:32–37, 2005.

[108] D. Lacroix, A. Van Lauwe, and D. Durand. *Physical Review C*, **69**:054604, 2004.

[109] J. Blocki, J. Randrup, W. J. Swiatecki, and C. F. Tsang. *Annals of Physics*, **105**:427, 1977.

[110] R. J. Charity, M. A. McMahan, G. J. Wozniak, R. J. McDonald, L. G. Moretto, D. G. Srantites, L. G. Sobotka, G. Guarino, A. Pantaleo, L. Fiore, A. Gobbi, and K. D. Hildenbrand. *Nuclear Physics A*, **483**:371–405, 1988.

[111] `http://caeinfo.in2p3.fr/theorie/hipse.htm`.

[112] S. Hudan, A. Chbihi, J. D. Frankland, A. Mignon, J. P. Wieleczko, G. Auger, N. Bellaize, B. Borderie, A. Botvina, R. Bougault, B. Bouriquet, A. M. Buta, J. Colin, D. Cussol, R. Dayras, D. Durand, E. Galichet, D. Guinet, B. Guiot, G. Lanzalone, 6 F. Lavaud P. Lautesse, 2 R. Legrain J. F. Lecolley, N. Le Neindre, O. Lopez, L. Manduci, J. Marie, 4 J. Normand L. Nalpas, M. Pârlog, P. Pawlowski, M. Pichon, E. Plagnol, M. F. Rivet, E. Rosato, R. Roy, J.C. Steckmeyer, G. Tabacaru, B. Tamain, A. van Lauwe, E. Vient, M. Vigilante, and C. Volant. *Physical Review C*, **67**:064613, 2003.

[113] D. Cussol, T. Lefort, J. Péter, G. Auger, Ch. O. Bacri, F. Bocage, B. Borderie, R. Bougault, R. Brou, Ph. Buchet, J. L. Charvet, A. Chbihi, J. Colin, R. Dayras, A. Demeyer, D. Doré, D. Durand, P. Eudes, E. de Filippo, J. D. Frankland, E. Galichet, E. Genouin-Duhamel, E. Gerlic, M. Germain, D. Gourio, D. Guinet, and P. Lautesse. *Physical Review C*, **65**:044604, 2002.

[114] D. Lacroix. private communications.

[115] A. Ono. private communications.

[116] A. Ono and H. Horiuchi. *Progress in Particle and Nuclear Physics*, **53**:501–581, 2004.

[117] A. Ono, H. Horiuchi, T. Maruyama, and A. Ohnishi. *Physical Review Letters*, **68**:2898–2900, 1992.

[118] G. F. Bertsch and S. Das Gupta. *Physics Reports*, **160**:189–233, 1988.

[119] W. Cassing, V. Metag, U. Mosel, and K. Niita. *Physics Reports*, **188**:363–449, 1990.

[120] A. Ono. *Physical Review C*, **59**:853–864, 1999.

[121] H. Horiuchi. *Nuclear Physics A*, **522**:257c–274c, 1991.

[122] A. Ono, P. Danielewicz, W. A. Friedman, W. G. Lynch, and M. B. Tsang. *Physical Review C*, **68**:051601, 2003.

[123] W. Bauhoff, E. Caurier, B. Grammaticos, and M. Ploszajczak. *Physical Review C*, **32**:1915, 1985.

[124] G. Audi, A. H. Wapstra, and C. Thibault. *Nuclear Physics A*, **729**:337–676, 2003.

[125] `http://hpc.msu.edu`.

[126] P. Danielewicz. *Nuclear Physics A*, **673**:375, 2000.

[127] X. Campi and J. Hüfner. *Physical Review C*, **24**:2199, 1981.

[128] A. S. Iljinov, M. V. Mebel, N. Bianchi, E. De Sanctis, C. Guaraldo, V. Lucherini, V. Muccifora, E. Polli, A. R. Reolon, and P. Rossi. *Nuclear Physics A*, **543**:517–557, 1992.

[129] D. Henzlová. *Systematic investigation of the isotopic distributions measured in the fragmentation of ^{124}Xe and ^{136}Xe projectiles.* PhD thesis, Czech Technical University, 2005.

[130] N. Bohr. *Nature*, **137**:344, 1936.

[131] W. Hauser and H. Feshbach. *Physical Review*, **87**:366–373, 1952.

[132] L. Morretto. *Nuclear Physics A*, **247**:211–230, 1975.

[133] H. J. Krappe, J. R. Nix, and A. J. Sierk. *Physical Review C*, **20**:992, 1979.

[134] H. A. Bethe. *Physical Review*, **50**:332–341, 1936.